Ina A. Oestroem

In-Silico Design of Cage-Type Cyclophanes

Florianópolis

Maio de 2019

Ina A. Oestroem

In-Silico Design of Cage-Type Cyclophanes

Dissertation submitted to the Graduation Program in Chemistry to obtain the Degree of Master in Chemistry, at the main area of Physical-Chemistry.

Universidade Federal de Santa Catarina
Departamento de Química
Programa de Pós-Graduação em Química

Supervisor: Prof. Dr. Giovanni Finoto Caramori

Florianópolis
Maio de 2019

Ficha de identificação da obra elaborada pelo autor,
através do Programa de Geração Automática da Biblioteca Universitária da UFSC.

Oestroem, Ina Araujo
In-Silico Design of Cage-Type Cyclophanes / Ina Araujo Oestroem ; orientador, Giovanni Finoto Caramori, 2019.
239 p.

Dissertação (mestrado) - Universidade Federal de Santa Catarina, Centro de Ciências Físicas e Matemáticas, Programa de Pós-Graduação em Química, Florianópolis, 2019.

Inclui referências.

1. Química. 2. Supramolecular. 3. Non-Covalent Interactions. 4. Cyclophanes. 5. Host-Guest. I. Caramori, Giovanni Finoto. II. Universidade Federal de Santa Catarina. Programa de Pós-Graduação em Química. III. Título.

Ina A. Oestroem

In-Silico Design of Cage-Type Cyclophanes

Dissertation submitted to the Graduation Program in Chemistry to obtain the Degree of Master in Chemistry, at the main area of Physical-Chemistry.

This dissertation was approved for the title of "Master in Chemistry", and approved in its final form by the Graduate Program in Chemistry.

Florianópolis, 31 de Maio de 2019

Vanderlei Gageiro Machado

Prof. Dr. Vanderlei Gageiro Machado
Coordenador do Programa de
Pós-Graduação em Química

Giovanni F. Caramori

Prof. Dr. Giovanni Finoto Caramori
Advisor

Prof. Dr. Juan Jacob Eduardo Humeres Allende
Universidade Federal de Santa Catarina

Prof. Dr. Josiel B. Domingos
Universidade Federal de Santa Catarina

Prof. Dr. Leone Carmo Garcia
Instituto Federal de Santa Catarina

Florianópolis
Maio de 2019

To my grandparents, in memoriam,
I wish you were still here to see this work.

To my mother,
for being such a strong woman.

To all women in science,
for making a huge difference.

Acknowledgements

To **Prof. Dr. Juan Jacob Eduardo Humeres Allende**, for keeping linked to chemistry after undergraduate, and inspiring me to return to the chemistry field after a five-year gap.

To **Prof. Dr. Giovanni F. Caramori**, for dedication, acuteness, the transmission of knowledge and participation in my training, and for making the path towards the end of this master dissertation smooth.

To **Alexandre O. Ortolan**, to have co-oriented me, even when no official acknowledgment of this was possible to be done. This work would not be the same if it were not for your support.

To my parents **Yara R. Guasque Araujo** and **Rubens Oestroem**, for the support, understanding, and dedicated parenthood. To my sister **Cora Oestroem**, for the good moments of coexistence. To my partner **Maíra B. Scirea**, for taking care of me, sharing her life, believing in my dreams, and for the love that never ends. To **Mia**, my beloved dog, which handled all the lack of attention and walks during the hard working days.

To the friends that were part of this journey: **Alechania Misturini** and **Felipe Schneider**, for all the help, great discussions, partnership, and patience that was required to coexist with me.

To **Prof. Dr. Mark Mascal**, for the collaboration with the deposited cylindrophanes x-ray structures, and for answering my endless emails.

To **Prof. Dr. Renato Parreira**, for the collaboration and with the computational resources.

To **CAPES** for a Master's scholarship (Grant nro. 1732086).

To ⟨**GE**|**EM**⟩, for computational resources.

To the high-quality public university **UFSC**, because knowledge should be accessible for everyone interested to learn.

To all the people who directly or indirectly contributed to the accomplishment of this work.

“The important thing is not to stop questioning.
Curiosity has its own reason for existence.
One cannot help but be in awe when he contemplates the mysteries of eternity,
It is enough if one tries merely to comprehend a little of this mystery each day.”
– Albert Einstein

“Change your life today.
Don’t gamble on the future, act now, without delay.”
– Simone de Beauvoir

Abstract

Introdução

Sistemas moleculares em química supramolecular têm uma grande importância para entender a bioquímica de seres vivos, e potencial aplicação nas áreas de medicina, farmácia, engenharia química e ambiental, entre outras. Com a evolução do conhecimento a cerca de interações intermoleculares, muitos estudos teóricos e experimentais tomaram como frente este tópico desenvolvendo ainda mais o conceito, o que levou a diversas aplicações dos sistemas supramoleculares. Ciclofanos do tipo gaiola são conhecidos por possuírem estruturas moleculares com ao menos um anel aromático, e cadeias carbônicas conectadas ao sistema π, formando uma cavidade. A modificação química estrutural em ciclofanos, com relação a natureza eletrônica dos anéis, e dos heteroátomos nas pontes saturadas, pode influenciar interações intramoleculares que estes têm com outras espécies, bem como suas interações intramoleculares.

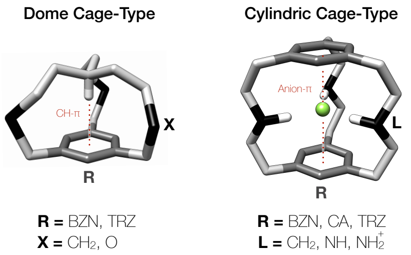

O presente projeto de pesquisa desvendou a natureza física das interações não covalentes em dois tipos de ciclofanos do tipo gaiola, através de estudos de estrutura eletrônica molecular dos grupos funcionais. O primeiro tipo de cilcofano com uma gaiola em formato de cúpula (*dome cage-type*), e o segundo com formato cilíndrico (*cylindric cage-type*). No

ciclofano tipo-cúpula, que possui um hidrogênio interno a gaiola e apontado em dieração ao centro de seu anel aromático, procurou-se encontrar a menor distância C–H$\cdots\pi$, bem como explicar por quais motivos esta estrutura é capaz de aproximar tais grupos funcionais. No **ciclofano tipo-cilíndro**, também conhecidos como cilindrofanos, que contém dois anéis arênicos, três pontes alífaticas conectadas ao sistema aromáticos nas posições 1,3,5, e um heteroátomolocalizado em uma posição equidistante aos anéis, estudou-se a influência que modificações nos grupos funcionais da gaiola do sistema aceptor têm na coordenação do ânion fluoreto.

Objetivos

O principal foco deste trabalho foi compreender a natureza física de interações não-covalentes nos dois tipos de ciclofanos apresentados na ilustração esquematica acima. Através de métodos de estrutura eletrônica molecular, procurou-se racionalizar a influência que as modificações estruturais propostas pudessem ter a cerca do problema químico específico de cada ciclofano. Os objetivos específicos foram:

- **Ciclofanos Tipo-Cúpula:** encontrar via estrutura eletrônica, qual ciclofano teria menor proximidade C–H$\cdots\pi$, verificar se a distância obtida é menor do que a reportada na literatura, e explicar porque a estrutura do ciclofano proposto é capaz de possuir tal proximidade extrema CH-π.
- **Ciclofanos Tipo-Cilindro:** propor modificações estruturais para se determinar a influência dos grupos funcionais relacionados a coordenação do ânion fluoreto, estudar as características estruturais das geometrias em seu estado fundamental, e corroborar estes valores com as técnicas de analise de função de onda, para determinar a natureza física das interações covalentes em cada um dos

sistemas ciclofano-fluoreto, e baseado no papel fundamental dos grupos funcionais da estudados, determinar qual receptor de ânion tem uma estrutura que potencialmente pode ser a mais seletiva ao fluoreto.

Metodologia

Através da Teoria Kohn-Sham do Funcional da Densidade (DFT), estruturas de mínimo energético dos compostos ciclofanos tipo-cúpulula foram obtidas com um funcional da densidade PBE0, e os ciclofanos tipo-cilindro com BP86. As funções de base utilizadas em ambos trabalhos foi Def2-TZPV, bem como as correções de dispersão BJ-D3 e relativisticas ZORA.

A natureza física das interações não-covalentes foram estudadas através análises da densidade eletrônica (NCI), da função de onda (NBO), e mapas de potencial eletrostático (MEP) em conjunto com a análise da decomposição da Energia (EDA), teoria quântica de átomos em moléculas (QTAIM).

Resultados e Discussão

Os **ciclofanos tipo-cúpula**, foram modelados com base no conhecimento reportado na literatura com relação as interações não-covalentes do tipo CH-π. Desta forma, acreditava-se que aneis aromáticos de maior acidez-π, estabilizariam melhor a proximidade dos grupos CH-π da gaiola do ciclofano. Entretanto observou-se que uma soma de fatores que vão desde, grupos capazes de diminuir a tensão acumulada nas pontes da estrutura ciclofano, bem como estabilizar e distribuir carga através de interação *through-bond*, ou *through-space*, resultou que a estrutura com o menor contato C–H$\cdots\pi$ contém um anel de triazina, e oxigênios nos heteroatomos de cada uma das três pontes. Nossos resultados, que foram publicados, propõem a menor distância intramolecular centralizada C–H$\cdots\pi$ até o momento, fundamentada pelos principais fatores que racionalizam e justificam tal proximidade. As análises QTAIM, NBO e NCI revelaram que esta distância intramolecular é estabilizada por uma interação com grande contribuição eletrostática, e de caráter covalente não desprezível. As reações isodésmicas, no entanto, revelaram que as energias envolvendo estes ciclofanos tensionados, é principalmente modulada pela capacidade das pontes de suportar a deformação imposta por toda a do ciclofano que comprime o grupo C–H contra o sistema aromático, ainda que estes resultados já estão publicados em *Journal of Organic Chemistry* (JOC).

A discussão dos resultados envolvendo os nove **ciclofanos tipo-cilíndro** seletivos a fluoreto estudados, focaram em dois tipos de interações intermoleculares: *(i)* de longa distância, regido pelo sistema π, e *(ii)* de curta distância, regido pelos ligantes das pontes. Verificou-se que os efeitos de curta distância dos ligantes nas pontes influencia muito mais na coordenação do ânion do que os sistema aromático. Desta forma, apesar do sistema reportado na literatura, que possui ácido cianúrico ($NH_2{}^+$) como sistema π, e grupos amônio como ligante nas pontes, ser realmente o melhor cilindrofano receptor para fluoreto, baseado nos valores de EDA, os efeitos dos heteroatomos ligantes são mais fortes no sistema contendo benzeno (**BZN**) e pontes carregadas ($NH_2{}^+$), devido sua proximidade ao fluoreto. Estes cilindrofanos devem ser excelentes candidatos para que se proponha novos cilindrofanos que estabilizem ainda mais o fluoreto

Considerações Finais

Os resultados aqui apresentados poderão contribuir significativamente para o *design* de novos compostos macrocíclicos funcionais, capazes de reconhecer ânions com mais especificidade, bem como apresentar as menores proximidades entre grupos fucionais não ligados. Futuros trabalhos pretendem modelar os ciclofanos com relação a (*i*) modificação químicas nas pontes para tornar os receptores fluorescentes, (*ii*) coordenar os sistemas aromáticos em centros metálicos, para que os cilindrofanos se tornem ainda mais seletivos ao fluoreto, *(iii)* estudar efeitos de solvatação, e como diferentes solventes influenciam no sistema cilindrofano-fluoreto.

Palavras-chaves: Ciclofanos. Interações não-covalente. DFT. EDA. NCI. NBO.

Abstract

The role of functional groups in supramolecular systems determines its ability to recognize other molecules, as well as to rearrange its conformation into a specific shape. Cyclophanes are strained molecular cages that possess unusual chemical behavior, arising from its congested framework. Not only such constrained molecular frameworks are a noteworthy synthetic challenge target, but they are also known for being part of the "Hall of Fame" of molecules with ultra-short non-bonded contacts, and to be selective to determined guests.

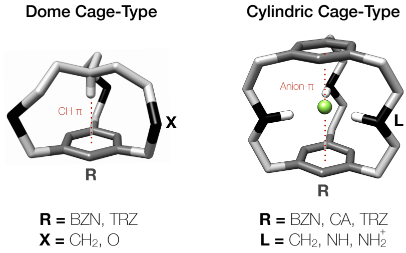

Molecular "iron maidens" are the *in*-isomer type of cyclophane in which a methine hydrogen is forced to be closer to the center of an aromatic ring. Cylindrophanes are fluoride selective hosts, which coordinate the anion through anion-π, H-bond, and ion-pair interactions. Both together are great examples that show how crucial such cyclophanes molecular framework is to be chemically investigated. The former molecule is a dome cage-type of cyclophane, whose main concern was the quest for insight towards the shortest C–H$\cdots\pi$ non-bonded. The latter, a cylindric-cage type of cyclophane, which unveiled the role of functional groups in the fluoride coordination. Functional group modifications were proposed to the dome cage-type scaffold to define to which cyclophane composition the shortest C–H$\cdots\pi$ belong, if the obtained proximity was competitive with the reported values in the literature, and to explain

why this iron maiden can sustain such extreme the C–H$\cdots\pi$ proximity. Likewise, the structural modifications proposed to the functional groups in the cylindrophanes were mainly done to determine the importance of the unorthodox anion-π interactions arising from the π-systems, and the strong short-range H-bond interactions from the bridges binding groups, to the guest stability.

The results provided here make use of an *avant-garde* theoretical approach that elucidated unique structural and energetic aspects of the cage-type of cyclophanes, evaluating, in the light of Kohn-Sham Density Functional Theory (DFT), with dispersion corrections (BJ-D3), both, the influence of the π-systems, and the nature of the heteroatoms located at the bridges. Rationalization of the physical nature of the non-covalent interactions was possible through the use of wave function, and electron density analysis such as Energy Decomposition Analysis (EDA), Natural Bond Orbitals (NBO), Quantum Atoms in Molecules (QTAIM)

Molecular iron maidens results propose the shortest intramolecular centered CH-π distance to date, which was supported by high field calculated ^{1}H NMR chemical shifts, CH-π interaction with significant stabilizing electrostatic component, and a high covalent character. The strained molecular iron maidens that can support such close contact have functional groups at the π-systems and the bridges that support the excessive strain. Hence they compress the C–H bond against the π-system. The role of cylindrophanes functional groups that coordinate the fluoride reveals that the guest stabilisation is mainly dependent on the non-covalent interactions with the bridge binding group. The ability of the ligands to better interact with the anion inside the cavity was found to be modulated by the cyclophane π-systems, in that the short-range effects of the binding groups are found to be the strongest in the cylindrophane containing benzene, not the π-acidic arenic systems. This was confirmed with EDA fragmentation scheme, NCI$_x$ analysis,

and red-shifted N–H stretches.

The remarkable findings presented in this dissertation not only highlight future synthetic targets that validate the calculations, and conclusions made, it provides vital information that will be used to develop novel cyclophanes, with different functionalities.

Keywords: Cyclophanes. Non-covalent interactions. DFT. EDA. NCI. NBO.

List of Figures

Figure 1 – Traditional definition of the supramolecular host-guest chemistry.[1] 54

Figure 2 – First recognized developments in supramolecular chemistry: (a) Crown-Ether (Pedersen), (b) Cryptand (Lehn) and (c) Spherands (Cram). Picture reproduced with rights permission.[1] 55

Figure 3 – Scheme showing different types of non-covalent interactions related to the physical nature of the different interacting groups. **Label:** **A**= acceptor, **D** = donor. 57

Figure 4 – (a) Electrostatic potential surface of benzene, and hexafluorobenze, respectively, (b) schematic representation of the anion induced dipole on the π-system. Picture reproduced with rights permission.[2] 58

Figure 5 – Permanent quadrupole moment (Q_{zz}, 1**B** $= 3.336 \times 10^{-40}$ C $\cdot\, m^2$) and polarizability ($\alpha_{||}$, Å^3) of benzene (**BZN**), cyanuric acid (**CA**), and s-triazine (**TRZ**), calculated in a B3LYP/Def2-TZVP level of theory.[3] Color-code: white = hydrogens, tan = carbons, blue = nitrogen, red = oxygen. 59

Figure 6 – Comparison of the Q_{zz} and $\alpha_{||}$ influence to the magnitude of the anion-π interaction with F$^-$. Values calculated in a MP2(full)/6-31++G**.[2] **Label:** isocyanuric **(ICA)**, thiocya-nuric **(TIA)**, dithiocyanuric **(DIA)**, and trithiocyanuric **(TTA)**.Picture reproduced with rights permission. 60

Figure 7 – 1,3,5-cyclophane framework, with two atoms at the aliphatic bridges. 62

Figure 8 – Synthesized molecular "Iron Maiden" by Robert A. Pascal, CSD cod. **RAZZIB**.[4] 64

Figure 9 – Macrocyle scaffolds of the 1,3,5-cyclophanes type prepared by (a) Robert A. Pascal, (b) Jean-Marie Lehn e (c) Cylindric format representation of the cyclophane cage. Picture reproduced with rights permission.[5,6] 65

Figure 10 – Cylindrophanes with different electronic character related to the aromatic rings of the systems: (a) benzene (**BZN**), (b) s-triazine (**TRZ**), (c) cyanuric acid (**CA**) e (d) boroxine (**BRX**). Picture reproduced with rights permission.[7] 66

Figure 11 – Generic model of the two cage-type cylindrophanes studied. Structural variable **R** represents scaffold modifications to the aromatic systems, **X** and **L** refer to changes in the backbone bridge heteroatomic group. 68

Figure 1 – Strained cyclophanes that have been synthesized: (a) *in*-isomer prepared by Ricci *et al.* in 1976 [8], (b) cyclophane **1** obtained by Pascal *et al.* in 1987 in an effort to synthesize tighter scaffolds[9] and (c) cyclophane **5** (**VAMMEB**) in 1989, possessing the shortest C$-$**H**$\cdots\pi$ proximity, as confirmed by its X-ray structure.[10] 75

Figure 2 – Synthesized cyclophane structures, accompanied by the CSD codes, **RAZZIB** and **VAMMEB**, of the compounds characterized by X-Ray chrystallography.[11] Color-code: tan = carbon, white = hydrogen, and yellow = sulfur. 76

Figure 3 – Molecular "Iron Maindens" model showing the structural variables that were changed, and the four compounds with shortest C$-$**H**$\cdots\pi$ Label: **R** = ring, **X** = bridge heteroatom, **BZN** = benzene, **TRZ** = triazine.[12] 79

Figure 4 – Optimized structures of compounds **1**–**4**, including selected individual centralized C−**H**$\cdots\pi$ distances (Å). Color-code: tan = carbon, blue = nitrogen, white = hydrogen, and red = oxygen. 81

Figure 5 – Selected C−**H**$\cdots\pi$ distances ($r_{\text{C-}\mathbf{H}}$, Å), C−**H** bond lengths ($r_{\text{C-}\mathbf{H}}$, Å) and their corresponding stretching frequencies ($\nu_{\text{C-}\mathbf{H}}$, cm^{-1}), differences of energy between isomers *in* and *out* ($\Delta E_{\text{in-out}} = E_{\text{out}} - E_{\text{in}}$, kcal·mol^{-1}), and calculated ^{1}H NMR chemical shifts^{a} for **H** (δ_{TMS}, ppm) of compounds **1**–**5**. The available experimental values are given in parentheses.[9,10] 82

Figure 6 – Selected donor-acceptor NBO interactions for compound **4**, and second order stabilisation energies ($\Delta E^{(2)}_{i\rightarrow j^*}$) for **1**–**4**. Color-code: gray = carbon, blue = nitrogen, white = hydrogen, and red = oxygen. . 84

Figure 7 – NCI color maps for cyclophane **2** (**R** = **BZN**), and **4** (**R** = **TRZ**). Color-code: tan = carbon, blue = nitrogen, white = hydrogen, and red = oxygen. . . . 85

Figure 8 – Top and bottom view of the NCI color maps for cyclophane **2** (**R** = **BZN**), and **4** (**R** = **TRZ**). Color-code: tan = carbon, blue = nitrogen, white = hydrogen, and red = oxygen. 87

Figure 9 – Iso Scheme - Color-code: tan = carbon, blue = nitrogen, white = hydrogen, and red = oxygen.Thermodynamic decomposition of strain energy (in kcal·mol^{-1}) by means of isodesmic reactions of iron maidens **1**–**4**. . 88

Figure 10 – Iso Scheme - Color-code: tan = carbon, blue = nitrogen, white = hydrogen, and red = oxygen. Thermodynamic decomposition of strain energy by means of isodesmic reactions of a molecular iron maiden, here exemplified by **1**. Broken covalent bonds were capped with relaxed hydrogen atoms (e.g., the first molecule in the right-hand side of (1) is methane). Apart from capping hydrogens, fragments colored with the same tone have the same geometry, but structures in grey were optimized entirely. Associated energies are shown 90

Figure 1 – Schematic representation of a cylindrophane host-guest (**HG**) system structure. Label: **H** = host, **G** = guest, **B** = bridges, **R** = rings, **L** = ligands. 95

Figure 2 – Cylindrophane model structures, organized in groups according to the chemical nature of **R** and **L**. Color-code: white = hydrogens, grey = carbons, blue = nitrogen, red = oxygen, black = ligand (**L**) group. . 97

Figure 3 – Scheme illustrating the host-guest system formation ($\mathbf{H} \rightarrow \mathbf{HG}$). 100

Figure 4 – Scheme representing initial and final states used to calculate the relative binding energies ($\Delta\Delta G_{\mathrm{bind}}$), which is the energy required to take F^- from the host-guest system $H_{i \cdot F^-}$ (Figure 2), and place it inside the cavity of the empty host H_j (*final state*). 102

Figure 5 – Scheme indicating structural parameters, and the analysed geometries average values (Å). The table values compare the structural modifications that take in **H** → **HG**, as indicated by the values before and after the | symbol. Detailed data is provided in Appendix B, B.1. The $H \cdots F^-$ and $\angle \beta$ values for hosts **1**–**9** were obtained placing dummy atom at the center of R_1 and R_2, and in the centroid axis of the **R**'s. Color-code: dim gray = **BZN**, **CA** and **TRZ**, **L**, black = backbone binding group s (**L**), white = hydrogens. 105

Figure 6 – Top view of optimized cylindrophanes conformation in **3**, **6**, and **9**, in contrast to their **HG** systems **3**·F^-, **6**·F^-, and **9**·F^-. 107

Figure 7 – Intramolecular interactions taking place in **6** and **9**, and it's **HG** systems **6**·F^- and **9**·F^-. 108

Figure 8 – Correlation graph that compares **R** and **L** framework variables of the different **HG** systems, showcasing the $H \cdots F^-$ values for the **HG**'s in Åin the form of (a) *short-distance effects*, and (b) *long-distance effects*.109

Figure 9 – Correlation graph that compares **R** and **L** framework variables of the different **HG** systems, showcasing the $R_1 \cdots R_2$ values for the **HG**'s in Å for the (a) *short-distance effects*, and (b) *long-distance effects*. . 111

Figure 10 – Top view of MEP maps (left to right) of **R** groups, **BZN**, **CA**, and **TRZ**. Maps for the neutral hosts **1**, **2**, **4**, **5**, **7**, and **8**, first and second row (**L** = CH_2, NH), with surface potential that ranges from -0.001 a.u.(red) to 0.002 a.u.(blue). Charged hosts **3**, **6**, **9** (**L** = NH_2^+) had a surface potential that ranges from 0.300 a.u.(red) to 0.550 a.u.(blue). All compounds had a consistent isovalue of 0.030 au. 114

Figure 11 – Correlation graph that compares **R** and **L** framework variables of the different **HG** systems, showcasing ΔE_{int}, ΔE_{prep}, and BDE interactions values for the **HG**'s in kcal·mol^{-1}. Detailed energy terms information for the EDA is given in Table 1). 118

Figure 12 – Correlation graph that compares **R** and **L** framework variables of the different **HG** systems, showcasing the Hirsfeld charge population values (au) for the fluoride ($q_{\mathbf{G}}$) in Table 1). 120

Figure 13 – Fragmentation scheme proposed to analyse the *short-distance effects*, and the *long-distance effects* in each one of the **HG**'s combination of **R** and **L**. The values for the bridges interactions with the fluoride (ΔE_{B}), and for the rings (ΔE_{R}) at the table are in kcal·mol^{-1} unit. 121

Figure 14 – Perspectives comparing the NCI_x for **HG**'s **1**·F^- (**BZN**, CH_2) and **3**·F^- (**BZN**, ${NH_2}^+$), in which their only difference is the **L** group. The *long-distance effects* are characterized by the green-blue bowl shaped surfaces, and the *short-distance effects* by the blue small rounded surfaces. Color-code: gray = carbon, cyan = nitrogen, and white = hydrogen. 124

Figure 15 – Top view comparing the NCI_x for **HG**'s **1**·F^- (**BZN**, CH_2) and **3**·F^- (**BZN**, ${NH_2}^+$), which differ by the **L** group. Color-code: gray = carbon, cyan = nitrogen, and white = hydrogen. 125

Figure 16 – Perspectives comparing the NCI_x for **HG**'s **4**·F^- (**CA**, CH_2) and **6**·F^- (**CA**, ${NH_2}^+$), in which their only difference is the **L** group. The *long-distance effects* are characterized by the green-blue bowl shaped surfaces, and the *short-distance effects* by the blue small rounded surfaces. Color-code: gray = carbon, cyan = nitrogen, white = hydrogen, and red = oxygen.126

Figure 17 – Top view comparing the NCI$_x$ for **HG**'s **4**·F$^-$ (**CA**, CH$_2$) and **6**·F$^-$ (**BZN**, NH$_2$$^+$), in which their only difference is the **L** group. Color-code: gray = carbon, cyan = nitrogen, and white = hydrogen. 127

Figure 18 – Top view (left) scheme showing the corners **a**, **b**, and **c** that are related to the cylindrophane asymmetric structures, and sideview (right) scheme showing the **L**-H bond length, H $\cdots$ F$^-$ non-covalent distance, and $\nu_{\mathbf{L}\text{-H}}$ **L** group internal hydrogen (**H**$_{in}$) bond frequency. Bond lengths, and non-covalent distances are shown in Å, and vibrational frequencies in cm^{-1}. Color-code: gray = carbon, black = **L** groups, and dim gray = **R** groups. 130

Figure 19 – Top view (above), and inside view (below) NCI$_x$ images comparing NH$_2$$^+$ analogues **3**·F$^-$, **6**·F$^-$, and **9**·F$^-$, showing corners **a**, **b**, and **c** in **3**·F$^-$. Arrow indicates how the inside views are seen. Color-code: gray = carbon, cyan = nitrogen, white = hydrogen, and red = oxygen. 131

Figure 20 – Relative binding energy ($\Delta\Delta G_{\text{bind}}$) heatmap, showing the exchange work of the F$^-$ in the different **HG** systems. The flux follows from *initial* to *final state*. The colors indicates which process is favorable (green), indifferent (yellow), and not probable (red). 135

Figure 21 – Cylindrophane conformers **6**$_{sym}$·F$^-$, and **6**·F$^-$ (above), and the geometry optimization calculated point group symmetries (below) with the lowest R values for the input, and output files. 137

Figure 22 – Free energy values comparison between the conformers **6**·F$^-$, and **6**$_{sym}$·F$^-$, in (a), and free energy associated with the different combinations of **6**, and **6**$_{sym}$, to form **6**·F$^-$, or **6**$_{sym}$·F$^-$ in (b). 138

Figure 23 – Conformers $\mathbf{6}_{sym}\cdot F^{-}$ (top), and $\mathbf{6}\cdot F^{-}$ (bottom), EDA energy terms in kcal·mol^{-1}. The EDA complete data is found in Table B8.Color-code: gray = carbon, cyan = nitrogen, white = hydrogen, and red = oxygen. . 139

Figure 24 – Perspectives are comparing the NCI$_x$ for **HG**'s $\mathbf{4}\cdot F^{-}$ (**CA**, CH_2) and $\mathbf{6}\cdot F^{-}$ (**CA**, NH_2^{+}), in which their only difference is the **L** group. The green-blue bowl-shaped surfaces characterize the *long-distance effects*, and the *short-distance effects* by the blue small rounded surfaces. Color-code: gray = carbon, cyan = nitrogen, white = hydrogen, and red = oxygen. . . . 141

Figure 1 – Representative illustration of further developments. Color-code: tan = carbon, white = hydrogen, blue = nitrogen, red = oxygen, and yellow = sulfur, green = fluoride, purple = lithium, cyan = molybdenum. . 147

Figure B1 – Cylindrophanes crystal structures deposited at Cambridge Structural Database (CSD). Perspective (right), and from the top (left), images of the cylindrophanes are classified according to: **(A) KISDIA** and **KISDEW** are cationic hosts selective to F^{-};[13, 14] **(B)** JIQSEH, JIQSAD, and KASLOF are neutral empty **H**; **(C)** PUJNOX, PUJNIR, QAFFAE and QAFDUW are neutral **H**'s coordinating Ag^{+} (silver) and Cu^{+} (cupper).[15, 16] Color-code: tan = carbon, blue = nitrogen, white = hydrogen, red = oxygen, and yellow = sulfur, green = F^{-}, silver = Ag^{+}, cupper = Cu^{+}. 186

Figure B2 – Cylindrophane structural parameters scheme. **(Top View)** Cylindrophane side distances r_A, r_B, r_C, and corners a, b, c; **(Side View)** **L**-H bond length, $\mathrm{H}\cdots\mathrm{F}^-$ contact, $\mathrm{R}_1\cdots\mathrm{R}_2$ height, and $\nu_{\textbf{L}\text{-H}}$ stretch; **(Perspective View)** distance $\mathbf{L}\cdots\mathrm{F}^-$, and angles α, β, and γ. Color-code: gray = bridge atoms, black = binding group atom ($\mathbf{L}_\mathrm{n}$) , white = binding group hydrogen H_n, dim gray = π-systems, green = F^- or dummy atom (**X**). 187

Figure B3 – Optimized structures of host **1**–**9**. The rows are separated by the π-systems (**R**): **BZN** (1st), **CA** (2nd), **TRZ** (3rd), and the columns by the binding groups (**L**): $\mathrm{CH_2}$ (1st), NH (2nd) and $\mathrm{NH_2}^+$ (3rd). Color-code: *grey* carbon, blue = nitrogen, white = hydrogen, red = oxygen. 188

Figure B4 – Optimized structures of host-guests **1**·F^-–**9**·F^- . The rows are separated by the π-systems (**R**): **BZN** (1st), **CA** (2nd), **TRZ** (3rd), and the columns by the binding groups (**L**): $\mathrm{CH_2}$ (1st), NH (2nd) and $\mathrm{NH_2}^+$ (3rd). Color-code: *grey* carbon, blue = nitrogen, white = hydrogen, red = oxygen, and green = F^-. 189

Figure B5 – MEP maps (left to right) **R** groups, **BZN**, **CA**, and **TRZ**, and **L** = $\mathrm{CH_2}$. Maps for the neutral **H**'s **1**, **4**, and **7** (**L** = $\mathrm{CH_2}$) with surface potential that ranges from -0.001 a.u.(red) to 0.002 a.u.(blue), and have an isovalue of 0.030 au. 193

Figure B6 – MEP maps (left to right) **R** groups, **BZN**, **CA**, and **TRZ**, and **L** = NH. Maps for the neutral **H**'s **2**, **5**, and **8** (**L** = NH) with surface potential that ranges from -0.001 a.u.(red) to 0.002 a.u.(blue) and have an isovalue of 0.030 au. 194

Figure B7 – MEP maps (left to right) **R** groups, **BZN**, **CA**, and **TRZ**, and **L** = NH_2^+. Charged **H**'s **3**, **6**, and **9** (**L** = NH_2^+) with surface potential that ranges from 0.003 a.u.(red) to 0.550 a.u.(blue), and isovalue of 0.030 au. 194

Figure B8 – Optimized structures of the π-systems (**R**) of **HG**'s **1**·F^-–**9**·F^- (**BZN**, **BZN**, and **TRZ**) considering the original **HG**'s atoms coordinates, except for the hydrogens added to the first carbon of the bridges. Color-code: *grey* = carbon, blue = nitrogen, white = hydrogen, red = oxygen, green = F^-. 196

Figure B9 – Optimized structures of the bridge (**B**) in **HG**'s **1**·F^-–**9**·F^- , conserving three atoms in each original **B** branch, and the **L**'s groups. The distances were kept fixed as in the optimized **HG** structure, and relaxed hydrogens were added to complete the terminal atoms valance. Color-code: *grey* = carbon, blue = nitrogen, white = hydrogen, red = oxygen, green = F^-. . . . 197

Figure B10–NCI_x image for cylindrophanes-fluoride host-guest systems **1**·F^-–**9**·F^- . The rows are classified by the π-systems **BZN** (1st), **CA** (1nd), and **TRZ** (3rd), and the columns by the binding groups CH_2 (1st), NH_2^+ (2nd), and (3rd). Color-code: gray = carbon, cyan = nitrogen, white = hydrogen, and red = oxygen. 198

Figure B11–Top view of the NCI_x image for cylindrophanes-fluoride host-guest sytems **1**·F^-–**9**·F^- . Color-code: gray = carbon, cyan = nitrogen, white = hydrogen, and red = oxygen. 200

Figure B12–NCI_x image comparing host **3** (**BZN**, NH_2^+), with host-guest **3**·F^-, showing the differences in the intramolecular interactions in **3**, and the **NCI**'s interactions in **3**·F^-. Color-code: gray = carbon, cyan = nitrogen, and white = hydrogen. 201

Figure B13–NCI$_x$ image comparing host **6** (**CA**, $NH_2{}^+$), with host-guest **6**·F^-, showing the differences in the intramolecular interactions in **6**, and the **NCI**'s interactions in **6**·F^-. Intramoleular interactions discussed in the geometry analysis section are marked by a circle. Color-code: gray = carbon, cyan = nitrogen, white = hydrogen, and red = oxygen. 201

Figure B14–NCI$_x$ image comparing host **9** (**TRZ**, $NH_2{}^+$), with host-guest **9**·F^-, showing the differences in the intramolecular interactions in **9**, and the **NCI**'s interactions in **9**·F^-. Intramoleular interactions discussed in the geometry analysis section are marked by a circle. Color-code: gray = carbon, cyan = nitrogen, and white = hydrogen. 202

Figure B15–Calculated Infrared Spectrum for pentane at BP86/Def2-TZVP level of theory. The noted peaks refer to the symmetric, and asymmetric C–H stretch in the third carbon.Color-code: tan = carbon, cyan = nitrogen, and white = hydrogen. 203

Figure B16–Calculated Infrared Spectrum for diethylamine at BP86-D3/Def2-TZVP level of theory. The noted peak refers to the N–H stretch.Color-code: tan = carbon, cyan = nitrogen, and white = hydrogen. 203

Figure B17–Calculated Infrared Spectrum for diethylammonium at BP86-D3/Def2-TZVP level of theory. The noted peak refers to the N–H stretch.Color-code: tan = carbon, cyan = nitrogen, and white = hydrogen. . . 204

Figure B18–Calculated Infrared Spectrum of compound **1**·F^-. The stretch frequency ($\nu_{\mathbf{L}\text{-H}}$) associated with $\mathbf{H}_{in}$ can found in Table B7, along with $H\cdots F^-$, and **L**-H. 205

Figure B19–Calculated Infrared Spectrum of compound **2**·F^-. The stretch frequency ($\nu_{\mathbf{L}\text{-H}}$) associated with $\mathbf{H}_{in}$ can found in Table B7, along with $H\cdots F^-$, and **L**-H. 206

Figure B20–Calculated Infrared Spectrum of compound **3**·F^-. The stretch frequency associated with $\mathbf{H}_{in}$, $H\cdots F^-$, and **L**-H can found in Table B7. The $\mathbf{H}_{out}$ frequencies, also assigned in the spectra, refer to the hydrogen bonded to **L** that remains outside the cavity. 206

Figure B21–Calculated Infrared Spectrum of compound **4**·F^-. The stretch frequency ($\nu_{\mathbf{L}\text{-H}}$) associated with $\mathbf{H}_{in}$ can found in Table B7, along with $H\cdots F^-$, and **L**-H. 207

Figure B22–Calculated Infrared Spectrum of compound **5**·F^-. The stretch frequency ($\nu_{\mathbf{L}\text{-H}}$) associated with $\mathbf{H}_{in}$ can found in Table B7, along with $H\cdots F^-$, and **L**-H. 207

Figure B23–Calculated Infrared Spectrum of compound **6**·F^-. The stretch frequency associated with $\mathbf{H}_{in}$, $H\cdots F^-$, and **L**-H can found in Table B7. The $\mathbf{H}_{out}$ frequencies, also assigned in the spectra, refer to the hydrogen bonded to **L** that remains outside the cavity. 208

Figure B24–Calculated Infrared Spectrum of compound **7**·F^-. The stretch frequency ($\nu_{\mathbf{L}\text{-H}}$) associated with $\mathbf{H}_{in}$ can found in Table B7, along with $H\cdots F^-$, and **L**-H. 208

Figure B25–Calculated Infrared Spectrum of compound **8**·F^-. The stretch frequency ($\nu_{\mathbf{L}\text{-H}}$) associated with $\mathbf{H}_{in}$ can found in Table B7, along with $H\cdots F^-$, and **L**-H. 209

Figure B26–Calculated Infrared Spectrum of compound **9**·F^-. The stretch frequency associated with $\mathbf{H}_{in}$, $H\cdots F^-$, and **L**-H can found in Table B7. The $\mathbf{H}_{out}$ frequencies, also assigned in the spectra, refer to the hydrogen bonded to **L** that remains outside the cavity. 209

Figure B27–Scheme representing initial and final states used to calculate the work, $\Delta\Delta G_{\text{bind}}$, as relative binding energies. The $\Delta\Delta G_{\text{bind}}$ is the energy required to take F^- from the **HG** system $H_{i\cdots F^-}$ (initial state), and place it inside the cavity of the empty **H** H_j (final state). 210

Figure B28–Top view comparing the NCI for **HG**'s $\mathbf{6}_{sym}\cdot F^{-}$ (**CA**, NH_2^+) and $\mathbf{6}\cdot F^{-}$ (**CA**, NH_2^+). Color-code: gray = carbon, cyan = nitrogen, and white = hydrogen. 212

Figure B29–Calculated Infrared spectrum displaying the $\nu_{\mathbf{L}\text{-H}}$ peaks for the external hydrogens ($\mathbf{H}_{out}$), and for the internal hydrogens ($\mathbf{H}_{in}$). 213

Figure C1 – The Jacob's ladder of DFT approximations to the exchange-correlation energy. The rungs represent different levels of approximation towards higher accuracy. 219

Figure C2 – EDA scheme presenting the first major step in the bond energy decomposition. In **Step I** the preparation energy (ΔE_{prep}) represents the geometry and electron density distortions of fragments **A** and **B**, into the final configuration they adopt in **AB**. . . . 225

Figure C3 – EDA scheme presenting the second major step in the bond energy decomposition. **Step II** shows how the interaction (ΔE_{int}) energy is decomposed into the three sub-steps of the electrostatic stabilisation (ΔV_{elstat}), Pauli repulsion (ΔE_{Pauli}), and orbital stabilisation (ΔE_{oi}). 226

Figure C4 – Energy levels diagram, showing the relationship betwen all the enrgy terms derived from the EDA method. Figure adapted from the work of Contreras *et. al.*.[17] 229

Figure C5 – NCIPLOT (left) of the reduced gradient ($s(r)$), as a function of the electron density ($\rho(r)$). Interacting phenol dimer (right), in a perspective, top, and front view, respectively. Figure adapted from the work of Contreras *et. al.*.[17] 230

Figure C6 – NCIPLOT (top-left) of the reduced gradient ($s(r)$), as a function of sign of the second Hessian eigenvalue of the electron density ($sign(\lambda_2) \cdot \rho(r)$). Interacting phenol dimer (top-right), indicating the relationship of the **NCI** colored surfaces, with the steep peaks generated at the CPs ($\nabla\rho(s)$), and colored according to the sign of $\nabla^2\rho(r)$. BGR gradient of colors that classify the type, and **NCI**'s strength. Figure adapted from the work of Contreras *et. al.*.[17] 231

Figure C7 – Three linear combinations of NOs, showing visually the difference between NBOs, NLMOs and MOs. Illustration reproduced based on images from the NBO program website.[18] 234

Figure C8 – Laplacian distribution of *o*-methylbenzoic acid: solid blue lines indicate charge depletion ($\nabla^2\rho < 0$), dashed blue lines indicate charge accumulation ($\nabla^2\rho > 0$), red spheres are bond critical points (BCPs), purple spheres are ring critical points (RCP), black lines are bond paths, red lines are zero flux surfaces.[19] 235

List of Tables

Table 1 – Energy Decomposition Analysis (kcal·mol^{-1}) and the Hirshfeld fragment charge analysis (a.u.) for compounds **1**·F^{-}–**9**·F^{-} . Values in parenthesis correspond to the percentage of each stabilising contribution (ΔV_{elstat} + ΔE_{oi} + ΔE_{disp} = 100%). 117

Table B1 – Selected geometrical parameters of the cylindrophanes hosts (**H**) **1**–**9** scaffolds (Figure B3). Labels of the parameters presented in this table are in accord to Figure B2, in which in the absence of a F^{-} anion, a dummy atom (**X**) was placed in the midpoint between the centroid axis of the **R** systems. 188

Table B2 – Selected geometrical parameters (Figure B2) of the cylindrophane scaffolds **1**·F^{-}–**9**·F^{-} interacting with F^{-} (Figure B4). All values presented in this table are in Å. 189

Table B3 – Selected angles of the **H**'s scaffold **1**–**9**, illustrated as indicated in Figure B2 perspective view, in the absence of the anionic guest a dummy atom **X** was positioned in the midpoint from the centroid of each π-systems. All angles values are in degrees (°). 191

Table B4 – Selected angles of the **HG** systems **1**·F^{-}–**9**·F^{-} , illustrated as indicated in Figure B2 perspective view. All angles values are in degrees (°). 192

Table B5 – Energy Decomposition Analysis (kcal·mol^{-1}) and the Hirshfeld fragment charge analysis (a.u.) for the ring (**R**) fragments illustrated in Figure B8, of compounds **1**·F^{-}–**9**·F^{-} . Values in parenthesis correspond to the percentage of each stabilising contribution (ΔV_{elstat} + ΔE_{oi} + ΔE_{disp} = 100%). 196

Table B6 – Energy Decomposition Analysis (kcal·mol^{-1}) and the Hirshfeld fragment charge analysis (a.u.) for the bridge fragments illustrated in Figure B9, of compounds **1**·F^{-}–**9**·F^{-} . Values in parenthesis correspond to the percentage of each stabilising contribution ($\Delta V_{\mathrm{elstat}}$ + ΔE_{oi} + ΔE_{disp} = 100%). 197

Table B7 – Selected **L** groups hydrogen stretch frequency ($\nu_{\mathbf{L}\text{-H}}$), and related geometry parameters H$\cdots$F^{-}, and **L**-H (Figure B2), for cylindrophane scaffolds **1**·F^{-}–**9**·F^{-} interacting with F^{-} (Figure B4). All values related to bond length or distance in this table are in Å, and the IR frequencies in cm^{-1}. 205

Table B8 – Energy Decomposition Analysis (kcal·mol^{-1}) and the Hirshfeld fragment charge analysis (a.u.) for compounds **6**·F^{-}, and the symmetric conformer $\mathbf{6}_{sym}$·F^{-} . Values in parenthesis correspond to the percentage of each stabilising contribution ($\Delta V_{\mathrm{elstat}}$ + ΔE_{oi} + ΔE_{disp} = 100%). 212

List of Abbreviations and Acronyms

Def2-TZVP	Ahlrichs Gaussianas functions with triple-ζ quality.
ADF	Amsterdam Density Functional.
ABNT	Associação Brasileira de Normas Técnicas.
AO	Atomic Orbital.
BSSE	basis set superposition error (BSSE).
B3LYP	Becke 3-parameter Lee-Yang-Parr hybrid density functional.
BP86	Becke Exchange, and Perdew correlation functionals.
BJ	Becke-Johnson Functions.
BZN	Benzene.
BGR	Blue-Green-Red gradient of color.
BCP	Bond Critical Point.
BDE	Bond Dissociation Energy.
BRX	Boroxine.
B	Bridges.
CSD	Cambridge Crystallographic Data.
CP	Counterpoise method.
CP	Critical Point.
CA	Cyanuric Acid.
DFT	Density Functional Theory.
DFT	Density Functional.
DIA	Dithiocyanuric.
EDG	Electron Donating Groups.

EWG	Electron Withdrawing Groups.
EDA	Energy Decomposition Analysis.
XC-DF	Exchange-Correlation Functional.
ETS	Extended Transition State.
GIAO	Gauge Including Atomic Orbitals Method.
GTO	Gaussian-Type Orbital.
GAMESS	General Atomic and Molecular Electronic Structure System.
GGA	Generalized Gradient Approximation.
D3	Grimme dispersion corrections.
GS	Ground State.
G	Guest.
X	Heteroatom.
HOMO	Highest Occupied Molecular Orbital.
HK	Hohenberg-Kohn.
HG	Host-Guest.
H	Host.
H-bond	Hydrogen bond.
IR	Infrared.
IUPAC	International Union of Pure and Applied Chemistry.
ICA	Isocyanuric.
6-31+G(d,p)	John Pople split-valence double-zeta diffuse and polarized basis set.
KS-DFT	Kohn-Sham Molecular Density Functional Theory.
KS-MO	Kohn-Sham Molecular Orbitals.
KS	Kohn-Sham.
L	Ligand groups in cyclophane.

LDA	Local Density Approximation.
LUMO	Lowest Unoccupied Molecular Orbital.
MP2	Møller-Plesset Second Order Perturbation Theory.
MSD	Mean Signed Deviation.
ORCA	Molecular electronic structure software.
MEP	Molecular Electrostatic Potential.
MO	Molecular Orbital.
NAO	Natural Atomic Orbital.
NBO	Natural Bond Orbital.
NHO	Natural Hybrid Orbital.
NPA	Natural Population Analysis.
NCIPLOT	Non-covalent Interactions index visualisation.
NCI_x	Non-covalent Interactions index.
NCI	Non-covalent Interactions.
NMR	Nuclear Magnetic Resonance.
R-value	Pearson correlation coefficient.
PBE0	Perdew-Burcke-Ernzerhof hybrid density functional.
PES	Potential Energy Surface.
QTAIM	Quantum Atoms in Molecules.
QM	Quantum Mechanics.
RYG	Red-Yellow-Green gradient of colors.
RBE	Relative Binding Energy.
RI	Resolution Identity approximation.
R	Ring groups in cyclophane.
def2	Second generation of default basis set.
STO	Slater-Type Orbital.

TZ2P	Slater–type basis sets with triple-ζ quality that include polarization effects.
SCS	Sprin Component Scaled correlation method.
TIA	Thiocyanuric.
TRZ	Triazine.
3D	Tridimensional.
TMS	Trimethylsilane.
TTA	Trithiocyanuric.
TZVP	Valence triple-ζ polarization Karlsruhe basis sets.
TZVPP	Valence triple-ζ with two sets of polarization functions.
vdW	van der Waals.
VMD	Visual Molecular Dynamics.
ZORA	Zero-Order Regular Approximation.

List of Symbols

$\mathrm{R}_1 \cdots \mathrm{R}_2$	π-systems distance from the centroid axis.
δ	^{1}H NMR resonance chemical shift.
ε_j^*	Acceptor anti-ligand NBO ϕ_j energy.
ϕ_j^*	Acceptor anti-ligand NBO.
ζ	Adjusted orbital exponent.
Å	Angstrom, length unit (10^{-10} m).
$\hat{\mathcal{A}}$	Antisymmetrization operator.
R_1	Bottom ring.
ΔG_{form}	Bridge free energy rotation.
Z_A	Charge in nucleus A.
$E_\mathrm{V}[\rho(r)]$	Core-electron potential functional.
C_n^{AB}	Dispersion coefficient.
E_disp	Dispersion energy.
ΔE_disp	Dispersion stabilisation energy.
R	Distance between fragments A-B.
ε_i	Donor empty NBO ϕ_i energy.
ϕ_i	Donor empty NBO.
$\Delta E_{i\to j^*}^{(2)}$	Donor-acceptor orbital second order stabilization energy.
$E[\rho(r)]$	Electron density functional.
$\nabla\rho(r)$	Electron density gradient.
$\rho(\mathbf{r})$	Electron density in point $\mathbf{r}$.
ρ	Electron density.

V_{elec}	Electronic Electrostatic potential.
ΔV_{elstat}	Electrostatic potential stabilisation energy.
V	Electrostatic potential.
e	Elementary charge (1,602×10^{-19} C).
ΔG_{H_j}	Empty host free energy.
$\Delta E_{\text{in-out}}$	Energy difference of *in/out* isomers.
$E_{\text{XC}}[\rho(r)]$	Exchange-correlation functional.
$\nu_{\text{XC}}(r)$	Exchange-correlation potential.
$\hat{F}$	Fock operator.
ΔE_{B}	Fragmented bridges ΔE_{int} energy.
ΔE_{R}	Fragmented rings ΔE_{int} energy.
ΔG	Free energy.
ΔE_{prep}	Geometry and electronic preparation energy.
$\rho_{\text{AB}}^{\text{GS}}$	Ground state electron density of interacting fragments A–B.
$\rho_{\text{A}}^{\text{GS}}$	Ground state electron density of interacting fragment A.
$\rho_{\text{B}}^{\text{GS}}$	Ground state electron density of interacting fragment B.
$\Psi_{\text{AB}}^{\text{GS}}$	Ground state wave function of interacting fragments A–B.
$\Psi_{\text{A}}^{\text{GS}}$	Ground state wave function of interacting fragment A.
$\Psi_{\text{B}}^{\text{GS}}$	Ground state wave function of interacting fragment B.
Ψ_0	Ground state wave function.
q_{G}	Guest Hirshfeld charge.
$\hat{\mathcal{H}}$	Hamiltonian operator.

$E_{\mathrm{H}}[\rho(r)]$	Hartree potential functional.
$\nu_{\mathrm{H}}(r)$	Hartree potential.
$\hat{\Gamma}$	Hermitian 1-electron projection operator.
q_{H}	Host Hirshfeld charge.
ΔG	Host-guest system free energy formation.
$\Delta G_{\mathrm{H}_i\cdot\mathrm{F}^-}$	Host-guest system free energy.
$\angle\,\beta$	Hydrogen bond angle.
$\mathbf{H}_{in}$	Inside cage hydrogen.
ΔE_{iso}	Isodesmic reaction energy.
ΔE_{iso}	Isodesmic reaction preparation energy.
$E_{\mathrm{K}}[\rho(r)]$	Kinetic energy functional.
$\hat{K}$	Kinetic energy operator.
E_{KS}	Kohn-Sham energy.
$\varepsilon_{\mathrm{KS}}$	Kohn-Sham energy.
ν_{KS}	Kohn-Sham operator.
φ_i	Kohn-Sham orbital.
$\hat{\nu}_{\mathrm{KS}}$	Kohn-Sham potential operator.
$\nu_{\mathrm{KS}}(r)$	Kohn-Sham potential.
$\nabla^2\rho(r)$	Laplacian of Electron density.
$\mathbf{L}\cdots\mathrm{F}^-$	Ligand distance to fluoride.
$V_{\mathrm{MEP}}(\mathbf{r})$	Molecular electrostatic potential in point $\mathbf{r}$.
$\lvert\Psi_2\rvert$	N-electron probability distribution.
q_i	Natural charge population (NPA) in atom A.
Θ_k	Natural orbital eigenfunction.
$\nu(r)$	Nuclear attractive potential.
V_{nuc}	Nucleus Electrostatic potential.
p_k	Occupancy of the eigenfunction.

ΔE_{oi}	Orbital stabilization energy.
$\rho^{\ddagger}_{\mathrm{B}}$	Orthonormalized electron density of interacting fragment B.
$\rho^{\ddagger}_{\mathrm{AB}}$	Orthonormalized electron density of interacting fragments A–B.
$\rho^{\ddagger}_{\mathrm{A}}$	Orthonormalized electron density of interacting fragment A.
E_{A}	Orthonormalized energy of fragment A.
E_{B}	Orthonormalized energy of fragment B.
E_{AB}	Orthonormalized energy of interacting fragments A–B.
$\Psi^{\ddagger}_{\mathrm{B}}$	Orthonormalized wave function of interacting fragment B.
$\Psi^{\ddagger}_{\mathrm{AB}}$	Orthonormalized wave function of interacting fragments A–B.
$\Psi^{\ddagger}_{\mathrm{A}}$	Orthonormalized wave function of interacting fragment A.
$\mathbf{H}_{out}$	Outer cyclophane-cage hydrogen.
$\Delta E_{\mathrm{Pauli}}$	Pauli repulsion energy.
ρ^{0}_{A}	Prepared state electron density of interacting fragment A.
ρ^{0}_{AB}	Prepared state electron density of interacting fragments A–B.
ρ^{0}_{B}	Prepared state electron density of interacting fragment B.
Ψ^{0}_{AB}	Prepared wave function of interacting fragments A–B.
Ψ^{0}_{A}	Prepared wave function of interacting fragment A.
Ψ^{0}_{B}	Prepared wave function of interacting fragment B.
$s(r)$	Reduced density gradient.

$\Delta\Delta G_{\mathrm{bind}}$	Relative binding energy.
δTMS	Relative NMR resonance chemical shift.
λ_2	Second eigenvalue of the density Hessian.
ΔE_{tot}	Total energy.
ΔE_{int}	Total interaction energy.
R_2	Upper ring.
N	Wave function normalization constant.
Ψ	Wave function.
cm^{-1}	Wavelength.

Contents

I CONCEPTUAL FRAMEWORK 51

1 STATE OF THE ART 53
1.1 Supramolecular and Host-Guest Chemistry 53
1.1.1 Non-Covalent Interactions 55
1.1.2 Physical Nature of Unprecedented Non-Covalent Interactions 57
1.2 Computer Aided Molecular Investigative Design . . 61
1.2.1 Cyclophanes as Molecular Cages 62
1.2.2 Frontiers of Non-Covalent Interactions in Cage-Like Cyclophanes 63
1.2.2.1 Dome Cage-Type Cyclophanes 63
1.2.2.2 Cylindric Cage-Type Cyclophanes 64

2 PRESENTATION 67
2.1 Purpose 68
2.2 Publications 69
2.2.1 Contribution to Included Papers 69
2.3 Further Published Papers 70
2.3.1 Contribution to Further Published Papers 71

II DOME CAGE-TYPE CYCLOPHANES 73

3 MOLECULAR “IRON MAIDENS” 75
3.1 Unusual Pyramidalized Hydrogens 75
3.2 Methodology 77
3.3 Comments and Remarks 78
3.3.1 Geometries 80
3.3.2 Non-Covalent Distance Analysis 82
3.3.3 Framework Strain Analysis 87

3.4 Concluding Remarks 90

III CYLINDRIC CAGE-TYPE CYCLOPHANES 93

4 FLUORIDE-SELECTIVE CYLINDROPHANES . . . 95
4.0.1 Investigative Design of Cylindrophanes 96
4.1 Methodology 99
4.2 Results and Discussion 102
4.2.1 Structural Parameters and Geometry Analyses 104
4.2.2 Non-Covalent Interaction Analysis 113
4.2.2.1 Molecular Electrostatic Potential (MEP) 114
4.2.2.2 Energy Decomposition Analysis (EDA) 115
4.2.2.3 Non-Covalent Interaction Index (NCI_x) 123
4.2.2.4 Vibrational Frequency Analysis (IR) 129
4.2.3 Host-Guest Binding Analysis 132
4.2.3.1 Relative Binding Energy (RBE) 133
4.2.4 Conformational Analysis 137
4.3 Concluding Remarks 143

IV OUTLOOKS 145

5 FURTHER DEVELOPMENTS 147

BIBLIOGRAPHY 149

APPENDIX 173

APPENDIX A – PAPER I 175

APPENDIX B – SUPPORT INFORMATION TO CYLINDRIC CAGE-TYPE CYCLOPHANES 185

B.1 Structural Parameters and Geometry Analyses . . . 185
B.2 Non-Covalent Interaction Analysis 192
B.2.1 Molecular Electrostatic Potential Maps (MEP) 192
B.2.2 Energy Decomposition Analysis (EDA) 194
B.2.3 Non-Covalent Interaction Index (NCI_x) 195
B.2.4 Vibrational Frequency Analysis (IR) 199
B.3 Host-Guest Analysis 204
B.3.1 Relative Binding Energy (RBE) 204
B.3.2 Conformational Analysis 211

APPENDIX C – COMPUTATIONAL METHODS . 215
C.1 Density Functional Theory (DFT) 215
C.1.1 Kohn-Sham Molecular Orbitals 217
C.1.2 Exchange-Correlation Density Functionals (XC-DF) . . 218
C.1.3 Basis Functions and Sets 220
C.2 Dispersion Corrections 221
C.3 Electron Density and Wave Function Analysis . . . 223
C.3.1 Molecular Electrostatic Potential Maps (MEPs) 224
C.3.2 Energy Decomposition Analysis (EDA) 225
C.3.3 Non-Covalent Index (NCI_x) 228
C.3.4 Natural Bond Orbital (NBO) 232
C.3.5 Quantum Atoms in Molecules (QTAIM) 235
C.4 Isodesmic and Homodesmotic Reactions 236

Part I

Conceptual Framework

1 State of the Art

Science has long sought to comprehend and explain complex things, such as the origin of life and the universe, leading to discoveries and advances in areas such as medicine and technology. Computational chemistry is concerned with studying molecules and molecular systems through theoretical models that can be validated by experiments, or interpreting empirical results theoretically. The advent of computational methods, in this regard, was vital to the rationalization, and development of theoretical chemistry, providing detailed information of molecular quantum effects, that rely on the intrinsic nature of molecules electronic structure.

Nature seen at the molecular level considers molecular systems in which different species interact through non-covalent interactions.[1,20] This concept arose in 1894 with Fischer's key-lock model, proposed to explain enzymatic reactions,[21] giving rise to fundamental principles such as molecular recognition, and molecular systems function, that became the genesis of a new field in science known as supramolecular chemistry.[22,23]

1.1 Supramolecular and Host-Guest Chemistry

The basis of many biological processes relies on molecular recognition, sensing and self-assembly.[24] Molecular structure and function coordinate molecular events such as transport, and regulation in biological systems.[25] In this sense, H. M. Powell, in 1948, studied the incorporation of small "guests" to "host" structures, demonstrating that atoms in molecules were able to be "connected" concisely, without the need of strong interactions.[26] Further development to Powell's design of high-selective hosts led to what we know as "host-guest" chemistry

(Figure 1).[20]

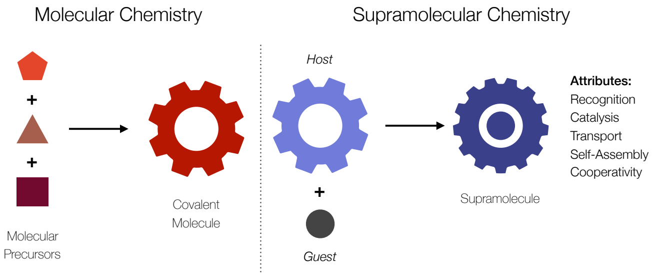
Molecular Chemistry
Supramolecular Chemistry
+
+
Molecular Precursors
Covalent Molecule
Host
+
Guest
Supramolecule
Attributes:
Recognition
Catalysis
Transport
Self-Assembly
Cooperativity

Figure 1 – Traditional definition of the supramolecular host-guest chemistry.[1]

The concept of the physical nature of non-covalent interactions between molecules,[27] was fundamental to redefine Fischer's static key-lock model. The concept of induced-fit, later introduced by Daniel Koshland in 1958, described a dynamic and cooperative-based process to explain recognition between biomolecules.[28,29]

The acknowledgment of intermolecular interactions, led Charles J. Pedersen, in 1967, to publish two seminal works that presented compounds he named as crown-ethers (Figure 2 (a)). Pedersen's work demonstrated that such compounds had a remarkable, and unexpected selective property that resulted in the accommodation of a guest molecule inside the crown-ether cavity.[30] The more complex and selective structures of the cryptands synthesized by Jean-Marie Lehn in 1969, officially introduced the term of "Supramolecular Chemistry" (Figure 2 (b)).[23,31] A short time later, in 1974, with the sophisticated spherand frameworks, Donald Cram and his wife Jane published their work named as "Host-Guest Chemistry"(Figure 2 (c)).[32]

Twenty years after the establishment of supramolecular, and host-guest chemistry, Pedersen, Cram, and Lehn were awarded with the Nobel Prize in 1987, for the synthesis, development, and application of molecules with high selectivity, unique structural interactions, chemical properties, and finally for elucidating the factors that determine the ability of these molecules to recognize and assemble one another.[23, 30, 33]

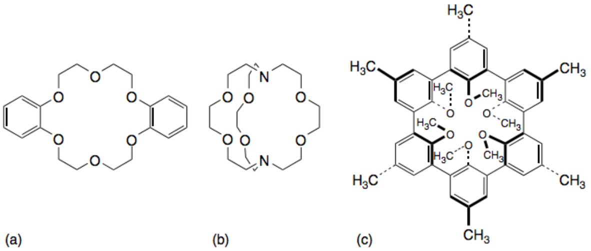

Figure 2 – First recognized developments in supramolecular chemistry: (a) Crown-Ether (Pedersen), (b) Cryptand (Lehn) and (c) Spherands (Cram). Picture reproduced with rights permission.[1]

1.1.1 Non-Covalent Interactions

Molecular recognition is crucial to prioritize the reaction between two or more specific molecules, considering a diverse chemical milieu. The ability to communicate in a selective, and additive manner, is an elementary property not only limited to biochemical systems (drug delivery, protein folding, receptor proteins) but also present in other areas such as materials science (molecular magnetism, conductors, sensors, catalysts).[34–36] Molecular communication depends on the combination, and the interplay of different types of non-covalent interactions that involve well-known weak forces, such as van der Waals, hydrogen bonds, electrostatic interactions, hydrophilic, hydrophobic, and π-π interactions (π-stacking).[27]

Different types of non-covalent interactions can occur within the same molecular structure, or between two or more molecules. These are known as intra, and intermolecular interactions, respectively, and are classified according to the physical nature of the forces existing between the interacting functional groups, as represented in the scheme of Figure

3.[37] Some examples are: halogen bonds, red and blue-shifting hydrogen bonds, C$-$**H**$\cdots\pi$, dihydrogen bonds, anion and cation-π interactions, etc.[37–39]

A type of non-covalent interaction involving cations and aromatic systems was disclosed by S. K. Burley and G.A. Petsko, in 1981, and 1986, respectively.[40, 41] Their work revealed, employing *ab initio* calculations combined with crystallographic studies of proteins, several peculiar interactions between the amino acid residues of proteins side chains.[42] Burley and Petsko observed that positively charged amino acid residues, e.g., ammonium groups, favorably interacted with the electron density of the aromatic portions in other amino acid residues, leading to the recognition of cation-π interactions.[43]

A decade later, Hans-Jorg Schneider published a series of articles, based on experimental studies, that revealed a possible unorthodox non-covalent interaction of negatively charged species interacting with the polarizable regions of π-systems in host-guest systems.[44–46] Only in 2002, Frontera *et. al.*, in a paper entitled as *"Anion-π Interactions: Do They Exist?"* that combined theoretical methods and an experimental data survey proved that anion-π interactions existed.[47] Since then, the anion-π class of non-covalent interactions has gained prominent attention among researchers in the field of supramolecular chemistry. [48]

Another remarkable type of unconventional non-covalent interaction is the weak CH-π hydrogen bond,[49–51] which would not be considered as a non-covalent interaction at all according to the **IUPAC GOLD BOOK** definition.[52] While most hydrogen bonds depend on their electrostatic character, which implies in their strength, recent concepts related to the physical nature of weak H-bonds, such as the CH-π, defines it more as an phenomenological bonding situation, since based on its energetic grounds, it would not be considered as a non-covalent interaction.[49, 53, 54] This modern perception of the hydrogen bonding, as well as other non-covalent interactions, supported by the advances of quantum chemical tools to assess the physical nature of

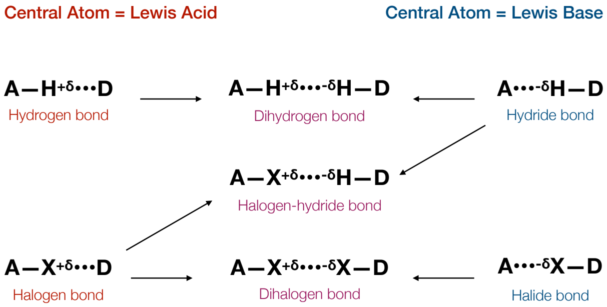
Central Atom = Lewis Acid
Central Atom = Lewis Base
A—H+δ•••D
Hydrogen bond
A—H+δ•••-δH—D
Dihydrogen bond
A•••-δH—D
Hydride bond
A—X+δ•••-δH—D
Halogen-hydride bond
A—X+δ•••D
Halogen bond
A—X+δ•••-δX—D
Dihalogen bond
A•••-δX—D
Halide bond

Figure 3 – Scheme showing different types of non-covalent interactions related to the physical nature of the different interacting groups. **Label:** **A**= acceptor, **D** = donor.

such interactions,[55–57] allowed for the discovery of many novel types of non-covalent interactions, namely dihydrogen bonds, [58–61] halogen bonds, [62–64] π-π interactions, [65–67] cation-π, [43,68–70] anion-π, [71,72] and the CH-π hydrogen bonds, [50,73,74] contributing profoundly to the understanding of complex chemical systems.

The boundaries of defying chemical bonds lead to the verification of molecular structures in the light of theories. In the realm of the non-covalent interactions in molecules, supramolecules, and molecular systems, computational tools are a key element to correctly outline the physical nature of these interactions on a quantum chemistry level.[75,76] Hence, the consolidation of theory,[38,77,78], and experiments, to shed light into chemical problems, is undoubtedly a step forward for the prospects of developing applications to many different fields, as well as to the endless pursuit to make new molecules.

1.1.2 Physical Nature of Unprecedented Non-Covalent Interactions

The physical nature of the anion-π interaction, ever since it was recognized, has been widely discussed,[48,79] and determined to be mainly dependent on the polarization and electrostatic effects of both:

the anion, and the π-system (Figure 4). Hence, one way to predict the strength related to this interaction is based on the evaluation of the permanent quadrupole moment (Q_{zz}), and the polarizability ($\alpha_{||}$) of the electronic π-cloud associated to the arenic portions in a molecule (Figure 5).

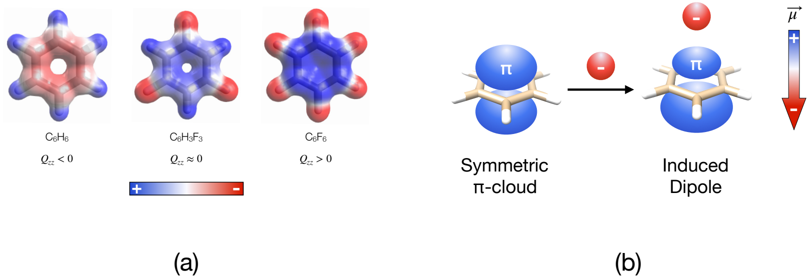

Figure 4 – (a) Electrostatic potential surface of benzene, and hexafluorobenze, respectively, (b) schematic representation of the anion induced dipole on the π-system. Picture reproduced with rights permission.[2]

In this sense, electron withdrawing substituents have been assigned to invert the signal of (Q_{zz}) of π-systems, indicating from an electrostatic viewpoint, the changes that occur in electron distribution above/below the ring plane, therefore in the local electron density of these regions (Figure 4).[48,79–81] The intrinsic polarizability ($\alpha_{||}$) of the aromatic rings reflects on the degree of modulation of the π-cloud, which in turn is affected by the polarization induced effect that is due to the presence of the anion (Figure 5).[48,82,83] Hence, contributions coming from the polarization, and dispersion components of the interacting system, the anion and the π-system, have to be accounted to asses the anion-π interaction energy.[84] The electrostatic contribution may be associated with the ring moiety quadrupole moment (Q_{zz}), which is related to the π electrons charge and current,[85] as well as to the anion-induced polarization effect (Figure 5).[84]

Frequently, the electrostatic component (Q_{zz}) overcomes the polarizability ($\alpha_{||}$) contribution to the non-covalent interaction being considered. Aromatic systems such as benzene (**BZN**), cyanuric acid (**CA**), and s-triazine (**TRZ**) are well-known examples that illustrate this behavior (Figure 5).[86] In this sense, based on a Q_{zz} judgment of these three rings, one can consider, for example, the **BZN** as a π-basic system, the **CA** ring a π-acid one, and the s-triazine as a borderline case.[87–89]

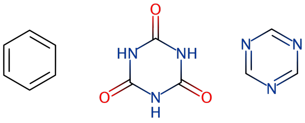

	BZN	**CA**	**TRZ**
Q_{zz} (**B**)	- 7.54	+ 8.66	+ 1.16
$\alpha_{||}$ (Å^3)	5.81	5.16	4.49

Figure 5 – Permanent quadrupole moment (Q_{zz}, $1\mathbf{B} = 3.336 \times 10^{-40}$ C$\cdot m^2$) and polarizability ($\alpha_{||}$, Å^3) of benzene (**BZN**), cyanuric acid (**CA**), and s-triazine (**TRZ**), calculated in a B3LYP/Def2-TZVP level of theory.[3] Color-code: white = hydrogens, tan = carbons, blue = nitrogen, red = oxygen.

In contrast to this unilateral point of view of the physical nature of the anion-π, electron-rich π-systems with electronegative groups, in which the interplay of energy contribution coming from Q_{zz}, and $\alpha_{||}$ is mostly reliant on the polarizable nature of the π-system electrons, have shown to deserved attention.[84] Frontera and collaborators, demonstrated this, in a combined crystallographic and computational study with an MP2(Full)/6-31++G** level of theory (Figure 6).[84] Their findings evinced that when cyanuric acids oxygens were replaced by one, two, and three sulfurs, changing the values of Q_{zz} and $\alpha_{||}$ for the substituted rings inversely, their anion-π interaction energies with F^-, Cl^-, and Br^- were similar, as presented in Figure 6), which shows that the physical nature of the anion-π interaction is modulated by these two physical components.[84] Therefore, Frontera *et. al.*, showed that the interplay of contribution between Q_{zz} and $\alpha_{||}$ to the anion-π interaction is modulated changing the electron nature of the π-systems.

Further studies exploring the ability of electron-rich systems to interact with anions by means of anion-π interactions, despite its contradictory basis, have been concisely published suggesting that different types of non-covalent interactions of counterintuitive nature can be discovered, or modulated to become favorable.[90] Moreover, the electronic character of the aromatic moiety can be tuned to become π-acidic through metal coordination, for instance.[68, 70, 91]

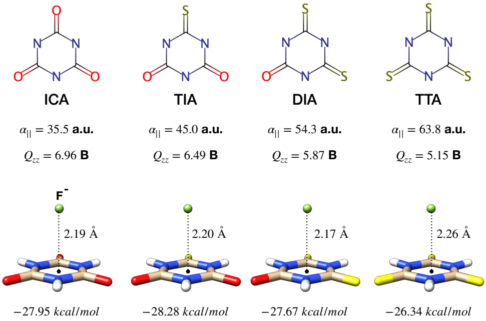

Figure 6 – Comparison of the Q_{zz} and $\alpha_{||}$ influence to the magnitude of the anion-π interaction with F^-. Values calculated in a MP2(full)/6-31++G**.[2] **Label:** isocyanuric **(ICA)**, thiocyanuric **(TIA)**, dithiocyanuric **(DIA)**, and trithiocyanuric **(TTA)**.Picture reproduced with rights permission.

The assessment of the anion-π interaction, based on $\alpha_{||}$ and Q_{zz}, is commonly applied to other weaker non-covalent interactions, such as the CH-π hydrogen-bond (**H**-Bond).[53, 92, 93] In this case, since considered a very weak **H**-Bond, the major component to describe the CH-π interaction energy, for example, would be based on the $\alpha_{||}$, not on electrostatic component Q_{zz}. What we will see in this work, is that beyond the electronic character of a molecule, its conformation may play a significant role, and this leads us to study each molecular system peculiarities individually, making sure that is not the case of an exception to the rules.

1.2 Computer Aided Molecular Investigative Design

Molecular design problems can be approached with different computational methods that range from molecular mechanics to quantum chemistry.[94–97] Creating molecular models aims to discover compounds that exhibit particular or specific behavior, as well as to implement the desired feature of a molecular system. One way to design molecules is through chemical intuition, which leads to a trial/error modifications of a known molecular framework that presents the desired property. The goal to that type of design strategy is to enhance molecular functional properties, being that the properties of the final product are unknown, but the choice for the molecular architecture modifications are made to achieve the desired molecular behavior or feature.[98]

Modeling is considered as a prior step, towards the synthesis of a molecule with a desired characteristic, or even to revisit covalent, and non-covalent bonds.[94,98] The usefulness of the obtained results of a computational method, and level of theory utilized, also depends on the complexity of the chemical system. The strategy chosen to build molecular models, its modifications, and the interpretation of findings is also critical to validate the solution of the initial statement.[98]

The strategy chosen to comprehend the role of certain groups or regions in a molecule, for example, active sites in an enzyme,[24] the selective cavity of a cryptand in a host-guest system,[1] or unexpected proximity of chemical groups in a strained molecule,[11] or between molecules,[59] relies heavily on how to treat the target molecule. This implies in the choice of framework modifications, hence, in the model utilized to explain the molecular problem successfully, as well as in the computational methods employed.[94,96]

1.2.1 Cyclophanes as Molecular Cages

Cyclophanes are a well-known class of macrocycle organic compounds that have been vastly studied because of their singular strained and rigid skeleton, as well as its chemical properties.[99,100] Cage-type cyclophanes can be mono, bicyclic, or with more complex scaffolds containing multiple heterocyclic aromatic units, and functionalized bridges (Figure 7).[101]

The first records on synthetic routes to obtain such cage-like cyclophanes belong to the work of C. J. Brown, and A. C. Farthing, from 1949.[102] Subsequently D. Cram, in 1951,[103] disseminated a variety of synthetic techniques, popularizing such cyclophane molecular cage category. [99,104]

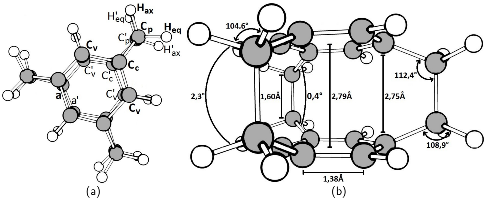

(a) (b)

Figure 7 – 1,3,5-cyclophane framework, with two atoms at the aliphatic bridges.

Cage-like cyclophanes can be modified to display a desired property, e.g., a particular host-guest system, or a twisted molecule with unique chemical features. Mark Mascal and Robert Pascal are recognized chemists whose works contributed with advances to the chemistry of medium size cylindric cyclophanes,[7] and smaller dome-shaped cyclophanes,[11] respectively. The results of their work inspired the two types of cyclophanes studied in this dissertation.

1.2.2 Frontiers of Non-Covalent Interactions in Cage-Like Cyclophanes

Designing small cages that present short contact groups proximities, or larger cyclophanes that present high host-guest efficiency, and selectivity, requires the correct manipulation of the energetic, and stereochemical components related to their scaffold.[22,27,105] For example, cylindrophanes may be designed to become selective receptors to fluoride anions,[7] in contrast to calixarenes, which have large conformational flexibility and are less selective host.[34] Another example are small congested cyclophanes, that present exclusive conformational in/out isomerism,[106,107] as well as ultra-short contacts.[11]

1.2.2.1 Dome Cage-Type Cyclophanes

Robert A. Pascal, along with Donald Cram, and Jean-Marie Lehn contributed greatly to experimental developments on the routes to obtain cyclophanes.[5,6,33,103] While Cram's and Lehn's research focused more on host-guest and supramolecular chemistry, Pascal was more interested in exotic twisted molecules.[11] Exploring a plethora of molecules that suited his interests, Pascal started to look for molecules that presented short-distances between methine hydrogens, and the center arenic ring.[11] Very short $\mathrm{C}{-}\mathbf{H}{\cdots}\pi$ group proximities may be considered as the "holly grail" of hydrogen bonds, as this implies into a strong CH-π hydrogen bond.[50] Although CH-π are considered as very weak hydrogen bonds, they influence the conformation of organic compounds,[54] molecular recognition[51] in proteins,[108] carbohydrates,[109] host-guest systems[110], as well as in the directionality of reacting organic species.[111]

A class of C_3 symmetric cyclophane that presents *in/out* isomerism,[106] and also has an intramolecular $\mathrm{C}{-}\mathbf{H}{\cdots}\pi$ close contact, was first produced in 1976, by Ricci *et. al.*.[8] This dome shaped cyclophane was only correctly characterized 9 years later by Pascal and Grossman, and presented a ^{1}H NMR septet in very high field region ($\delta_{\text{in-H}}$= -1.68 ppm),[112]

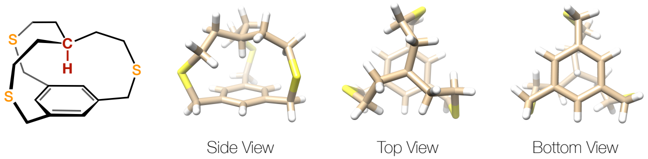

Side View Top View Bottom View

Figure 8 – Synthesized molecular "Iron Maiden" by Robert A. Pascal, CSD cod. **RAZZIB**.[4]

not assigned in Ricci's paper. The high field ^{1}H NMR finding of such macrocycle was later found to belong actually to the *in*-isomer (Figure 8),[4] not the *out*-isomer, as Ricci imagined.[8]

The strained molecule is shown in Figure 8, named molecular "Iron Maiden",[11] was the first experimental evidence that disclosed the *in*-isomer of the bicyclic compound containing an aliphatic hydrogen projected toward the center the aromatic ring.[4] Further attempts were made to synthesize dome cage-like cyclophanes with reduced $\mathrm{C{-}\mathbf{H}}\cdots\pi$ distances, changing the heteroatoms at the aliphatic bridges, and reducing its size, but these compounds were hard to crystallize, and resulted in small yields (2-10 %).[9–11] The quest for Insight into ultrashort $\mathrm{C{-}\mathbf{H}}\cdots\pi$ proximities in molecular "Iron Maidens" remained though, and is presented in the Section II of this study.[12] The main questions raised from Pascal's work regarding enforced $\mathrm{C{-}\mathbf{H}}\cdots\pi$ proximities, were how short they can be, and whether or not they were $\mathrm{C{-}\mathbf{H}}\cdots\pi$ interactions. A complete study on designed framework modifications of the molecular "Iron Maiden" revealed the compounds with possible shortest $\mathrm{C{-}\mathbf{H}}\cdots\pi$ proximity, yet to be obtained, and also explained into detail what aspects of the congested cyclophane contributed to such intramolecular proximity.[12]

1.2.2.2 Cylindric Cage-Type Cyclophanes

Exploring ligand molecule geometries to study anion coordination chemistry, Denis Heyer and Jean-Marie Lehn, obtained, in 1986, cylindric shaped host molecule containing ammonium and guanidinium groups as binding sites.[6] At the same time, Robert A. Pascal *et. al.* published the synthesis of a neutral 1,3,5-cyclophane, that possibly coordinated a F^-, as indicated by proton, and fluorine NMR characterization in DMSO (Figure 9).[5]

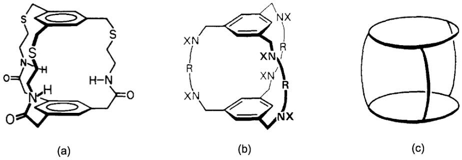

Figure 9 – Macrocyle scaffolds of the 1,3,5-cyclophanes type prepared by (a) Robert A. Pascal, (b) Jean-Marie Lehn e (c) Cylindric format representation of the cyclophane cage. Picture reproduced with rights permission.[5,6]

Hansen *et. al.*, in 1998, reported the synthesis and crystal structure of a metal–arene interaction, described as three center, two-electron σ complexation, in the scaffold of a cylindric cage-type cylcophane, containing different heteroatomic binding groups at the bridges.[113] The same type of host, named by Mascal as cylindrophane, acting as a ligand for sandwich complexation of Ag^+, Cu^+, was reported in three other following works.[13,15,16]

In 2006, Mascal, designed four different cylindrophanes using a B3LYP/6-31+G(d,p) level of theory, to investigate their sandwich complexes with F^- and Cl^-. The main focus of his work was to study the anion-π interaction in the bicyclic hosts containing three $NH_2{}^+$ binding groups, to check if cylindrophanes were selective to F^-, instead of Cl^- (Figure 10).[7] Soon later, the synthesis of the cylindrophane-fluoride selective system, based on the cylindrophane (c) (Figure 10), was reported.[14]

The rigid framework of cylindrophanes enables it to be selective based on its steric-fit, i.e., the size of the backbones bridges decides whether or not Cl$^-$ or F$^-$ fit the cavity.[7] Furthermore, the π-acidic nature of the π-system, enhances the anion-π interaction stabilisation.[48] For instance, the described effects that different substituents have on the electron nature of the arene moiety, concerning the anion-π interaction, allowed M. Mascal to choose between the four different types of studied cylindrophanes,[7] based on the fact that positive Q_{zz} values of the ring portions on cylindrophanes, would intensify the magnitude of the anion-π interactions.[65, 86, 114, 115] Accordingly, he considered host in Figure 10 **(a)**, as a poor host to anions, and picked host **(b)** to synthesize.[7, 14]

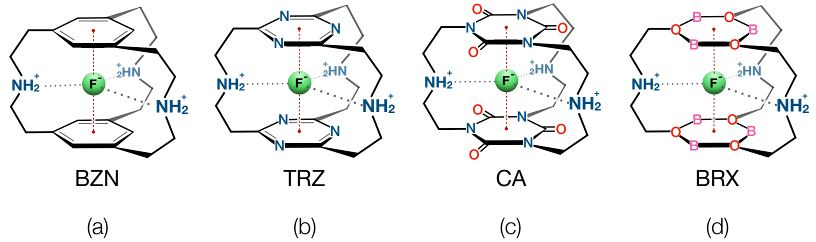

Figure 10 – Cylindrophanes with different electronic character related to the aromatic rings of the systems: (a) benzene (**BZN**), (b) s-triazine (**TRZ**), (c) cyanuric acid (**CA**) e (d) boroxine (**BRX**). Picture reproduced with rights permission.[7]

The attempt to rationalize the cylindrophane framework variables enables the creation of numerous host structures. The different properties of each molecular framework can be investigated with computational methods, in the particular supramolecule situation, revealing essential aspects of the electronic structure of the receptor to coordinate other species. Host architecture changes may be made to determine the role of each structural variable to the host-guest interaction. The calculated results of these framework modifications, reveals how sensitive the cage is to changes made to the different scaffold interacting sites, contributing to a deeper understanding of the cylindrophane molecular cage, and leading to further developments into novel compounds with unique features and different possible applications.[1]

2 Presentation

The results reported in this dissertation are separated into two independent parts (Part II and Part III), which presents the two different types of cyclophane frameworks (Figure 11) that were investigated. Since Part II, and III are independent, they should be approached this way, i.e., they have different methodologies, labels of the compounds and their structural variables, as well as the numbering of the compounds. Symbols and abbreviations of terms, in contrast, are the same for the entire dissertation, unless presented differently, and if so, have an explanation to it.

Part II, was written in a comment and remarks style since it presents a published work.[12] In Chapter 3, the main features, methods, results, and conclusions of the paper: **Quest for Insight into Ultrashort C-H$\cdots\pi$ Proximities in Molecular "Iron Maidens". *The Journal of Organic Chemistry*, v. 83, n. 9, p. 5114-5122, 2018** are presented, and the full article is found in Appendix A. Support Information to this work is not present in this here but is found at the **ACS Publishing** website.

Part III, is presented in Chapter III in a manuscript format, which is intended to be published as soon as possible. This chapter discusses the consequences of the cylindrophane scaffold modifications concerning the non-covalent interactions present in the host-guest system. The structural and geometry analysis (Part III, Chapter 4.2.1), reveals how the changes to the molecular architecture of cylindrophanes influence in the formation of the host-guest system. This analysis is complemented by the examination of the effects that the framework changes have on the magnitude of the non-covalent interactions contributing to the cylindrophane-fluoride interacting system (Chapter III, Section 4.2.2).

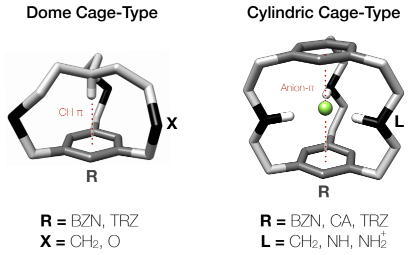

Figure 11 – Generic model of the two cage-type cylindrophanes studied. Structural variable **R** represents scaffold modifications to the aromatic systems, **X** and **L** refer to changes in the backbone bridge heteroatomic group.

A binding energy analysis (Part III, Chapter 4.2.3) reveals the relative binding energy associated with the exchange of the fluoride anion from one host, to the others. Finally, a comparison made between the cylindrophane conformational isomers C_1, and C_3v (Chapter III, Section 4.2.4), addresses the energetic differences between them as empty hosts, as well as in the host-guest system. The Support Information to all the manuscript results and discussions presented in Chapter III, is included in the Appendix B.

Part IV includes the outlooks that are being further developed (Chapter 5) from the results obtained here. A brief overview of the computational methods employed in this work is found in Appendix C, disclosing the primary references, and equations that describe the methods.

2.1 Purpose

The main goal of this work is to understand from a computational chemistry perspective, the role of functional groups in congested molecular scaffolds (Figure 11). The focus is then, to characterize the unorthodox non-covalent interactions of close contacts that exist in the cyclophanes scaffolds. Two cage-types of cyclophanes frameworks are presented here to this objective: a dome cage-type, and a cylindric cage-type (Figure 11).

Molecular architecture modifications are proposed to this objective, placing different substituents in the rings (**R**), heteroatoms (**X**), and in the binding groups (**L**) of the cyclophanes structures (Figure 11), to verify how electronic and structural changes, and influences the magnitude of existent non-covalent interactions.

It is intended to define the role that the structural variables **R**, **X**, and **L** have on the cyclophanes framework, to shed light on the proposed chemical problems regarding non-covalent interactions that take place in these two molecular systems, and evaluate the mechanism by which the magnitude of these interactions are modulated.

2.2 Publications

This dissertation resulted in the following publications, which are referred to in the text by their indicated Roman numerals.

I. **ØSTRØM, I**, ORTOLAN, A. O., SCHNEIDER, S. S. F., CARAMORI, F. G, PARREIRA, L. T. R. Quest for Insight into Ultrashort C-H $\cdots\pi$ Proximities in Molecular “Iron Maidens”. *The Journal of Organic Chemistry*, v. 83, n. 9, p. 5114-5122, 2018.

II. **ØSTRØM, I**, ORTOLAN, A. O., CARAMORI, F. G, PARREIRA, L. T. R, MASCAL, M. Functional Groups Role in Fluoride-Selective Cylindrophane. (Submitted manuscript)

All of the reprints included in this dissertation have the rights permission from the respective publishers.

2.2.1 Contribution to Included Papers

Paper I: I directed the planning of the study, did the background literature study, performed electronic structure calculations, analysed the output data, wrote the initial manuscript and contributed to the continued writing process.

Paper II: I directed the planning of the study, did the background literature study, performed all electronic structure calculations, analysed the output data, wrote the initial manuscript and contributed to the continued writing process.

2.3 Further Published Papers

During the progress and development of this master dissertation, contributions to collaborator's works were possible and served to further understanding of supramolecular chemistry in different molecular systems, as well as to different computational methods, and its interpretation. Discussions of results and collaboration resulted in the following papers, which are not presented or discussed in this dissertation:

I. ORTOLAN, A. O., **ØSTRØM, I**, CARAMORI, F. G, PARREIRA, L. T. R., SILVA, H. E., BICKELHAUPT. F. M. Tuning Heterocalixarenes to Improve Their Anion Recognition: A Computational Approach. *The Journal of Physical Chemistry A*, v.122, n. 12, p. 3328-3336, 2018.

II. ORTOLAN, A. O., **ØSTRØM, I**, CARAMORI, F. G, PARREIRA, L. T. R., BICKELHAUPT. F. M. Anion Recognition by Organometallic Calixarenes: Analysis from Relativistic DFT Calculations. *Organometallics*, v.37, n. 13, p. 2167-2176, 2018. 3328-3336, 2018.

III. MUCELINI, J., **ØSTRØM, I**, ORTOLAN, A. O., ANDRIANI, K., CARAMORI, F. G, PARREIRA, L. T. R., LAALI, K. K. The Complexity of [Janusene−Ag]$^+$ Host-Guest System: Dual Non-Covalent Interactions in Enforced Proximities. (Submitted manuscript)

2.3.1 Contribution to Further Published Papers

Paper I: I helped in the visual aspects of representative images, analysed the data related to the manuscript, helped with the initial manuscript and contributed to the continued writing process.

Paper II: I helped in the visual aspects of representative images, analysed the data related to the manuscript, helped with the initial manuscript and contributed to the continued writing process.

Paper III: I directed the planning of the manuscript contents, did the background literature study, helped in the visual aspects of representative images, analysed the results, re-wrote the initial manuscript and contributed to the continued writing process.

Part II

Dome Cage-Type Cyclophanes

3 Molecular “Iron Maidens”

3.1 Unusual Pyramidalized Hydrogens

Molecular “iron maidens” are a dome-shaped cage-like cyclophane, included in the class of the *in*-isomers[106], that have an apical methine hydrogen directed towards the center of its π-system.[11] Because of its congested inward hydrogen, it displays unusual spectroscopic features, and noteworthy low yields (Figure 1).

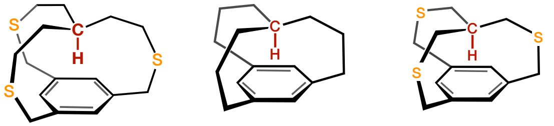

5.5 % yield	11 % yield	4 % yield
δH_{in} = - 1.68 ppm	δH_{in} = - 4.03 ppm	δH_{in} = - 2.84 ppm
$\nu_{C-H} = 3100$ cm^{-1}	$\nu_{C-H} = 3325$ cm^{-1}	$\nu_{C-H} = 3260$ cm^{-1}

Figure 1 – Strained cyclophanes that have been synthesized: (a) *in*-isomer prepared by Ricci *et al.* in 1976 [8], (b) cylophane **1** obtained by Pascal *et al.* in 1987 in an effort to synthesize tighter scaffolds[9] and (c) cyclophane **5** (**VAMMEB**) in 1989, possessing the shortest $\mathrm{C-}\mathbf{H}\cdots\pi$ proximity, as confirmed by its X-ray structure.[10]

The 2018’s published work, named *Quest for Insight into Ultrashort* $C-\boldsymbol{H}\cdots\pi$ *Proximities in Molecular “Iron Maidens”*,[12] was inspired by Robert A. Pascal’s mini-review: *Molecular “Iron Maidens”: Ultrashort Nonbonded Contacts in Cyclophanes and Other Crowded Molecules.*[11] Robert’s quest for insight, though, began in 1976, when he read a paper published by Ricci,[8] in which the latter described the synthesis, and characterization of a twisted *out*-isomer cyclophane. Ricci’s compound, nicknamed later by Pascal as molecular “Iron Maiden” (Figure 1), had a printed ^{1}H NMR ($\delta = 0$ to 8 ppm) with no assignments of signals, and did not display the methine resonance peak.[8]

After nine years of the NMR misinterpretation on Ricci's work,[8] the synthesis and characterization of the "Iron Maiden",[112] assigning that the compound obtained was actually the *in*-isomer, was published. Only in 1996 its X-Ray structure was disclosed, confirming that the cyclophane was really the *in*-isomer.[4] During this period, several attempts to synthesize in-geometries with even shorter $\mathrm{C-}\mathbf{H}\cdots\pi$ distances were made to evaluate the methine hydrogen reactivity, and stability of the *in/out* isomers.[9,112] This led to the achievement of the crystallographic structure of **5**, with a value of $r_{\text{C-}\mathbf{H}\cdots\pi} = 1.68$ Å, $\delta =$ -2.84 ppm, and $\nu_{\text{C-}\mathbf{H}} = 3260$ cm^{-1}! (Figure 1 e 2).[10]

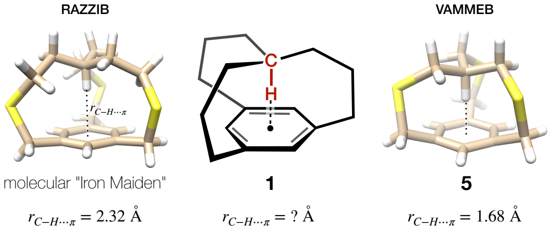

Figure 2 – Synthesized cyclophane structures, accompanied by the CSD codes, **RAZZIB** and **VAMMEB**, of the compounds characterized by X-Ray chrystallography.[11] Color-code: tan = carbon, white = hydrogen, and yellow = sulfur.

Up to this date, and as far as it has been correctly documented,[11] the shortest $r_{\text{C-}\mathbf{H}\cdots\pi}$ proximity experimentally obtained, belongs to an adamantanophane that has an intramolecular $r_{\text{C-}\mathbf{H}\cdots\pi}$ of 1.64 Å, and a high field ^{1}H NMR resonance of $\delta =$ - 4.08 ppm.[116] Although compound **1** structure has not been figured out, its spectroscopic characteristics strongly indicate that its $r_{\text{C-}\mathbf{H}\cdots\pi}$ should be at least somewhere near the adamantophane $\mathrm{C-}\mathbf{H}\cdots\pi$ record of 1.64 Å, that Lemmerz *et. al* obtained in 1993.[116]

The preliminary findings motivated the creation and development of this work. The main focus was to tune the $r_{\text{C-}\mathbf{H}\cdots\pi}$ distance with structural modifications, changing the functional groups from the deposited crystallographic structure of **5** (**VAMMEB**), to explain in the light of electronic structure methods, what electronic, and conformational effects could justify such proximity. Thereby the paper published discussed: **(i)** which functional group configuration presented the shortest methine proximity, **(ii)** what electronic effects stabilized the *in*-isomer, and finally, **(iii)** of the candidates with the shortest $\text{C}-\mathbf{H}\cdots\pi$, what framework had the *in*-isomer more stable the *out*-isomer, being an eligible synthetic target.[12]

This was done carefully by analysing the electron distribution on the cyclophane structure with QTAIM,[117] the orbital interactions by means of NBO analysis,[75, 118, 119] evaluating the non-covalent weak forces qualitatively with NCI,[120] and checking if the *in*-isomer was more stable than the *out*-isomer, by means of isodesmic reactions, which determined which structure is the most competitive synthetic target.

3.2 Methodology

Geometry optimizations and numerical vibrational frequency calculations were carried out with the ORCA software (v.3.0.1),[121] at the DFT-D level, employing the hybrid density functional PBE0 of Ernzerhof-Scuseria,[122] and Adamo-Barone[123] (25% of Hartree-Fock exchange), with a triple-zeta quality basis set (Def2-TZVPP).[124, 125] Geometries proved to be a potential energy true minimum, presenting no imaginary eigenvalues in the Hessian matrix. The RIJCOSX approximation was applied optimize the computational cost of calculations.[126] Long-range dispersion effects were corrected with (D3),[127, 128] and Becke-Johnson damping functions.[129, 130] To validate the geometries obtained with PBE0, the main discussed frameworks were also optimized with correlated spin-component scaled second order perturbation theory (RI-SCS-MP2/Def2-TZVPP)[124, 125, 131–133]

Nuclear magnetic resonance (NMR) chemical shifts were computed with Gauge-Including Atomic Orbital approach (GIAO)[134,135], as implemented in ADF2016[136–138] (PBE0-D3/TZ2P[135,139]). The reported GIAO values are relative to tetramethylsilane (TMS) by the use of the experimental chemical shift **5** (−2.84 ppm).[10] The methods of Non-Covalent Interactions index (NCI), Natural Bond Orbitals (NBO), and Quantum Theory of Atoms in Molecules (QTAIM), in the same level of theory, was employed (PBE0-D3(BJ)/Def2-TZVPP). The NCI analysis[120] employed the NCIPLOT[140] code, and was visualized with the VMD software.[141] The NBO method[75,118,119] was employed using GAMESS-US v.2013 (R1).[142] QTAIM analysis[117] was employed as implemented in MultiWFN 3.3.9.[143]

Isodesmic reactions determined the strain in compounds **1**–**4** was evaluated through hypothetical reactions that evaluate relative stability, and repulsion between the methine group and the aromatic moiety, and the amount of strain supported by the tethering bridges, and the aromatic rings.[144–147]

3.3 Comments and Remarks

The quest for insight towards finding the closest C−**H**$\cdots\pi$ in the molecular "Iron Maiden" scaffold led to the creation of a total of forty different compounds, which are presented, and discussed at the Support Information of the published work, which is not included here. The original paper, **Quest for Insight into Ultrashort C-H $\cdots\pi$ Proximities in Molecular "Iron Maidens".** ***The Journal of Organic Chemistry*****, v. 83, n. 9, p. 5114-5122, 2018**, is found in Appendix A, given the rights and permissions from **ACS Publications** to do it so. Hereby, it will be presented the main results in a commented fashion, and remarks will be addressed to allow the reader to understand how the work was developed, and the findings published.[12]

The investigative design on the cyclophane framework mainly focused in two functional groups structural variables: **(i)** the π-system (**R**), **(ii)** and the heteroatom (**X**) at the aliphatic chains (Figure 3). Changes were made to **R**, and **X** of the *in*-isomer structure, parting from the deposited X-Ray structure of the cyclophane with shortest C−**H**···π distance, CSD cod. **VAMMEB** (Figure 2).[9] The proposed framework modification in the **R** included π-systems such benzene, cyanuric acid, triaminobenze, trithiocyanuric acid, trifluorobenzene, trihydroxybenzene, trinitrobenzene, and s-triazine, to evaluate the electronic effects caused by **R** on the C−**H**···π distances. The choice for the heteroatom group **X** at the bridges was made by varying atom types, hence the size, electrostatic and dispersive nature, as well. The starting choices were X = CH_2, S, NH_2^+, NH, and O.

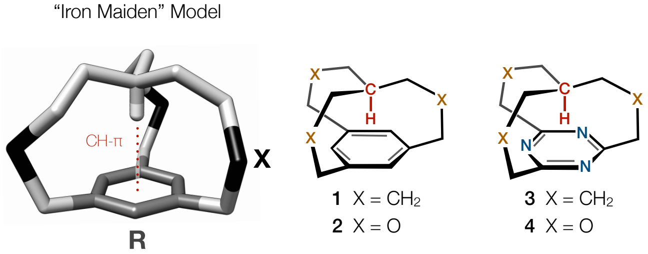

1 X = CH_2
2 X = O

3 X = CH_2
4 X = O

Figure 3 – Molecular "Iron Maindens" model showing the structural variables that were changed, and the four compounds with shortest C−**H**···π Label: **R** = ring, **X** = bridge heteroatom, **BZN** = benzene, **TRZ** = triazine.[12]

Overall structures, four compounds seemed reasonable to be discussed in detail, as shown in Figure 3. Not only they presented the shortest C−**H**···π distances among all structures optimized, but of all cyclophane scaffolds proposed, they also conveyed the impression that they could be reasonable synthetic targets based on such evidence. It worth to mention here as well, that compound **1** was characterized by Pascal *et. al.*,[9] but unfortunately didn't produce crystals.

3.3.1 Geometries

The rationale behind the choice of the functional groups to build all the cyclophanes was mainly done based on the π-basic, and π-acid characters of **R**'s. The chemical nature of the **X** atoms at the bridges mainly changed the bond length with the carbon in the vicinity, making the methine **H** come closer to the π-system. Therefore, **R** groups were picked based on reported values of their Q_{zz} and $\alpha_{||}$ (Figure 5),[48, 79] which in principle should modulate C−**H**$\cdots\pi$ distance based on the physical nature of the CH-π weak **H**-bond.[49, 50, 93, 110]

The cyclophanes that presented the shortest C−**H**$\cdots\pi$ contact were **1**–**4**, and their optimized structures are shown in Figure 4. Calculations with different level of theory were done at the X-Ray structure of **5**, the synthesized compound (**VAMMEB**),[10] to validate the consistency on the level of theory employed (PBE0-D3/Def2-TZVPP). Therefore **5** structure was optimized also at the RI-SCS-MP2/Def2-TZVPP level,[124, 125, 131–133], and compared to the PBE0-D3/Def2-TZVPP results. The mean signed deviation (MSD) was similar to both levels, indicating that the employed DFT functional was adequate, and had the advantage of being less computationally demanding.

The shortest calculated C−**H**$\cdots\pi$ distance of all forty optimized structure belongs to the cyclophane **4**, which contains the s-triazine (**TRZ**) as the ring (**R**), and oxygen as the heteroatom (**X**). Since the choices made for **R**'s groups were done based on the idea that a weak CH-π **H**-Bond could explain the C−**H**$\cdots\pi$ proximity, i.e., that **R**'s with larger values of polarizability ($\alpha_{||}$) would favor the proximity, the fact that the **TRZ** analogues had shorter C−**H**$\cdots\pi$ than **BZN** had to be explained (Figure 4).

The physical nature of the very weak CH-π interaction is mainly dispersive nature, and may be evaluated through the polarizability ($\alpha_{||}$) of the aromatic moieties (Figure 5.[49, 82] In contrast to CH-π weak **H**-Bonds, strong **H**-Bonds have significant electrostatic contributions

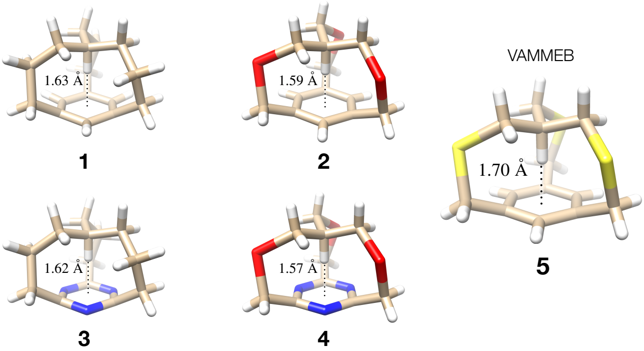

Figure 4 – Optimized structures of compounds **1**–**4**, including selected individual centralized C−**H**$\cdots\pi$ distances (Å). Color-code: tan = carbon, blue = nitrogen, white = hydrogen, and red = oxygen.

to their physical nature. Therefore the quadrupole moment (Q_{zz}) is the main contributor to explain the C−**H**$\cdots\pi$ distances found in the cyclophanes with **TRZ**.[49]

In fact, comparing the $\alpha_{||}$ and Q_{zz} values between **BZN**, and **TRZ** (Figure 5),[87–89] evinces that the significant difference between the two π-systems are Q_{zz}, which suggests at first glance, that the cyclophanes having **TRZ** had to be favored by a stronger electrostatic component contribution coming from the **R** and would have shorter C−**H**$\cdots\pi$ contacts.

This contradictory, yet interesting finding led to understand further the physical nature of the interactions taking place into detail, evaluating the orbital stabilisation, as well as charge distribution of the system, so that the unorthodox strong electrostatic CH-π **H**-Bond could be explained.

3.3.2 Non-Covalent Distance Analysis

The non-covalent distances, possible interactions, structural and spectroscopic uniqueness that related to the C−**H**$\cdots\pi$ of the *in*-isomers had to be addressed and explained. These aspects were examined in the light of computational methods that provided the required data that was utilized to relate aspects of the electronic, and orbital system of the cyclophanes, to the geometry analysis of their scaffolds. The calculated methine **H** ^{1}H NMR chemical shift ($\delta^{\mathrm{calc.}}_{\mathrm{TMS}}$) for **1** was found to be −4.11 ppm (Figure 5), in excellent agreement with −4.03 ppm, the reported value in the literature (Figure 5). [9] The blue-shifted calculated IR vibrational frequency ($\nu_{\mathrm{C-H}}$ = 3476 cm^{-1}) agreed to the unusual C(sp^3)−H = 1.052 Å bond length as well (Figure 5).

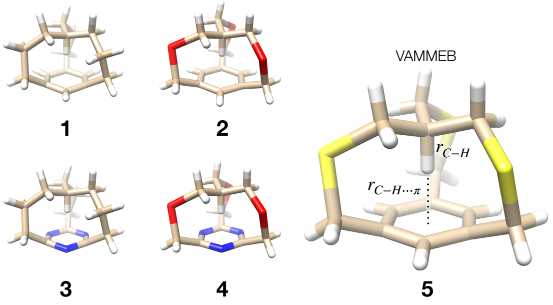

Structure	$r_{\mathrm{C\text{-}\mathbf{H}}\cdots\pi}$	$r_{\mathrm{C\text{-}\mathbf{H}}}$	$\nu_{\mathrm{C\text{-}\mathbf{H}}}$	$\Delta E_{\mathrm{in\text{-}out}}$	$\delta^{\mathrm{calc.}}_{\mathrm{TMS}}$
1	1.631	1.061	3476 (3325)	13.1	−4.11 (−4.03)
2	1.586	1.058	3502	3.7	−4.31
3	1.619	1.055	3543	8.7	−3.50
4	1.574	1.052	3580	−2.9	−3.82
5	1.703 (1.695)	1.066 (1.086)	3408 (3260)	9.1	−2.84 (−2.84)

Figure 5 – Selected C−**H**$\cdots\pi$ distances ($r_{\mathrm{C\text{-}\mathbf{H}}}$, Å), C−**H** bond lengths ($r_{\mathrm{C\text{-}\mathbf{H}}}$, Å) and their corresponding stretching frequencies ($\nu_{\mathrm{C\text{-}\mathbf{H}}}$, cm^{-1}), differences of energy between isomers *in* and *out* ($\Delta E_{\mathrm{in\text{-}out}} = E_{\mathrm{out}} - E_{\mathrm{in}}$, kcal·mol^{-1}), and calculated ^{1}H NMR chemical shifts^a for **H** (δ_{TMS}, ppm) of compounds **1**–**5**. The available experimental values are given in parentheses.[9, 10]

In other words, the shortest C−**H**$\cdots\pi$ also has the smallest

$C(sp^3)-H$, that compared to a $C(sp)-H$ (1.086 Å) reveals a higher *p character*.[148] A possible explanation to this phenomena, is based on the crowded architecture of the *in* cyclophane,[149] and can related with charge reorganization, leading to a polarization of $C(sp^3)-H$ bond. The results of the atomic charges obtained from QTAIM [117] were employed to evaluate the assumption made to explain the short $r_{\text{C-}\mathbf{H}}$. The measurable quantum expectation values of charges given by QTAIM, [19] supports the fact that high field ^{1}H NMR chemical shifts are related with stronger shielding effects in **3** and **4** (**TRZ**), compared to **1** and **2** (**BZN**). The blue-shifted $\nu_{\text{C-}\mathbf{H}}$ in the super short $r_{\text{C-}\mathbf{H}}$ is also explained by the QTAIM charges, which shows more electron density at bond critical points of the C-**H** bond, which is associated with larger bond orders.

Another finding to be noted, shown in table of Figure 5, is that only **4** presented its *out*-isomer form more stable (-2.9 kcal·mol^{-1}) than isomer *in* (Table in 5). Additionally, **4** had also the shortest $\mathrm{C}-\mathbf{H}\cdots\pi$ distance (1.574 Å) (Figure 4), i.e., most probably indicating that the extremely short $\mathrm{C}-\mathbf{H}\cdots\pi$ contact in **4** entails into other effects that favor the *out*-isomer.

The values presented in Figure 6 show the sum of the NBO second order stabilisation energies ($\Delta E^{(2)}_{i\rightarrow j^*}$), related to donations from $\sigma(\mathrm{C}-\mathbf{H})$ to the σ^*, and π^* orbitals of the bridge neighboring groups C−H, C−C and C−O, as well as to the **R**'s groups. Selected $\mathrm{C}-\mathbf{H}\cdots\pi$ distances ($r_{\text{C-}\mathbf{H}\cdots\pi}$, Å) are presented for comparison.

NBO analysis evaluated the total energy stabilisation provided by the donor-acceptor interactions within the cyclophanes scaffolds (Figure 6). It was observed that while donor-acceptor interactions between **H** and the bridges are only present in "oxygen-bridged" compounds (see $\sigma(\mathrm{C}-\mathbf{H})\rightarrow\sigma^*(\mathrm{C}-\mathrm{O})$ values for **2** and **4** in Figure 6), methine **H** donor-acceptor interactions with the **R** unit is only observed with the **TRZ** ring (see $\sigma(\mathrm{C}-\mathbf{H})\rightarrow\pi^*(\text{ring})$ values for **3** and **4** in Figure 6). Compound **4**, which has an oxygen at the bridges, and the **TRZ** as π-systems, was used to exemplify these effects, as displayed in Figure 6.

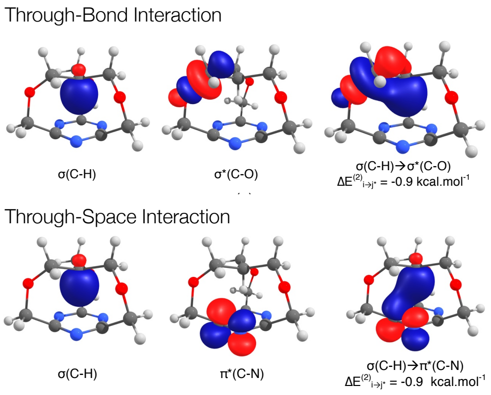
Through-Bond Interaction
σ(C-H)
σ*(C-O)
σ(C-H)→σ*(C-O)
ΔE(2)i→j* = -0.9 kcal.mol-1
Through-Space Interaction
σ(C-H)
π*(C-N)
σ(C-H)→π*(C-N)
ΔE(2)i→j* = -0.9 kcal.mol-1

	$\Delta E^{(2)}_{i\to j^*}$ (kcal·mol^{-1})			
Interactions	**1**	**2**	**3**	**4**
σ(C$-$**H**)$\to$ σ^*(C$-$H)	-8.6	-8.2	-8.3	-8.2
σ(C$-$**H**)$\to$ σ^*(C$-$C)	-3.1	-3.2	-1.9	-2.1
σ(C$-$**H**)$\to$ σ^*(C$-$O)	-	-2.4	-	-2.8
σ(C$-$**H**)$\to$ π^*(**R**)	-	-	-3.1	-2.9
TOTAL	-11.7	-13.8	-13.3	-16.0
$r_{\text{C-}\mathbf{H}\cdots\pi}$(Å)	1.631	1.596	1.619	1.574

Figure 6 – Selected donor-acceptor NBO interactions for compound **4**, and second order stabilisation energies ($\Delta E^{(2)}_{i\to j^*}$) for **1**–**4**. Color-code: gray = carbon, blue = nitrogen, white = hydrogen, and red = oxygen.

The orbitals stabilisation effects illustrated in this image, represent the *through-bond* and *through-space* interactions. While the *through-bond* interaction happens between σ(C$-$**H**) donor NBO, and σ^* of the heteroatomic aliphatic chain neighbor C$-$O acceptor NBO, the *through-space* interaction is shown to happen between σ(C$-$**H**) donor NBO, and π^* acceptor NBO of **TRZ** (Figure 6). These two types of orbital stabilisation effects are typical of cyclophanes structures, and have been already studied by Caramori *et. al.*.[150, 151]

In compound **4**, which has the smallest $r_{\text{C-}\mathbf{H}\cdots\pi}$, the *through-bond* interaction (Figure 6) happens in the oxygen donor-acceptor interaction between the σ(C$-$H) bonding, and the σ^*(C$-$O) anti-bonding orbitals (- 2.8 kcal·mol^{-1}). The *through-space* interaction in Figure 6, is seen from **TRZ** donor-acceptor interactions between the σ(C−H) bonding and the π^* anti-bonding orbitals of the C−N bonds of **R** (-2.9 kcal·mol^{-1}). Notice that cyclophane **4** is the only compound out of the four analysed, in which the four types of orbitals stabilisation interactions is present, therefore its resulting orbital stabilisation energy is the highest (- 16.0 kcal·mol^{-1}).

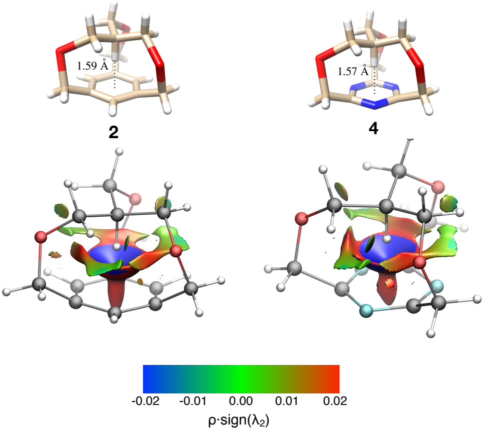

Figure 7 – NCI color maps for cyclophane **2** (**R** = **BZN**), and **4** (**R** = **TRZ**). Color-code: tan = carbon, blue = nitrogen, white = hydrogen, and red = oxygen.

The intramolecular interactions profile in cyclophanes **1**–**4**, was qualitatively evaluated employing the NCI analysis [120,140]. The NCI is a topological technique that enables the visualization of the non-covalent interactions in a molecular structure, by creating colored surfaces in regions of the molecular scaffold that are characterized by reduced density gradient (s(ρ)), and low electron density ($\rho(r) < 0.06$).s(ρ). The surfaces created represent regions of non-covalent interactions likelihood and the color printed differentiates the character of the interaction into attractive (blue), repulsive (red), or weak non-covalent interactions (green)(Appendix C.3.3).[140] The distinction of the physical nature of the interactions is made by correlating each point of the specific regions with the second eigenvalue of the electron density Hessian (λ_2) which accounts for the accumulation (blue) or depletion (red) of density in the plane perpendicular to the interaction.

The resulting NCI image for cyclophanes **2** and **4** (Figure 7), shows the colored maps for the two compounds which had the shortest $\mathrm{C{-}\mathbf{H}\cdots\pi}$ distances, and differ by their **R** groups, **BZN**, and **TRZ**, respectively. Strong, attractive interactions are seen, painted in blue, between the methine **H** and the center of the **R**'s, and appeared to the structures of **1**–**4**. The blue surfaces, characterize strong **H**-Bonds, indicating that $\mathrm{C{-}\mathbf{H}\cdots\pi}$ contacts in these cyclophanes are not merely of dispersive in nature, but electrostatic, and with a noticeable covalent character, associated due to the surface bowl format.

This electrostatic character observed, corroborates with the fact that shorter $\mathrm{C{-}\mathbf{H}\cdots\pi}$ distances are observed in the compounds having **TRZ** (**3** and **4**), instead of **BZN** (**1** and **2**), as is reinforced by the Q_{zz} values of **TRZ**, in contrast to **BZN**, shown in Figure 5.[3] Hence the shorter $\mathrm{C{-}\mathbf{H}\cdots\pi}$ proximity seen in **3** and **4**, which have **TRZ** ring, instead of **1** and **2**, makes sense if associated with the atypical nature of the CH-π interaction observed in these *in*-isomers. Moreover, the top/bottom view of the NCI colored surface map in **2** and **4** (Figure 8), shows that an extra **H**-Bond contribution between the **H** and the N atoms of the **TRZ** units, as it can be seen by the larger, and rounded blue areas at the bottom view in compound **4** (Figure 8). The smaller repulsive regions observed (red), also suggest that despite the electrostatic CH-π interaction between the methine **H** and **R**'s, the crowded cyclophane framework also deals with repulsive steric effects that result from the ultra-short group contacts.

Overall, the non-covalent interactions taking place in the squeezed dome-shaped framework of the “Iron Maidens”, seen from a QTAIM, NBO, and NCI approach, corroborate to conclude that the enforced $\mathrm{C{-}\mathbf{H}\cdots\pi}$ proximity in the “Iron Maiden” framework items from the

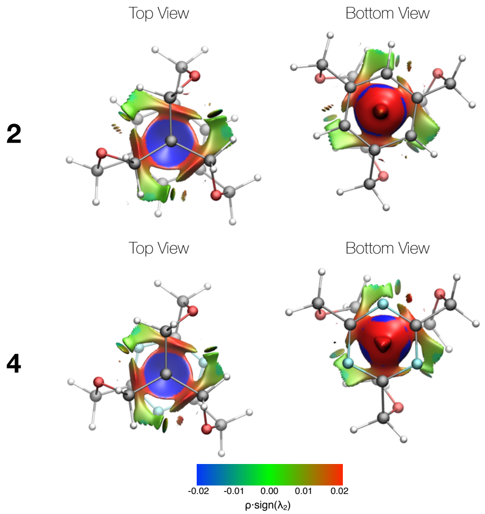

Figure 8 – Top and bottom view of the NCI color maps for cyclophane **2** (**R** = **BZN**), and **4** (**R** = **TRZ**). Color-code: tan = carbon, blue = nitrogen, white = hydrogen, and red = oxygen.

interplay of significant stabilising electrostatic component, with considerable covalent character, which characterizes a strong CH-π **H**-Bond, in contrast to typical weak, and dispersion driven CH-π **H**-Bonds.[49]

3.3.3 Framework Strain Analysis

Hypothetical isodesmic reactions provided strain energy values to explain if the apical methine **H** proximity to the **R** moieties, resulted from an attractive interaction, or an enforced framework strain condition. To evaluate these structural aspects in the cyclophane, a fragmentation profile was set considering the parts of the *in*-isomer that suffered the most from strain (Figure 9). Hence, fragmentation resulted in three parts, i.e., a ring, a bridge, and methine, as depicted in Figure 9. These original fragments were then capped with relaxed hydrogen atoms that were subsequently optimized alone, i.e., keeping the remaining atoms fixed, precisely as in the original cyclophane. The same chosen cyclophane fragment structures were also completely optimized with no constraints, leading to “perfect” fragments in the sense that their geometry optimization corresponds to a minimum in the potential energy surface, in order to obtain the preparation energy to describe the cyclophane system (Figure 9).

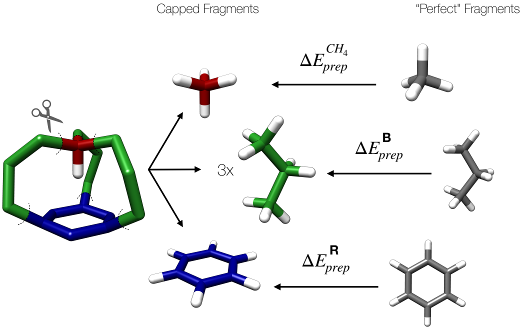

	1	**2**	**3**	**4**
$\Delta E_{\text{prep}}^{\text{total}}$	12.4	14.2	10.0	10.8
$3\Delta E_{\text{prep}}^{\mathbf{B}}$	7.4	8.2	7.2	8.1
$\Delta E_{\text{prep}}^{\mathbf{R}}$	4.7	5.6	2.2	2.1
$\Delta E_{\text{prep}}^{\text{CH}_4}$	0.3	0.4	0.5	0.6

Figure 9 – Iso Scheme - Color-code: tan = carbon, blue = nitrogen, white = hydrogen, and red = oxygen.Thermodynamic decomposition of strain energy (in kcal·mol^{-1}) by means of isodesmic reactions of iron maidens **1**–**4**.

A comparison between the “perfect” optimized fragments, to the original partially optimized capped ones, yields the preparation energies for each fragment: the bridges ($\Delta E_{\text{prep}}^{\mathbf{B}}$), the ring ($\Delta E_{\text{prep}}^{\mathbf{R}}$), and the methine ($\Delta E_{\text{prep}}^{\text{CH}_4}$) (Figure 9). In other words, $\Delta E_{\text{prep}}^{\mathbf{B}}$, ($\Delta E_{\text{prep}}^{\mathbf{R}}$), and $\Delta E_{\text{prep}}^{\text{CH}_4}$) account for the amount of energy required for “perfect” fragments to be distorted into the capped ones. Thus, the total preparation energy ($\Delta E_{\text{prep}}^{\text{total}}$) is equal to the sum of the fragments energies, multiplied by the number of fragments required to “rebuild” the original strained “Iron Maidens” framework, as in Equation **1**.

$$\Delta E_{\text{prep}}^{\text{total}} = 3\Delta E_{\text{prep}}^{\mathbf{B}} + \Delta E_{\text{prep}}^{\mathbf{R}} + \Delta E_{\text{prep}}^{\text{CH}_4} \quad \textbf{(1)}$$

Once the preparation energy for each fragment is obtained, a complete set of hypothetical reactions can be built following the same guideline, to analyse specific attributes of any molecular system. In the case of the dome-shaped cyclophane, the goal was to understand the relationship between the strain built at the aliphatic chains, and energy associated with interaction arising from the $\mathrm{C{-}\mathbf{H}}\cdots\pi$ proximity. Hence, three hypothetical reactions, were built: $\Delta E^{1}_{\mathrm{iso}}$, $\Delta E^{2}_{\mathrm{iso}}$, and $\Delta E^{\mathrm{CH_4}/\pi}_{\mathrm{int}}$, shown in Figure 10. The association of these isodesmic reactions, with the preparation energies of the cyclophane fragments, results in Equation **2**.

$$\Delta E^{1}_{\mathrm{iso}} = \Delta E^{2}_{\mathrm{iso}} - \Delta E^{\mathrm{CH_4}/\pi}_{\mathrm{int}} - 3\Delta E^{\mathbf{B}}_{\mathrm{prep}} - \Delta E^{\mathbf{R}}_{\mathrm{prep}} - \Delta E^{\mathrm{CH_4}}_{\mathrm{prep}} \quad \mathbf{(2)}$$

The analysis of a set of hypothetical reactions revealed that the most substantial contribution to the total energy released comes from the bridges bonding/repulsion term $\Delta E^{1}_{\mathrm{iso}}$ (Figure 10). Isodesmic reactions also revealed that the overall strain accumulated in the “Iron maiden” is more significant when the ring is **BZN** ($\Delta E^{1}_{\mathrm{iso}}$ = -126.2 kcal·mol^{-1}). In order to evaluate the balance between interaction and strain in the cyclophanes, an energy decomposition was done, since it bears neither direct effects of covalent bonding between bridges and ring/methane nor their respective pairwise repulsion $\Delta E^{2}_{\mathrm{iso}}$ (Figure 10).

Comparison between $\Delta E^{1}_{\mathrm{iso}}$ and $\Delta E^{2}_{\mathrm{iso}}$ in terms of percentages, enables to compute the amount of strain at the aliphatic chains (Figure 10). This bridge strain accounted for more than half of total strain energy (58–60%) in the structures containing **BZN**, and even more for the structures with triazine (73–75%). This indicates that the **TRZ** compounds are more flexible since they hold more strain at the bridges, hence can reduce part of the framework strain, due to this higher degree of mobility. Altogether the findings from the isodesmic reactions revealed that shorter $\mathrm{C{-}\mathbf{H}}\cdots\pi$ distances are also associated with highly strained bridges, leading to larger $\mathrm{C{-}\mathbf{H}}\cdots\pi$ repulsion that is associated with the close contact. This excess of torsion is slightly relieved in the **TRZ** systems, due to more extensive structural flexibility of its π-system.

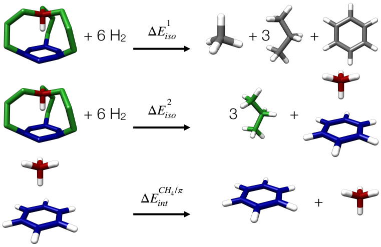

	1	**2**	**3**	**4**
$\Delta E^{1}_{\mathrm{iso}}$	−126.2	−122.8	−112.7	−120.5
$\Delta E^{2}_{\mathrm{iso}}$	−100.5	−93.0	−88.4	−92.9
$\Delta E^{\mathrm{CH_4}/\pi}_{\mathrm{int}}$	−13.3	−15.6	−14.3	−16.7

Figure 10 – Iso Scheme - Color-code: tan = carbon, blue = nitrogen, white = hydrogen, and red = oxygen. Thermodynamic decomposition of strain energy by means of isodesmic reactions of a molecular iron maiden, here exemplified by **1**. Broken covalent bonds were capped with relaxed hydrogen atoms (e.g., the first molecule in the right-hand side of (1) is methane). Apart from capping hydrogens, fragments colored with the same tone have the same geometry, but structures in grey were optimized entirely. Associated energies are shown

3.4 Concluding Remarks

The physical nature of the CH-π weak **H**-Bond on the compressed skeleton of the molecular “Iron Maidens”, revealed in the light of QTAIM, NBO and NCI analyses, that the ultra-short C−**H**$\cdots\pi$ distances in these compounds is sustained by an interplay between a significant stabilising electrostatic component of an actual enforced strong CH-π **H**-Bond, which presents a remote covalent character.

Two particularly short C−**H**$\cdots\pi$ distances were obtained: 1.574 Å, for the cyclophane containing a **TRZ** ring and oxygen as the **X** group at the aliphatic chains (**4**), and 1.586 Å, in an analogue cyclophane with **BZN** instead (**2**). Methine ^{1}H chemical shifts for *in*-isomers with shortest C−**H**$\cdots\pi$ distances, **4** and **2**, were calculated to be −3.82 and −4.31 ppm, respectively, and are related to charge distribution, and stronger shielding effects at the methine **H**’s, as supported by QTAIM, and NPA charges (Figure 5).

The excessively short non-covalent proximity in **4** makes the *in*-isomer unstable, indicating that its C−**H**$\cdots\pi$ might represent an actual borderline of such C−**H**$\cdots\pi$ contacts. This affirmation was associated by the fact that its *out*-isomer is energetically more favorable than its inward version only for compound **4** (Figure 5).

The latter reasoning left compound **2**, supposedly, as the most reliable candidate to become an actual inwardly pyramidalized cyclophane, having the shortest C−**H**$\cdots\pi$ distance, if experimentally obtained, and that would be even shorter than any experimental data reported to date for such cyclophanes![11]

Finally, isodesmic reactions revealed that the C−**H**$\cdots\pi$ proximity is tuned mainly by the ability of the bridges to support the strain imposed by the cyclophanes structure, hence compressing the C−H bond against the π-system. It also revealed that **TRZ** as the π-system, leads to shorter C−**H**$\cdots\pi$ distances because this **R** can bare more strain due to its higher degree of flexibility, compared to **BZN**. All of the exciting findings associated to the molecular "Iron Maiden" scaffold lead to the conjecture that the excess of the C−**H**$\cdots\pi$ functional group contacts, characterized a non-covalent proximity limit, in that this boundary condition might lie between **2** and **4**, i.e., around 1.58 Å.

Part III

Cylindric Cage-Type Cyclophanes

4 Fluoride-Selective Cylindrophanes

Molecular cage architectures (Figure 1) that present high efficiency, affinity, and selectivity to host other species require the correct energetic and stereochemical parameters to comprise a supramolecular host-guest (**HG**) interacting system in a determined process, and environment. [22, 27, 101, 105]

Non-covalent interactions (**NCI**) coordinate supramolecular systems self-assembly and molecular recognition,[39, 80, 152] by means of a wide range of attractive and repulsive forces of different nature, and directionality, for example, hydrogen bonds, [92, 153–155] dihydrogen bonds, [58–60] π-stacking. [65, 114] The cation-π, [43, 69] and anion-π, [48, 79, 156] interactions are commonly related to host-guest (**HG**) systems, such as cylindrophanes,[14, 16] calyxarenes,[72, 91] or sophisticated interlocked receptors,[157, 158] and for this reason they increasingly receive attention.[43, 48]

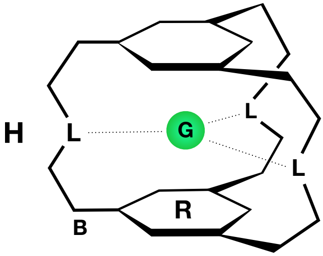

Figure 1 – Schematic representation of a cylindrophane host-guest (**HG**) system structure. Label: **H** = host, **G** = guest, **B** = bridges, **R** = rings, **L** = ligands.

Quantum chemistry tools are widely used to study the physical nature of chemical bonding.[55–57] In this sense, technological advances remarkably promoted the efficient implementation of methods with improved reliability to investigate chemical systems.[77,159] This breakthrough was notably relevant to understand the different intermolecular interactions, allowing to the development of new materials, [160–162] for example. Calculations performed with supramolecular systems containing non-covalent interactions, can either lead to empirical validation, or instead, aid the rationalization of results experimentally obtained.[65,78,86,114,115,163,164] There are a plethora of papers that make use of computational tools for both purposes, highlighting future challenges for this field concerning anion coordination with the aid of theory.[81,165–167]

The anion-π interaction uniqueness has been a controvert topic among chemists,[47,71,168–170] due to the counterintuitive idea that negatively charged species could interact with an aromatic π-cloud. Eventually, numerous anion-π based studies lead to advances and to the development of supramolecular systems,[157,158,171], catalysis, [35,36,172,173] medicinal chemistry and biochemistry,[174–176] all of which support the continuity to raise insight on this specific **NCI**. Increasingly attention has been given to receptors capable to selectively recognize and coordinate fluoride,[177,178] highlighting the challenges to be overcome such as anion coordination in aqueous systems, neutral anion-π receptors, which have not yet been observed, or the synthesis of novel metallated receptors that interact more strongly with anions.[68,70,91]

4.0.1 Investigative Design of Cylindrophanes

Cylindrophanes are adjustable molecular cages: they can form sandwich-type inclusion complexes with Ag^+ and Cu^+ cations (Figure B4),[13,15,16,86,179,180] and they are also suitable to host anions.[6,33,181] *In silico* design of the cylindrophane **6** rigid cage (Figure 2),[7] based in functional group chemistry, indicated that the framework configuration of this compound is suitable to selectively coordinate fluoride anions through the interplay between hydrogen bonds (H-bond), ion-pairing, and anion$-\pi$ interactions.[7,14] Subsequent synthesis of the unprecedented fluoride selective host-guest system not only highlighted the actual existence of anion$-\pi$ interactions, but also proved that they are selective to fluoride anions, instead of chlorides, in a methanol/water medium.[14]

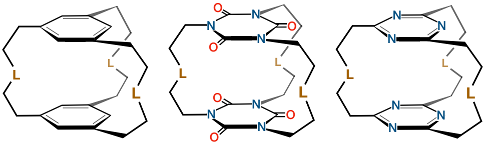

BZN		**CA**		**TRZ**	
	L		**L**		**L**
1	CH_2	**4**	CH_2	**7**	CH_2
2	NH	**5**	NH	**8**	NH
3	NH_2^+	**6**	NH_2^+	**9**	NH_2^+

Figure 2 – Cylindrophane model structures, organized in groups according to the chemical nature of **R** and **L**. Color-code: white = hydrogens, grey = carbons, blue = nitrogen, red = oxygen, black = ligand (**L**) group.

Unlike typical anion receptors, such as calixarenes, cucurbiturils, pillarenes, and tripodal receptors, no further attention has been given to propose novel cylindrophane frameworks, nor computational analysis has been done to the cylindrophane-fluoride system crystallographic structure.[34, 152] In contrast to **6** (Figure 2), most neutral cryptands-like receptors have been designed based on the anion coordination through multiple NH or $NH_2{}^+$ binding groups,[182] which means that anion-π interactions are not part the **NCI**'s that coordinate the negatively charged species inside the host. The steric fit in host **6** allows it to coordinate the F^-, and forces the ligands at the bridges to be near the coordinated anion. This enforced proximity of functional groups in the rigid cyclophanes scaffold is known to yield unexpected structural behavior that arises from the balance of **NCI**'s and framework flexibility.[12] The interplay and cooperation of **NCI**'s, that rearrange the host framework requiring structural adjustments that optimize the **HG** ground state,[11] is a fact that can be used to study how different functional groups influence the **HG** interactions.

Rational design of the cylindrophane-fluoride system (Figure 1), must take into account the fact that it posses a rigid 3D pocket formed by three backbone bridges and a ligand (**L**) atom that can be modified, and two aromatic moieties (**R**). The **R** portions are modulated by electron withdrawing groups (**EWG**) or electron donating groups (**EDG**), tuning the π-system to become π-basic or π-acidic.[86] This impacts directly in the magnitude and signal of the permanent quadrupole moment (Q_{zz}),[85] as well as the intrinsic polarizability ($\alpha_{||}$) (Figure 5, Part I) of **R** rings, which are crucial to describe the physical nature of anion-π interaction.[48, 79, 156, 164] Changes in the binding(**L**) groups at the bridges, affect the anion coordination directly through *short-distance effects*, which are characterized by the enforced proximity of **L** to the guest (**G**).

Selective cylindrophanes design relies specifically on changing: ***(i)*** the number of atoms at the bridges connecting the π-systems, affecting the cage steric fit, ***(ii)*** the nature of the binding group (**L**) which provide extra stabilisation by means of enforced *short-distance effects*, and ***(iii)*** the chemical nature of the aromatic moieties (**R**), affecting the guest coordination through *long-distance effects* weaker interactions.

This present study explains the role of **R** and **L** in the cylindrophane-fluoride systems presented in Figure 2. The proposed scaffold modifications are: ***(a)*** **L** = CH_2, NH, and NH_2^+ at the backbone bridges, and ***(b)*** **R** = benzene (**BZN**), cyanuric acid (**CA**), and s-triazine (**TRZ**) as π-systems. The **L** groups with different chemical nature act as binding ligands, and affect directly the F^- coordination due to its enforced proximity (*short-distance effects*). Likewise, the chosen **R** rings have different Q_{zz} and $\alpha_{||}$ profiles (Figure 5, Part I), and affect the magnitude of the anion-π interaction (*long-distance effects*), therefore the anion coordination. For the sake of simplicity, the nine **HG** systems are classified according to **R** analogues categories: **BZN** group (**1-3**), **CA** group (**4-6**), **TRZ** group (**7-9**), i.e., having different types of **L**'s: CH_2, NH, NH_2^+, respectively. The cylindrophane-fluoride systems, are addressed by the following nomenclature: **1**·F$^-$–**9**·F$^-$.

The theoretical cylindrophane design in 2006,[7] used the hybrid functional B3LYP,[183,184] and the Pople's[185] valence double-zeta polarized basis set 6-31+G(d,p). Moreover, it corrected the basis set superposition error (BSSE) with the Boys and Bernardi[186] counterpoise method (CP), which only provides an estimate of the BSSE. The correct choice of the DFT functional, accounting for dispersion corrections, in conjunction with high quality, polarized basis set was part of this work, to correctly address the weak interactions energy values, and to obtain the correct optimized structures, starting from the reported experimental results.[14] The reasoning of the **NCI**'s in the cylindrophane skeleton with an updated level of theory presented here, aims to serve as a guide to motivate the production of novel anion selective hosts, acknowledging the structural properties that **L** and **R** represent in the cylindrophane framework, and showcasing the importance of the collaboration between computational and experimental chemistry.[187]

4.1 Methodology

Geometry optimization and numerical vibrational frequency calculations for all systems were carried out with ORCA software (v.3.0.1).[121] Cyclophane structures were designed based on deposited crystallographic structures from the Cambridge Structural Database (CSD) cod. **KISDIA** and **KISDEW**,[14] and their optimization was calculated with no symmetry constraint. Geometric parameters were analysed for the host (**H**) without anion and the host-guest (**HG**) system, and their structural parameters were presented relative to one another, as schematically represented in Figure 3.

DFT-D3 level of theory calculations was used with the GGA functional of Becke and Perdew (BP86),[188,189] in conjunction with a default Ahlrich's all-electron relativistic balanced triple-ζ quality basis set Def2-TZVP,[124] which has been specifically designed for SCF

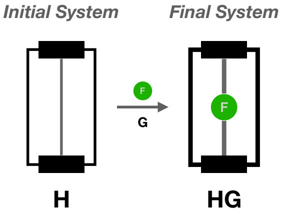

$H \rightarrow HG$
$1 \rightarrow 1{\cdot}F^-$
$2 \rightarrow 2{\cdot}F^-$
$3 \rightarrow 3{\cdot}F^-$
$4 \rightarrow 4{\cdot}F^-$
$5 \rightarrow 5{\cdot}F^-$
$6 \rightarrow 6{\cdot}F^-$
$7 \rightarrow 7{\cdot}F^-$
$8 \rightarrow 8{\cdot}F^-$
$9 \rightarrow 9{\cdot}F^-$

Figure 3 – Scheme illustrating the host-guest system formation (**H** → **HG**).

calculations and accounts for polarization.[190] Atom-pairwise dispersion correction was applied to describe long-range dispersion effects with Grimme's empirical dispersion correction and Becke-Johnson damping functions, D3(BJ).[127,129,130,191,192] The relativistic optimized triple-zeta quality TZ2P basis set[139] was employed, in conjunction to scalar ZORA Hamiltonian.[193–195] Computational efficiency at the Hartree-Fock exchange integrals was improved applying RI approximation.[196] Absence of negative eigenvalues in the Hessian matrix confirmed that the obtained optimized structures correspond to a true minimum on the potential energy surface (PES). Molecular Electrostatic Potential maps (MEP) used consistent isovalues and color scaling for the related compounds. The isovalue is the cutoff electron density from the molecular calculations used to define the outer boundary of the molecule.

Hirshfeld charge population analysis,[197–199] and the canonical Energy Decomposition Analysis (EDA),[200–202] calculated at 2016 version of the ADF software package,[138,203,204] were applied to describe the magnitude and physical nature of the host-guest system.[205,206] EDA provides the total interaction energy (ΔE_{int}) of the host-guest systems, which results from the decomposed energy terms: Pauli repulsion (ΔE_{Pauli}), electrostatic (ΔV_{elstat}), orbital interaction (ΔE_{oi}) and dispersion (ΔE_{disp}), as shown in Equation 4.1.

$$\Delta E_{\text{int}} = \Delta V_{\text{elstat}} + \Delta E_{\text{Pauli}} + \Delta E_{\text{oi}} + \Delta E_{\text{disp}} \tag{4.1}$$

The bond dissociation energy (BDE) of the host-guest system was calculated by adding the ΔE_{prep} to the ΔE_{int}, as in Equation 4.2.

$$-\text{BDE} = \Delta E_{\text{int}} + \Delta E_{\text{prep}} \tag{4.2}$$

The ΔE_{prep} is the energy difference between the single point optimization of the host structure to the host-guest system (ΔE_{int}), and it accounts the conformation strain, and charge reorganization energy required for the **H** to assume its conformation in the **HG**.

Non-Covalent Interactions index (NCI_x) analysis, employed with the NCIPLOT code,[140] and visualized with the VMD software,[141] provided qualitative information regarding the physical nature and spatial distribution of the non-covalent interactions in the studied compounds.[120]

Free energies (ΔG), calculated with ORCA software (v.3.0.1)[121] with corrected rotational entropy, provided the Relative Binding Energies (RBE), considering ideal thermodynamic conditions ($T = 298.15$ K, $P = 1.00$ atm, $\text{R} = 8.315$ J/molK). The scheme in Figure 4 represents initial and final states considered in Equation 4.3. The RBE ($\Delta\Delta G_{\text{bind}}$) is a path independent work, that represents the energy cost related to the exchange of the F^- from a **HG** ($\Delta G_{\text{H}_i\cdot\text{F}^-}$), at the *initial state*, to an empty **H** (ΔG_{H_j}), in the *final state*, as in Equation 4.3.

$$\Delta\Delta G_{\text{bind}} = \Delta G_{\text{final}} - \Delta G_{\text{initial}} \tag{4.3}$$

$$\Delta\Delta G_{\text{bind}} = (\Delta G_{\text{H}_{i\cdot\text{F}^-}} + \Delta G_{\text{H}_j})_{\text{final}} - (\Delta G_{\text{H}_i} + \Delta G_{\text{H}_{j\cdot\text{F}^-}})_{\text{initial}} \tag{4.4}$$

As represented in Figure 4, and stated in Equation 4.4, the *initial state* considers one of the **HG**'s **1**$\cdot\text{F}^-$–**9**$\cdot\text{F}^-$ as $\text{H}_{i\cdot\text{F}^-}$, and one of the empty hosts **1**–**9** in H_j, and the *final state* considers that the F^- has moved from $\text{H}_{i\cdot\text{F}^-}$ to H_j.

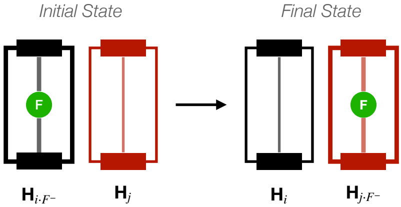

Figure 4 – Scheme representing initial and final states used to calculate the relative binding energies ($\Delta\Delta G_{\text{bind}}$), which is the energy required to take F^- from the host-guest system $H_{i \cdot F^-}$ (Figure 2), and place it inside the cavity of the empty host H_j (*final state*).

4.2 Results and Discussion

Cyclophanes **1**–**9** (Figure B4) were modeled based on the deposited crystallographic structures of the empty host **6**, and the obtained **HG** system that resembles **6**·F^- (Figures B4). Their main structural difference are the long hydrophobic chains bonded to the **L** group, in **KISDEW** and **KISDIA** (Figure B1), which were replaced by a hydrogen (**L** = $NH_2{}^+$) in **6**·F^-, and its analogues with different **R**'s, i.e., **3**·F^- (**BZN**), **9**·F^- (**TRZ**).

Similar synthesized cylindrophane structures containing two **R** groups, three aliphatic bridges with five atoms total, with a functional group **L** at the middle position, are illustrated in Figure B1 with their CSD codes, at the Appendix B, B.1. Average values presented here were selected based on their relevance. Regardless, the complete geometry data set for all compounds are found at the Appendix B, B.1, where the tables and corresponding images for all systems are presented.

Geometry optimization was done to the empty **H**'s (Figure B3, Table B1,B3), then F^- was placed inside the cavity to optimize the **HG** systems (Figure B4, Table B2,B4). Figure B2 illustrates all geometry parameters to the empty hosts **1**–**9** (Table B1), and host-guest systems **1**·F^-–**9**·F^- (Table B2). Cyclophanes framework angles are provided in detail for the empty **H**'s **1**–**9** (Table B3), and the **HG**'s **1**·F$^-$–**9**·F$^-$ (Table B4), in the Appendix B, B.1.

Evaluation of the non-covalent interactions in the cylindrophanes framework discussed in section 4.2.2, is based on electron density and wave function analysis. This part is dedicated to explain the nature of the **NCI**'s in the **HG** systems, and to address how the different functional groups work in cooperation to enhance the **HG** interactions. For this matter, Molecular Electrostatic Potential maps (MEP), in section 4.2.2.1, shows visual representations of the electron distribution in the surface of the empty hosts **1**–**9**, the Energy Decomposition Analysis (EDA), provides quantitative values of the energy associated with the **HG** interaction, in section 4.2.2.2, and the dissociation energy related to each structure. Moreover, EDA approach is used in a fragmentation scheme (Figure 13) to shed light on the energy contribution of the **L** and **R** functional groups. This fragmentation is done to better assess in a isolated form, the interactions of the bridges (**B**) (Figure B9, Table B6) in the **HG**'s, as well as the for the rings (**R**) (Figure B8, Table B5), keeping closed-shell fragments atoms positions fixed, as in the original **HG** systems.

The Non-Covalent Interactions index analysis (NCI$_x$), in Section 4.2.2.3, is a topological analysis of the electron density that creates surfaces in regions within the **HG** systems in which non-covalent interactions occurs. It also determines the **NCI**'s strength based on a gradient of colors that is dependent on the sign of the second eigenvalue of the Hessian matrix. The NCI$_x$ analysis corroborates with the Vibrational Frequency Analysis in section 4.2.2.4, underlining the findings related to the non-covalent interactions in **HG**'s with the different functional groups, through their Infrared (IR) Spectra. The complete data set for the IR spectra is given at the support information located in the in Appendix B, B.2.4.

The Binding Energy Analysis, proposed in section 4.2.3, provides the relative binding energy ($\Delta\Delta G_{\text{bind}}$) for the **HG** systems. The

$\Delta\Delta G_{\mathrm{bind}}$ correlates the exchange energy that is required to move the anion from the cavity of one **HG** system to different empty **H**'s (Figure 4). The results for the **HG**/**H** cavity exchange are shown in the form of a skew-symmetric matrix that is painted as a heatmap (Figure 20), discerning with different colors and $\Delta\Delta G_{\mathrm{bind}}$ values which **HG**/**H** cavity replacements are favorable, and which are not.

All **H** and **HG** systems were optimized without symmetry restrictions. Therefore they differ to the theoretically studied systems by Mascal and collaborators,[7] which were forced to have a C_{3h} symmetry. Since the modeled framework here is based on experimental results, comparison between the structures of **H**'s and **HG**'s (Figure B2,) with **KISDEW** and **KIDIA** (Figure B1), shows that they belong to C_s point group and that they are alike. Some aspects of the C_s isomer structures are discussed in section 4.2.1, with additional analysis of the conformers in section 4.2.4. The latter part is dedicated to explaining the energetic differences between the conformational isomers C_{3h} ($\mathbf{H}_{sym}$), and C_s (**H**) when they are empty, as well as to when they interact with the fluoride anion.

4.2.1 Structural Parameters and Geometry Analyses

In supramolecular chemistry, *allosteric effects* refer to the cooperativity arising from the interplay of two or more **NCI**'s. For cylindrophanes reported here, *allosteric effect* is related to the unexpected structural behavior of some **HG**'s to favor specific **NCI**'s to accommodate the anion. This allosteric behavior is associated with preorganization effects and is not only seen in the **HG**'s conformations, but also in how it changes to form the **HG**'s.[1,207] Thus, acknowledging the structural modifications in the **H** → **HG** process ((Figure 3)), as well as in each final **HG** system, enables to understand the *allosteric effects* that occur the cylindrophanes, shedding light on the role of **R** and **L** groups.[208–210]

The structural parameters of the optimized cylindrophane frameworks (Figure 2), and the geometries average values discussed in this section, are depicted in the scheme of Figure 5. The analysed parameters were the distance of the **L**'s internal hydrogen ($\mathbf{H}_{in}$) to the F^- ($H\cdots F^-$), the $\mathbf{L}$-$\mathbf{H}_{in}$ bond length (**L**-H), the **L**-$H\cdots F^-$ hydrogen bond angle ($\angle\,\beta$), and the cylindrophane π-systems distances ($R_1\cdots R_2$). The format of the values shown in Figure 5 compare **H** to **HG** (**H**|**HG**). The first value in each column refers to the empty **H** structure, and the second value to the formed **HG** system. The $H\cdots F^-$ distances and $\angle\,\beta$ angles in the empty hosts are hypothetical. It considers a dummy atom placed in the midpoint position between the **R**'s centroid axis, instead of a F^-. Comparing the geometry parameters in the empty **H**, to the formed **HG** systems, yields the geometry preparation values of the $\mathbf{H} \rightarrow \mathbf{HG}$ process, and relate to structural the deformities required to accommodate the anion.

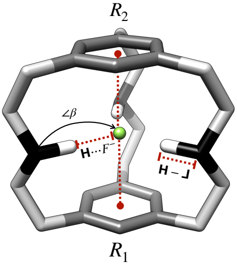

$\mathbf{H} \rightarrow \mathbf{HG}$	$\mathbf{L}-H$	$H\cdots F^-$	$\angle\beta$	$R_1\cdots R_2$
$\mathbf{1} \rightarrow \mathbf{1}\cdot\mathbf{F}^-$	1.10|1.12	1.90|1.80	174.2|173.2	5.24|5.46
$\mathbf{2} \rightarrow \mathbf{2}\cdot\mathbf{F}^-$	1.03|1.06	2.09|1.74	170.8|178.3	4.93|5.42
$\mathbf{3} \rightarrow \mathbf{3}\cdot\mathbf{F}^-$	1.04|1.10	2.27|1.62	165.8|175.2	4.68|5.48
$\mathbf{4} \rightarrow \mathbf{4}\cdot\mathbf{F}^-$	1.10|1.11	1.76|1.87	179.5|169.9	5.24|5.18
$\mathbf{5} \rightarrow \mathbf{5}\cdot\mathbf{F}^-$	1.02|1.05	1.97|1.78	176.3|178.6	4.94|5.25
$\mathbf{6} \rightarrow \mathbf{6}\cdot\mathbf{F}^-$	1.05|1.07	3.42|1.68	109.1|173.8	3.55|5.17
$\mathbf{7} \rightarrow \mathbf{7}\cdot\mathbf{F}^-$	1.10|1.12	1.75|1.82	175.5|166.2	5.24|5.30
$\mathbf{8} \rightarrow \mathbf{8}\cdot\mathbf{F}^-$	1.02|1.05	2.05|1.73	159.2|175.2	4.96|5.28
$\mathbf{9} \rightarrow \mathbf{9}\cdot\mathbf{F}^-$	1.05|1.08	3.14|1.61	113.0|177.8	3.34|5.34

Figure 5 – Scheme indicating structural parameters, and the analysed geometries average values (Å). The table values compare the structural modifications that take in $\mathbf{H} \rightarrow \mathbf{HG}$, as indicated by the values before and after the | symbol. Detailed data is provided in Appendix B, B.1. The $H\cdots F^-$ and $\angle\,\beta$ values for hosts **1**–**9** were obtained placing dummy atom at the center of R_1 and R_2, and in the centroid axis of the **R**'s. Color-code: dim gray = **BZN**, **CA** and **TRZ**, **L**, black = backbone binding group s (**L**), white = hydrogens.

The five atoms at the bridges limit cylindrophane steric selectivity to the anionic guest. Moreover, its odd number of atoms directs the equidistant binding groups (**L**) towards the center of the cavity, as illustrated in Figure 1, which favors the guest coordination.[7] Since the molecular cages have distinct chemical environment related to the different **R** and **L** groups (Figure 2), the final **HG** interaction in each system should have different physical nature. For example, the **HG** with the **CA** rings have good anion-π receptors, and the **BZN** weak receptors, likewise, the compounds with CH_2 at the bridges have a poor H-bond donor, and the **HG**'s with NH_2^+ have a suitable H-bond donor.

The aromatic moieties studied compare **BZN** with two different triazines, i.e., a 1,3,5-triazine (**TRZ**), and a 1,3,5-triazine-2,4,6-triol (**CA**). The s-triazine (**TRZ**) has similar properties to benzene (**BZN**), such as aromaticity,[211] but it also has different reactivity, Q_{zz}, and $\alpha_{||}$, which makes them good candidates to be compared in the cyclophanes architecture. The chemical differences and similarities, when analysing the physical nature of the non-covalent interactions in the **HG** systems, enables to determine how sensitive the supramolecular system is to changes in its functional groups, determining how the F^- coordination is tuned.

The role of **L** is to stabilize F^- with strong *short-range* non-covalent interactions, that arise from the cage enforced groups proximities. Therefore, putting **L**'s of different chemical nature in this type of bonding situation, helps to see how dependent the F^- coordination is to the binding groups.[182, 212, 213] For this matter, the chosen **L** groups were a neutral aliphatic group ($\mathbf{L} = CH_2$), a neutral polar group ($\mathbf{L} = NH_2$), and a charged species ($\mathbf{L} = NH_2^+$). Framework modifications that take place related to the enforced proximity of the $\mathbf{H}_{in}$ towards F^-, named as *short-distance effects*, are represented by three different types of H-bonds that are formed between the $\mathbf{H}_{in}$ donors with the F^-, which is the proton acceptor (A^-): $C{-}\mathbf{H}\cdots A^-$, $N{-}\mathbf{H}\cdots A^-$, and $NH^+{-}\mathbf{H}\cdots A^-$. Likewise, structural modifications related to the π-systems and and their Q_{zz} and $\alpha_{||}$ values (Figure 5, Part I), named *long-distance effects*, are classified as: π-basic ($\mathbf{R} = \mathbf{BZN}$), a poor anion-$\pi$ receptor, neutral ($\mathbf{R} = \mathbf{TRZ}$), and π-acid ($\mathbf{R} = \mathbf{CA}$), a good anion-π receptor.

The fact that **1**·F$^-$–**9**·F$^-$ and **1**–**9** were analysed in gas phase with no symmetry restriction resulted in twisted structures for **6** and **9** due to intramolecular interactions. This behavior in solution state depends on the nature of the solvent,[165,207,214] which would influence in the intramolecular interactions, changing the final empty host conformation.

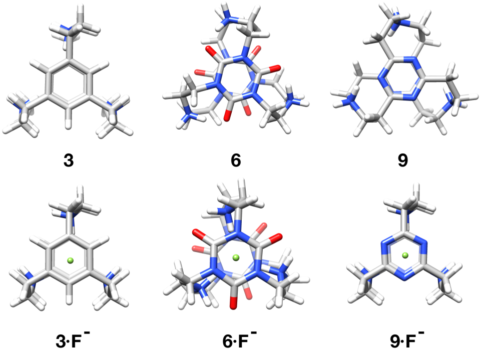

3 **6** **9**

3·F$^-$ **6·F$^-$** **9·F$^-$**

Figure 6 – Top view of optimized cylindrophanes conformation in **3**, **6**, and **9**, in contrast to their **HG** systems **3**·F$^-$, **6**·F$^-$, and **9**·F$^-$.

Since **H** and **G** species concentration is always smaller than the solvent, the F$^-$ coordination can only compete against solvation, when the receptor binding sites offers enough stabilising interactions to the guest, which is characterized by a high complementarity between **H** and **G**. In this sense, **6** and **9** conformation distortions indicates that such **H**'s offers more significant number of stabilising non-covalent interactions, and also shows that the **NCI**'s that composes the final **HG** system must overcome those intramolecular interactions so that the F$^-$ can enter into the cavity, resulting in a high complementary between the host and the fluoride.

Figure 6 shows the optimized structures of **H** systems **3**, **6**, and **9**, having **L** = $NH_2{}^+$ in common, which differ in their conformation to **HG** systems **3**·F$^-$, **6**·F$^-$, **9**·F$^-$. The **BZN** hosts analogues (**1**–**3**), lack

H-bond receptor groups in the π-systems to form the intramolecular interactions, as characterized by its high degree of symmetry. In contrast, **H** structures **6** and **9** display an helical twisted framework that is composed by six H-bonds (Figure 7), classified in two types: (I) three from NH_2^+ internal hydrogen, with the nitrogen atom in **TRZ** in **9** ($d_{NH\cdots N}$ = 1.90 Å, $\angle\beta_{NH\cdots N}$ = 143.50°), and the oxygen in **CA** in **6** ($d_{NH\cdots O}$ = 1.74 Å, $\angle\beta_{NH\cdots O}$ = 159.01°), (II) and three formed between the hydrogen of the carbon neighbor to the **L** group, i.e., belonging to the first CH_2 next to NH_2^+ in the bridge backbone, with the same H-bond acceptor, i.e., nitrogen from **TRZ** in **9** ($d_{CH\cdots N}$ = 2.36 Å, $\angle\beta_{CH\cdots N}$ = 133.19°), and oxygen from **CA** in **6** ($d_{CH\cdots O}$ = 2.25 Å, $\angle\beta_{CH\cdots O}$ = 151.93°). Furthermore, the distortion that still exists in **6**·F^-, in contrast to **9**·F^- implies that although its intramolecular interactions are weakened in **HG**, they still exist to some degree (see Figures 6 and 7).

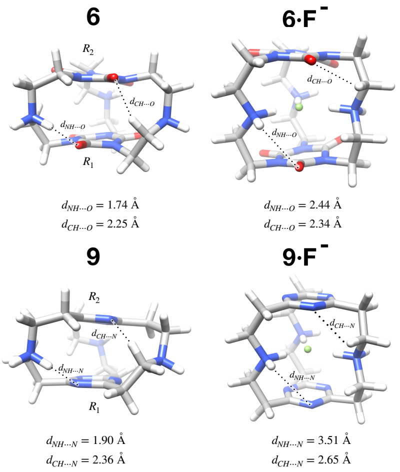

Figure 7 – Intramolecular interactions taking place in **6** and **9**, and it's **HG** systems **6**·F^- and **9**·F^-.

The reported experimental data of the synthesized analogue to **6**, **KISDEW**,[14] briefly comment about the host-guest system degree of distortion stemming from the cyanuric acid rings. In contrast to the distorted structures analysed here, the authors report the cylindrophane asymmetry as an "*guache* kink" associated to the bridges conformation.[14] Notice that **KISDEW** and **KISDIA** (analogue to **6**·F^-) have extended aliphatic groups bonded to a charged NH binding group, which here are replaced by hydrogen ($\mathbf{H}_{out}$) that sits outside the cage framework. This $\mathbf{H}_{out}$ is bonded to suitable H-bond donors in **3**·F^-, **6**·F^-, and **9**·F^-, but the distortions only take place in frameworks that have functional H-bond receptors, i.e., the **TRZ** and **CA** π-systems. Hence, the distortions seen here do not arise from the conformation of the bridges solely, but also from the intramolecular interactions formed between the bridges and the π-systems, confirming why no sign of distortion is seen in **3** and **3**·F^- (Figure 6).

HG H···F^- Distances (Å)

HG Groups	CH_2	NH	NH_2^+
BZN	1.80	1.74	1.62
CA	1.87	1.78	1.68
TRZ	1.82	1.73	1.61

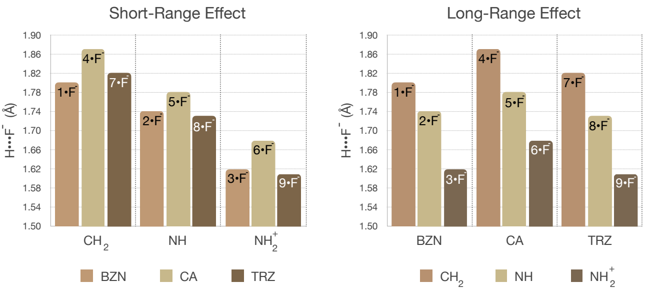

(a) (b)

Figure 8 – Correlation graph that compares **R** and **L** framework variables of the different **HG** systems, showcasing the H···F^- values for the **HG**'s in Åin the form of (a) *short-distance effects*, and (b) *long-distance effects*.

The graphs in Figure 8 shows the values for the H···F^- distances, and in Figure 9, which the values for $R_1 \cdots R_2$ distances. Both graphs in each illustration are essentially the same, but organized differently, sorting out the **(a)** *short-distance effects*, and **(b)** *long-distance effects*. Comparative graphs enables to see the different trends that are associated to the **R** and **L** groups influence to $H \cdots F^-$, and $R_1 \cdots R_2$ distances, accordingly. The $H \cdots F^-$ and $R_1 \cdots R_2$ parameters are the main structural parameters associated to the *short-distance effects*, and *long-distance effects*. For example, Figure 8 (a) shows that $H \cdots F^-$ becomes smaller when **L** is $CH_2 > NH > NH_2{}^+$. Figure 8 (b), shows that $H \cdots F^-$ upon modifying **R** groups changes to a less extent, and follows the **L** group tendency. In the same manner, Figure 9 (a) shows that $R_1 \cdots R_2$ is not much dependent on the **L** groups, in contrast to the graph in Figure 9 (a), which clearly displays a trend related to the cage $R_1 \cdots R_2$ distance enlargement that follows **CA** < **TRZ** < **BZN**. While **BZN** in **1**·F⁻–**3**·F⁻ is considered a weak **R** group to host anions,[48] s-triazine (**TRZ**) lies on the borderline being able to interact with both cations and anions,[87–89] the cyanuric acid (**CA**), on the other hand, is a much accepted anion-π receptor due to its π-acidic nature, and in fact has proved to be so.[14, 48, 86] Despite this fact, **BZN** and **TRZ** are widely known as good π-systems to form metallated compounds, and these metal-**R** complexes have proved to be effective in tunning the aromatic system to become electron deficient,[68, 70, 72, 146] hence **BZN** and **TRZ** should be considered as good candidates to form novel metallated cylindrophane systems with $NH_2{}^+$ groups to coordinate anions.

The $H \cdots F^-$ **HG**'s values in Figure 5 show that **3**·F⁻ ($H \cdots F^-$ = 1.62 Å), is only 0.01 Å longer than in **9**·F⁻ ($H \cdots F^-$ = 1.61 Å), being that the latter presents the shortest $H \cdots F^-$ among all **HG** systems. The only cases in which the $H \cdots F^-$ increases in **H** → **HG**, are in **4** ·F⁻ (1.76 to 1.87 Å), and **7**·F⁻ (1.75 to 1.82 Å), which have **CA**, and **TRZ** π-systems respectively, with the CH_2 groups. The same compounds also are the only **HG** system with decreased $\angle \beta$ angles, compared to the hypothetical hydrogen bond angle in the empty host, i.e., 179.5° to 169.9° in **4**·F⁻, and 175.5° to 166.2° in **7**·F⁻.

Longer **L**-H bond lengths are seen in all **HG**'s systems in different ranges that reflect the strength of the hydrogen bonding formation with the **L** groups. The $\angle\beta$ angle in the **HG** system is used to indicate the directionality of the formed H-bonds, and also relate to their magnitude, in that stronger H-bonds have angles closer to 180°.[215] The highest $\angle\beta$ angle values belong to $\mathbf{2}{\cdot}F^-$ (178.3°), $\mathbf{5}{\cdot}F^-$ (178.6°), and $\mathbf{9}{\cdot}F^-$ (177.8°), of which, the only compound that also has the shortest $H\cdots F^-$ distance is $\mathbf{9}{\cdot}F^-$, which has the **TRZ**, and $NH_2{}^+$ groups. Although **CA** is the best anion-π receptor, it seems that the π-acidic nature of **R** is compensated by diminishing the *short-distance effects* of the **L** groups at the bridges. This is seen by the aforementioned longer $H\cdots F^-$ values in **L** analogues $\mathbf{3}{\cdot}F^-$, $\mathbf{6}{\cdot}F^-$, and $\mathbf{9}{\cdot}F^-$ with the different π-systems, and also in all **L** analogues, i.e., the **HG** systems with **CA** always have the longer $H\cdots F^-$ distances between binding group analogues.

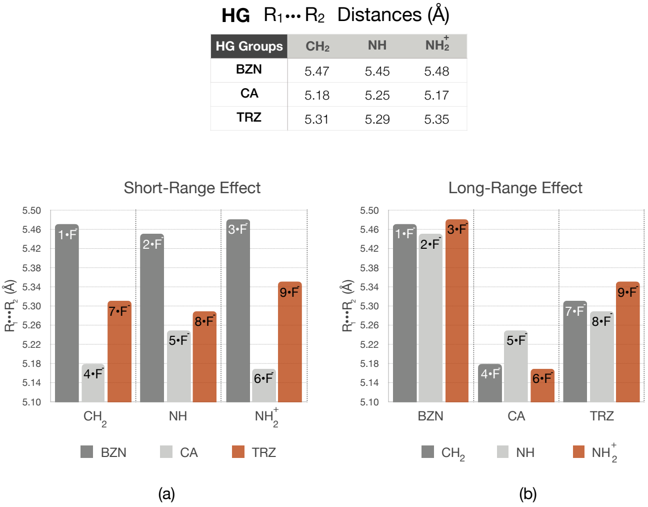

HG $R_1\cdots R_2$ Distances (Å)

HG Groups	CH_2	NH	NH_2^+
BZN	5.47	5.45	5.48
CA	5.18	5.25	5.17
TRZ	5.31	5.29	5.35

(a)

(b)

Figure 9 – Correlation graph that compares **R** and **L** framework variables of the different **HG** systems, showcasing the $R_1\cdots R_2$ values for the **HG**'s in Å for the (a) *short-distance effects*, and (b) *long-distance effects*.

The $R_1\cdots R_2$ distance reflects the contribution that **R** has in the coordination of the anion (*long-distance effects*), hence to the anion-π interaction in **HG** (Figure 5, Figure 9 (b)). Therefore, as it's seen in **HG** systems, the $R_1 \cdots R_2$ distance follows: **BZN** > **TRZ** > **CA**. More considerable $R_1 \cdots R_2$ distances to better accommodate the anion inside the cylindrophane cavity are expected, which is indicated by positive values of $\Delta(R_1 \cdots R_2)$ in **HG** when compared to **H**. It is also expected that **HG** systems with the same π-systems should present similar $R_1 \cdots R_2$ distances, due to having the same contribution to *long-distance effects* anion-π interactions.

The $R_1 \cdots R_2$ distance in **L** analogues for the empty hosts is similar, except for compounds **6** and **9**, which present the framework distortion. For example, **L** analogues **1** (5.24 Å), **4** (5.24 Å), and **7** (5.24 Å), or **2** (4.93 Å), **5** (4.94 Å) and **8** (4.96 Å), one can see that the $R_1 \cdots R_2$ values are similar when the host is empty. Once the fluoride sits inside the cavity, $R_1 \cdots R_2$ distances changes differently in the same compounds, i.e., **1**·F^- (5.46 Å), **4**·F^- (5.18 Å), and **7**·F^- (5.30 Å), or **2**·F^- (5.42 Å), **5**·F^- (5.25 Å) and **8**·F^- (5.28 Å). That is a clear indication of the *long-distance effects*, which is, the **HG**'s with the same **L** have similar $R_1 \cdots R_2$ distances in empty hosts, but their final $R_1 \cdots R_2$ completely changes when the anion is in the cavity of the cylindrophane.

It seems, that **HG**'s containing benzene π-systems have increased participation of **L** and the bridges arising from an approximation of these groups towards the guest (*short-distance effects*), comparing **L** analogues $H \cdots F^-$ distances. It is also visible, as indicated by the $R_1 \cdots R_2$ distances (*long-distance effects*) that the **HG**'s with good anion-π receptors, i.e., **CA** and **TRZ** have smaller $R_1 \cdots R_2$ values than the **L** analogues. Interestingly, the only **HG** that presents a negative $\Delta R_1 \cdots R_2$ (-0.06 Å), i.e., shorter $R_1 \cdots R_2$ value in the **HG** when compared to its empty **H**, is **4**·F^- (**L** = CH_2; **R** = **CA**), which is related to the fact that it has a good anion-π receptor, and a bad **L** H-bond donor.

These “allosteric effects” shows that when **L** is not a good H-bond donor (CH_2), but **R** is a good anion-π receptor (**CA**), the cage changes its geometry to enhance the **NCI**’s capable of stabilising the **HG** system. This is also confirmed by $\Delta(H \cdots F^-)$ positive values in **4**|**4**·F^-, and **7**|**7**·F^-, i.e., the $H \cdots F^-$ distance in the empty **H** for these **L** analogues, compared to the $H \cdots F^-$ in **HG**, shows that the bridges containing CH_2 tend to become more distant from the F^- guest. Additionally, **7**|**7**·F^- also has the smallest $\Delta(R_1 \cdots R_2)$ (= + 0.07 Å), which again reinforces the idea that systems having poor binding groups (**L** = CH_2), hence weaker *short-distance effects*, forces the **R** groups to enhance its anion-π interaction.

In resume, average structural parameters $H \cdots F^-$, **L**-H, $\angle \beta$, and $R_1 \cdots R_2$ illustrated in Figure 5, correlating **H** to **HG** in the **H** → **HG** process, indicates that **R** and **L** act in cooperation to stabilise the guest in the cylindrophane cavity. Exceptionally, hosts **6** and **9** present intramolecular interactions (Figure 6 and 7) that distort the macrocycle framework. Comparison of the analysed structural parameters in Figure 5, sheds light on the *allosteric effects* that modify the cylindrophane scaffold from a geometry analysis perspective, in order to balance the contribution of **R**’s and **L**’s groups to the anion coordination. Therefore, we recognize that the cylindrophane framework, even though it is a rigid cage, is capable of rearranging its conformation to enhance the participation of **R**’s and **L**’s, through proximity. Despite the analysed scaffold modifications effects to accommodate F^-, further electron and wave function correlated examination must be done to evaluate the **NCI**’s taking place, accounting for electron distribution and density in these systems providing insights regarding how much **L** and **R** can contribute to the **HG** stabilisation.

4.2.2 Non-Covalent Interaction Analysis

The methods that are capable to extract useful information from the wave functions of the optimized structures are presented in this section. Qualitative and quantitative computational techniques are employed to asses the quantum chemical nature of the **NCI**'s in each **HG** system, taking into account electronic structure information.

4.2.2.1 Molecular Electrostatic Potential (MEP)

Molecular Electrostatic Potential maps (MEP) are derived from the electron density of the optimized structures and colored according to the energy values on the molecules isovalue surface.[66, 216] In this sense, MEP's can qualitatively predict how electrons are distributed along the electron density surface of the **H**'s, showing which regions of the molecular framework concentrate or deplete charge. This visual aspect of the MEP's is used to see how the different **L**'s affect the electron distribution on the surface of the rings **R**.

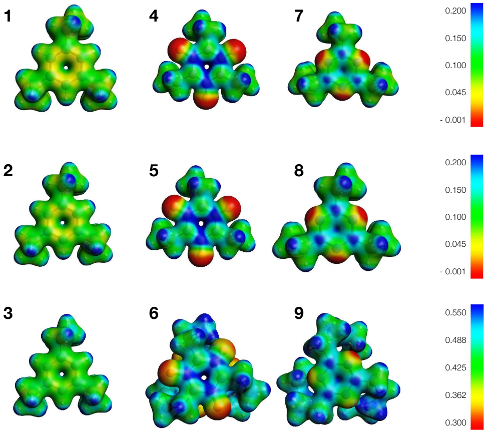

Figure 10 – Top view of MEP maps (left to right) of **R** groups, **BZN**, **CA**, and **TRZ**. Maps for the neutral hosts **1**, **2**, **4**, **5**, **7**, and **8**, first and second row (**L** = CH$_2$, NH), with surface potential that ranges from -0.001 a.u.(red) to 0.002 a.u.(blue). Charged hosts **3**, **6**, **9** (**L** = NH$_2^+$) had a surface potential that ranges from 0.300 a.u.(red) to 0.550 a.u.(blue). All compounds had a consistent isovalue of 0.030 au.

MEPs top view for hosts **1**–**9**, showing the outer part of their

π-systems is illustrated in Figure 10. The charged hosts (**3**, **6**, and **9**) on the third row have different surface potential (0.300 a.u.(red) to 0.550 a.u.(blue), to the remaining hosts (-0.001 a.u.(red) to 0.002 a.u.(blue)), therefore comparison based on colors, can only be done to the compounds of the first and second row. The perspectives view, aligned with the top view for the compounds with CH_2 at the **L** groups of the bridges (Figure B5), NH (Figure B6), and $NH_2{}^+$ (Figure B7) can be found at the support information (Appendix B, B.2.1).

The columns in Figure 10, show that **L** groups affect the electron density on the surface of the π-systems. Looking at the rows, the charge distribution differences relate to nature of the π-systems, which are classified as π-basic (**BZN**), π-neutral (**TRZ**), and π-acidic (**CA**).[48, 79, 87–89] Introducing **EWG** and **EDG** at the bridges, or the π-systems changes the electron distribution on the surface of the cylindrophanes. This is clear by looking at the MEP's color of the π-systems analogues, which show that the balance in charge distribution depends on the nature of the **R** rings, and also in **L**'s at the bridges. For instance, when we change the **L** group from CH_2 to NH, comparing **1** and **2**, or **7** and **8**, the electron density on the surface of the **BZN**, and **TRZ** respectively, appear to be less concentrated in the π-system with the more electronegative $NH_2{}^+$. Comparison between **4** and **5** is not visually detectable. Perspective views of the hosts structures (Appendix B, B.2.1, Figures B5, B6, B7) showing the effect that **R** has on the **L** groups, does not present significantly detectable changes. The most significant changes that are seen from the MEP maps of all the hosts (**1**–**9**) is related to the **L** affecting the electron distribution in the **R** moieties, in that electron poor **L**, such as $NH_2{}^+$, withdraws electrons from the π-systems, and electron-rich, such as CH_2, do not.

4.2.2.2 Energy Decomposition Analysis (EDA)

Quantitative analysis of the non-covalent interactions utilizing EDA defines valuable analytical information regarding the physical nature of the interactions in each **HG** system.[200,201] The energy terms values for **1**·F^-–**9**·F^- are shown in Table 1, and additional EDA values can be found in Appendix B, B.2.2. The theoretical background of the EDA is in Appendix C, C.3.2.

The two fragments considered in Table 1 are the host (**H**), and the fluoride anion (**G**). The total ΔE_{int} energy value is composed in the Pauli repulsion term (ΔE_{Pauli}), which accounts for electron-electron repulsion, the electrostatic potential attraction (ΔV_{elstat}), which considers a static quasiclassical charge density along the host and guest fragments, the stabilising orbital energies (ΔE_{oi}), and the induced dipole attractive forces (ΔE_{disp}). Preparation energy term (ΔE_{prep}), also known as the strain energy, accounts for structural and electronic changes associated with the transformations required for the **HG** formation. The bond dissociation energy (BDE), accounts for ΔE_{int} plus ΔE_{prep}, considering, therefore, the strain energy that is required for the host rearrangement to receive the F^- inside its cavity.

The correlation graphic in Figure 11, compares the ΔE_{int} values between the cylindrophanes having different **L**'s and **R**'s groups (Table in Figure 11). The two graphics refer to the same ΔE_{int} information, but are organized differently: **(a)***short-distance effects*, and **(b)***long-distance effects*. The ΔE_{int} changes in each **L** analogue with a different **R** (*short-distance effects* Figure 11 (a)), is mainly related to the enforced proximity interactions between **L** and the F^-, and the nature of the binding groups CH_2, NH, and $NH_2{}^+$. Hence, each column separates the **HG**'s different binding groups. Different π-systems affect ΔE_{int}, comparing the **R**'s analogues with the different **L**'s are presented in the *long-distance effects* graph (Figure 11 (b), in which each column separates the **HG**'s different π-systems, i.e., **BZN**, **CA**, and **TRZ**.

Significant changes are better seen in the *short-distance effects* (Figure 11 (a)), and they are due to the different **L** groups CH_2, NH, and $NH_2{}^+$. For the **L** analogues **3**·F^- (-317.0 kcal·mol^{-1}), **6**·F^- (-342 kcal·mol^{-1}), and **9**·F^- (-336.7 kcal·mol^{-1}), the ΔE_{int} is mainly affected

Table 1 – Energy Decomposition Analysis (kcal·mol^{-1}) and the Hirshfeld fragment charge analysis (a.u.) for compounds **1**·F^{-}–**9**·F^{-} . Values in parenthesis correspond to the percentage of each stabilising contribution ($\Delta V_{\text{elstat}} + \Delta E_{\text{oi}} + \Delta E_{\text{disp}} = 100\%$).

HG	ΔE_{int}	ΔE_{prep}	BDE	ΔE_{Pauli}	ΔV_{elstat}	ΔE_{oi}	ΔE_{disp}	$q_{\mathbf{G}}$	$q_{\mathbf{H}}$
1·F^{-}	-26.1	2.4	23.7	64.4	-24.9 *(28%)*	-60.4 *(67%)*	-5.1 *(5%)*	-0.796	-0.204
2·F^{-}	-51.9	9.0	42.9	64.3	-47.8 *(41%)*	-63.3 *(54%)*	-5.2 *(5%)*	-0.797	-0.203
3·F^{-}	-317.0	28.5	288.5	86.3	-320.0 *(79%)*	-78.0 *(19%)*	-5.3 *(2%)*	-0.763	2.763
4·F^{-}	-56.4	2.1	54.2	61.5	-55.6 *(47%)*	-56.9 *(48%)*	-5.4 *(5%)*	-0.812	-0.188
5·F^{-}	-80.3	4.62	75.7	62.3	-78.0 *(55%)*	-59.3 *(41%)*	-5.3 *(4%)*	-0.812	-0.188
6·F^{-}	-342.5	38.6	303.8	78.6	-346.6 *(82%)*	-68.8 *(16%)*	-5.7 *(1%)*	-0.798	2.798
7·F^{-}	-40.4	9.8	30.6	64.8	-42.4 *(40%)*	-57.7 *(55%)*	-5.1 *(5%)*	-0.809	-0.191
8·F^{-}	-66.2	4.8	61.4	68.6	-67.8 *(50%)*	-61.9 *(46%)*	-5.1 *(4%)*	-0.805	-0.195
9·F^{-}	-336.7	45.7	291.0	85.9	-344.1 *(81%)*	-73.3 *(17%)*	-5.2 *(2%)*	-0.782	2.782

by the H$\cdots$F^{-} enforced proximity, and also by the different π-systems. The ΔV_{elstat} values in Table 1, show how the π-systems contribute to the ΔE_{int}, for example, comparing **L** analogues, the stabilising ΔV_{elstat} term always follows: **CA** > **TRZ** > **BZN**.

While the ΔE_{prep} energy in all **HG**'s with **L** = CH$_2$ ranges between 2.1 to 9.8 kcal·mol^{-1}, and 4.6 to 9.0 kcal·mol^{-1} when **L** = NH, in compounds with NH$_2{}^{+}$ it ranges from 28.5 to 45.7. The most considerable ΔE_{prep} difference seen between the **L** analogues with different π-systems are found in compounds **3**·F^{-} (28.5 kcal·mol^{-1}), **6**·F^{-} (38.6 kcal·mol^{-1}), and **9**·F^{-} (45.7 kcal·mol^{-1}). The intramolecular driven distortions occurring in hosts **6** (**CA**, NH$_2{}^{+}$), and **9** (**TRZ**, NH$_2{}^{+}$), explains the higher ΔE_{prep} that is required for these systems to form their **HG**'s. In contrast to **6**·F^{-} and **9**·F^{-}, their **L** analogue **3**·F^{-}, which presented higher conformational symmetry, has a lower ΔE_{prep}. Differences in ΔE_{prep} between neutral hosts that containing CH$_2$ and NH, and the charged hosts with NH$_2{}^{+}$ (**3**·F^{-}, **6**·F^{-}, and **9**·F^{-}), is due to required charge reorganization for these systems to interact with the negatively charged species. The highest ΔE_{Pauli} energy values are seen for the **L** analogues containing NH$_2{}^{+}$, e.g., **3**·F^{-} (86.3 kcal·mol^{-1}), **6**·F^{-} (78.6 kcal·mol^{-1}), and **9**·F^{-} (85.9kcal·mol^{-1}). Higher ΔE_{Pauli} values reflect the shorter H$\cdots$F^{-} seen in these **HG** systems, i.e., the shortest H$\cdots$F$^-$ distances belongs to **3**$\cdot$F$^-$ (1.62 Å) and **9**$\cdot$F$^-$ (1.61 Å), in contrast to **6**$\cdot$F$^-$ (1.68 Å), therefore, their higher ΔE_{Pauli} energy values make sense.

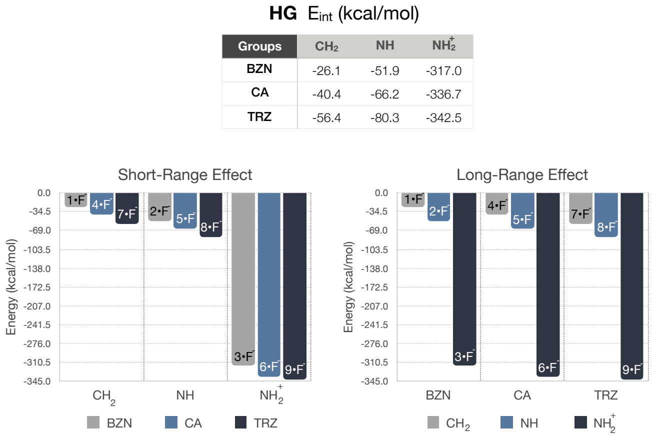

HG E_{int} (kcal/mol)

Groups	CH_2	NH	NH_2^+
BZN	-26.1	-51.9	-317.0
CA	-40.4	-66.2	-336.7
TRZ	-56.4	-80.3	-342.5

(a) (b)

Figure 11 – Correlation graph that compares **R** and **L** framework variables of the different **HG** systems, showcasing ΔE_{int}, ΔE_{prep}, and BDE interactions values for the **HG**'s in kcal·mol^{-1}. Detailed energy terms information for the EDA is given in Table 1).

The binding energy of the **HG**'s complexes is associated with BDE because it takes into account the ΔE_{int} and the ΔE_{prep} energies. Larger BDE values are associated with higher binding affinities between the **HG** systems. The fact that **6**$\cdot$F$^-$ and **9**$\cdot$F$^-$, have the highest ΔE_{prep} energy values that are associated to their charged **L**'s, and their distorted hosts, means that the final BDE energy values for these compounds are reduced, in contrast to their analogue **3**$\cdot$F$^-$. Despite that, the final BDE for the NH_2^+ analogues follows: **6**$\cdot$F$^-$ (303.8 kcal·mol^{-1}) > **9**$\cdot$F$^-$ (291.0 kcal·mol^{-1}) > **3**$\cdot$F$^-$ (288.5 kcal·mol^{-1}). This trend reflects the fact that **3**$\cdot$F$^-$ has the worst anion-π receptor, i.e., **BZN**, **TRZ** the intermediate, and **CA** the best.

The *short-* and *long distances effects* graphs in Figure 12, show the correlation of Hirshfeld charge population analysis for the F^-. The values of the Hirshfeld charge population analysis for the host ($q_{\mathbf{H}}$) and the guest ($q_{\mathbf{G}}$), is also included in Table 1. Analysing the F^- charge ($q_{\mathbf{G}}$) in the **HG**'s shows how much of the initial anion charge (- 1 *e*) was transferred to the cyclophane cage, which reveals how much charge coming from the anion the host can stabilize. The graphs in Figure 12 enable us to see how much the different **R** and **L** groups affect the host as a charge receptor. In this sense, smaller F^- charge values indicate that more charge has been transferred to the cylindrophane host. The F^- charge values evince how well a particular **R** group performs with different **L**'s, and also how well a certain **L** performs with different **R**'s.

The graph in Figure 12 (b) standouts because it shows that overall different cylindrophanes containing **BZN**, **CA**, and **TRZ**, the smallest values for $q_{\mathbf{G}}$, no matter what **L**, belong to the **HG**'s with **BZN**! This strongly indicates that *short-distance effects* are enhanced in cylindrophanes hosts that have poor anion-π receptors ($\mathbf{3}\cdot F^-$).

To see how the **L**'s in the bridges interact with the F^- in each one of the **HG**, and doing the same for the **R** groups, i.e., isolating **R** and **L** in each **HG** system, and looking into their ΔE_{int} with the F^-, fragmentation of the cylindrophane cage was proposed. Figure 13 shows the fragmentation scheme to study the bridges (ΔE_{B}), and ring (**R**) groups in the light of EDA. The illustration of the fragmented **HG**'s individually, Figure B8 and B9, are included at the Appendix B, B.2.2. The **R** fragments consider the first carbon that connects the backbone bridges and its two hydrogens. The bridges fragments (**B**) contain three atoms that remained from removing the carbon connected to the π-systems. The "broken" bonds between the π-systems and the backbone bridges were capped with relaxed hydrogens to complete their valence. These hydrogens were then optimized, constraining all other atoms in the original **HG** coordinates. Energy Decomposition Analysis was applied to each one of the **B**'s and **R**'s, and the values of the resulting

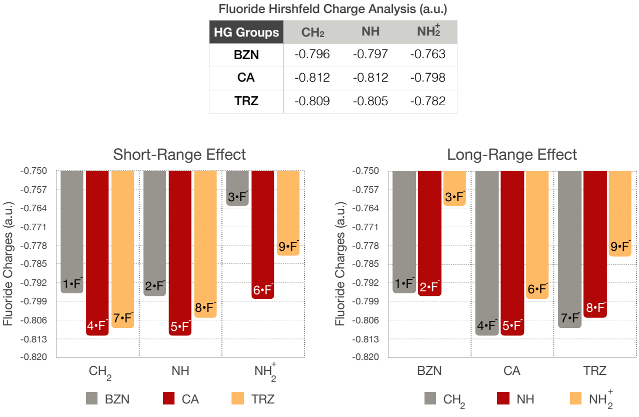

Fluoride Hirshfeld Charge Analysis (a.u.)

HG Groups	CH_2	NH	NH_2^+
BZN	-0.796	-0.797	-0.763
CA	-0.812	-0.812	-0.798
TRZ	-0.809	-0.805	-0.782

(a)

(b)

Figure 12 – Correlation graph that compares **R** and **L** framework variables of the different **HG** systems, showcasing the Hirsfeld charge population values (au) for the fluoride (q_G) in Table 1).

interaction are shown in Figure 13. For the sake of simplicity, the full EDA data, containing all the energy terms were added to Appendix B, B.2.2, in Table B6 and B5.

Note that adding ΔE_R to ΔE_B for any **HG** system (Figure 13), does not yield the **HG** systems ΔE_{int} values (Table1), since the isolated fragments do not account for many structural and electronic aspects that are intrinsic to the cylindrophane cages. The first thing that stands out in Figure 13, are the ΔE_B values, in contrast to the ΔE_R, when we change the character of **L** in contrast to the π-system.

The ΔE_R energy differences in the **R**'s group analogues vary their interaction energy depending on the $R_1 \cdots R_2$ of the **HG** system, i.e., small differences seen in ΔE_R for systems with the same π-systems are because they have different $R_1 \cdots R_2$ distances. Furthermore, the energy difference between ΔE_B and ΔE_R, reveals the disparity that exists in terms of contribution coming from **R** and **B** to the **HG** interacting system. Finally, comparing ΔE_{B} values for the **L** analogues with different **R**'s shows how the π-system influences in the proximity of the bridges towards the anion, depending on how stabilising the **R** to the anion-π interaction (*long-distance effects*).

The ΔE_{B} values (Figure 13) in the **L** analogues **2**·F^{-} (-63.8 kcal·mol^{-1}), **5**·F^{-} (-62.3 kcal·mol^{-1}), and **8**·F^{-} (-63.4 kcal·mol^{-1}), shows that the cylindrophanes containing NH, with **BZN** or **TRZ** are more stabilising than in **CA**. The same is true to NH_2^+ analogues, i.e., **3**·F^{-} (-342.8 kcal·mol^{-1}), **6**·F^{-} (-337.9 kcal·mol^{-1}), **9**·F^{-} (-343.3 kcal·mol^{-1}). In contrast to NH and NH_2^+, the ΔE_{B} values for the CH_2 analogues follow the stabilising order: **4**·F^{-} (-36.9 kcal·mol^{-1}) $>$ **7**·F^{-} (-39.0 kcal·mol^{-1}) $>$ **1**·F^{-} (-36.1 kcal·mol^{-1}). Although the ΔE_{B} values differences are not significant in CH_2 and NH, they are approximately 5 kcal·mol^{-1} in NH_2^+ analogues, comparing **3**·F^{-} and **9**·F^{-}, to **6**·F^{-}. This indicates that NH and NH_2^+, which are good H-bond donors, have enhanced *short-distance effects* in the **HG** containing **TRZ**, and **BZN** when compared to **CA**. The opposite is true when the **L** group is a bad H-bond donor, i.e., CH_2.

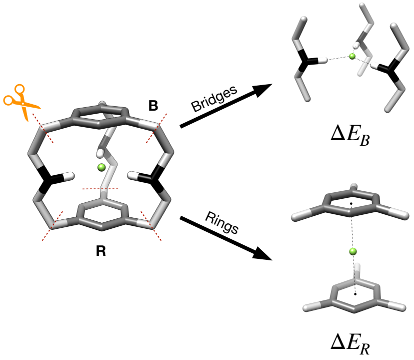

HG	ΔE_{B}	ΔE_{R}
1·F^{-}	-36.1	-6.0
2·F^{-}	-63.8	-7.5
3·F^{-}	-342.8	-7.0
4·F^{-}	-36.9	-47.0
5·F^{-}	-62.3	-47.6
6·F^{-}	-337.9	-46.0
7·F^{-}	-37.0	-25.3
8·F^{-}	-63.4	-26.3
9·F^{-}	-343.3	-25.5

Figure 13 – Fragmentation scheme proposed to analyse the *short-distance effects*, and the *long-distance effects* in each one of the **HG**'s combination of **R** and **L**. The values for the bridges interactions with the fluoride (ΔE_{B}), and for the rings (ΔE_{R}) at the table are in kcal·mol^{-1} unit.

The most stabilising ΔE_R values belong to **CA**, followed by **TRZ**, and **BZN**, as expected. They do no change much between the π-systems analogues, which tells that the different **L** groups do not influence much on the π-systems proximity to the F^-. The energy contribution from ΔE_R is only comparable to ΔE_B when the π-systems is **CA**, and when the **L** group is CH_2, other than that, the ΔE_B values always overcome ΔE_R. For instance, the ΔE_B values for CH_2 analogues **1**$\cdot F^-$ (-36.1 kcal$\cdot$mol^{-1}), **4**$\cdot F^-$ (-36.9 kcal$\cdot$mol^{-1}), and **7**$\cdot F^-$ (-37.0 kcal$\cdot$mol^{-1}), reflecting the contribution of the **L** groups, are only surpassed by ΔE_R in **4**$\cdot F^-$ (-47.0 kcal$\cdot$mol^{-1}).

Values of the other energy terms that are found in the Appendix B for the bridges in Table B6, show that for all **HG** systems, while $NH_2{}^+$ binding groups contributes to the ΔE_B significantly with the ΔV_elstat energy values, NH shows a balance between ΔV_elstat and ΔE_oi, and $NH_2{}^+$ has a more stabilising ΔE_oi. For instance, in **4**$\cdot F^-$, **5**$\cdot F^-$, and **6**$\cdot F^-$, the highest energy contributions come from ΔE_oi (61 %) in **4**$\cdot F^-$, balance between ΔE_oi (48 %) and ΔV_elstat (49 %) in **5**$\cdot F^-$, and ΔV_elstat (84 %) in **6**$\cdot F^-$. Likewise for the ΔE_R values in Table B5, we see that **HG** with **BZN** ΔE_R values are mainly due to ΔE_oi (89 to 90%), **CA** a balance in the contribution of ΔV_elstat (47 to 49%) and ΔE_oi (45 to 47%), and ΔE_R values for the cylindrophanes containing the **TRZ** are mainly due to ΔE_oi term (63 to 65%). The balance between ΔE_oi and ΔV_elstat contribution to the ΔE_R in the cylindrophane containing **CA** as π-systems is quite remarkable since its ability to act as an anion-π receptor is usually associated to its Q_{zz} value, which accounts for the anion-π interaction electrostatic component.

Overall the EDA ΔE_int and BDE values in Table 1, and the ΔE_B and ΔE_R in Figure 13, show that stabilising contribution coming from the π-systems, follows the expected Q_{zz} trend values (Figure 5, Part I), i.e., **CA** > **TRZ** > **BZN**, and the same foreseen trend follows the contribution coming from the **L** groups, i.e., $NH_2{}^+ > NH > CH_2$, but **R**. Furthermore, it also reveals that the contribution to the total energy coming from $NH_2{}^+$ is enhanced in the **TRZ** and **BZN**, i.e., when the π-systems are not good anion-π receptors, and this is due to the $H \cdots F^-$ closer contacts in these **HG** systems. The better anion-π receptor **CA** was found to contribute significantly with ΔE_{oi} energy term, in contrast to the usual electrostatic physical nature reported in the literature.[48]

4.2.2.3 Non-Covalent Interaction Index (NCI_x)

Non-Covalent Interactions index (NCI_x)[120] and the NCIPLOT[140] methods provide visual aspects of non-covalent interactions in terms of their locations and strength. The regions within a molecular framework characterized as non-covalent interactions are located based on the topological analysis of the electron density ($\rho(r)$) and its derivatives ($\nabla\rho$), both of which are used to define the locations in which deviation from a homogeneous electron density occurs. An isosurface is created to represent the regions associated with non-covalent interactions. The strength of the **NCI**'s is characterized by a scale of colors BGR (blue-green-red), which differentiates the types of interactions taking place, based on the sign of the second eigenvalue of the Hessian matrix electron density. The resulting 3D models provide a visual understanding of where the weak interactions happen and discern it into strongly attractive interactions (blue), repulsive interactions (red), and weak interactions (green). A detailed explanation of the method is provided in Appendix C, Section C.3.3.

The complete set of NCI_x images for host-guest systems $\mathbf{1}\cdot F^-$–$\mathbf{9}\cdot F^-$ is found at the Appendix B, B.2.3, in Figure B10. In order to identify the types of **NCI**'s involved in each **HG** based on colors and locations, the specific framework regions between the F^-, **L**, and **R** reflecting both the *short-distance effects* and *long-distance effects* were analysed. The NCI_x images showing intramolecular non-covalent interactions that occur in in hosts **3**, **6**, and **9**, are presented in Appendix B, in Figures B12, B13, and B14. The figures are showing **NCI**'s

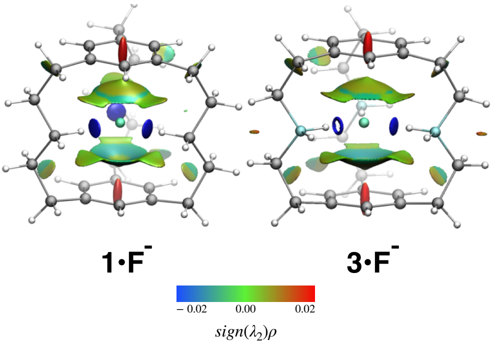

Figure 14 – Perspectives comparing the NCI_x for **HG**'s $\mathbf{1}{\cdot}F^-$ (**BZN**, CH_2) and $\mathbf{3}{\cdot}F^-$ (**BZN**, ${NH_2}^+$), in which their only difference is the **L** group. The *long-distance effects* are characterized by the green-blue bowl shaped surfaces, and the *short-distance effects* by the blue small rounded surfaces. Color-code: gray = carbon, cyan = nitrogen, and white = hydrogen.

at the empty hosts **3** (**BZN**, ${NH_2}^+$), **6** (**CA**, ${NH_2}^+$), and **9** (**TRZ**, ${NH_2}^+$), compare the frameworks of the empty hosts with the occupied cylindrophane, enabling to recognize different types of intramolecular interactions in each **HG** system. These images illustrate very well the discussion about the ΔE_{prep} term of these compounds, in which hosts containing **CA**, and **TRZ** presented higher ΔE_{prep} values, affecting their final ΔE_{int} more than the **L** group analogue with **BZN**.

The illustrations in Figure 14 and 15, shows **HG**'s containing **BZN** with CH_2 ($\mathbf{1}{\cdot}F^-$), and **BZN** with ${NH_2}^+$ ($\mathbf{3}{\cdot}F^-$), which despite being considered poor π-system to host anions, **BZN** actually interacts with the fluoride by means of anion-π interactions, characterized by the blue-green bowl-shaped surface format between the F^- and the π-systems. The color of this surface indicates that this **NCI** is not a repulsive interaction; it is an attractive dispersive interaction. Notice that the blue surface representing a strong electrostatic **NCI** between the guest and cylindrophane **L** groups is existent even when the latter groups are the apolar CH_2 group in $\mathbf{1}{\cdot}F^-$.

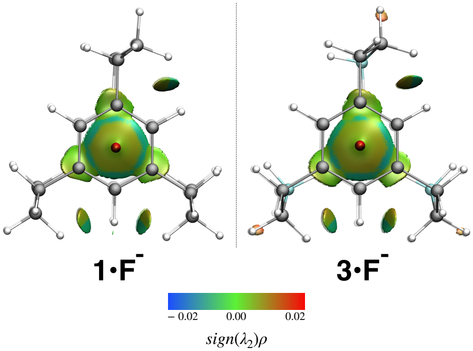

Figure 15 – Top view comparing the NCI$_x$ for **HG**'s **1**·F$^-$ (**BZN**, CH$_2$) and **3**·F$^-$ (**BZN**, NH$_2{}^+$), which differ by the **L** group. Color-code: gray = carbon, cyan = nitrogen, and white = hydrogen.

The enforced proximity situation in the cylindrophane cage, in which the polarizable **BZN** rings are found to be equidistant (~ 2.74 Å) to the fluoride anion, results in a anion-π interaction that although is weak, are mainly due to the ΔE_{oi} term (Table B6). The blue surfaces generated between CH$_2$ and F$^-$ in **1**·F$^-$ (Figure 14), is characteristic of a H-bond with electrostatic (Figure 14). This means that even when **L** is a poor binding group, such as in CH$_2$, the enforced bonding situation results in a strong **NCI**.

A similar situation is found in **HG** **3**·F$^-$ (**BZN**, NH$_2{}^+$), with the difference that the surface between the two **BZN** groups is more extensive (see top view in Figure 15, and 8), and instead of having three blue rounded surfaces representing the electrostatic C−**H**$\cdots$A$^-$ between the three NH$_2{}^+$ groups and the F$^-$, it has only two. One of the two surfaces resembles a "doughnut", which suggests that the proximity of the NH$_2{}^+$ groups to the F$^-$ in **3**·F$^-$ is so small, that this strong H-bond between one of the NH$_2{}^+$ to the F$^-$ has a certain degree of covalency. Since the latter contains the NH$_2{}^+$ binding groups, it makes sense that the blue surface that is gone in **3**·F$^-$ represent a low-barrier hydrogen bond, in which the hydrogen atom is equally shared between the H-bond donor and acceptor. The fact that **3**·F^- contains the **BZN** π-systems reinforces the hypothesis that when the cylindrophane has a poor anion-π receptor, the bridges **L** groups compensate the **BZN** lack of contribution to stabilize the **HG** system, by approaching the F^- as much as possible. This observation was verified at the geometry analysis section, associating it to *allosteric effects*, since the cylindrophane cage changes its structural arrangement to better interact with the guest. The values in the Table B2 support this hypothesis, showing that the $H \cdots F^-$ in **1**·F^- are 1.80, 1.78, and 1.81 Å, and in **3**·F^- they are 1.60, 1.50, and 1.75 Å respectively.

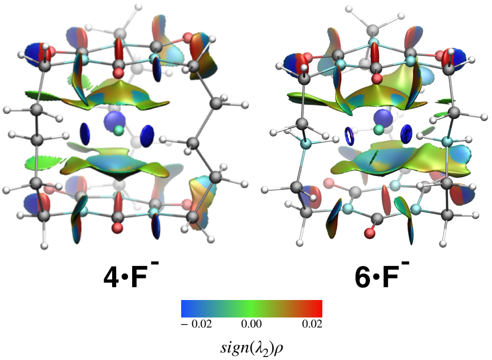

Figure 16 – Perspectives comparing the NCI_x for **HG**'s **4**·F^- (**CA**, CH_2) and **6**·F^- (**CA**, $NH_2{}^+$), in which their only difference is the **L** group. The *long-distance effects* are characterized by the green-blue bowl shaped surfaces, and the *short-distance effects* by the blue small rounded surfaces. Color-code: gray = carbon, cyan = nitrogen, white = hydrogen, and red = oxygen.

In contrast to **1**·F^- and **3**·F^-, compounds **4**·F^- and **6**·F^-, presented in Figure 16 and 17, have the **CA** π-systems instead, but the same CH_2 and $NH_2{}^+$ binding groups, respectively. Figure 16 shows that the **HG**'s framework in **4**·F^- and **6**·F^-, present more intramolecular interactions between the functional groups within the host framework.

These intramolecular interactions are characterized by the small blue-red surfaces that appear between the **CA** π-system and the bridges (see the top view in Figure 17), indicating a partial attractive (blue), and repulsive (red) interaction that is due to the congestion of functional groups. The distortion that seen in **6**$\cdot$F$^-$, due to intramolecular interactions (see Figure 6), is easy to detect by the larger surfaces that come across the internal part of the cylindrophane, towards the outside groups. The NCI$_x$ images showing the intramolecular interactions in **6** and **9** empty hosts are presented in Appendix B, C.3.3, in Figure B13 for **CA**, and B14 for **TRZ**.

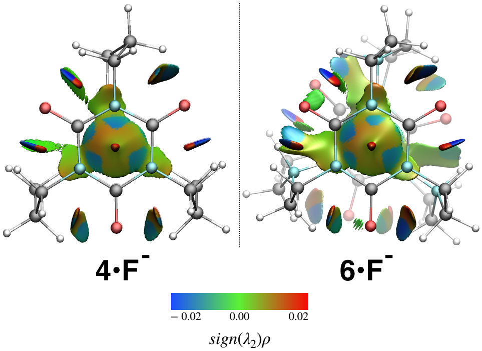

Figure 17 – Top view comparing the NCI$_x$ for **HG**'s **4**$\cdot$F$^-$ (**CA**, CH$_2$) and **6**$\cdot$F$^-$ (**BZN**, NH$_2$$^+$), in which their only difference is the **L** group. Color-code: gray = carbon, cyan = nitrogen, and white = hydrogen.

The three blue rounded surfaces characteristic of electrostatic H-bonds, from **4**$\cdot$F$^-$ to **6**$\cdot$F$^-$, remains the same amount, being that one of them also presents some degree of covalency in **6**$\cdot$F$^-$, which is characterized by the blue doughnut-shaped surface (Figure 16. Geometry parameters in Table B2 shows that the $\mathrm{H}\cdots\mathrm{F}^-$ values are 1.87, 1.85, and 1.89 Å for **4**$\cdot$F$^-$, and 1.67, 1.57, and 1.78 Å, which are slightly longer than the aforementioned values of **1**$\cdot$F$^-$ and **3**$\cdot$F$^-$. Comparing the results of the cylindrophanes containing **BZN** and **CA**, supports the idea that the cylindrophane cage with poor anion-π receptor, compensates the inability of the π-systems to stabilise the guest, enhancing the *short-distance effects*, explains why **3**·F^- has only two blue surfaces, the "doughnut", and the rounded (Figure 14), and **6**·F^- has two rounded and one "doughnut" (Figure 16).

The different size and colors of the surfaces encountered in cylindrophanes with **BZN** and **CA** (Figures 15 17), can be related with a discussion published by Wheeler and Houk, in a paper entitled "*Are Anion/π Interactions Actually a Case of Simple Charge-Dipole Interactions?*".[169] Their work relates the anion-π interactions to direct interactions between the functional groups of the π-systems, to the negatively charged species, and not the center of the π-systems directly, as the anion-π is defined.[48, 79] Houk and Wheeler claim that the extra availability of functional groups in π-systems that are capable of interacting with anions is directly associated with the aromatic systems that are considered as functional anion-π receptors. They show that such π-systems better stabilize the anion charge, due to the effect of **EWG** in the aromatic rings.

In summary, cylindrophanes NCI_x analysis for CH_2 and ${NH_2}^+$ binding groups analogues containing **BZN**, and **CA** π-systems, reveals that anion-π interactions are existent even in **HG**'s containing **BZN** as the anion-π receptor. Likewise, strong electrostatic H-bonds are found in **HG**'s when **L** is the CH_2, despite being a poor H-bond donor. The H-bonds arising from the **L**'s are enhanced when **L** is ${NH_2}^+$. An extra approximation of at least one of the ${NH_2}^+$ groups was characterized by the "doughnut"shaped surface in **3**·F^- ($H\cdots F^- = 1.60$ Å), and **6**·F^- ($H\cdots F^- = 1.57$ Å). In **3**·F^-, the absence of a blue rounded or "doughnut" shaped surface, suggested that the $H\cdots F^-$ in one of the ${NH_2}^+$ is a low-barrier H-bond, in which the hydrogen is equally shared between **L** and F^-. Correlation between the NCI_x images with the geometry analysis distances shows that cylindrophane cages can rearrange its framework to enhance the **NCI**'s that stabilize the guest, resembling a *allosteric effect.* Further quantitative findings should be pursued to investigate the disappearance of the blue shaped surfaces in **3**·F^-.

4.2.2.4 Vibrational Frequency Analysis (IR)

Vibrational frequency calculation is mandatory to validate theoretical structures as minima on the Potential Energy Surface (PES). Molecular vibrations are obtained from its dependency on the second derivative of the energy to the nuclear position of the atoms in the optimized molecular geometry. Bond stretches numerical evaluation provides the theoretical Infra Red (IR) Spectrum representing the intensity and normal modes, of the peaks associated with bond stretches.[94,96] IR spectroscopy is considered as a molecular fingerprint. It exploits the fact that molecules absorb electromagnetic radiation in a determined range of frequency that is characteristic of their functional groups. Therefore, vibrational energies are affected by the shape of the PES, the masses of the atoms bonded to one another, and the associated vibronic coupling, and are directly associated with bond strength.[94]

A schematic representation of the structural parameters evaluated for **3**·F^-, **6**·F^-, and for **9**·F^- is shown in Figure 18. The top view (left) shows corners **a**, **b**, and **c**, which are all different due to the cylindrophane asymmetric structure. The side view (right), shows **L** group internal hydrogen ($\mathbf{H}_{in}$) stretch frequency ($\nu_{\mathbf{L}\text{-H}}$), the **L**-H bond length, and and $H \cdots F^-$ contacts. The table in Figure 18, shows geometry parameters values associated to each corner. The **HG** systems IR spectra plots, and data related to the other **HG**'s are included in Appendix B, B.2.4. Figure 19 illustrates the NCI_x image for these **HG** systems. The top view of the **HG**'s are associated to corners **a**, **b**, and **c**, and the inside view for the aforementioned hosts follows the arrow indicated in Figure 19.

The $H \cdots F^-$ distances reflects the strength of the H-bond formed between $\mathbf{H}_{in}$ and the F^-, and **L**-H and $\nu_{\mathbf{L}\text{-H}}$ reflect the $\mathbf{L}$–$\mathbf{H}_{in}$ bond strength (Side view in Figure 18). Strong H-bonds must have

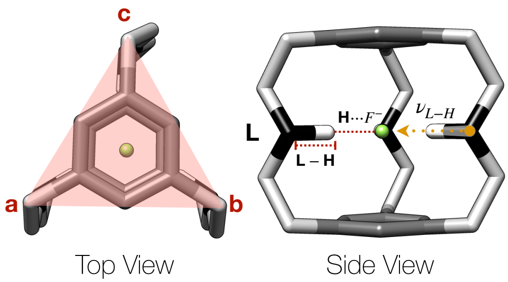

HG	$r_{\mathbf{L}-\mathrm{H_a}}$	$\nu_{\mathbf{L}-\mathrm{H_a}}$	$\mathrm{H_a}\cdots\mathrm{F}^-$	$r_{\mathbf{L}-\mathrm{H_b}}$	$\nu_{\mathbf{L}-\mathrm{H_b}}$	$\mathrm{H_b}\cdots\mathrm{F}^-$	$r_{\mathbf{L}-\mathrm{H_c}}$	$\nu_{\mathbf{L}-\mathrm{H_c}}$	$\mathrm{H_c}\cdots\mathrm{F}^-$
3·F$^-$	1.09	2458	1.60	1.11	2193	1.50	1.11	2734	1.75
6·F$^-$	1.07	2732	1.67	1.08	2536	1.57	1.06	2897	1.78
9·F$^-$	1.08	2562	1.61	1.09	2444	1.56	1.07	2740	1.66

Figure 18 – Top view (left) scheme showing the corners **a**, **b**, and **c** that are related to the cylindrophane asymmetric structures, and sideview (right) scheme showing the **L**-H bond length, $\mathrm{H}\cdots\mathrm{F}^-$ non-covalent distance, and $\nu_{\mathbf{L}\text{-H}}$ **L** group internal hydrogen ($\mathbf{H}_{in}$) bond frequency. Bond lengths, and non-covalent distances are shown in Å, and vibrational frequencies in cm^{-1}. Color-code: gray = carbon, black = **L** groups, and dim gray = **R** groups.

short $\mathrm{H}\cdots\mathrm{F}^-$ contacts, longer **L**-H lengths, and be accompanied by a red-shifted $\nu_{\mathbf{L}\text{-H}}$ frequency. To evaluate how much $\nu_{\mathbf{L}\text{-H}}$ are red-shifted, the diethylammonium N–H bond stretch, shown the IR spectrum of Figure B17 (Appendix B, B.2.4), was calculated (BP86-D3/Def2-TZVP) to compare with the $\mathrm{NH_2}^+$ $\nu_{\mathbf{L}\text{-H}}$ stretch. Compounds **3**·F$^-$, **6**·F$^-$, and **9**·F$^-$ are $\mathrm{NH_2}^+$ binding group analogues, and differ concerning their π-systems, i.e., **BZN**, **TRZ**, and **CA** rings, respectively. Differences related to the *short-distance effects* in these **HG**'s has to be associated with the different π-systems, which in turn sheds light on how the π-systems tune the **L** group's interaction with F$^-$.

The $\mathrm{H}\cdots\mathrm{F}^-$ contacts associated to corners **a**–**c** (Figure 18) indicate that the non-covalent distances follow $\mathrm{H_b}\cdots\mathrm{F}^- < \mathrm{H_a}\cdots\mathrm{F}^- < \mathrm{H_c}\cdots\mathrm{F}^-$ for **3**·F$^-$, **6**·F$^-$, and **9**·F$^-$. Furthermore, the $\mathrm{H}\cdots\mathrm{F}^-$ distance values are in agreement with the trends seen in the **L**-H bond length, i.e.,

$r_{\mathbf{L}-\mathrm{H_b}} > r_{\mathbf{L}-\mathrm{H_a}} > r_{\mathbf{L}-\mathrm{H_b}}$. Naturally, the $\nu_{\mathbf{L}\text{-}\mathrm{H}}$ frequencies for the $\mathbf{H}_{in}$ in the three **L** group analogues, follows the same criteria: $\nu_{\mathbf{L}-\mathrm{H_b}} > \nu_{\mathbf{L}-\mathrm{H_a}} > \nu_{\mathbf{L}-\mathrm{H_b}}$. Hence, shorter $\mathrm{H} \cdots \mathrm{F}^-$ proximities are accompanied by weaker **L**-H bonds, and a red-shifted $\nu_{\mathbf{L}\text{-}\mathrm{H}}$ frequency in compounds **3**·F$^-$, **6**·F$^-$, and **9**·F$^-$. Comparing the values of **L**-H, $\mathrm{H} \cdots \mathrm{F}^-$, and $\nu_{\mathbf{L}\text{-}\mathrm{H}}$ in each corner for the different π-systems shows that stronger *short-distance effects* are associated with the **HG**'s π-systems following **BZN** > **TRZ** > **CA**. This indicates that the **L** groups at the backbone bridges are influenced by the π-systems, in that the worst anion-π receptors present the strongest *short-distance effects*.

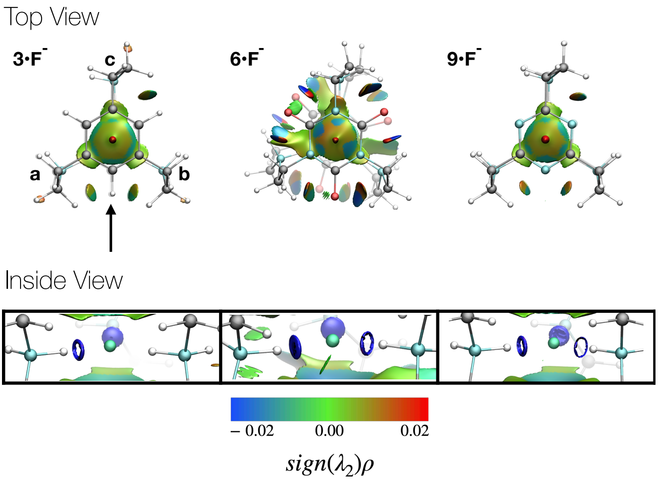

Figure 19 – Top view (above), and inside view (below) NCI$_x$ images comparing $\mathrm{NH_2}^+$ analogues **3**·F$^-$, **6**·F$^-$, and **9**·F$^-$, showing corners **a**, **b**, and **c** in **3**·F$^-$. Arrow indicates how the inside views are seen. Color-code: gray = carbon, cyan = nitrogen, white = hydrogen, and red = oxygen.

The inside view in Figure 18 shows that **3**·F$^-$ (left) has two rounded surfaces, being that one has a doughnut shape, **6**·F$^-$ (middle) presents one doughnut and two rounded surfaces, and the analogue containing **TRZ** in **9**·F$^-$ (right), presents a thin and a thick doughnut, and an extra rounded surfaces. The blue rounded surfaces are always associated with corner **c** in all three compounds, and the doughnut-shaped surfaces to corner **a**. In the case **9**·F^- (**R** = **TRZ**), the thinner doughnut is associated to corner **b**, and in **3**·F^- (**R** = **BZN**) corner **b** has no surface at all. The $H \cdots F^-$ in this corner is so short (1.50 Å) that it can be considered a bond with a high degree of covalency!

According to the Vibrational Frequency Analysis, in conjunction with the NCI_x section, the $NH_2{}^+$ ligand shows stronger *short-distance effects* in the**HG** containing **BZN** as π-systems, followed by **TRZ**, and **CA**. This trend is the opposite sequence expected for the π-systems in terms of anion-π receptors (see Figure 5), Part I). This finding is in agreement with the NCI_x analysis, which further indicates that the $H_b \cdots F^-$ is short enough to be considered a covalent bond. This is evinced by the fact that there no NCI_x between $H_b \cdots F^-$, and that the short $H \cdots F^-$ contact has 1.50 Å. Further evaluation of this hypothesis is meant to be done by calculating the pK_a, ^{1}H NMR shifts, and QTAIM charge distribution in the $\mathbf{H}_{in}$'s.

4.2.3 Host-Guest Binding Analysis

This section describes the binding in the cylindrophane-fluoride system from two viewpoints: **(i)** the relative binding free energy (RBE) of the **HG** systems, and **(ii)** the differences between C_{3h} and C_s conformational isomers of the cylindrophane host. The first correlates the RBE's in the fluoride-cylindrophane cavity exchange, evincing the fluoride affinity to the different hosts. The results are presented in a skew-symmetric matrix with $\Delta\Delta G_{\mathrm{bind}}$ values painted according to an RYG (red-yellow-green) gradient of colors, that are associated with the amount of work in the **HG** systems exchange. The second analysis enables to define the conformers differences in binding the F^-, to determine the energy difference related to the inter-conversion of isomers, as well as to the processes related to the host-guest system's formation.

4.2.3.1 Relative Binding Energy (RBE)

Association of free energy values with molecular systems driving forces are attributed to stability and specificity in a host-guest system formation.[1,22,27] In this sense, analysis related to host-guest systems free energies raises insight whether a determined process will take place, or not.[217] In order to provide such information, quantification of the host-guest binding spontaneity is provided by the relative binding energy (RBE) parameter, which describes the amount of work related to the exchange of the fluoride anion binding a host ($\mathbf{H}_i$), to a different empty host ($\mathbf{H}_j$).

The RBE values quantify the affinity that each cylindrophane-fluoride system has. The main factors that lead to a high host-guest binding affinity and specificity are charge complementarity and the steric fit. The balance between bound and unbound states of the host-F^- system, in which an equilibrium is formed between a structurally defined host-guest system ($\mathbf{H}_iF^-$), and the empty host ($\mathbf{H}_i$) and guest (F^-) separate from each other, are defined according to Equation 4.5.

$$\mathbf{H}_i + F^- \rightleftharpoons \mathbf{H}_i \cdot F^- \tag{4.5}$$

Considering a high affinity and specificity, the equilibrium in 4.5 is displaced to the right, towards the formation of the $\mathbf{H}_iF^-$ system. If in a determined process, the formed $\mathbf{H}_iF^-$ system encounters another different empty host ($\mathbf{H}_j$), and a new equilibrium is defined, as described in Equation 4.6.

$$\mathbf{H}_i \cdot F^- + \mathbf{H}_j \rightleftharpoons \mathbf{H}_i + \mathbf{H}_j \cdot F^- \tag{4.6}$$

The equilibrium in Equation 4.6 represents the competition between the two hosts to the F^- guest. Therefore, higher host-guest bonding affinity and specificity favor one side of the equilibrium in Equation 4.6. Since the relative binding free energy is a state function, the $\mathbf{H}_i\mathrm{F}^-$ in the presence of the empty host $\mathbf{H}_j$ is considered the *initial state*, and the empty host $\mathbf{H}_i$ and the $\mathbf{H}_j\mathrm{F}^-$ system, the *final state*. Since the F^- interaction with the medium can be disregarded, hence the relative binding free energy ($\Delta\Delta G_{\mathrm{bind}}$) is defined by Equation 4.7.

$$\Delta\Delta G_{\mathrm{bind}} = (\Delta G_{\mathrm{H}_{i\cdot\mathrm{F}^-}} + \Delta G_{\mathrm{H}_j})_{\mathrm{final}} - (\Delta G_{\mathrm{H}_i} + \Delta G_{\mathrm{H}_{j\cdot\mathrm{F}^-}})_{\mathrm{initial}} \tag{4.7}$$

The $\Delta\Delta G_{\mathrm{bind}}$ values presented are the antisymmetric square matrix in Figure 20. The diagonal elements are null, and transpose equals its negative, i.e., if $\Delta\Delta G_{\mathrm{ij}}$ denotes the entry on the i-th row, and j-th column, the $\Delta\Delta G_{\mathrm{bind}}$ values obtained follow the skew-symmetric matrix condition determined in Equations 4.8, 4.9, and 4.10. Further details related to the specific calculation $\Delta\Delta G_{\mathrm{bind}}$ were reserved to the Appendix B, B.3.1.

$$\Delta\Delta G_{\mathrm{ij}} = -\Delta\Delta G_{\mathrm{ji}} \tag{4.8}$$

$$\forall \quad i, j = [1, 2, 3 \cdots 9] \tag{4.9}$$

$$\Delta\Delta G_{\mathrm{bind}} \begin{cases} = 0, & \text{if } i = j \\ \neq 0, & \text{otherwise} \end{cases} \tag{4.10}$$

Compound $\mathbf{6}\cdot\mathrm{F}^-$ (**CA**, $\mathrm{NH_2}^+$) at the sixth row, is the **HG** analogue that was modeled by Mascal, and subsequently obtained in laboratory.[7,14] For this compound, running across the columns that represent the *final state*, we see that there are no other empty hosts among the remaining cylindrophanes-F^- systems, that in the conditions stated by Equation 4.6, leads to a favorable $\Delta\Delta G_{\mathrm{bind}}$ value. The two "orange" values belong to $\mathbf{3}\cdot\mathrm{F}^-$ (**BZN**) and $\mathbf{9}\cdot\mathrm{F}^-$ (**TRZ**), which are **L** binding groups analogues to $\mathbf{6}\cdot\mathrm{F}^-$, and they represent the least unfavorable exchanges.

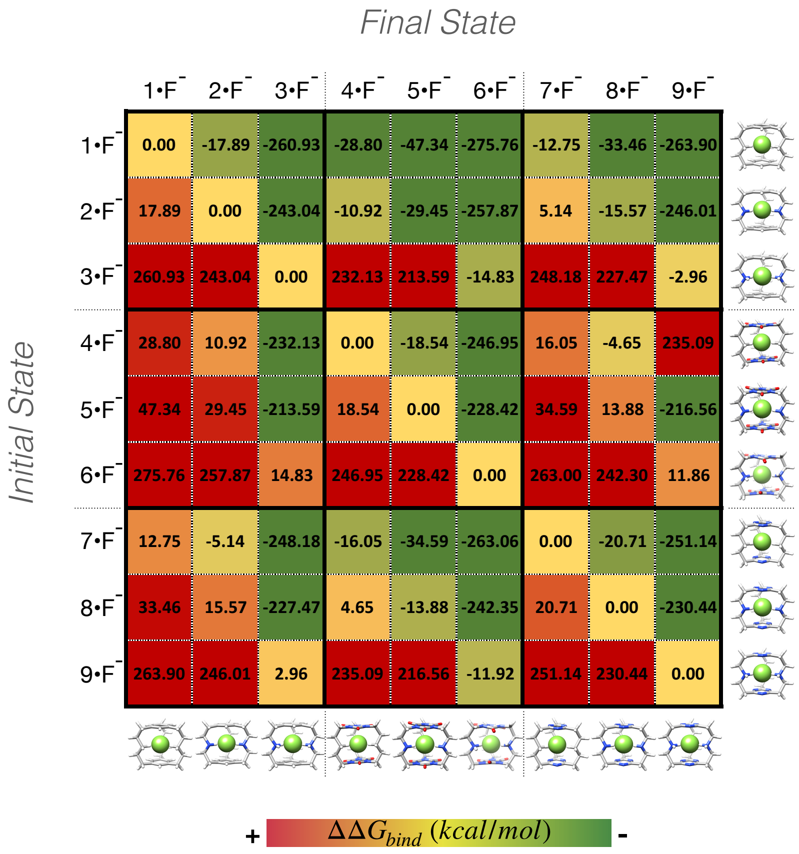

	$1\bullet F^-$	$2\bullet F^-$	$3\bullet F^-$	$4\bullet F^-$	$5\bullet F^-$	$6\bullet F^-$	$7\bullet F^-$	$8\bullet F^-$	$9\bullet F^-$
$1\bullet F^-$	0.00	-17.89	-260.93	-28.80	-47.34	-275.76	-12.75	-33.46	-263.90
$2\bullet F^-$	17.89	0.00	-243.04	-10.92	-29.45	-257.87	5.14	-15.57	-246.01
$3\bullet F^-$	260.93	243.04	0.00	232.13	213.59	-14.83	248.18	227.47	-2.96
$4\bullet F^-$	28.80	10.92	-232.13	0.00	-18.54	-246.95	16.05	-4.65	235.09
$5\bullet F^-$	47.34	29.45	-213.59	18.54	0.00	-228.42	34.59	13.88	-216.56
$6\bullet F^-$	275.76	257.87	14.83	246.95	228.42	0.00	263.00	242.30	11.86
$7\bullet F^-$	12.75	-5.14	-248.18	-16.05	-34.59	-263.06	0.00	-20.71	-251.14
$8\bullet F^-$	33.46	15.57	-227.47	4.65	-13.88	-242.35	20.71	0.00	-230.44
$9\bullet F^-$	263.90	246.01	2.96	235.09	216.56	-11.92	251.14	230.44	0.00

Figure 20 – Relative binding energy ($\Delta\Delta G_{\text{bind}}$) heatmap, showing the exchange work of the F$^-$ in the different **HG** systems. The flux follows from *initial* to *final state*. The colors indicates which process is favorable (green), indifferent (yellow), and not probable (red).

In contrast to compound **6**·F^-, the **HG** system in the first row, i.e., **1**·F^- (**BZN**, CH_2), has all of its $\Delta\Delta G_{\text{bind}}$ values with different tones of green, indicating that in a given process, if any other hosts are available, the exchange of the F^- between the different cavities is favored.

Based on the main **NCI**'s that define the cylindrophane-fluoride system, i.e., the hydrogen bonds between **L** groups and the fluoride (*short-distance effects*), and the anion-π interactions of **R** groups with the anion (*long-distance effects*), host **6**·F^- is the best candidate to coordinate the anion, and **1**·F^- the worse, as it was stated by Mascal's work.[7] This is explained by the π-systems and the **L** groups in these hosts. Despite that, the *short-distance effects* and *long-distance effects* are essential aspects to be considered in the design of novel cylindrophane systems. Thus we cannot disregard the fact that ${NH_2}^+$ binding groups have enhanced *short-distance effects* in the **3**·F^- and **9**·F^-.

Predictive exchanges patterns are easy to recognize in Figure 20. For example, for any of the **HG**'s at the first three rows, all of which contain **BZN** as the π-systems, the only case in which most of the cavity exchange is not spontaneous, is for compound **3**·F^- (**BZN**, ${NH_2}^+$). The only $\Delta\Delta G_{\text{bind}}$ spontaneous for **3**·F^-, are to the ${NH_2}^+$ analogues containing **CA** (**6**·F^-), or **TRZ** (**9**·F^-), because π-systems are better anion-π receptors (Figure 5, Part I). The third row running across the columns shows that the only green values are in the sixth column, compound **6**·F^- ($\Delta\Delta G_{\text{bind}}$ = - 14.88 kcal·mol^{-1}), and in the last column, compound **9**·F^- ($\Delta\Delta G_{\text{bind}}$ = - 2.96 kcal·mol^{-1}).

The intuitive RBE heatmap shows, qualitatively and quantitatively, how host cavities exchange process is spontaneous or not. It allows to choose any compound in the rows as entries (*initial state*), and any other in the columns as the *final state*. Following the color gradient that represents $\Delta\Delta G_{\text{bind}}$ values is enough to determine the spontaneity of the exchange process described in Equation 4.7. Therefore, it provides further insights towards the **HG** systems that can be further tuned to become novel cylindrophane-fluoride systems.

4.2.4 Conformational Analysis

In contrast to this unhindered rotation, inhibiting groups, therefore are capable of increasing the rotational energy barrier, enabling the phenomenon to be experimentally observed, and the separation between the two conformers.[218]

Molecules stereochemistry can be used to plan synthesis since molecular reactivity affects reaction mechanisms, which in turn depend on the reactants conformations.[219] In host-guest systems, conformational analysis can explain inclusion rates, and also determine which conformer interacts better with the guest.[1,27]

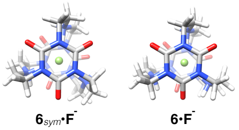

System	*input*	*output*
$\mathbf{6}_{sym}$	C_{3h}	C_3
$\mathbf{6}_{sym}\cdot\mathrm{F}^-$	C_{3h}	C_3
6	C_s	C_2
$\mathbf{6}\cdot\mathrm{F}^-$	C_s	C_s

Figure 21 – Cylindrophane conformers $\mathbf{6}_{sym}\cdot\mathrm{F}^-$, and $\mathbf{6}\cdot\mathrm{F}^-$ (above), and the geometry optimization calculated point group symmetries (below) with the lowest R values for the input, and output files.

The series of papers on the synthesis, characterization, and applications of different cylindrophanes hosts to metals[13,15,16,180] and anions[14] (see Figure B1), by Mascal *et. al.*, reported two features related to the cylindrophane geometry: **(i)** the *gauche*/*anti* stereochemistry of the bridge atoms and related effects in their symmetries, and **(ii)** the synthesized regioisomers that presented 1,2,4- and 1,3,5- bridges positions connected to aromatic rings. A third symmetry aspect of the cylindrophane cage, which was not reported, is the conformation of the bridges.

An imaginary frequency in $\mathbf{6}\cdot\mathrm{F}^-$ optimization led to the unnoticed structure of the $\mathbf{6}_{sym}\cdot\mathrm{F}^-$ conformer (Figure 21). The *symmetric* form of $\mathbf{6}\cdot\mathrm{F}^-$ was considered a mistake since it did not resemble the crystal structure of **KISDIA** (Figure B1), the main compound of interest. Deposited crystal structures of cylindrophane cages (see Appendix B, Figure B1), shows that the only cryptand that presented a conformational symmetry with respect to the bridges, was the thia analogue (**QAFFAE** and **QAFDUW**) to the aza-cylindrophane containing a **BZN** as the π-systems (look for **JIQSEH** in Figure B1), exactly as host **2**.[13] The thia-cylindrophane contains sulfur atom as **L** groups and **BZN** as a **R** group, and despite presenting short-range η_6 coordination, and longer-range aryl centroid-metal contact with Cu(I) and Ag(I), a rare condition for such metals, the crystal structure of the empty thia-cylindrophane was not deposited.[13]

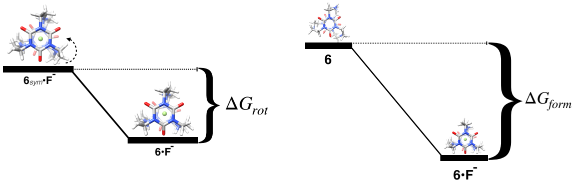
$\mathbf{6}_{sym}\cdot\mathrm{F}^-$
$\mathbf{6}\cdot\mathrm{F}^-$
ΔG_{rot}
$\mathbf{6}$
ΔG_{form}
$\mathbf{6}\cdot\mathrm{F}^-$

(a) (b)

Rotation Energy (kcal/mol)

initial $\rightleftharpoons$ *final*	ΔG_{rot}
$\mathbf{6}_{sym} \rightleftharpoons \mathbf{6}$	- 2.75
$\mathbf{6}_{sym}\cdot\mathrm{F}^- \rightleftharpoons \mathbf{6}\cdot\mathrm{F}^-$	- 2.69

Formation Energy (kcal/mol)

initial $\rightleftharpoons$ *final*	ΔG_{form}
$\mathbf{6}_{sym} + \mathrm{F}^- \rightleftharpoons \mathbf{6}_{sym}\cdot\mathrm{F}^-$	- 299.56
$\mathbf{6}_{sym} + \mathrm{F}^- \rightleftharpoons \mathbf{6}\cdot\mathrm{F}^-$	- 302.25
$\mathbf{6} + \mathrm{F}^- \rightleftharpoons \mathbf{6}\cdot\mathrm{F}^-$	- 299.50
$\mathbf{6} + \mathrm{F}^- \rightleftharpoons \mathbf{6}_{sym}\cdot\mathrm{F}^-$	- 296.81

Figure 22 – Free energy values comparison between the conformers $\mathbf{6}\cdot\mathrm{F}^-$, and $\mathbf{6}_{sym}\cdot\mathrm{F}^-$, in (a), and free energy associated with the different combinations of $\mathbf{6}$, and $\mathbf{6}_{sym}$, to form $\mathbf{6}\cdot\mathrm{F}^-$, or $\mathbf{6}_{sym}\cdot\mathrm{F}^-$ in (b).

The unintentional obtaining of $\mathbf{6}_{sym}\cdot\mathrm{F}^-$, raised several questions that concerned which of the two conformers was energetically favored to form the host-F$^-$ systems (ΔG_{form}), and what was the energy difference between the conformers (ΔG_{rot}), revealing which of the two is more stable. To shed light on the raised points, the bridge free energy rotation (ΔG_{rot}) comparing $\mathbf{6}_{sym}$ to **6**, and $\mathbf{6}_{sym}\cdot$F$^-$ to **6**$\cdot$F$^-$ was calculated (Figure 22 (a)). Free energy formation (ΔG_{form}) of the **HG**'s systems in different combinations are represented in Figure 22 (b). Since we do not consider solvation effects, the equilibrium are related to an ideal gas phase reaction (details in Appendix B, B.3.2).

EDA (Figure 23), and NCI$_x$ analysis (Figure 24) were employed to investigate the **HG** interaction. Figure 23 shows most of the energy terms associated with the **HG** interaction in $\mathbf{6}_{sym}\cdot$F$^-$ and **6**$\cdot$F$^-$. The complete data with ΔE_{prep}, BDE, and the percentage of each stabilising contribution values is at Appendix B, B.3.2, in Table B8. The perspective NCI$_x$ images for $\mathbf{6}_{sym}\cdot$F$^-$, and **6**$\cdot$F$^-$, are shown in Figure 24, and the top view of the conformers was included to Appendix B, B.3.2.

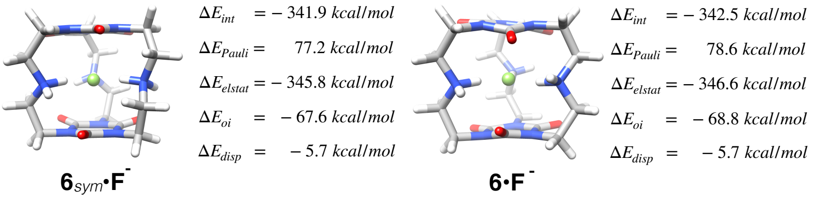
ΔE_{int} = – 341.9 kcal/mol
ΔE_{Pauli} = 77.2 kcal/mol
ΔE_{elstat} = – 345.8 kcal/mol
ΔE_{oi} = – 67.6 kcal/mol
ΔE_{disp} = – 5.7 kcal/mol
$\mathbf{6}_{sym}\cdot\mathbf{F}^-$
ΔE_{int} = – 342.5 kcal/mol
ΔE_{Pauli} = 78.6 kcal/mol
ΔE_{elstat} = – 346.6 kcal/mol
ΔE_{oi} = – 68.8 kcal/mol
ΔE_{disp} = – 5.7 kcal/mol
$\mathbf{6}\cdot\mathbf{F}^-$

Figure 23 – Conformers $\mathbf{6}_{sym}\cdot$F$^-$ (top), and **6**$\cdot$F$^-$ (bottom), EDA energy terms in kcal$\cdot$mol^{-1}. The EDA complete data is found in Table B8.Color-code: gray = carbon, cyan = nitrogen, white = hydrogen, and red = oxygen.

Optimization of the conformers (Figure 21) shows that the output point group symmetries change considerably from the input symmetries. The design of **6**$\cdot$F$^-$ by Mascal,[7, 14] considered a constrained C_{3h} point group for the cylindrophane hosts, which means that the conformer studied theoretically resembles $\mathbf{6}_{sym}\cdot$F$^-$, instead of **6**$\cdot$F$^-$. The only crystallographic cylindrophane structure that has C_{3h} symmetry, are the thia-analogues of the aza-host **2**, coordinating Ag(I) and Cu(I), therefore we cannot affirm that the thia-analogue will present the same point group in solid state (**QAFFAE** and **QAFDUW**, in Figure B1).

Rotation ΔG_{rot} values in Figure 22 (a), show that the equilibrium between $\mathbf{6}_{sym}$ and **6**, or $\mathbf{6}_{sym}\cdot F^-$ and $\mathbf{6}\cdot F^-$, favors the asymmetric conformer by about $\sim$ 2.72 kcal·mol^{-1}. Formation ΔG_{form} values in Figure 22 (b), shows that $\mathbf{6}\cdot F^-$ is the **HG** system that has the most favored formation, even when parting from the $\mathbf{6}_{sym}$ empty host. Separating the four equilibrium in Figure 22 (b) in two situations, the first being the formation of either $\mathbf{6}_{sym}\cdot F^-$, or $\mathbf{6}\cdot F^-$, starting exclusively from $\mathbf{6}_{sym}$, and the second being the opposite, i.e., parting from **6** to get $\mathbf{6}\cdot F^-$ or $\mathbf{6}_{sym}\cdot F^-$, the correlation ΔG_{form} values of the two situations, is always the same free energy associated with the ΔG_{rot} free energy difference from the conformers (- 2.69 kcal·mol^{-1}).

The ΔG_{form} values presented in Figure 22 (a), cannot be considered relevant enough to be associated with stereoselectivity of the cyclotrimerization reaction that forms the different conformers since the energy difference between the two conformers is not considerable.[211] Furthermore, experimental and calculated information of kinetics, transition states, and mechanisms to form the cylindrophane stereoisomers, as well as the bridges rotation energy barrier, are unknown. The cylindrophanes **6** and $\mathbf{6}\cdot F^-$ are simpler than the synthesized **KISDEW** and **KISDIA** (Figure B1), which perhaps has its bridge rotation hampered by the constrained long aliphatic chains attached to it. Complete cyclophane conformers framework evaluation, determining transition state, rates of reactions and mechanism, are specific topics to be further developed.[220, 221] For instance, addressing the free energy difference in the reaction rate-limiting steps and transition states, with the use of the Curtin–Hammett principle,[220] enables better assess the stereoselectivity of the conformers, and this can be done theoretically with isodesmic reactions.[94, 96]

Energy decomposition analysis (Figure 23) shows that the

ΔE_{int} energy difference is insignificant, i.e, - 0.6 kcal·mol^{-1} more stable in $\mathbf{6}\cdot\text{F}^-$, than in $\mathbf{6}_{sym}\cdot\text{F}^-$. The ΔE_{prep} energy term is slightly higher in $\mathbf{6}\cdot\text{F}^-$ (ΔE_{prep} = 78.63 kcal·mol^{-1}), than in $\mathbf{6}_{sym}\cdot\text{F}^-$ (ΔE_{prep} = 77.17 kcal·mol^{-1}). Dispersion (ΔE_{disp}) energy contribution can be considered the same, and the Pauli repulsion is 1.4 kcal·mol^{-1} higher in $\mathbf{6}\cdot\text{F}^-$, which makes sense since the sideway bridges implicated in a staggered framework. Therefore, the F$^-$ interacts better with the cavity of $\mathbf{6}\cdot\text{F}^-$ is mainly due to ΔV_{elstat} and ΔE_{oi} stabilising contribution, which altogether contribute with an extra - 2.0 kcal·mol^{-1} to $\mathbf{6}\cdot\text{F}^-$, when compared to $\mathbf{6}_{sym}\cdot\text{F}^-$. The slightly higher ΔE_{int} and ΔE_{oi} values in $\mathbf{6}\cdot\text{F}^-$ can be attributed to the fact that one of its bridges is turned side-way.

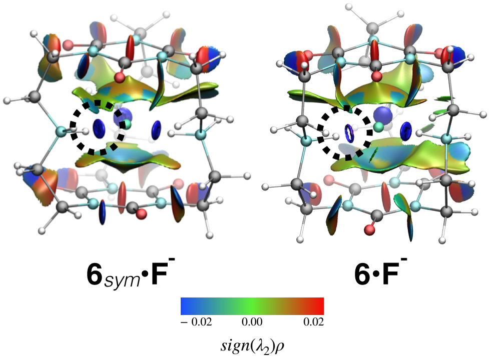

6$_{sym}$•**F**$^-$ **6•F**$^-$

Figure 24 – Perspectives are comparing the NCI$_x$ for **HG**'s $\mathbf{4}\cdot\text{F}^-$ (**CA**, CH$_2$) and $\mathbf{6}\cdot\text{F}^-$ (**CA**, NH$_2$$^+$), in which their only difference is the **L** group. The green-blue bowl-shaped surfaces characterize the *long-distance effects*, and the *short-distance effects* by the blue small rounded surfaces. Color-code: gray = carbon, cyan = nitrogen, white = hydrogen, and red = oxygen.

The NCI$_x$ surfaces in Figure 24, presents the perspective view of the host-guest conformers. The top view of the NCI$_x$ analysis is in Appendix B, B.3.2, in Figure B28. The top view in Figure B28, allows us to see how the surfaces are differently distributed, and that $\mathbf{6}_{sym}\cdot\text{F}^-$ is slightly more twisted than **6**·F$^-$. The most important difference arising from the *short-distance effects* of the bridges is evinced by the blue doughnut surface that is present in **6**·F$^-$, and not in **6**$_{sym}$·F$^-$ (circulated in Figure 24). This is due to the proximity of the internal hydrogen (**H**$_{in}$) of the binding groups in **6**·F$^-$ that are in corner **b**. The fact that the asymmetric conformer has one of the bridges turned sideways enables it to reach the F$^-$ to closer proximity. The $r_{\mathbf{L}-\mathrm{H_b}}$ is 1.57 Åfor **6**·F$^-$, and 1.68 Åfor **6**$_{sym}$·F$^-$, and the latter has the same H$\cdots$F$^-$ distance in corners **a**–**c**. Furthermore, the $\nu_{\mathbf{L}-\mathrm{H_b}}$ for **6**·F$^-$ is 2536 cm^{-1} (Figure 18), in contrast to 2694 cm^{-1} (Figure B29), confirming the red-shift in the IR spectrum (IR spectra plots are in Appendix B, B.2.4, and B.3.2).

In summary, the free energy difference between conformers **6**$_{sym}$·F$^-$ and **6**·F$^-$ is small enough to indicate that perhaps **6**$_{sym}$·F$^-$ exists (Figure 22). Further calculations with a higher level of theory, other methods and density functionals, namely MP2 and B3LYP, respectively, need to be done to confirm that the energy differences are not merely spurious. Transition states energy barriers, as well as kinetic, and mechanistic studies, can be done to explain why **6**·F$^-$ is observed, instead of **6**$_{sym}$·F$^-$. EDA ΔE_{int} energy terms in **6**·F$^-$ are slightly more stable than in **6**$_{sym}$·F$^-$, by about -0.6 kcal·mol^{-1}, which is insignificant. The $\Delta V_{\mathrm{elstat}}$ and ΔE_{oi} terms appeared to be 2 kcal·mol^{-1} more stabilising in **6**·F$^-$, than in **6**$_{sym}$·F$^-$, and this is due to the sideways turned bridge. The NCI$_x$ analysis showed that **6**·F$^-$ can approximate more the NH$_2{}^+$ group's internal hydrogen (**H**$_{in}$) towards the F$^-$ anion (Figure 24). The doughnut-shaped surface present in **6**·F$^-$, and not in **6**$_{sym}$·F$^-$, confirmed that one **L** group in **6**·F$^-$ can come closer to the F$^-$ by 0.11 Å. This stronger H$_\mathrm{b}\cdots$F$^-$ interaction is supported by the red-shift in the $\nu_{\mathbf{L}-\mathrm{H_b}}$ frequency (2536 cm^{-1}) in **6**·F$^-$, compared to a diethylammonium (3305 cm^{-1}) optimized in the same level of theory (Figure B17).

4.3 Concluding Remarks

Investigative design of the cylindrophane-fluoride system based on functional group roles of **R** and **L** groups defined their influence to *long-distance effects* (anion-π interactions), and *short-distance effects* (H-bond interactions), respectively. The **L** groups studied were CH_2, NH, and $NH_2{}^+$, and the **R** groups were **BZN**, **CA**, and **TRZ**. Binding group CH_2, NH, and $NH_2{}^+$ represent the worse, intermediate, and best H-bond donors. Likewise, the best anion-π receptor is **CA**, **TRZ**, and **BZN** representing the worse receptor.

The physical nature of the non-covalent interactions in the different **HG** systems was done with the Energy Decomposition (EDA) (Section 4.2.2.2, and B.2.2), Non-Covalent Index (NCI) (Section 4.2.2.3), and Vibrational Frequency analysis (Section 4.2.2.4). The analyses revealed that the best host-guest system to stabilise the fluoride anion is **6**·F^-, which contains **CA** as the anion-π receptor, and $NH_2{}^+$ ligand for the H-bond with F^-. It was found that the binding groups coordinating F^- are affected by different π-systems. Fragmentation of the cylindrophane cage isolating rings (**R**) and the bridges (**B**), both coordinating the F^- (Table 1), showed that the best π-systems interaction with the F^- proved to be in hosts containing the **CA** ring when the binding groups are CH_2. Likewise, the best efficiency of the isolated bridges interacting with the F^- appears to belong to the structures containing $NH_2{}^+$ when the π-systems is **BZN**. Enhanced effectiveness of $NH_2{}^+$ in **3**·F^-, was validated by the shortest $H\cdots F^-$ proximities of **L** groups at the bridges, which is also related to a higher ΔE_{oi} term (Table B6). The **L** groups internal hydrogen ($\mathbf{H}_{in}$) in corner **b** (Figure 18), is so close to the F^- guest ($r_{\mathbf{L}-\mathrm{H_b}} = 1.50$ Å), that it did not present a NCI_x surface, indicating that a low-barrier H-bond with high degree of covalency exists possibly exists (Section 4.2.2.3, and B.2.4). Vibrational Frequency Analysis of this bonding situation (Section 4.2.2.4, and B.2.4) highlighted the high degree of covalency found in $\mathbf{H}_{in}$ of corner **b** by the red-shifted $\nu_{\mathbf{L}-\mathrm{H_b}}$ of the $NH_2{}^+$ hydrogen (2193 cm^{-1}). Further investigation must be done to define if $H_b \cdots F^-$ proximity is considered the shortest contacts between these atoms, as well as to address the degree of covalency better.

Binding energy analysis (Section 4.2.3.1, and B.3.1), provided the relative binding energies ($\Delta\Delta G_{\text{bind}}$) for the F^- guest exchange work to different cylindrophane cryptands. The intuitive heatmap presented in the form of an antisymmetric matrix (Figure 20), shows which host-guest systems exchanges are spontaneous (green), and which are not (red). The RBE heatmap is used to select potential hosts to be redesigned into novel cylindrophane cages.

Conformational analysis (Section 4.2.4, and B.3.2), showed the energy differences between the conformers $\mathbf{6}\cdot F^-$ and $\mathbf{6}_{sym}\cdot F^-$, which differ by the conformation of the bridges. Stereoisomers free energy rotations differences (ΔG_{rot}), and cylindrophane-F^- free energy formation (ΔG_{form}) revealed that the energy difference between the conformers is small enough to indicate that it is possible that $\mathbf{6}_{sym}$ and $\mathbf{6}_{sym}\cdot F^-$ exists. Host-guest (**HG**) interactions assessed by EDA and NCI$_x$, revealed that the asymmetric conformer ($\mathbf{6}\cdot F^-$) stabilises the fluoride better. Their ΔE_{int} difference is small (- 0.6 kcal·mol^{-1}), and arises from more stabilising contribution of the ΔE_{oi} and ΔV_{elstat} energy terms (-2 kcal·mol^{-1}). The NCI$_x$ analysis confirmed the EDA observation, showing that while **L** groups in $\mathbf{6}\cdot F^-$ present the doughnut surface in corner **b**, the symmetric conformer $\mathbf{6}_{sym}\cdot F^-$ does not. Further study needs to be done with different methods, and level of theory to confirm the small ΔG_{rot} and ΔG_{form} free energy differences, as well as the EDA values.

Finally, considering all of the most important findings, we conclude that $\mathbf{3}\cdot F^-$ and $\mathbf{9}\cdot F^-$, containing $NH_2{}^+$ as a **L** group, and **BZN** and **TRZ** as a **R** group, are the best candidates to develop novel hosts. Since they are not the best anion-π receptor, the **BZN** and **TRZ** can be coordinated by a metal, thus tuning the π-systems to become π-acidic.

Part IV

Outlooks

5 Further Developments

Further developments based on the results presented in this dissertation are resumed in the schematic representation of Figure 1. There are actually other ideas that are also being designed, but the intention in this last section is only to disclose a few developments.

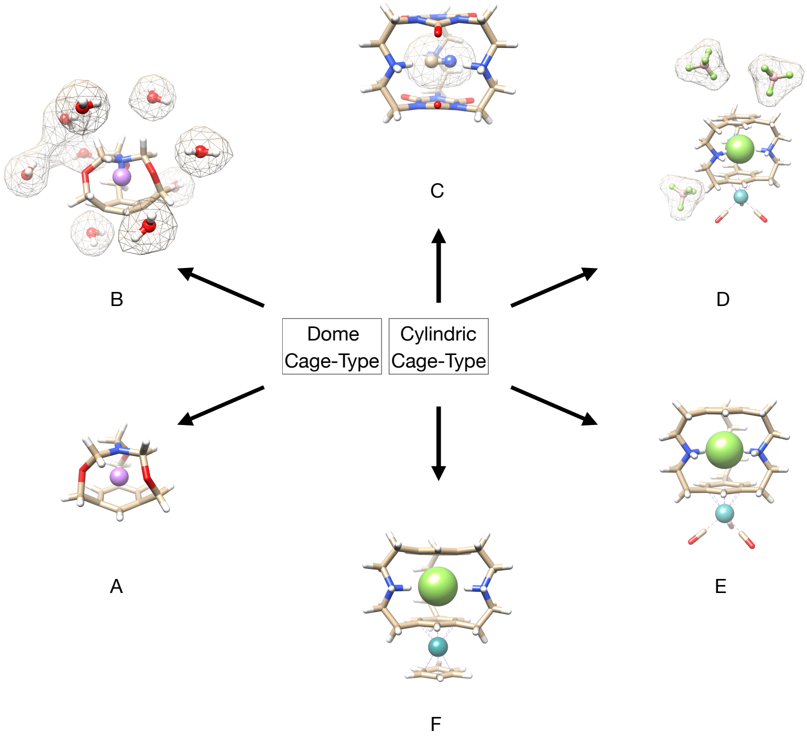

Figure 1 – Representative illustration of further developments. Color-code: tan = carbon, white = hydrogen, blue = nitrogen, red = oxygen, and yellow = sulfur, green = fluoride, purple = lithium, cyan = molybdenum.

From the Part II, in which the molecular iron maindens were addressed, we developed structures **A** and **B**. Structures **C**, **D**, **E**, **F**, are new cylindrophane cages that are being modelled from the conclusions of Part III. The lithium "scavenger" framework (Figure 1 A and B), was inspired by the molecular iron maiden. Their main difference is that instead of having methine hydrogen, it has a nitrogen atom at the apical position of the cyclophane cage, and the oxygens as heteroatoms at the bridges. The functionalization of the dome cage-type cyclophane was made to enhance the non-covalent interactions that coordinate the lithium cation inside the cage. We are modeling the lithium-selective host to study the host-guest system in gas phase in **A**, and then calculate implicit, and explicit solvent effects, as in **B**. The ideas that derive from the cylindrophane framework can be resumed in two: **(i)** a cylindrophane-cyanide system with fluorescent properties, and **(ii)** cylindrophane-fluoride system containing benzene as the π-systems, coordinated by various metals, and in different types of complexes. The steric fit of the cylindrophane enables it to be selective to fluoride and has shown to be suitable to host cyanide as well (Figure 1 C). Since the crystallographic structure **KISDIA** (Figure B1), has long aliphatic chains attached to the **L** groups, we intend to modify these chains so that the cylindrophane can display luminescent properties. The structures **D**, **E**, and **F**, are being studied based findings in Part III, that showed the **L** groups at the bridges have enhanced *short-distance effects* when the π-systems is benzene. Therefore, the structures in Figure 1 represent compound **3**$\cdot$F$^-$ coordinated by metals. We intend to study different types of metallated systems, also considering the presence of counter ions, to compare with our findings. We hope that future experimental results validate the finding reported in this *in silico* design of cage-type cyclophanes.

Bibliography

1 STEED, J. W.; ATWOOD, J. L.; GALE, P. A. *Supramolecular Chemistry: From Molecules to Nanomaterials.* 2nd. ed. [S.l.]: John Wiley & Sons, Ltd., 2012. 3790 p. Citado 8 vezes nas páginas 21, 53, 55, 61, 66, 104, 133, and 137.

2 MAHARRAMOV, A. M. et al. (Ed.). *Non-Covalent Interactions in the Synthesis and Design of New Compounds.* New Jersey: John Wiley & Sons, Inc., 2016. 480 p. Citado 3 vezes nas páginas 21, 58, and 60.

3 JOHNSON, R. *Computational Chemistry Comparison and Benchmark Database, NIST Standard Reference Database 101.* National Institute of Standards and Technology, 2002. Disponível em: <http://cccbdb.nist.gov/>. Citado 3 vezes nas páginas 21, 59, and 86.

4 PASCAL, R. A. et al. A cyclophane bridged by an inwardly pyramidalized olefin. *Tetrahedron Lett.*, v. 37, n. 45, p. 8125–8128, 1996. ISSN 00404039. Citado 4 vezes nas páginas 21, 64, 64, and 76.

5 PASCAL, R. A.; SPERGEL, J.; Van Engen, D. Synthesis and X-ray crystallographic characterization of a (1,3,5)cyclophane with three amide N-H groups surrounding a central cavity. A neutral host for anion complexation. *Tetrahedron Lett.*, v. 27, n. 35, p. 4099–4102, 1986. Citado 4 vezes nas páginas 22, 63, 65, and 65.

6 HEYER, D.; LEHN, J.-m. Anion Coordination Chemistry - Synthesis and Anion Binding Features of Cyclophane Type Macrobicyclic Anion Receptor Molecules. *Tetrahedron Lett.*, v. 27, n. 48, p. 5869–5872, 1986. Citado 5 vezes nas páginas 22, 63, 65, 65, and 96.

7 MASCAL, M. Precedent and theory unite in the hypothesis of a highly selective fluoride receptor. *Angew. Chem. Int. Ed.*, v. 45, n. 18, p. 2890–2893, 2006. Citado 10 vezes nas páginas 22, 62, 63, 65, 66, 96, 104, 105, 134, and 139.

8 RICCI, A.; DANIELI, R.; ROSSINI, S. Macrocyclic sulphide synthesis: trithia[n n+1, 2n+4][2n+1]metacyclophanes. *Journal of the Chemical Society, Perkin Transactions 1*, Royal Society of Chemistry (RSC), n. 16, p. 1691, 1976. Citado 4 vezes nas páginas 22, 63, 75, and 75.

9 PASCAL, R. A.; GROSSMAN, R. B.; ENGEN, D. V. Synthesis of in-[34, 10][7]metacyclophane: projection of an aliphatic hydrogen toward the center of an aromatic ring. *Journal of the American Chemical Society*, American Chemical Society (ACS), v. 109, n. 22, p. 6878–6880, 1987. Citado 7 vezes nas páginas 22, 64, 75, 76, 79, 82, and 82.

10 PASCAL, R. a.; WINANS, C. G.; Van Engen, D. Small, strained cyclophanes with methine hydrogens projected toward the centers of aromatic rings. *J. Am. Chem. Soc.*, v. 111, n. 8, p. 3007–3010, 1989. ISSN 0002-7863. Citado 7 vezes nas páginas 22, 64, 75, 76, 78, 80, and 82.

11 PASCAL, R. A. Molecular "iron maidens": Ultrashort nonbonded contacts in cyclophanes and other crowded molecules. *European J. Org. Chem.*, n. 18, p. 3763–3771, 2004. ISSN 1434193X. Citado 9 vezes nas páginas 22, 61, 62, 63, 63, 75, 76, 91, and 97.

12 ØSTRØM, I. et al. Quest for insight into ultrashort C-H$\cdots\pi$ proximities in molecular iron maidens. *The Journal of Organic Chemistry*, American Chemical Society (ACS), v. 83, n. 9, p. 5114–5122, 2018. Citado 7 vezes nas páginas 22, 64, 67, 75, 78, 79, and 97.

13 MASCAL, M. et al. On the nature of arene $\eta6$ interactions in the solid state and the use of cylindrophanes as ligands for sandwich complexation of metals with longer- range interactions with the benzene ring. *Eur. J. Inorg. Chem.*, n. 3, p. 485–490, 2000. Citado 5 vezes nas páginas 28, 65, 96, 137, and 186.

14 MASCAL, M. et al. Fluoride-selective host based on anion-π interactions, ion pairing, and hydrogen bonding: Synthesis and fluoride-ion sandwich complex. *Angew. Chem. Int. Ed.*, v. 46, n. 46, p. 8782–8784, 2007. Citado 10 vezes nas páginas 28, 65, 95, 96, 99, 108, 134, 137, 186, and 187.

15 MASCAL, M. et al. S-cylindrophanes: from metal tweezers to metal sandwiches. *Angew. Chem. Int. Ed.*, v. 38, n. 13/14, p. 1968–1971, 1999. Citado 5 vezes nas páginas 28, 65, 96, 137, and 186.

16 MASCAL, M. et al. Design, synthesis and metal binding properties of a mixed-donor macrobicycle. *Chem. Commun.*, n. 3, p. 355–356, 1998. Citado 6 vezes nas páginas 28, 65, 95, 96, 137, and 186.

17 CONTRERAS-GARCÍA, J.; YANG, W.; JOHNSON, E. R. Analysis of hydrogen-bond interaction potentials from the electron density:

Integration of noncovalent interaction regions. *The Journal of Physical Chemistry A*, American Chemical Society (ACS), v. 115, n. 45, p. 12983–12990, 2011. Citado 4 vezes nas páginas 33, 229, 230, and 231.

18 GLENDING, E.; LANDIS, C.; WEINHOLD, F. *MO vs. NBO Analysis: What's the Difference?* 2019. Disponível em: <http://nbo.chem.wisc.edu/tut_cmo.htm>. Citado 2 vezes nas páginas 34 and 234.

19 BADER, R. F. W.; MATTA, C. F. Atomic charges are measurable quantum expectation values: A rebuttal of criticisms of qtaim charges. *J. Phys. Chem. A*, American Chemical Society (ACS), v. 108, n. 40, p. 8385–8394, Oct 2004. ISSN 1520-5215. Citado 4 vezes nas páginas 34, 83, 235, and 236.

20 DESIRAJU, G. R. Chemistry beyond the molecule. *Nature*, v. 412, n. 6845, p. 397–400, 2001. Citado 2 vezes nas páginas 53 and 54.

21 FISCHER, E. Einfluss der Configuration auf die Wirkung der Enzyme. *E. Ber. Dt. Chem. Ges.*, v. 27, n. 3, p. 2985–2993, 1894. Citado na página 53.

22 LEHN, J.-m. *Supramolecular Chemistry: Concepts and Perspectives.* 1st. ed. Weinheim: VCH, 1995. 274 p. Citado 4 vezes nas páginas 53, 63, 95, and 133.

23 LEHN, J.-M. Supramolecular Chemistry: Receptors, Catalysts, and Carriers. *Science*, v. 227, n. 4689, p. 849, 1985. Citado 2 vezes nas páginas 53 and 54.

24 ATKINSON, I. M.; LINDOY, L. F. *Self Assembly in Supramolecular Systems.* [S.l.]: Royal Society of Chemistry, 2000. Citado 2 vezes nas páginas 53 and 61.

25 NORO, S. et al. A New, Methane Adsorbent, Porous Coordination Polymer [{CuSiF6 (4, 4'-bipyridine) 2}n]. *Angew. Chem. Int. Ed.*, v. 39, n. 12, p. 2081–2084, 2000. Citado na página 53.

26 POWELL, H. M. The Structure of Molecular Compounds Part IV: Clathrate Compounds. *J. Am. Chem. Soc.*, p. 61–73, 1948. Citado na página 53.

27 SCHALLEY, C. A. *Analytical Methods in Supramolecular Chemistry.* 2nd. ed. Berlin: Wiley-VCH, 2012. 814 p. Citado 6 vezes nas páginas 54, 55, 63, 95, 133, and 137.

28 KOSHLAND, D. E. The key–lock theory and the induced fit theory. *Angew. Chem. Int. Ed.*, n. 33, p. 2375–2378, 1994. Citado na página 54.

29 KOSHLAND, D. E. Application of a theory of enzyme specificity to protein synthesis. *Proc. Natl. Acad. Sci.*, v. 44, n. 2, p. 98–104, 1958. Citado na página 54.

30 PEDERSEN, C. J. Cyclic Polyethers and Their Complexes with Metal Slats. *J. Am. Chem. Soc.*, v. 89, n. 26, p. 7017–7036, 1967. Citado na página 54.

31 LEHN, J.-M. From supramolecular chemistry towards constitutional dynamic chemistry and adaptive chemistry. *Chem. Soc. Rev.*, v. 36, n. 2, p. 151–60, 2007. Citado na página 54.

32 Cram, J. M., Cram, D. Host-Guest Chemistry. *Science*, v. 183, n. 4127, p. 803–809, 1974. Citado na página 54.

33 CRAM, D. J. The Design of Molecular Hosts, Guests, and Their Complexes. *Angew. Chem. Int. Ed.*, v. 27, n. 8, p. 1009–1020, 1988. Citado 3 vezes nas páginas 55, 63, and 96.

34 NABESHIMA, T. *Synergy in Supramolecular Chemistry*. [S.l.]: CRC Press, 2014. Citado 3 vezes nas páginas 55, 63, and 97.

35 DOMOTO, Y. et al. Anion-π Catalysis. *J. Am. Chem. Soc.*, n. 136, p. 2101–2111, 2014. Citado 2 vezes nas páginas 55 and 96.

36 NEEL, A. J. et al. Exploiting non-covalent π interactions for catalyst design. *Nature*, Nature Publishing Group, v. 543, n. 7647, p. 637–646, 2017. Citado 2 vezes nas páginas 55 and 96.

37 ROZA, G. A. D. Alberto Otero de la (Ed.). *Non-covalent Interactions in Quantum Chemistry and Physics: Theory and Applications*. 1st edition. ed. Amsterdam, Netherlands: Elsevier, 2017. 476 p. Citado na página 56.

38 HOBZA, P.; ŘEZÁČ, J. Introduction: Noncovalent Interactions. *Chem. Rev.*, v. 116, n. 9, p. 4911–4912, 2016. Citado na página 56.

39 SCHEINER, S. *Noncovalent Forces*. [S.l.]: Springer Berlin Heidelberg, 2015. 528 p. Citado 2 vezes nas páginas 56 and 95.

40 MEOT-NER, M.; DEAKYNE, C. a. Unconventional ionic hydrogen bonds. 2. $NH^+ \cdots \pi$ complexes of onium ions with olefins and benzene derivatives. *J. Am. Chem. Soc.*, v. 107, n. 2, p. 474–479, 1985. Citado na página 56.

41 PERUTZ, M. F. et al. Hemoglobin as a Receptor of Drugs and Peptides: X-ray Studies of the Stereochemistry of Binding. *J. Am. Chem. Soc.*, v. 108, n. 5, p. 1064–1078, 1986. Citado na página 56.

42 PETSKO, G. A.; S. K. Burley. Amino-aromatic interactions in proteins. *FEBS Lett.*, v. 203, n. 2, p. 139–143, 1986. Citado na página 56.

43 MA, J. C.; DOUGHERTY, D. A. The Cation-π Interaction. *Chem. Rev.*, n. 97, p. 1303–1324, 1997. Citado 2 vezes nas páginas 56 and 95.

44 SCHNEIDER, H.-J.; WERNER, F.; BLATTER, T. Attractive interactions between negative charges and polarizable aryl parts of host-guest systems. *J. Phys. Org. Chem.*, v. 6, n. 10, p. 590–594, 1993. Citado na página 56.

45 SCHNEIDER, H. J. et al. Complexation of nucleosides, nucleotides, and analogs in an azoniacyclophane. Van der Waals and electrostatic binding increments and NMR shielding effects. *J. Am. Chem. Soc.*, v. 114, n. 20, p. 7704–7708, 1992. Citado na página 56.

46 SCHNEIDER, H.-J. Mechanisms of Molecular Recognition: Investigations of Organic Host-Guest Complexes. *Angew. Chem. Int. Ed.*, v. 30, n. 11, p. 1417–1436, 1991. Citado na página 56.

47 FRONTERA, A. et al. Anion-π Interactions: Do They Exist? *Angew. Chem. Int. Ed.*, v. 114, n. 18, p. 3389–3392, 2002. Citado 2 vezes nas páginas 56 and 96.

48 FRONTERA, A. et al. Putting anion-π interactions into perspective. *Angew. Chem. Int. Ed.*, v. 50, n. 41, p. 9564–9583, 2011. Citado 10 vezes nas páginas 56, 57, 66, 80, 95, 98, 110, 115, 123, and 128.

49 TSUZUKI, S.; FUJII, A. Nature and physical origin of ch/π interaction: Significant difference from conventional hydrogen bonds. *Phys. Chem. Chem. Phys.*, The Royal Society of Chemistry, v. 10, p. 2584–2594, 2008. Citado 3 vezes nas páginas 56, 80, and 87.

50 TSUZUKI, S. CH/π interactions. *Annu. Rep. Prog. Chem., Sect. C P hys. Chem.*, n. 108, p. 69–95, 2012. ISSN 0260-1826. Citado 3 vezes nas páginas 56, 63, and 80.

51 NISHIO, M. et al. The CH/π interaction: Significance in molecular recognition. *Tetrahedron*, v. 51, n. 32, p. 8665–8701, 1995. Citado 2 vezes nas páginas 56 and 63.

52 HYDROGEN bond. In: IUPAC Compendium of Chemical Terminology. [S.l.]: IUPAC, 1997. Citado na página 56.

53 DESIRAJU, G.; STEINER, T. *The Weak Hydrogen Bond*. [S.l.]: Oxford University Press, 2001. Citado 3 vezes nas páginas 56, 60, and 190.

54 UMEZAWA, Y. et al. CH/π interaction in the conformation of organic compounds. A database study. *Tetrahedron*, v. 55, n. 33, p. 10047–10056, 1999. ISSN 00404020. Citado 2 vezes nas páginas 56 and 63.

55 DYKSTRA, C. et al. *Theory and Applications of Computational Chemistry: The First Forty Years*. [S.l.]: Elsevier Science, 2005. Citado 2 vezes nas páginas 57 and 95.

56 PASTORCZAK, E.; CORMINBOEUF, C. Perspective: Found in translation: Quantum chemical tools for grasping non-covalent interactions. *The Journal of Chemical Physics*, AIP Publishing, v. 146, n. 12, p. 120901, 2017. Citado 2 vezes nas páginas 57 and 95.

57 NON-COVALENT Interactions in Quantum Chemistry and Physics. [S.l.]: Elsevier, 2017. Citado 3 vezes nas páginas 57, 95, and 221.

58 ZONG, J.; MAGUE, J. T.; PASCAL, R. A. Exceptional steric congestion in an in,in-bis(hydrosilane). *J. Am. Chem. Soc.*, American Chemical Society (ACS), v. 135, n. 36, p. 13235–13237, 2013. ISSN 1520-5126. Citado 2 vezes nas páginas 57 and 95.

59 MANDAL, N.; PRATIK, S. M.; DATTA, A. Exploring ultrashort hydrogen–hydrogen nonbonded contacts in constrained molecular cavities. *J. Phys. Chem. B.*, American Chemical Society (ACS), v. 121, n. 4, p. 825–834, 2017. ISSN 1520-5207. Citado 3 vezes nas páginas 57, 61, and 95.

60 RÖSEL, S. et al. London dispersion enables the shortest intermolecular hydrocarbon $\mathrm{H}\cdots\mathrm{H}$ contact. *Journal of the American Chemical Society*, American Chemical Society (ACS), v. 139, n. 22, p. 7428–7431, 2017. Citado 2 vezes nas páginas 57 and 95.

61 CUSTELCEAN, R.; JACKSON, J. E. Dihydrogen bonding:structures, energetics, and dynamics. *Chem. Rev.*, v. 101, n. 7, p. 1963–1980, 2001. ISSN 0009-2665. Citado na página 57.

62 METRANGOLO, P. et al. Halogen bonding based recognition processes: A world parallel to hydrogen bonding. *Accounts of Chemical Research*, American Chemical Society (ACS), v. 38, n. 5, p. 386–395, 2005. Citado na página 57.

63 CIANCALEONI, G. et al. Bonding analysis in homo- and heterotrihalide species: A charge displacement study. *European Journal of Inorganic Chemistry*, Wiley, v. 2016, n. 23, p. 3804–3812, 2016. Citado na página 57.

64 SCHNEIDER, F. S. S. et al. Bond analysis in dihalogen-halide and dihalogen-dimethylchalcogenide systems. *European Journal of Inorganic Chemistry*, Wiley, v. 2018, n. 8, p. 1007–1015, 2018. Citado na página 57.

65 WHEELER, S. E. Understanding Substituent Effects in Noncovalent Interactions Involving Aromatic Rings. *Acc. Chem. Res.*, v. 46, n. 4, p. 1029–1038, 2013. Citado 3 vezes nas páginas 57, 66, and 95.

66 WHEELER, S. E.; HOUK, K. N. Through-space effects of substituents dominate molecular electrostatic potentials of substituted arenes. *Journal of Chemical Theory and Computation*, American Chemical Society (ACS), v. 5, n. 9, p. 2301–2312, 2009. Citado 3 vezes nas páginas 57, 114, and 225.

67 SINNOKROT, M. O.; VALEEV, E. F.; SHERRILL, C. D. Estimates of the ab initio limit for π-π interactions: The benzene dimer. *Journal of the American Chemical Society*, American Chemical Society (ACS), v. 124, n. 36, p. 10887–10893, 2002. Citado na página 57.

68 CARAMORI, G. F. et al. Ruthenophanes: Evaluating Cation-π Interactions in $[\mathrm{Ru}(\eta_6\text{-}\mathrm{C}_{16}\mathrm{H}_{12}\mathrm{R}_4)(\mathrm{NH}_3)_3]^{2+/3+}$ Complexes. A Computational Insight. *Organometallics*, n. 33, p. 2301–2312, 2014. Citado 4 vezes nas páginas 57, 60, 96, and 110.

69 ORTOLAN, A. O. et al. Role of the cation formal charge in cation-π interaction. A survey involving the [2.2.2]paracyclophane host from relativistic DFT calculations. *New J. Chem.*, The Royal Society of Chemistry, v. 39, n. 12, p. 9963–9968, 2015. Citado 2 vezes nas páginas 57 and 95.

70 GALEMBECK, S. E. et al. Metal-ligand bonding situation in ruthenophanes containing multibridged cyclophanes. *Organometallics*, v. 36, n. 18, p. 3465–3470, 2017. Citado 4 vezes nas páginas 57, 60, 96, and 110.

71 GIESE, M.; ALBRECHT, M.; RISSANEN, K. Experimental investigation of anion–π interactions - applications and biochemical relevance. *Chem. Commun.*, v. 52, n. 9, p. 1778–1795, 2016. Citado 2 vezes nas páginas 57 and 96.

72 ORTOLAN, A. O. et al. How the Electron-Deficient Cavity of Heterocalixarenes Recognizes Anions: Insights from Computation. *Phys. Chem. Chem. Phys.*, v. 19, p. 24696–24705, 2017. Citado 3 vezes nas páginas 57, 95, and 110.

73 CARROLL, W. R. et al. A molecular balance for measuring aliphatic CH-π interactions. *Org. Lett.*, v. 13, n. 16, p. 4320–4323, 2011. Citado na página 57.

74 NIJAMUDHEEN, A. et al. Molecular balances based on aliphatic CH-π and lone-pair-π interactions. *J. Phys. Chem. Lett.*, American Chemical Society (ACS), v. 3, n. 11, p. 1493–1496, 2012. ISSN 1948-7185. Citado na página 57.

75 REED, A. E.; CURTISS, L. a.; WEINHOLD, F. Intermolecular interactions from a natural bond orbital, donor-acceptor viewpoint. *Chem. Rev.*, v. 88, n. 6, p. 899–926, 1988. Citado 4 vezes nas páginas 57, 77, 78, and 232.

76 STONE, A. *The Theory of Intermolecular Forces, 2nd Edition*. [S.l.]: Oxford University Press, 2013. 352 p. Citado na página 57.

77 HOBZA, P.; ZAHRADNÍK, R.; MÜLLER-DETHLEFS, K. The World of Non-Covalent Interactions: 2006. *Collect. Czech. Chem. Commun.*, v. 71, n. 4, p. 443–531, 2006. Citado 2 vezes nas páginas 57 and 96.

78 MÜLLER-DETHLEFS, K.; HOBZA, P. Noncovalent Interactions: A Challenge for Experiment and Theory. *Chem. Rev.*, v. 100, n. 1, p. 143–168, 2000. Citado 2 vezes nas páginas 57 and 96.

79 CHIFOTIDES, H. T.; DUNBAR, K. R. Anion-π Interactions in Supramolecular Architectures. *Acc. Chem. Res.*, v. 46, n. 4, p. 894–906, 2013. Citado 6 vezes nas páginas 57, 80, 95, 98, 115, and 128.

80 MOLINA, P.; ZAPATA, F.; CABALLERO, A. Anion recognition strategies based on combined noncovalent interactions. *Chem. Rev.*, v. 117, n. 15, p. 9907–9972, 2017. Citado 2 vezes nas páginas 58 and 95.

81 ZHAO, J. et al. Anion coordination chemistry: From recognition to supramolecular assembly. *Coordination Chemistry Reviews*, Elsevier BV, v. 378, p. 415–444, 2019. Citado 2 vezes nas páginas 58 and 96.

82 SEN, K. D. *Atomic and Molecular Polarizability.* [S.l.]: World Scientific Pub Co Inc, 1992. Citado 2 vezes nas páginas 58 and 80.

83 MAHAN, G. D.; SUBBASWAMY, K. R. *Local Density Theory of Polarizability.* [S.l.]: Springer US, 1990. Citado na página 58.

84 FRONTERA, A. et al. Anion-π interactions in cyanuric acids: A combined crystallographic and computational study. *Chem. Eur. J.*, v. 11, n. 22, p. 6560–6567, 2005. Citado na página 58.

85 WILLIAMS, J. H. The molecular electric quadrupole moment and solid-state architecture. *Accounts of Chemical Research*, American Chemical Society (ACS), v. 26, n. 11, p. 593–598, 1993. Citado 2 vezes nas páginas 58 and 98.

86 MASCAL, M.; ARMSTRONG, A.; BARTBERGER, M. D. Anion-aromatic bonding: A case for anion recognition by π-acidic rings. *J. Am. Chem. Soc.*, v. 124, n. 22, p. 6274–6276, 2002. Citado 5 vezes nas páginas 59, 66, 96, 96, and 110.

87 ZHENG, W.; WONG, N.-B.; TIAN, A. Anion-tri-s-triazine bonding: A case for anion recognition. *J. Phys. Chem. A*, v. 109, n. 9, p. 1926–1932, 2005. Citado 4 vezes nas páginas 59, 81, 110, and 115.

88 MOOIBROEK, T. J.; GAMEZ, P. The s-triazine ring, a remarkable unit to generate supramolecular interactions. *Inorg. Chim. Acta*, v. 360, p. 381 – 404, 2007. Citado 4 vezes nas páginas 59, 81, 110, and 115.

89 GARAU, C. et al. Dual binding mode of s-triazine to anions and cations. *Org. Lett.*, v. 5, n. 13, p. 2227–2229, 2003. Citado 4 vezes nas páginas 59, 81, 110, and 115.

90 GARAU, C. et al. Anion–π interactions: must the aromatic ring be electron deficient? *New J. Chem.*, v. 27, n. 2, p. 211–214, 2003. Citado na página 60.

91 ORTOLAN, A. O. et al. Anion recognition by organometallic calixarenes: Analysis from relativistic DFT calculations. *Organometallics*, American Chemical Society (ACS), v. 37, n. 13, p. 2167–2176, jun 2018. Citado 2 vezes nas páginas 60 and 95.

92 ARUNAN, E. et al. Defining the hydrogen bond: An account (iupac technical report). *Pure Appl. Chem., PAC*, v. 83, n. 8, p. 1619–1636, 2011. ISSN 0033-4545, 1365-3075. Citado 2 vezes nas páginas 60 and 95.

93 FRONTERA, A. et al. Weak CH/π Interaction Participates in the Diastereoselectivity of a Host-Guest Complex in the Presence of Six Strong Hydrogen Bonds. *Org. Lett.*, v. 5, n. 7, p. 1135–1138, 2003. Citado 2 vezes nas páginas 60 and 80.

94 JENSEN, F. *Introduction to Computational Chemistry*. 2nd ed.. ed. [S.l.]: John Wiley & Sons Ltd, 2007. Citado 9 vezes nas páginas 61, 129, 140, 217, 218, 222, 223, 235, and 236.

95 YOUNG, D. C. *Computational Chemistry - A pratical guide for applying techniques to real-world problems*. [S.l.]: John Wiley & Sons, Inc, 2001. Citado na página 61.

96 CRAMER, C. *Essentials of Computational Chemistry - Theories and Models*. [S.l.]: John Wiley & Sons Ltd, 2004. 541 p. Citado 8 vezes nas páginas 61, 129, 140, 218, 222, 223, 224, and 236.

97 CHEMISTRY, C.; MODELING, M. *Computational Chemistry and Molecular Modeling*. [S.l.]: Springer-Verlag Berlin Heidelberg, 2008. 37–52 p. Citado na página 61.

98 ACHENIE, L.; VENKATASUBRAMANIAN, V.; GANI, R. *Computer Aided Molecular Design: Theory and Practice*. [S.l.]: Elsevier Science, 2002. Citado na página 61.

99 CRAM, D. J.; CRAM, J. M. Cyclophane chemistry: bent and battered benzene rings. *Acc. Chem. Res.*, v. 4, n. 1958, p. 204–213, 1971. Citado na página 62.

100 KEEHN, P. *Cyclophanes*. New York: Academic Press, 1983. Citado na página 62.

101 HENNING, H.; GLEITER, R. *Modern Cyclophane Chemistry*. Weinheim: Wiley-VCH, 2004. 581 p. Citado 2 vezes nas páginas 62 and 95.

102 BROWN, C. J.; FARTHING, A. C. Preparation and Structure of Di-p-Xylylene. *Nature*, v. 164, n. 4178, p. 915–916, 1949. Citado na página 62.

103 CRAM, D. J.; STEINBERG, H. Macro Rings. I. Preparation and Spectra of the Paracyclophanes. *J. Am. Chem. Soc.*, v. 73, n. 12, p. 5691–5704, 1951. Citado 2 vezes nas páginas 62 and 63.

104 KEEHN, P. M.; ROSENFELD, S. M. *Cyclophanes*. [S.l.]: Academic Press, 1983. 725 p. Citado na página 62.

105 LYBRAND, T. P.; MCCAMMON, J. a.; WIPFF, G. Theoretical calculation of relative binding affinity in host-guest systems. *Proc. Natl. Acad. Sci. USA*, v. 83, n. 4, p. 833–835, 1986. Citado 2 vezes nas páginas 63 and 95.

106 ALDER, R. W.; EAST, S. P. In/Out Isomerism. *Chem. Rev.*, v. 96, n. 6, p. 2097–2111, 1996. ISSN 0009-2665. Citado 3 vezes nas páginas 63, 63, and 75.

107 VUJOVIĆ, M. et al. in/out Isomerism of cyclophanes: a theoretical account of 2,6,15-trithia-[3 <sup>4,10</sup>][7]metacyclophane and [3 <sup>4,10</sup>][7]metacyclophane as well as their halogen substituted analogues. *Phys. Chem. Chem. Phys.*, v. 19, n. 14, p. 9500–9508, 2017. ISSN 1463-9076. Citado na página 63.

108 BRANDL, M. et al. CH-π interactions in proteins. *J. Mol. Biol.*, v. 307, p. 357–377, 2001. Citado na página 63.

109 LI, P. et al. The CH-π interactions of methyl ethers as a model for carbohydrate–n-heteroarene interactions. *Organic Letters*, American Chemical Society (ACS), v. 16, n. 19, p. 5064–5067, 2014. Citado na página 63.

110 TAKAHASHI, H. et al. CH/π interactions as demonstrated in the crystal structure of host/guest compounds. A database study. *Tetrahedron*, v. 56, n. 34, p. 6185–6191, 2000. ISSN 00404020. Citado 2 vezes nas páginas 63 and 80.

111 NISHIO, M. CH/π hydrogen bonds in organic reactions. *Tetrahedron*, v. 61, n. 29, p. 6923–6950, 2005. Citado na página 63.

112 PASCAL, R. A.; GROSSMAN, R. B. A comment on the structure and proton NMR spectrum of 2, 8, 17-trithia[45, 12][9]metacyclophane. *The Journal of Organic Chemistry*, American Chemical Society (ACS), v. 52, n. 20, p. 4616–4617, 1987. Citado 2 vezes nas páginas 63 and 76.

113 HANSEN, J. et al. sym-[5.5.5]heterocyclophanes: structurally well-defined, mixed π/heteroatom-donor macrobicyclic cages. *Journal of the Chemical Society, Perkin Transactions 1*, Royal Society of Chemistry (RSC), n. 20, p. 3371–3376, 1998. Citado na página 65.

114 RAJU, R. K. et al. Substituent effects on non-covalent interactions with aromatic rings: Insights from computational chemistry. *ChemPhysChem*, v. 12, n. 17, p. 3116–3130, 2011. Citado 2 vezes nas páginas 66 and 95.

115 GARAU, C. et al. A Topological Analysis of the Electron Density in Anion-π Interactions. *ChemPhysChem*, v. 4, n. 12, p. 1344–1348, 2003. Citado 2 vezes nas páginas 66 and 96.

116 LEMMERZ, R.; NIEGER, M.; VÖGTLE, F. New Highly Strained Adamantanophanes. *J. Chem. Soc., Chem. Commun.*, p. 1168–1170, 1993. Citado na página 76.

117 THE Quantum Theory of Atoms in Molecules: From Solid State to DNA and Drug Design. [S.l.]: Wiley-VCH, 2007. Citado 4 vezes nas páginas 77, 78, 83, and 236.

118 WEINHOLD, F.; LANDIS, C. R. Natural Bond Orbitals and Extensions of Localized Bond Concepts. *Chem. Educ. Res. Pract.*, v. 2, n. 2, p. 91, 2001. Citado 3 vezes nas páginas 77, 78, and 232.

119 GLENDENING, E. D.; LANDIS, C. R.; WEINHOLD, F. Natural bond orbital methods. *Wiley Interdiscip. Rev. Comput. Mol. Sci.*, v. 2, n. 1, p. 1–42, 2012. Citado 3 vezes nas páginas 77, 78, and 232.

120 JOHNSON, E. R. et al. Revealing noncovalent interactions. *Journal of the American Chemical Society*, American Chemical Society (ACS), v. 132, n. 18, p. 6498–6506, 2010. Citado 6 vezes nas páginas 77, 78, 85, 101, 123, and 228.

121 NEESE, F. The ORCA program system. *Wiley Interdiscip. Rev. Comput. Mol. Sci.*, v. 2, n. 1, p. 73–78, 2012. Citado 3 vezes nas páginas 77, 99, and 204.

122 ERNZERHOF, M.; SCUSERIA, G. E. Assessment of the Perdew-Burke-Ernzerhof exchange-correlation functional. *J. Chem. Phys.*, v. 110, n. 11, p. 5029–5036, 1999. Citado 2 vezes nas páginas 77 and 219.

123 ADAMO, C.; BARONE, V. Toward reliable density functional methods without adjustable parameters: The PBE0 model. *J. Chem.*

Phys., v. 110, n. 13, p. 6158–6170, 1999. Citado 2 vezes nas páginas 77 and 219.

124 WEIGEND, F.; AHLRICHS, R. Balanced basis sets of split valence, triple zeta valence and quadruple zeta valence quality for H to Rn: Design and assessment of accuracy. *Phys. Chem. Chem. Phys.*, v. 7, n. 18, p. 3297, 2005. Citado 4 vezes nas páginas 77, 80, 99, and 220.

125 WEIGEND, F. Accurate Coulomb-fitting basis sets for H to Rn. *Phys. Chem. Chem. Phys.*, v. 8, n. 9, p. 1057, 2006. Citado 3 vezes nas páginas 77, 80, and 220.

126 NEESE, F. et al. Efficient, approximate and parallel Hartree-Fock and hybrid DFT calculations. A chain-of-spheres' algorithm for the Hartree-Fock exchange. *Chem. Phys.*, v. 356, n. 1-3, p. 98–109, 2009. Citado na página 77.

127 GRIMME, S. et al. A consistent and accurate ab initio parametrization of density functional dispersion correction (DFT-D) for the 94 elements H-Pu. *J. Chem. Phys.*, v. 132, n. 15, p. 154104, 2010. Citado 3 vezes nas páginas 77, 100, and 222.

128 GRIMME, S. et al. Dispersion-Corrected Mean-Field Electronic Structure Methods. *Chem. Rev.*, v. 116, p. 5105–5154, 2016. Citado na página 77.

129 JOHNSON, E. R.; BECKE, A. D. A post-Hartree-Fock model of intermolecular interactions. *J. Chem. Phys.*, v. 123, n. 2, p. 024101, 2005. Citado 3 vezes nas páginas 77, 100, and 222.

130 GRIMME, S.; EHRLICH, S.; GOERIGK, L. Effect of the damping function in dispersion corrected density functional theory. *J. Comput. Chem.*, v. 32, n. 7, p. 1456–1465, 2011. Citado 3 vezes nas páginas 77, 100, and 222.

131 WEIGEND, F. et al. Ri-mp2: Optimized auxiliary basis sets and demonstration of efficiency. *Chem. Phys. Lett.*, Elsevier BV, v. 294, n. 1-3, p. 143–152, Sep 1998. ISSN 0009-2614. Citado 3 vezes nas páginas 77, 80, and 220.

132 GRIMME, S. Improved second-order møller–plesset perturbation theory by separate scaling of parallel- and antiparallel-spin pair correlation energies. *J. Chem. Phys.*, AIP Publishing, v. 118, n. 20, p. 9095–9102, May 2003. ISSN 1089-7690. Citado 2 vezes nas páginas 77 and 80.

133 SZABO, A.; OSTLUND, N. S. *Modern Quantum Chemistry: Introduction to Advanced Electronic Structure Theory (Dover Books on Chemistry)*. [S.l.]: Dover Publications, 2012. Citado 2 vezes nas páginas 77 and 80.

134 SCHRECKENBACH, G.; ZIEGLER, T. Calculation of NMR shielding tensors using gauge-including atomic orbitals and modern density functional theory. *The Journal of Physical Chemistry*, American Chemical Society (ACS), v. 99, n. 2, p. 606–611, 1995. Citado na página 78.

135 KRYKUNOV, M.; ZIEGLER, T.; LENTHE, E. van. Hybrid density functional calculations of nuclear magnetic shieldings using slater-type orbitals and the zeroth-order regular approximation. *International Journal of Quantum Chemistry*, Wiley-Blackwell, v. 109, n. 8, p. 1676–1683, 2009. Citado na página 78.

136 GUERRA, C. F. et al. Towards an order-n DFT method. *Theor. Chem. Acc.*, Springer Nature, v. 99, n. 6, p. 391–403, nov 1998. Citado 2 vezes nas páginas 78 and 221.

137 VELDE, G. te et al. Chemistry with ADF. *Journal of Computational Chemistry*, Wiley, v. 22, n. 9, p. 931–967, 2001. Citado 2 vezes nas páginas 78 and 221.

138 BAERENDS, E. J. et al. *ADF2016, SCM, Theoretical Chemistry, Vrije Universiteit, Amsterdam, The Netherlands, https://www.scm.com.* 2016. Citado 3 vezes nas páginas 78, 100, and 221.

139 Van Lenthe, E.; BAERENDS, E. J. Optimized Slater type basis sets for the elements 1 118. *J. Comput. Chem.*, v. 24, n. 9, p. 1142–1156, 2003. Citado 2 vezes nas páginas 78 and 100.

140 CONTRERAS-GARCÍA, J. et al. NCIPLOT: A program for plotting noncovalent interaction regions. *J. Chem. Theory Comput.*, v. 7, n. 3, p. 625–632, 2011. Citado 4 vezes nas páginas 78, 85, 101, and 123.

141 HUMPHREY, W.; DALKE, A.; SCHULTEN, K. VMD: Visual molecular dynamics. *J. Mol. Graph.*, v. 14, n. 1, p. 33–38, 1996. Citado 2 vezes nas páginas 78 and 101.

142 SCHMIDT, M. W. et al. General atomic and molecular electronic structure system. *J. Comput. Chem.*, v. 14, n. 11, p. 1347–1363, 1993. Citado na página 78.

143 LU, T.; CHEN, F. Multiwfn: A multifunctional wavefunction analyzer. *Journal of Computational Chemistry*, Wiley-Blackwell, v. 33, n. 5, p. 580–592, 2011. ISSN 0192-8651. Citado na página 78.

144 MULLER, P. Glossary of terms used in physical organic chemistry. *Pure & Appl. Chem.*, v. 66, p. 1077–1184, 1994. Citado 2 vezes nas páginas 78 and 236.

145 GEORGE, P.; GLUSKER, J. P.; BOCK, C. W. Homodesmotic reaction energies show little or no aromatic stabilization in 1,6-methano[10]annulene. *J. Mol. Struct. (Theochem.)*, v. 235, p. 193–196, 1991. Citado 2 vezes nas páginas 78 and 236.

146 EIS, M. J. van et al. Structures and strain energies of small [n]metacyclophanes. *J. Chem. Soc. Perkin Trans. 2*, p. 793–801, 2000. Citado 3 vezes nas páginas 78, 110, and 236.

147 CARAMORI, G. F.; GALEMBECK, S. E. A computational study of tetrafluoro-[2.2]cyclophanes. *J. Phys. Chem. A*, v. 112, n. 46, p. 11784–11800, 2008. Citado 2 vezes nas páginas 78 and 236.

148 HOBZA, P.; HAVLAS, Z. Blue-shifting hydrogen bonds. *Chem. Rev.*, American Chemical Society (ACS), v. 100, n. 11, p. 4253–4264, nov 2000. Citado na página 83.

149 ALLINGER, N. L. *Molecular Structure: Understanding Steric and Electronic Effects from Molecular Mechanics*. New Jersey: John Wiley & Sons, Inc., 2010. 356 p. Citado na página 83.

150 CARAMORI, G. F.; GALEMBECK, S. E.; LAALI, K. K. A computational study of [2.2]cyclophanes. *J. Org. Chem.*, v. 70, n. 8, p. 3242–3250, 2005. Citado na página 84.

151 CARAMORI, G. F.; GALEMBECK, S. E. Computational study about through-bond and through-space interactions in [2.2]cyclophanes. *The Journal of Physical Chemistry A*, American Chemical Society (ACS), v. 111, n. 9, p. 1705–1712, mar 2007. Citado na página 84.

152 BALLESTER, P. Anion binding in covalent and self-assembled molecular capsules. *Chemical Society Reviews*, Royal Society of Chemistry (RSC), v. 39, n. 10, p. 3810, 2010. Citado 2 vezes nas páginas 95 and 97.

153 MAHARRAMOV KAMRAN T. MAHMUDOV, M. N. K. A. J. L. P. A. M. (Ed.). *Non-covalent Interactions in the Synthesis and Design*

of New Compounds. New Jersey: John Wiley & Sons, Inc., 2016. 480 p. Citado na página 95.

154 STRUBLE, M. D. et al. Modulating "jousting" C-F$\cdots$H-C interactions with a bit of hydrogen bonding. *J. Org. Chem.*, American Chemical Society (ACS), v. 79, n. 1, p. 1–6, 2013. Citado na página 95.

155 LOPEZ, A. H. D. et al. The Two Faces of Hydrogen-Bond Strength on Triple AAA-DDD Arrays. *ChemPhysChem*, v. 14, n. 17, p. 3994–4001, 2013. Citado na página 95.

156 SCHOTTEL, B. L.; CHIFOTIDES, H. T.; DUNBAR, K. R. Anion-π interactions. *Chem. Soc. Rev.*, Royal Society of Chemistry (RSC), v. 37, n. 1, p. 68–83, 2008. Citado 2 vezes nas páginas 95 and 98.

157 GALE, P. A. et al. Anion receptor chemistry: Highlights from 2016. *Coordination Chemistry Reviews*, Elsevier BV, v. 375, p. 333–372, 2018. Citado na página 95.

158 CABALLERO, A.; ZAPATA, F.; BEER, P. D. Interlocked host molecules for anion recognition and sensing. *Coordination Chemistry Reviews*, Elsevier BV, v. 257, n. 17-18, p. 2434–2455, 2013. Citado na página 95.

159 HOBZA, P.; ŘEZÁČ, J. Benchmark Calculations of Interaction Energies in Noncovalent Complexes and Their Applications. *Chem. Rev.*, v. 116, n. 9, p. 5038–5071, 2016. Citado na página 96.

160 AJAYAN, P. M.; TOUR, J. M. Materials science: Nanotube composites. *Nature*, Springer Nature, v. 447, n. 7148, p. 1066–1068, 2007. Citado na página 96.

161 RAVVA, M. K.; RISKO, C.; BRÉDAS, J.-L. Noncovalent interactions in organic electronic materials. In: *Non-Covalent Interactions in Quantum Chemistry and Physics*. [S.l.]: Elsevier, 2017. p. 277–302. Citado na página 96.

162 ZHU, C. et al. Non-covalent interactions for carbonaceous materials: impacts of doping, curving and their combination. *Physical Chemistry Chemical Physics*, Royal Society of Chemistry (RSC), v. 20, n. 34, p. 22228–22240, 2018. Citado na página 96.

163 DAWSON, R. E. et al. Experimental evidence for the functional relevance of anion-π interactions. *Nat. Chem.*, Nature Publishing Group, v. 2, n. 7, p. 533–538, 2010. Citado na página 96.

164 BAUZÁ, A.; MOOIBROEK, T. J.; FRONTERA, A. Towards design strategies for anion-π interactions in crystal engineering. *CrystEngComm*, Royal Society of Chemistry (RSC), v. 18, n. 1, p. 10–23, 2016. Citado 2 vezes nas páginas 96 and 98.

165 COCKROFT, S. L. Screening solvent effects in anion recognition. *Chem*, Elsevier BV, v. 3, n. 3, p. 383–384, 2017. Citado 2 vezes nas páginas 96 and 107.

166 LIU, Y. et al. Anion binding in solution: Beyond the electrostatic regime. *Chem*, Elsevier BV, v. 3, n. 3, p. 411–427, 2017. Citado na página 96.

167 LIM, J. Y.; BEER, P. D. Sigma-hole interactions in anion recognition. *Chem*, Elsevier BV, v. 4, n. 4, p. 731–783, 2018. Citado na página 96.

168 BEER, P. D.; GALE, P. A. Anion Recognition and Sensing: The State of the Art and Future Perspectives. *Angew. Chem. Int. Ed.*, n. 40, p. 486–516, 2001. Citado na página 96.

169 WHEELER, S. E.; HOUK, K. N. Are anion/π interactions actually a case of simple charge-dipole interactions? *The Journal of Physical Chemistry A*, American Chemical Society (ACS), v. 114, n. 33, p. 8658–8664, 2010. Citado 2 vezes nas páginas 96 and 128.

170 HAY, B. P.; CUSTELCEAN, R. Anion-π interactions in crystal structures: Commonplace or extraordinary? *Crystal Growth & Design*, American Chemical Society (ACS), v. 9, n. 6, p. 2539–2545, 2009. Citado na página 96.

171 BUSSCHAERT, N. et al. Applications of Supramolecular Anion Recognition. *Chem. Rev.*, v. 115, n. 15, p. 8038–8155, 2015. Citado na página 96.

172 ZHAO, Y. et al. Selective acceleration of disfavored enolate addition reactions by anion-π interactions. *Chem. Sci.*, Royal Society of Chemistry, v. 6, n. 11, p. 6219–6223, 2015. Citado na página 96.

173 AKAMATSU, M.; SAKAI, N.; MATILE, S. Electric-field-assisted anion-π catalysis. *Journal of the American Chemical Society*, American Chemical Society (ACS), v. 139, n. 19, p. 6558–6561, 2017. Citado na página 96.

174 ELLENBARGER, J. F. et al. Anion-π interactions in computer-aided drug design: Modeling the inhibition of malate synthase by phenyl-diketo acids. *Journal of Chemical Information and Modeling*, American Chemical Society (ACS), v. 58, n. 10, p. 2085–2091, 2018. Citado na página 96.

175 LUCAS, X. et al. A thorough anion-π interaction study in biomolecules: on the importance of cooperativity effects. *Chemical Science*, Royal Society of Chemistry (RSC), v. 7, n. 2, p. 1038–1050, 2016. Citado na página 96.

176 SMITH, M. S. et al. An anion-π interaction strongly stabilizes the β-sheet protein WW. *ACS Chemical Biology*, American Chemical Society (ACS), v. 12, n. 10, p. 2535–2537, 2017. Citado na página 96.

177 CAMETTI, M.; RISSANEN, K. Recognition and sensing of fluoride anion. *Chemical Communications*, Royal Society of Chemistry (RSC), n. 20, p. 2809, 2009. Citado na página 96.

178 CAMETTI, M.; RISSANEN, K. Highlights on contemporary recognition and sensing of fluoride anion in solution and in the solid state. *Chem. Soc. Rev.*, Royal Society of Chemistry (RSC), v. 42, n. 5, p. 2016–2038, 2013. Citado na página 96.

179 MASCAL, M. A statistical analysis of halide $\cdots$ H–A (A = OR, NR_2, N^+R_3) hydrogen bonding interactions in the solid state. *J. Chem. Soc. Perk. T. 2*, n. 10, p. 1999–2001, 1997. Citado na página 96.

180 MASCAL, M. Statistical analysis of C-H$\cdots$N hydrogen bonds in the solid state: There are real precedents. *Chem. Commun.*, n. 3, p. 303–304, 1998. Citado 2 vezes nas páginas 96 and 137.

181 SAVAGE, P. B.; HOLMGREN, S. K.; GELLMAN, S. H. Anion and Ion Pair Complexation by a Macrocyclic Phosphine Oxide Disulfoxide. *J. Am. Chem. Soc.*, v. 116, n. 9, p. 4069–4070, 1994. Citado na página 96.

182 KAUR, N. et al. Anion sensing with chemosensors having multiple NH recognition units. *TrAC Trends in Analytical Chemistry*, Elsevier BV, v. 95, p. 86–109, 2017. Citado 2 vezes nas páginas 97 and 106.

183 LEE, C.; YANG, W.; PARR, R. G. Development of the colle-salvetti correlation-energy formula into a functional of the electron density. *Physical Review B*, American Physical Society (APS), v. 37, n. 2, p. 785–789, jan. 1988. Citado 2 vezes nas páginas 99 and 220.

184 BECKE, A. D. A new mixing of hartree-fock and local density-functional theories. *The Journal of Chemical Physics*, AIP Publishing, v. 98, n. 2, p. 1372–1377, 1993. Citado na página 99.

185 DITCHFIELD, R.; HEHRE, W. J.; POPLE, J. A. Self-consistent molecular-orbital methods. IX. an extended gaussian-type basis for molecular-orbital studies of organic molecules. *The Journal of Chemical Physics*, AIP Publishing, v. 54, n. 2, p. 724–728, 1971. Citado 2 vezes nas páginas 99 and 220.

186 BOYS, S.; BERNARDI, F. The calculation of small molecular interactions by the differences of separate total energies. some procedures with reduced errors. *Molecular Physics*, Informa UK Limited, v. 19, n. 4, p. 553–566, 1970. Citado na página 99.

187 HOPMANN, K. H. How to make your computational paper interesting and have it published. *Organometallics*, American Chemical Society (ACS), v. 38, n. 3, p. 603–605, 2019. Citado na página 99.

188 BECKE, A. D. Density-Functional Exchange-Energy Approximation with Correct Asymptotic Behavior. *Phys. Rev. A*, v. 38, n. 6, p. 3098–3100, 1988. Citado 2 vezes nas páginas 99 and 220.

189 PERDEW, J. P. Density-Functional Approximation for the Correlation Energy of the Inhomogeneous Electron Gas. *Phys. Rev. B*, v. 33, n. 12, p. 8822–8824, 1986. Citado 2 vezes nas páginas 99 and 220.

190 SURE, R.; BRANDENBURG, J. G.; GRIMME, S. Small atomic orbital basis set first-principles quantum chemical methods for large molecular and periodic systems: A critical analysis of error sources. *ChemistryOpen*, Wiley, v. 5, n. 2, p. 94–109, 2015. Citado na página 100.

191 GRIMME, S. Semiempirical GGA-type density functional constructed with a long-range dispersion correction. *J. Comput. Chem.*, v. 27, n. 15, p. 1787–1799, 2006. Citado 3 vezes nas páginas 100, 222, and 228.

192 GRIMME, S. Density functional theory with London dispersion corrections. *Wiley Interdiscip. Rev. Comput. Mol. Sci.*, v. 1, n. 2, p. 211–228, 2011. Citado 2 vezes nas páginas 100 and 221.

193 LENTHE, E. van; SNIJDERS, J. G.; BAERENDS, E. J. The Zero-Order Regular Approximation for Relativistic Effects: The Effect of

Spin-Orbit Coupling in Closed Shell Molecules. *J. Chem. Phys.*, v. 105, n. 15, p. 6505, 1996. Citado na página 100.

194 LENTHE, E. van; BAERENDS, E. J.; SNIJDERS, J. G. Relativistic Total Energy Using Regular Approximations. *J. Chem. Phys.*, v. 101, n. 11, p. 9783, 1994. Citado na página 100.

195 LENTHE, E. van; EHLERS, A. w.; BAERENDS, E. J. Geometry Optimizations in the Zero Order Regular Approximation for Relativistic Effects. *J. Chem. Phys.*, v. 110, n. 18, p. 8943, 1999. Citado na página 100.

196 NEESE, F. An improvement of the resolution of the identity approximation for the formation of the coulomb matrix. *Journal of Computational Chemistry*, v. 24, n. 14, p. 1740–1747. Citado na página 100.

197 HIRSHFELD, F. L. Bonded-atom Fragments for Describing Molecular Charge Densities. *Theor. Chim. Acta*, v. 44, n. 2, p. 129–138, 1977. Citado na página 100.

198 WIBERG, K. B.; RABLEN, P. R. Comparison of Atomic Charges Derived via Different Procedures. *J. Comput. Chem.*, v. 14, n. 12, p. 1504–1518, 1993. Citado na página 100.

199 GUERRA, C. F. et al. Voronoi deformation density (VDD) charges: Assessment of the mulliken, bader, hirshfeld, weinhold, and VDD methods for charge analysis. *J. Comput. Chem.*, v. 25, n. 2, p. 189–210, 2004. Citado na página 100.

200 BICKELHAUPT, F. M.; BAERENDS, E. J. Kohn-Sham Density Functional Theory: Predicting and Understanding Chemistry. *Rev. Comput. Chem.; K.B. Lipkowitz D.B. Boyd, Eds.; Wiley, New York*, v. 15, p. 1–86, 2000. Citado 3 vezes nas páginas 100, 116, and 225.

201 ZIEGLER, T.; RAUK, A. Carbon Monoxide, Carbon Monosulfide, Molecular Nitrogen, Phosphorus Trifluoride, and Methyl Isocyanide as σ Donors and π Acceptors. A Theoretical Study by the Hartree-Fock-Slater Transition-State Method. *Inorg. Chem.*, v. 18, n. 7, p. 1755–1759, 1979. Citado 3 vezes nas páginas 100, 116, and 225.

202 ZIEGLER, T.; RAUK, a. Calculation of Bonding Energies by Hartree-Fock Slater Method .1. Transition-State Method. *Theor. Chim. Acta*, v. 46, n. 1, p. 1–10, 1977. Citado 2 vezes nas páginas 100 and 225.

203 VELDE, G. te et al. Chemistry with ADF. *J. Comput. Chem.*, v. 22, n. 9, p. 931–967, 2001. Citado na página 100.

204 GUERRA, C. F. et al. Towards an order- N DFT method. *Theor. Chem. Accounts Theory, Comput. Model. (Theoretica Chim. Acta)*, v. 99, n. 6, p. 391–403, 1998. Citado na página 100.

205 HOPFFGARTEN, M. V.; FRENKING, G. Energy decomposition analysis. *Wiley Interdiscip. Rev. Comput. Mol. Sci.*, v. 2, n. 1, p. 43–62, 2012. Citado 2 vezes nas páginas 100 and 225.

206 FRENKING, G.; BICKELHAUPT, M. The EDA Perspective of Chemical Bonding. In: *Chem. Bond.* [S.l.: s.n.], 2014. cap. Chapter 4. Citado 2 vezes nas páginas 100 and 225.

207 CRAM, D. J. Preorganization: From solvents to spherands. *Angewandte Chemie International Edition in English*, Wiley, v. 25, n. 12, p. 1039–1057, 1986. Citado na página 104.

208 REBEK, J. et al. Allosteric effects in organic chemistry: binding cooperativity in a model for subunit interactions. *Journal of the American Chemical Society*, American Chemical Society (ACS), v. 107, n. 25, p. 7481–7487, 1985. Citado na página 104.

209 QIAO, B. et al. Electrostatic and allosteric cooperativity in ion-pair binding: A quantitative and coupled experiment–theory study with aryl–triazole–ether macrocycles. *Journal of the American Chemical Society*, American Chemical Society (ACS), v. 137, n. 30, p. 9746–9757, 2015. Citado na página 104.

210 HUNTER, C. A.; ANDERSON, H. L. What is cooperativity? *Angewandte Chemie International Edition*, Wiley, v. 48, n. 41, p. 7488–7499, 2009. Citado na página 104.

211 BARTHOLOMEW, D. 1, 3, 5-triazines. In: *Comprehensive Heterocyclic Chemistry II*. [S.l.]: Elsevier, 1996. p. 575–636. Citado 2 vezes nas páginas 106 and 140.

212 KANG, S. O.; BEGUM, R. A.; BOWMAN-JAMES, K. Amide-Based Ligands for Anion Coordination. *Angew. Chemie Int. Ed.*, v. 45, n. 47, p. 7882–7894, 2006. Citado na página 106.

213 KANG, S. O.; DAY, V. W.; BOWMAN-JAMES, K. Cyclophane capsule motifs with side pockets. *Organic Letters*, American Chemical Society (ACS), v. 10, n. 13, p. 2677–2680, 2008. Citado na página 106.

214 KIM, D. Y. et al. Solvent-Driven structural changes in anion-π complexes. *J. Chem. Theory Comput.*, v. 4, n. 7, p. 1162–1169, 2008. Citado na página 107.

215 STEINER, T. The hydrogen bond in the solid state. *Angewandte Chemie International Edition*, Wiley, v. 41, n. 1, p. 48–76, 2002. Citado 2 vezes nas páginas 111 and 190.

216 NARAY-SZABO, G.; FERENCZY, G. G. Molecular electrostatics. *Chemical Reviews*, American Chemical Society (ACS), v. 95, n. 4, p. 829–847, jun. 1995. Citado na página 114.

217 ANSLYN, E. V.; DOUGHERTY, D. A. *Modern Physical Organic Chemistry*. [S.l.]: University Science, 2005. Citado na página 133.

218 FREE rotation (hindered rotation, restricted rotation). In: IUPAC Compendium of Chemical Terminology. [S.l.]: IUPAC, 1997. Citado na página 137.

219 ZWEIFEL, G. S. *Modern Organic Synthesis: An Introduction, 2nd Edition*. [S.l.]: Wiley, 2017. Citado na página 137.

220 SEEMAN, J. I. Effect of conformational change on reactivity in organic chemistry. evaluations, applications, and extensions of curtin-hammett winstein-holness kinetics. *Chemical Reviews*, American Chemical Society (ACS), v. 83, n. 2, p. 83–134, abr. 1983. Citado na página 140.

221 DALE, J. Conformational aspects of many-membered rings. *Angewandte Chemie International Edition in English*, Wiley, v. 5, n. 12, p. 1000–1021, 1966. Citado na página 140.

222 HOHENBERG, P.; KOHN, W. Inhomogeneous electron gas. *Physical Review*, American Physical Society (APS), v. 136, n. 3B, p. B864–B871, 1964. Citado na página 215.

223 KOHN, W.; SHAM, L. J. Self-consistent equations including exchange and correlation effects. *Physical Review*, American Physical Society (APS), v. 140, n. 4A, p. A1133–A1138, 1965. Citado na página 215.

224 TSIPIS, A. C. DFT flavor of coordination chemistry. *Coordination Chemistry Reviews*, Elsevier BV, v. 272, p. 1–29, 2014. Citado na página 218.

225 PERDEW, J. P. Jacob's ladder of density functional approximations for the exchange-correlation energy. In: *AIP Conference Proceedings*. [S.l.]: AIP, 2001. Citado na página 218.

226 PERDEW, J. P. et al. Prescription for the design and selection of density functional approximations: More constraint satisfaction with fewer fits. *The Journal of Chemical Physics*, AIP Publishing, v. 123, n. 6, p. 062201, 2005. Citado na página 218.

227 GüELL, M. et al. Importance of the basis set for the spin-state energetics of iron complexes. *The Journal of Physical Chemistry A*, American Chemical Society (ACS), v. 112, n. 28, p. 6384–6391, jul. 2008. Citado na página 221.

228 HOBZA, P.; MULLER-DETHLEFS, K. *Non-Covalent Interactions: Theory and Experiment (Theoretical and Computational Chemistry Series)*. 1st edition. ed. Cambridge, England: Royal Society of Chemistry, 2009. 238 p. Citado na página 221.

229 POLITZER, P.; LAURENCE, P. R.; JAYASURIYA, K. Molecular electrostatic potentials: an effective tool for the elucidation of biochemical phenomena. *Environmental Health Perspectives*, Environmental Health Perspectives, v. 61, p. 191–202, 1985. Citado na página 225.

230 MOROKUMA, K. Molecular orbital studies of hydrogen bonds. III. c=o$\cdots$h-o hydrogen bond in $H_2CO\cdots H_2O$ and $H_2O\cdots 2H_2O$. *The Journal of Chemical Physics*, AIP Publishing, v. 55, n. 3, p. 1236–1244, 1971. Citado na página 225.

231 SHULL, H.; LöWDIN, P.-O. Natural spin orbitals for helium. *The Journal of Chemical Physics*, AIP Publishing, v. 23, n. 8, p. 1565–1565, 1955. Citado na página 232.

232 BADER, R. *Atoms in Molecules : a Quantum Theory*. Oxford New York: Clarendon Press, 1990. Citado na página 235.

233 HEHRE, W. J. et al. Molecular orbital theory of the electronic structure of organic compounds. v. molecular theory of bond separation. *Journal of the American Chemical Society*, American Chemical Society (ACS), v. 92, n. 16, p. 4796–4801, 1970. Citado na página 236.

234 PONOMAREV, D. A.; TAKHISTOV, V. V. What are isodesmic reactions? *Journal of Chemical Education*, American Chemical Society (ACS), v. 74, n. 2, p. 201, 1997. Citado na página 236.

Appendix

APPENDIX A – Paper I

The paper (Manuscript ID: jo-2018-00461t) QUEST FOR INSIGHT INTO ULTRASHORT C–H$\cdots\pi$ PROXIMITIES IN MOLECULAR “IRON MAIDENS”, J. Org. Chem., 2018, 83 (9), pp 5114–5122, DOI: 10.1021/acs.joc.8b00461, was reprinted with rights and permissions from American Chemical Society (ACS), and with approval from Dr. Olaf G. Wiest associate editor.

JOC The Journal of Organic Chemistry
Article
Cite This: *J. Org. Chem.* 2018, 83, 5114−5122
pubs.acs.org/joc

Quest for Insight into Ultrashort C−H···π Proximities in Molecular “Iron Maidens”

Ina Østrøm,[†] Alexandre O. Ortolan,[†] Felipe S. S. Schneider,[†] Giovanni F. Caramori,[*,†] and Renato L. T. Parreira[‡]

[†]Departamento de Química, Universidade Federal de Santa Catarina, Campus Universitário Trindade, CP 476, Florianópolis, Santa Catarina 88040-900, Brazil

[‡]Núcleo de Pesquisas em Ciências Exatas e Tecnológicas, Universidade de Franca, 14404-600 Franca, São Paulo, Brazil

Supporting Information

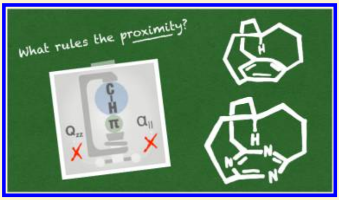

ABSTRACT: Molecular iron maidens are a strained type of cyclophane in which a methine hydrogen, by the action of the bridges, is placed closer to the center of an aromatic ring. Such constrained molecular frameworks are in fact a noteworthy synthetic challenge. The present study provides a comprehensible theoretical analysis that elucidates unique structural and energetic aspects of this class of molecules, evaluating, in the light of quantum chemistry, both the influence of the aromatic moiety, from π-basic to π-acid, and the nature of the heteroatoms located at the bridges. Our results not only propose the shortest intramolecular centered C−H···π distance to date, which is supported by calculated ^{1}H chemical shifts, but also shed light on the main factors that rationalize and justify such proximity. QTAIM, NBO, and NCI analyses allow us prematurely to conclude that the ultrashort C−H···π distance is sustained by an interplay between a large stabilizing electrostatic component with a non-negligible covalent character. However, the energetics involving such strained molecular scaffolds, addressed by means of isodesmic reactions, revealed that the C−H···π proximity is modulated mainly by the capacity of the bridges to support the strain imposed by the whole structure, hence compressing the C−H bond against the π-system.

1. INTRODUCTION

Noncovalent interactions have gained increased attention, primarily due to their role in the supramolecular chemistry of complex biological systems.[1] Different types of noncovalent interactions can be highlighted, including hydrogen bonds,[2−4] dihydrogen bonds,[5−8] halogen bonds,[9−11] those involving π-systems as π−π interactions,[12] cation-π,[13−16] anion-π,[17,18] and also the C−H···π interactions.[19−21] The latter have occupied a noticeable position due to the role they play in molecular recognition mechanisms of proteins,[22] as well as in other host−guest molecular systems.[23] In this scenario, cyclophanes[24] have been playing a crucial role, especially in host−guest chemistry, due to their cage-like structures,[25] becoming an alluring class of organic compounds. For instance, theoretical studies and further experimental results obtained for cylindrophanes revealed that they are not only able to discriminate guests of different sizes and but also can be selective to fluoride, certifying, in the context of anion−π interactions, that theory and practice supplement each other.[26,27]

The quest for insight into the synthesis of exotic twisted molecules was started in 1986 by Robert Pascal, who became interested in molecules able to exhibit very short C−H···π distances.[28] In 1976, Ricci et al.,[29] obtained the *out* isomer of cyclophane presented in Figure 1a. Ten years later, Pascal and Grossman[30] not only characterized such a synthetic product but also verified the presence of the *in* isomer (Figure 1a), in which the methine **H** is placed in a forced manner close to the center of an aromatic ring. This constrained molecular structure displays a ^{1}H NMR septet with a chemical shift in a very high field region ($\delta_{\text{in}-\text{H}} = -1.68$ ppm),[28] and, due to its conformation, the *in* isomer was named the molecular “iron maiden”.[28] Further examples of structures presenting *in*−*out* isomerism, including strained cyclophanes can be found in a review by Alder and East.[31]

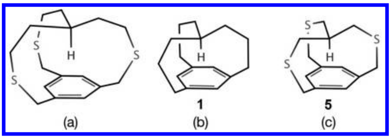

Figure 1. Examples of strained cyclophanes that have been synthesized: (a) *in* isomer of the cyclophane prepared in 1976 by Ricci et al.,[29] (b) cyclophane **1** obtained by Pascal et al. in 1987 in an effort to synthesize tighter scaffolds,[32] and (c) cyclophane **5** synthesized in 1989 that has hitherto been the structure with the shortest C−**H**···π proximity, as confirmed by its X-ray structure.[33]

Additional efforts to synthesize iron maidens containing even shorter centralized C−H···π distances, such as in cyclophane **1** (Figures 1 and 2), did not lead to the formation of crystals.

Received: February 16, 2018
Published: April 16, 2018

Downloaded via UNIV FED DE SANTA CATARINA on April 1, 2019 at 22:32:07 (UTC).
See https://pubs.acs.org/sharingguidelines for options on how to legitimately share published articles.

ACS Publications © 2018 American Chemical Society

DOI: 10.1021/acs.joc.8b00461

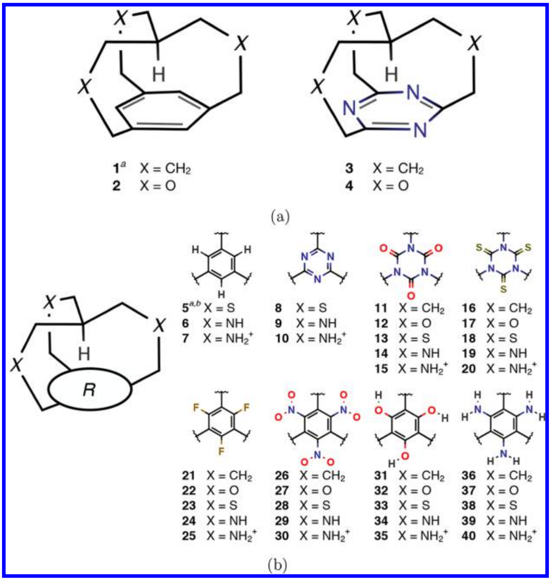

Figure 2. Strained cyclophane structures discussed through the text (a) and schematic representation of the remaining compounds presented in the Supporting Information (b). a: Experimental values of ^1H NMR are available for **1** and **5**.[32,33] b: Crystallographic data for **5** are also available.[33]

However, the obtained product displayed a ^1H NMR chemical shift of $\delta_{in-H} = -4.03$ ppm and an IR C−H stretch of 3325 cm^{-1}, indicating that **1** could potentially represent the structure obtained experimentally with the shortest C−**H**···π distance already reported.[32] Despite the difficulties faced by Pascal and co-workers to synthesize and obtain crystals of these molecular cages, finally in 1989 they obtained the cyclophane **5** shown in Figure 1c.[33] This compressed structure presented a C−**H**···π distance of 1.68 Å and spectral features (^1H NMR $\delta_{in-H} = -2.84$ ppm, $\nu_{C-H} = 3260$ cm^{-1}) similar to **1** (Figure 1b).[33]

In the present work, structural aspects of *in* cyclophanes are elucidated from a computational perspective by varying the nature of both (i) the bridges (X = CH_2, S, NH_2^+, NH, and O) but keeping it with three bonded atoms, as in cyclophane **1**, which is the molecular structure of experimental reference[32] and represents hitherto the most compressed scaffold already synthesized; and (*ii*) the π-basic and π-acid character of the aromatic moieties, including rings such as benzene, cyanuric acid, triaminobenze, trithiocyanuric acid, trifluorobenzene, trihydroxybenzene, trinitrobenzene, and *s*-triazine, allowing us to evaluate the electronic effects caused by these aromatic portions on the C−H···π distances, as schematically represented in Figure 2. Such combinations generate cyclophanes **1**−**40** (Figures 2a, b and S1, S2, Supporting Information), of which four are highlighted in the present study (**1**−**4**) since they exhibited the shortest distances between the methine **H** and the centroid of aromatic portions, as detailed in Table S1, Supporting Information. This theoretical study not only reveals the shortest intramolecular centralized C−H···π distance but also sheds light on the physical reasoning that justifies the C−H···π proximity in this class of compounds.

2. METHODOLOGY

Geometries were optimized at the DFT-D level of theory, employing the hybrid density functional PBE0 of Ernzerhof-Scuseria[34] and Adamo-Barone[35] (25% of Hartree-Fock exchange), in conjunction with a triple-ζ quality basis set of Ahlrich and co-workers (def2-TZVPP).[36,37] The RIJCOSX approximation was applied to speed up the calculation of the HF exchange integrals.[38] The description of long-range dispersion effects was taken into account by the Grimme's dispersion correction[39,40] (D3) together with Becke-Johnson damping functions.[41,42] All obtained geometries were verified to correspond to a minimum on the potential energy surface by the absence of imaginary eigenvalues in the Hessian matrix. Geometry optimizations of a chosen group of cyclophanes performed with correlated spin-component scaled second order perturbation theory (RI-SCS-MP2/def2-TZVPP)[36,37,43−45] were also taken into account in order to validate the geometries obtained with PBE0. Geometry optimizations and numerical vibrational frequency calculations were carried out with ORCA software (v.3.0.1).[46]

Nuclear magnetic resonance (NMR) chemical shifts were computed with the gauge-including atomic orbital approach (GIAO),[47,48] as implemented in ADF2016[49−51] (PBE0-D3/TZ2P[48,52]). The reported GIAO values are relative to tetramethylsilane (TMS) by the use of the experimental chemical shift of the cyclophane depicted in Figure 1c (−2.84 ppm[33]). The electronic structure of all compounds was also studied by means of the noncovalent interactions index (NCI), natural bond orbitals (NBO), and quantum theory of atoms in molecules (QTAIM), in which the same level of theory was employed (PBE0-D3(BJ)/def2-TZVPP). NCI analysis[53] was performed with the NCIPLOT[54] code and visualized with VMD software.[55] The NBO method[56−58] was performed using GAMESS-US v.2013 (R1).[59]

DOI: 10.1021/acs.joc.8b00461
J. Org. Chem. 2018, 83, 5114−5122

Table 1. Geometry Parameters of 5 Calculated with PBE0-D3/def2-TZVPP and RI-SCS-MP2/def2-TZVPP Levels and Contrasted with Available Crystallographic[33] Data[a]

	parameter (Å)							
	C_3–A	C_3–B	H–B	C_1–S	C_2–S	A–C_1	C_2–C_3	A–B
X-ray[a]	3.098	3.120	2.199	1.848	1.831	1.496	1.520	1.391
PBE0-D3(BJ)[avg]	3.078	3.118	2.211	1.839	1.823	1.498	1.529	1.391
RI-SCS-MP2[avg]	3.072	3.101	2.204	1.849	1.835	1.504	1.536	1.399

[a] Mean signed deviation (MSD) from experiment = −0.002 Å (PBE0-D3) and −0.002 Å (RI-SCS-MP2). Mean absolute error (MAE) = 0.008 Å (PBE0-D3) and 0.009 Å (RI-SCS-MP2). For details, see Figure 3 and Table S1.

Table 2. Selected C−H···π Distances ($r_{\text{C-H}\cdots\pi}$, Å), C−H Bond Lengths ($r_{\text{C−H}}$, Å), and Their Corresponding Stretching Frequencies ($\nu_{\text{C-H}}$, cm^{-1}), Differences of Energy between Isomers *In* and *Out* ($\Delta E_{\text{in−out}} = E_{\text{out}} − E_{\text{in}}$, kcal·mol^{-1}), and Calculated ^{1}H NMR Chemical Shifts[a] for H (δ_{TMS}, ppm) of Compounds 1−5[b]

structure	$r_{\text{C-H}\cdots\pi}$	$r_{\text{C-H}}$	$\nu_{\text{C-H}}$	$\Delta E_{\text{in−out}}$	$\delta^{\text{calc.}}_{\text{TMS}}$
1	1.631	1.061	3476 (3325)	13.1	−4.11 (−4.03)[32]
2	1.586	1.058	3502	3.7	−4.31
3	1.619	1.055	3543	8.7	−3.50
4	1.574	1.052	3580	−2.9	−3.82
5	1.703 (1.695)	1.066 (1.086)	3408 (3260)	9.1	−2.84 (−2.84)[33]

[a] Relative chemical shifts were taken as $\delta^{\text{calc.}}_{\text{TMS}} = \delta_{\text{ref}} − \delta_{\text{abs}}$, where $\delta_{\text{ref}} = \delta^{\text{exp.}}_{\text{TMS}}(\mathbf{5}) + \delta_{\text{abs}}(\mathbf{5})$, in which $\delta^{\text{exp.}}_{\text{TMS}}(\mathbf{5})$ is the experimental chemical shift for the synthesized cyclophane **5**, and $\delta_{\text{abs}}(\mathbf{5})$ is its respective calculated absolute value. [b] The available experimental values are given in parentheses.[32,33]

QTAIM analysis[60] was employed as implemented in MultiWFN 3.3.9.[61] The strain in compounds **1**−**4** was evaluated by means of isodesmic reactions, which are hypothetical reactions used to evaluate relative stability and repulsion between the methine group and the aromatic moiety, and the amount of strain supported by the tethering bridges and aromatic rings.[62−66]

3. RESULTS AND DISCUSSION

3.1. Geometries. In order to evaluate the structural effects caused by the nature of different aromatic moieties on the strained cyclophane framework, the following aromatic rings were considered: *s*-triazine (TRZ), benzene (BZN), cyanuric acid (CA), trithiocyanuric acid (TCA), trifluorobenzene (TFB), triaminobenzene (TAB), trihydroxybenzene (THB), and trinitrobenzene (TNB). Furthermore, to comprehend the effects that stem from the bridges, the following substitutions were considered: X = O, S, NH, NH_2^+, and CH_2. The structures of all cyclophanes **1**−**40** are schematically represented in Figure 2, and their optimized structures are reported in Figures S1 and S2 (Supporting Information).

Among the 40 studied compounds (**1**−**40**), cyclophanes **1**−**4** were chosen to rationalize the proximity of the methine hydrogen **H** to the π-system since their structures resemble the structure of **1** closely, which was synthesized in 1987,[32] and also because they exhibit the shortest calculated C−H···π distances (Tables 2 and S2). Moreover, cyclophanes **1**−**4** can be considered as suitable candidates to be synthesized, whereas most of the other calculated structures were used to rationalize the physical nature of such strained frameworks. It is also important to highlight that calculations with the structure of **5** were used to validate the employed methodology, since **5** is the compound for which crystallographic data are reported in the literature.[33]

Comparisons between the calculated (PBE0-D3/def2-TZVPP) and the available crystallographic structure[33] of **5** lead to a mean signed deviation (MSD) of −0.002 Å (Table 1). This geometric difference is expected due to lattice effects. For comparison, the structures of compounds (**1**−**4**) were optimized at the RI-SCS-MP2/def2-TZVPP level of theory,[36,37,43−45] which led to a MSD similar to that of PBE0-D3, indicating that the adopted functional is adequate for studying such systems. Since no restrictions were imposed during the geometry optimization procedure, the obtained structures do not present a perfect C_{3v} symmetry (root-mean-square displacements of atomic coordinates necessary to apply the C_{3v} point group equal 0.335 and 0.320 Å for PBE0-D3 and RI-SCS-MP2, respectively). A benchmark study on molecular iron maidens recently published by Vujović and co-workers[67] confirmed that hybrid and dispersion corrected functionals are the most effective for reproducing the X-ray geometry data.[33] Therefore, our findings allow us to assert that the calculated structures are reliable for employment in further analysis.

Among the four compounds in quest (**1**−**4**), the shortest calculated C−H···π distance belongs to cyclophane **4**, which contains the *s*-triazine (TRZ) ring and oxygen as the bridge heteroatom. At first glance, this proximity could be simply interpreted as stemming from the smaller van der Waals radius of nitrogen atoms at the TRZ ring, but it is not the case, as presented in the following discussion.

On the basis of the physical nature of the C−H···π interaction, which is a weak type of H-bond, the dispersion component, represented by the polarizability ($\alpha_{\parallel}$), plays a major role over the electrostatic component, typified by the quadrupole moment (Q_{zz}). In contrast, in a strong H-bond, the opposite reasoning is found, i.e., the Q_{zz} overcomes the $\alpha_{\parallel}$ in terms of importance.[68] According to results previously reported,[69] the TRZ ring does not exhibit significant Q_{zz} or $\alpha_{\parallel}$ values, which is a decisive fact to support that neither the weak C−H···π interaction nor the strong H-bond concepts can be employed to justify the short distance between the methine **H** and the TRZ ring.[70,71]

Notably, among the 40 studied cyclophanes, only **4** presented a more stable *out* isomer (−2.9 kcal·mol^{-1}) than the *in* isomer (Table 2). In addition, **4** has also the shortest C−H···π distance (1.574 Å), suggesting that this framework represents a borderline case, in which the proximity between the nonbonded groups is so extreme that the *out* isomer is favored. After a careful search in the literature, it has becoming evident that the calculated C−H···π proximity in **4** is predicted to be even closer than the hitherto shortest C−H···π distance experimentally reported for cyclophanes.[32,33]

3.2. C−H···π Distance Analysis.

The electronic and structural uniqueness of the *in* isomers encompass a combination of factors, including the compressed molecular framework and nonbonded contacts, and unexpected bond lengths can be highlighted. In this sense, the calculated ^{1}H NMR chemical shift for the methine **H** of **1** was found to be −4.11 ppm (Table 2), in excellent agreement with an experimental report (−4.03[32]). The calculated IR vibrational frequency (ν_{C-H} = 3476 cm^{-1}) evinces a blue-shifted type of methine interaction, which agrees with the unusual C(sp^3)−H bond length as well (Table 2). In the case of the shortest C−H···π distance (1.574 Å) found in **4** and in contrast to what would be expected, the C(sp^3)−H bond length is also the shortest one (1.052 Å). This noteworthy extra short bond distance displays a calculated blue-shifted IR vibrational frequency (ν_{C-H} = 3580 cm^{-1}), which agrees with the unpredicted C(sp^3)−H bond length. In other words, as the methine **H** comes closer to the centroid of the aromatic moiety, the C(sp^3)−H becomes shorter, resembling a C(sp)−H (1.086 Å), i.e., with a higher *p* character,[72] rather than the opposite. Such a situation might stem from the strained architecture of the *in* cyclophane,[73] and it is possibly related to charge reorganization, leading to polarization of the C(sp^3)−H bond.

The above-mentioned properties are totally in line with atomic charges and bond strengths obtained with QTAIM,[60] which are measurable quantum expectation values,[74] and were obtained for the selected structures (Figure 3, Table 3). The results presented in Table 3 support the fact that high field ^{1}H NMR chemical shifts are related to stronger shielding, as revealed by the more negative QTAIM charge on **H** in **3** and **4**, when compared with that in **1** and **2** (Tables 3 and S5). Also the blue-shifted C−H stretch to a stronger C−H bond was observed, which again is supported by QTAIM, displaying more electron density at bond critical points, which is associated with larger bond orders (Table S4). Atomic charges, based on natural population analysis[75] (NPA) are also shown for comparison, exhibiting the same trend as QTAIM charges, despite the more negative charge values observed.

The energy stabilization provided by the donor−acceptor interactions in **1**−**4** (Table 4 and Figure 4) was evaluated by means of NBO analysis. Donor−acceptor interactions between **H** and the bridges are only present in “oxygen-bridged” compounds. Similarly, the **H** donor−acceptor interaction with

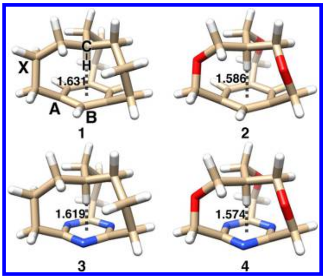

Figure 3. Optimized structures of compounds **1**−**4**, including selected individual centralized C−**H**···π distances (Å) and the atomic labeling (X, A, and B) used to discuss QTAIM charge analysis (Table 3). Color-code: tan = carbon, blue = nitrogen, white = hydrogen, and red = oxygen.

Table 4. Sum of NBO Second Order Stabilization Energies ($\Delta E^{*(2)}_{i\to j}$): Donations from σ(C−H) to the σ* and π* Orbitals of the Bridge Surrounding Groups C−H, C−C, and C−O, and to the Aromatic Ring[a]

interactions	$\Delta E^{*(2)}_{i\to j}$ (kcal·mol^{-1}) 1	2	3	4
σ(C−**H**) → σ*(C−H)	−8.6	−8.2	−8.3	−8.2
σ(C−**H**) → σ*(C−C)	−3.1	−3.2	−1.9	−2.1
σ(C−**H**) → σ*(C−O)		−2.4		−2.8
σ(C−**H**) → π*(ring)			−3.1	−2.9
total	−11.7	−13.8	−13.3	−16.0
$r_{C\text{-}H\cdots\pi}$(Å)	1.631	1.596	1.619	1.574

[a]Selected C−**H**···π distances ($r_{C\text{-}H\cdots\pi}$, Å) are presented for comparison.

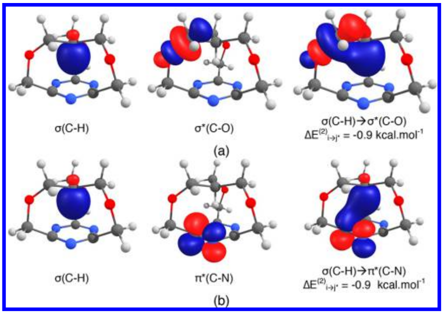

Figure 4. Representation of selected donor−acceptor NBO interactions for compound **4**, with their respective second order stabilization energies ($\Delta E^{*(2)}_{i\to j}$): (a) through-bond interaction between the σ(C−**H**) donor NBO and σ* of the bridging neighbor C−O acceptor NBO; and (b) through-space interaction between the σ(C−**H**) donor NBO and π* acceptor NBO of the triazine ring. Color-code: gray = carbon, blue = nitrogen, white = hydrogen, and red = oxygen.

Table 3. QTAIM Charges (in Units of *e*) Labeled According to Figure 3[a]

structure	H	C	A^{avg}	B^{avg}	X^{avg}
1	0.021 (0.333)	0.048 (−0.397)	−0.020 (−0.002)	−0.038 (−0.231)	0.047 (−0.394)
2	0.034 (0.353)	0.019 (−0.513)	−0.029 (−0.071)	−0.029 (−0.184)	−1.056 (−0.515)
3	−0.028 (0.254)	0.067 (−0.330)	1.050 (0.480)	−1.189 (−0.523)	0.044 (−0.391)
4	−0.015 (0.273)	0.039 (−0.439)	1.048 (0.423)	−1.168 (−0.480)	−1.042 (−0.496)

[a]NPA charges (same units) are given in parentheses for comparison.

DOI: 10.1021/acs.joc.8b00461
J. Org. Chem. 2018, 83, 5114−5122

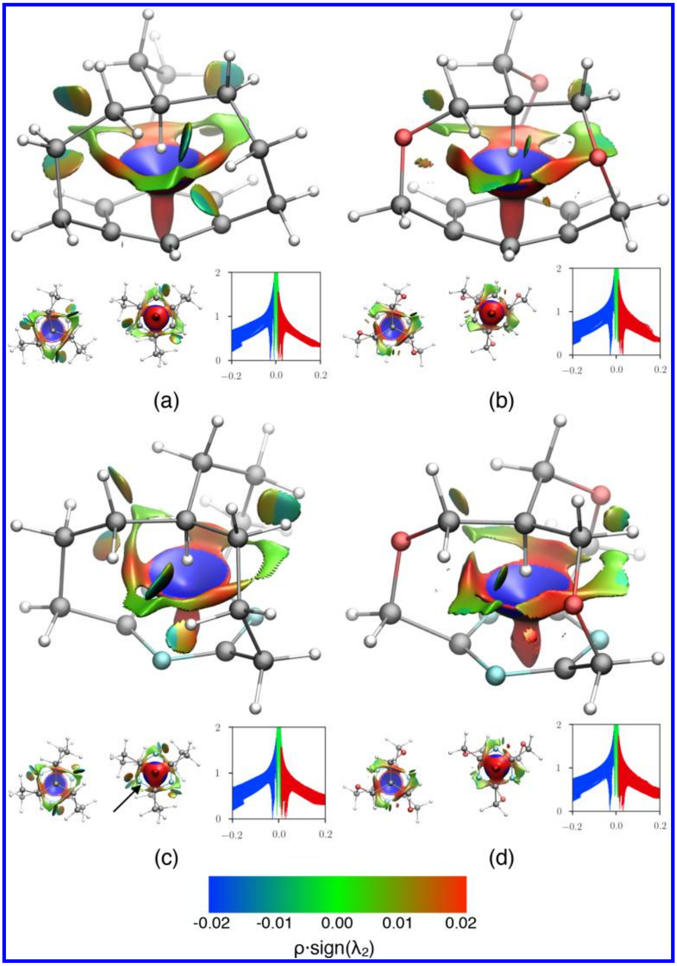

Figure 5. Perspective, superior, and inferior views of NCI, along with plots of the reduced density gradient ($s \propto |\nabla_\rho|/\rho^{4/3}$, a.u.) versus sign($\lambda_2$)·$\rho$ (a.u.) of (a) **1**, (b) **2**, (c) **3**, and (d) **4**. The bottom left corner black arrow in c exemplifies hydrogen bonds taking place between the methine hydrogen and the triazine nitrogens. Color-code: gray = carbon, cyan = nitrogen, white = hydrogen, and red = oxygen.

the aromatic unit is only observed with the TRZ ring. Hence, in **4**, *through-bond* stabilizing interactions are seen between **H** and the oxygen of the bridges and also *through-space* interactions with the TRZ unit. The oxygen at the bridges allows a donor−acceptor interaction between the σ(C−H) bonding and the σ*(C−O) antibonding orbitals. In the same way, the TRZ ring allows donor−acceptor interactions between the σ(C−H) bonding and the π* antibonding orbitals of the C−N bonds of the ring (Figure 4a). In summary, by considering the σ(C−**H**) → π*(ring) interactions in **3** and **4**, an inverse relationship between the C−H···π distances and the NBO second order stabilization energies is observed, i.e., slightly longer C−H···π distances are related to a slightly more stabilizing second order energy values, supporting the above-mentioned effects. Stabilizing donor−acceptor interactions between the methine **H** and the C−H and C−C NBO orbitals of the neighboring groups located at the bridges are shown as well in Table 4 and discussed in detail in the Support Information.

Qualitative information regarding the intramolecular interactions in cyclophanes **1**−**4** was obtained by means of NCI

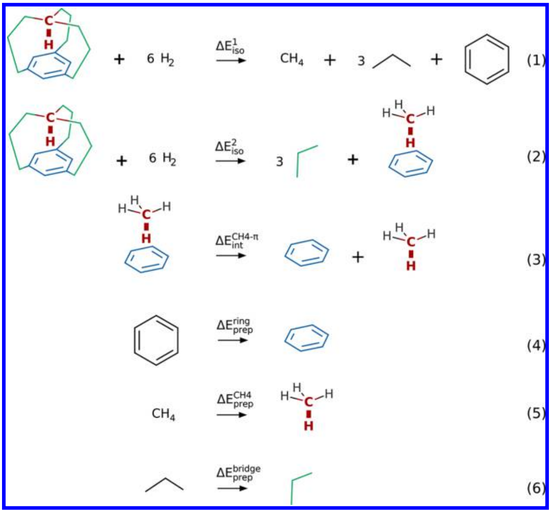

Figure 6. Thermodynamic decomposition of strain energy by means of isodesmic reactions of a molecular iron maiden, here exemplified by **1**. Broken covalent bonds were capped with relaxed hydrogen atoms (e.g., the first molecule on the right-hand side of reaction 1 is methane). Apart from capping hydrogens, fragments colored with the same tone have the same geometry, but structures in black were completely optimized. Associated energies are shown in Table 5.

analysis.[53,54] Through this technique, a strong attractive interaction is observed (bowl-shaped blue region in Figure 5) between the methine **H** and the center of the aromatic rings of compounds (**1**−**4**). Blue surfaces characterize strong hydrogen bonds, which indicates that the C−H···π interactions in these compounds are not simply dispersive but mainly electrostatic with a noticeable covalent character, also supported by NBO analysis. Residual repulsive red regions, located at the bottom of the attractive bowl-shaped blue surface, are also observed. These red regions suggest that besides the noncovalent interaction between the **H** and the ring, the compressed iron maiden framework also produces regions of repulsive character that result from the steric effects present in the molecular scaffold. Attractive C−H···π interactions are accentuated in compounds **3** and **4** as a result of hydrogen bonding between the **H** and the nitrogen atoms of the triazine units (small blue regions at the bottom of the bowl-shaped surface indicated by the arrow in Figure 5 c). Curiously, NCI analysis did no reveal any interaction between the **H** and methylene or oxygen groups.

One way to think of the interactions taking place, which are able to stabilize the resulting crowded molecule, is to consider the contribution of both the electrostatic hydrogen bonding and a dispersion driven C−H···π interaction. Analyzing the combination of information obtained from the QTAIM, NBO, and NCI, one can prematurely conclude that the ultrashort C−H···π distance is sustained by an interplay between a large stabilizing electrostatic component with a non-negligible covalent character, resembling a strong H-bond, in contrast to the C−H···π dispersion driven weak H-bond interaction. However, it is important to take into account the energetics involving such strained molecular scaffolds, and for that reason, different schemes of isodesmic reactions are presented and discussed in the next section

3.3. Isodesmic Reactions.

Isodesmic reactions provide useful thermodynamic information, which are convenient to clarify to which extent the methine hydrogen proximity to aromatic moieties results from an actual interaction or, in contrast, whether it stems from the molecular framework strain. In this sense, isodesmic reaction schemes were employed (Figure 6) in order to evaluate the tension encompassed in the cyclophane structure **1**−**4** by considering not only the entire cyclophane structure but also different portions of the structure such as bridges and rings (Figure 6, reactions 1−6).

According to Figure 6, the total strain energy, $\Delta E^{1}_{\mathrm{iso}}$, denotes the total energy released by the cyclophane structure when the latter is decomposed into its fundamental components: ring (either BZN or TRZ), bridges (propane or dimethyl ether), and methane. In the schematic reactions, bonds were always capped with hydrogen atoms to keep the correct valence, and the resultant geometries were optimized according to the color scheme presented in Figure 6, in which structures bearing equal colors have roughly equal geometries, but structures depicted in black were completely optimized. For instance, on the right-hand-side of the reaction scheme 1 (Figure 6), which contains methane, propane, and benzene, all structures were fully optimized without constraints. However, the propane on the right-hand-side of reaction scheme 2 has, apart from capping hydrogens, the same geometry as the bridges in the iron maiden, and for that reason both are depicted in green (Figure 6). The same procedure is kept for other components described in color. $\Delta E^{2}_{\mathrm{iso}}$ depicts both the bonding and repulsion accumulated between three bridges and the compressed methane-ring moiety, while $\Delta E^{\mathrm{CH_4\text{-}\pi}}_{\mathrm{int}}$ describes the repulsion due to the compression of a methane against the ring at the C−H⋯π distance found in the iron maiden. The energy preparation terms, $3\Delta E_{\text{prep}}^{\text{bridge}}$, $\Delta E_{\text{prep}}^{\text{ring}}$, and $\Delta E_{\text{prep}}^{\text{CH}_4}$ represent the energy necessary to deform the isolated constituents from their isolated geometry to the geometry they have to acquire in the iron maiden structures. The energetics of isodesmic reactions depicted in Figure 6 can be mathematically described according to eqs 1−3.

$$\Delta E_{\text{iso}}^{1} = \Delta E_{\text{iso}}^{2} - \Delta E_{\text{int}}^{\text{CH}_4\text{-}\pi} - 3\Delta E_{\text{prep}}^{\text{bridge}} - \Delta E_{\text{prep}}^{\text{ring}} - \Delta E_{\text{prep}}^{\text{CH}_4} \tag{1}$$

$$\Delta E^{2-1} = \Delta E_{\text{iso}}^{2} - \Delta E_{\text{iso}}^{1} = -\Delta E_{\text{int}}^{\text{CH}_4\text{-}\pi} + \Delta E_{\text{prep}}^{\text{total}} \tag{2}$$

$$\Delta E_{\text{prep}}^{\text{total}} = 3\Delta E_{\text{prep}}^{\text{bridge}} + \Delta E_{\text{prep}}^{\text{ring}} + \Delta E_{\text{prep}}^{\text{CH}_4} \tag{3}$$

The values reported in Table 5 reveal that the largest energetic contribution to the total released energy, $\Delta E_{\text{iso}}^{1}$, comes from the bridge bonding/repulsion term ($\Delta E_{\text{iso}}^{2}$), accounting for 76−80% of $\Delta E_{\text{iso}}^{1}$ ranging from −88.4 to −100.5 kcal·mol^{-1}, which causes the total energy values, $\Delta E_{\text{iso}}^{1}$, to vary between −112.7 and −126.2 kcal·mol^{-1}. Both $\Delta E_{\text{iso}}^{1}$ and $\Delta E_{\text{iso}}^{2}$ are larger in magnitude when the ring is benzene, when compared with triazine, which means that the overall accumulated strain in the iron maiden is larger when the ring is benzene.

Table 5. Thermodynamic Decomposition of Strain Energy (in kcal·mol^{-1}) by Means of Isodesmic Reactions of Iron Maidens 1−4 (Figure 6 and Text)[a]

	1	2	3	4
$\Delta E_{\text{iso}}^{1}$	−126.2	−122.8	−112.7	−120.5
$\Delta E_{\text{iso}}^{2}$	−100.5	−93.0	−88.4	−92.9
ΔE^{2-1}	25.7	29.8	24.3	27.5
$\Delta E_{\text{int}}^{\text{CH}_4-\pi}$	−13.3	−15.6	−14.3	−16.7
$\Delta E_{\text{prep}}^{\text{total}}$	12.4	14.2	10.0	10.8
$3\Delta E_{\text{prep}}^{\text{bridge}}$	7.4	8.2	7.2	8.1
$\Delta E_{\text{prep}}^{\text{ring}}$	4.7	5.6	2.2	2.1
$\Delta E_{\text{prep}}^{\text{CH}_4}$	0.3	0.4	0.5	0.6

[a] The horizontal line serves only to separate preparation energies from the rest.

In order to evaluate the balance between interaction and strain in iron maidens, an energy decomposition was performed (ΔE^{2-1}, eq 2) since it bears neither direct effects of covalent bonding between bridges and ring/methane nor their respective pairwise repulsions. $\Delta E_{\text{int}}^{\text{CH}_4-\pi}$ represents a release of 13.3−16.7 kcal in strain energy in all cases, accounting for 52−61% of ΔE^{2-1} in magnitude, which indicates that CH_4-π contacts are always repulsive in **1**−**4**. $\Delta E_{\text{int}}^{\text{CH}_4-\pi}$ is around 2−3 kcal·mol^{-1} more repulsive for bridges containing oxygen but only around 1 kcal·mol^{-1} more repulsive for triazine rings. Since $\Delta E_{\text{int}}^{\text{CH}_4-\pi}$ was calculated without the presence of bridges, its differences should only be due to the strain caused by the bridges on the ring and the C−**H** bond. This induced tension is further evinced by the larger $\Delta E_{\text{prep}}^{\text{total}}$ values observed for **2** (14.2 kcal·mol^{-1}) and **4** (10.8 kcal·mol^{-1}), which have bridges with oxygen atoms, when, respectively, compared to their CH_2 counterparts **1** (12.4 kcal·mol^{-1}) and **3** (10.0 kcal·mol^{-1}).

Bridge strain ($3\Delta E_{\text{prep}}^{\text{bridge}}$) accounts for more than half of the total strain energy (58−60%) in the structures containing benzene and even more than that for the structures with triazine (73−75%). $3\Delta E_{\text{prep}}^{\text{bridge}}$ is within 7.2−8.2 kcal·mol^{-1} in all cases; the above difference in percentage is due to the larger $\Delta E_{\text{prep}}^{\text{ring}}$ of benzene rings (4.7−5.6 kcal·mol^{-1}) when compared with that of triazine (2.1−2.2 kcal·mol^{-1}). This indicates that triazine is slightly more flexible and can be more easily distorted than the benzene ring. In contrast, $\Delta E_{\text{prep}}^{\text{CH}_4}$ is always smaller than 0.6 kcal·mol^{-1}, accounting for 5% of $\Delta E_{\text{prep}}^{\text{total}}$ in the largest case (**4**).

A direct, quantitative relationship between the C−H⋯π distance and $\Delta E_{\text{int}}^{\text{CH}_4-\pi}$ is to be stressed (Pearson's r^2 of 0.9724, Table 5), indicating that short C−H⋯π distances are accompanied by large C−H⋯π repulsions. A similar relationship can be found between C−H⋯π distance and $3\Delta E_{\text{prep}}^{\text{bridge}}$ (r^2 = 0.8196). All in all, shorter C−H⋯π distances are to be found together with highly strained bridges, which accounts for larger C−H⋯π repulsions as a result of proximity. Indeed, Ringer et al. have obtained a shallow minimum (around −1.45 kcal·mol^{-1}) for the methane−benzene complex and found the rather long C−H⋯π distance of 2.7 Å (CCSD(T)/CBS).[76] This confirms that our repulsive values are due to very short C−H⋯π distances.

4. CONCLUSIONS

In summary, ultrashort, centroid-directed C−H⋯π proximities bearing unique spectroscopic features were theoretically studied in the framework of the molecular "iron maidens". Two particularly short C−H⋯π distances were obtained: 1.574 Å, for the cyclophane containing a triazine ring and oxygen as the heteroatom at the bridges (**4**), and 1.586 Å, in a similar cyclophane with benzene ring (**2**). Methine ^{1}H chemical shifts for *in* isomers were calculated as −3.82 and −4.31 ppm, respectively (Table 2). Since it was found that the *out* isomer of **4** is more energetically favorable than its *in* isomer (Table 2), compound **2** might be a stronger candidate for a challenged synthesis.

Both above-mentioned C−H⋯π proximities represent distances shorter than any experimental data reported to date for such cyclophanes. This close proximity of nonbonded groups makes the *in* isomer steadily unstable, which might represent an actual borderline for such C−H⋯π contacts. This leads us to conjecture that this boundary might lie between **2** and **4**, i.e., around 1.58 Å. Isodesmic decompositions support this hypothesis, highlighting that the C−H⋯π proximity is modulated mainly by the capacity of the bridges to support the strain imposed by the whole framework, hence compressing the C−H bond against the π-system. We expect that the present contribution will be able to propel experimental chemistry frontiers ahead by providing a modest example of how computational theoretical contributions can lead to practical discoveries.

■ ASSOCIATED CONTENT

Ⓢ Supporting Information

The Supporting Information is available free of charge on the ACS Publications website at DOI: 10.1021/acs.joc.8b00461.

Computational methodologies, geometry coordinates, and data for QTAIM, NBO, and NCI, and GIAO ^{1}H NMR analyses (PDF)

■ AUTHOR INFORMATION

Corresponding Author

*E-mail: giovanni.caramori@ufsc.br.

ORCID

Felipe S. S. Schneider: 0000-0001-8090-2976

Giovanni F. Caramori: 0000-0002-6455-7831
Renato L. T. Parreira: 0000-0002-5623-9833

Notes

The authors declare no competing financial interest.

■ ACKNOWLEDGMENTS

We thank Professor Antônio Carlos Joussef for the fruitful discussions about these systems. I.Ø. thanks CAPES for a Master's scholarship (grant 1732086). A.O.O. and F.S.S.S. thank CNPq for Ph.D. scholarships (grants 142339/2015-6 and 140485/2017-1). G.F.C. thanks CNPq (grants 302408/2014-2 and 311963/2017-0) for a research fellowship. R.L.T.P. thanks FAPESP (grant 2011/07623-8) and CAPES (grant 88881.068346/2014-01) for financial support.

■ REFERENCES

(1) Maharramov, A. M. *Non-covalent Interactions in the Synthesis and Design of New Compounds*; John Wiley & Sons: Hoboken, NJ, 2016.
(2) Arunan, E.; Desiraju, G. R.; Klein, R. A.; Sadlej, J.; Scheiner, S.; Alkorta, I.; Clary, D. C.; Crabtree, R. H.; Dannenberg, J. J.; Hobza, P.; Kjaergaard, H. G.; Legon, A. C.; Mennucci, B.; Nesbitt, D. J. *Pure Appl. Chem.* **2011**, *83*, 1619−1636.
(3) Struble, M. D.; Strull, J.; Patel, K.; Siegler, M. A.; Lectka, T. *J. Org. Chem.* **2014**, *79*, 1−6.
(4) Lopez, A. H. D.; Caramori, G. F.; Coimbra, D. F.; Parreira, R. L. T.; da Silva, É. H. *ChemPhysChem* **2013**, *14*, 3994−4001.
(5) Zong, J.; Mague, J. T.; Pascal, R. A. *J. Am. Chem. Soc.* **2013**, *135*, 13235−13237.
(6) Mandal, N.; Pratik, S. M.; Datta, A. *J. Phys. Chem. B* **2017**, *121*, 825−834.
(7) Rosel, S.; Quanz, H.; Logemann, C.; Becker, J.; Mossou, E.; Canadillas-Delgado, L.; Caldeweyher, E.; Grimme, S.; Schreiner, P. R. *J. Am. Chem. Soc.* **2017**, *139*, 7428−7431.
(8) Custelcean, R.; Jackson, J. E. *Chem. Rev.* **2001**, *101*, 1963−1980.
(9) Metrangolo, P.; Neukirch, H.; Pilati, T.; Resnati, G. *Acc. Chem. Res.* **2005**, *38*, 386−395.
(10) Ciancaleoni, G.; Arca, M.; Caramori, G. F.; Frenking, G.; Schneider, F. S. S.; Lippolis, V. *Eur. J. Inorg. Chem.* **2016**, *2016*, 3804−3812.
(11) Schneider, F. S. S.; Caramori, G. F.; Parreira, R. L. T.; Lippolis, V.; Arca, M.; Ciancaleoni, G. *Eur. J. Inorg. Chem.* **2018**, *2018*, 1007−1015.
(12) Sinnokrot, M. O.; Valeev, E. F.; Sherrill, C. D. *J. Am. Chem. Soc.* **2002**, *124*, 10887−10893.
(13) Ma, J. C.; Dougherty, D. A. *Chem. Rev.* **1997**, *97*, 1303−1324.
(14) Caramori, G. F.; Garcia, L. C.; Andrada, D. M.; Frenking, G. *Organometallics* **2014**, *33*, 2301−2312.
(15) Ortolan, A. O.; Caramori, G. F.; Frenking, G.; Muñoz-Castro, A. *New J. Chem.* **2015**, *39*, 9963−9968.
(16) Galembeck, S. E.; Caramori, G. F.; Misturini, A.; Garcia, L. C.; Orenha, R. P. *Organometallics* **2017**, *36*, 3465−3470.
(17) Giese, M.; Albrecht, M.; Rissanen, K. *Chem. Rev.* **2015**, *115*, 8867−8895.
(18) Ortolan, A. O.; Caramori, G. F.; Bickelhaupt, F. M.; Parreira, R. L. T.; Munoz-Castro, A.; Kar, T. *Phys. Chem. Chem. Phys.* **2017**, *19*, 24696−24705.
(19) Carroll, W. R.; Zhao, C.; Smith, M. D.; Pellechia, P. J.; Shimizu, K. D. *Org. Lett.* **2011**, *13*, 4320−4323.
(20) Tsuzuki, S. *Annu. Rep. Prog. Chem., Sect. C: Phys. Chem.* **2012**, *108*, 69.
(21) Nijamudheen, A.; Jose, D.; Shine, A.; Datta, A. *J. Phys. Chem. Lett.* **2012**, *3*, 1493−1496.
(22) Brandl, M.; Weiss, M. S.; Jabs, A.; Suhnel, J.; Hilgenfeld, R. *J. Mol. Biol.* **2001**, *307*, 357−377.
(23) Li, P.; Parker, T. M.; Hwang, J.; Deng, F.; Smith, M. D.; Pellechia, P. J.; Sherrill, C. D.; Shimizu, K. D. *Org. Lett.* **2014**, *16*, 5064−5067.
(24) Gleiter, R. *Modern Cyclophane Chemistry*; Wiley-VCH: Weinheim, Germany, 2004.
(25) Balzani, V. *Supramolecular Chemistry*; Springer: Dordrecht, The Netherlands, 1992.
(26) Mascal, M. *Angew. Chem., Int. Ed.* **2006**, *45*, 2890−2893.
(27) Mascal, M.; Yakovlev, I.; Nikitin, E. B.; Fettinger, J. C. *Angew. Chem., Int. Ed.* **2007**, *46*, 8782−8784.
(28) Pascal, R. *Eur. J. Org. Chem.* **2004**, *2004*, 3763−3771.
(29) Ricci, A.; Danieli, R.; Rossini, S. *J. Chem. Soc., Perkin Trans. 1* **1976**, *1*, 1691.
(30) Pascal, R. A.; Grossman, R. B. *J. Org. Chem.* **1987**, *52*, 4616−4617.
(31) Alder, R. W.; East, S. P. *Chem. Rev.* **1996**, *96*, 2097−2111.
(32) Pascal, R. A.; Grossman, R. B.; Van Engen, D. *J. Am. Chem. Soc.* **1987**, *109*, 6878−6880.
(33) Pascal, R. A.; Winans, C. G.; Van Engen, D. *J. Am. Chem. Soc.* **1989**, *111*, 3007−3010.
(34) Ernzerhof, M.; Scuseria, G. E. *J. Chem. Phys.* **1999**, *110*, 5029−5036.
(35) Adamo, C.; Barone, V. *J. Chem. Phys.* **1999**, *110*, 6158−6170.
(36) Weigend, F.; Ahlrichs, R. *Phys. Chem. Chem. Phys.* **2005**, *7*, 3297.
(37) Weigend, F. *Phys. Chem. Chem. Phys.* **2006**, *8*, 1057.
(38) Neese, F.; Wennmohs, F.; Hansen, A.; Becker, U. *Chem. Phys.* **2009**, *356*, 98−109.
(39) Grimme, S.; Antony, J.; Ehrlich, S.; Krieg, H. *J. Chem. Phys.* **2010**, *132*, 154104.
(40) Grimme, S.; Hansen, A.; Brandenburg, J. G.; Bannwarth, C. *Chem. Rev.* **2016**, *116*, 5105−5154.
(41) Johnson, E. R.; Becke, A. D. *J. Chem. Phys.* **2005**, *123*, 024101.
(42) Grimme, S.; Ehrlich, S.; Goerigk, L. *J. Comput. Chem.* **2011**, *32*, 1456−1465.
(43) Weigend, F.; Haser, M.; Patzelt, H.; Ahlrichs, R. *Chem. Phys. Lett.* **1998**, *294*, 143−152.
(44) Grimme, S. *J. Chem. Phys.* **2003**, *118*, 9095−9102.
(45) Szabo, A.; Ostlund, N. S. *Modern Quantum Chemistry: Introduction to Advanced Electronic Structure Theory (Dover Books on Chemistry)*; Dover Publications, 2012.
(46) Neese, F. *Wiley Interdiscip. Rev. Comput. Mol. Sci.* **2012**, *2*, 73−78.
(47) Schreckenbach, G.; Ziegler, T. *J. Phys. Chem.* **1995**, *99*, 606−611.
(48) Krykunov, M.; Ziegler, T.; van Lenthe, E. *Int. J. Quantum Chem.* **2009**, *109*, 1676−1683.
(49) Fonseca Guerra, C.; Snijders, J. G.; te Velde, G.; Baerends, E. J. *Theor. Chem. Acc.* **1998**, *99*, 391−403.
(50) te Velde, G.; Bickelhaupt, F. M.; Baerends, E. J.; Fonseca Guerra, C.; van Gisbergen, S. J. A.; Snijders, J. G.; Ziegler, T. *J. Comput. Chem.* **2001**, *22*, 931−967.
(51) Baerends, E. J. et al.. *ADF2016, SCM, Theoretical Chemistry*; Vrije Universiteit: Amsterdam, The Netherlands. https://www.scm.com.
(52) Van Lenthe, E.; Baerends, E. J. *J. Comput. Chem.* **2003**, *24*, 1142−1156.
(53) Johnson, E. R.; Keinan, S.; Mori-Sanchez, P.; Contreras-Garcia, J.; Cohen, A.; Yang, W. *J. Am. Chem. Soc.* **2010**, *132*, 6498−6506.
(54) Contreras-García, J.; Johnson, E. R.; Keinan, S.; Chaudret, R.; Piquemal, J. P.; Beratan, D. N.; Yang, W. *J. Chem. Theory Comput.* **2011**, *7*, 625−632.
(55) Humphrey, W.; Dalke, A.; Schulten, K. *J. Mol. Graphics* **1996**, *14*, 33−38.
(56) Weinhold, F.; Landis, C. R. *Chem. Educ. Res. Pract.* **2001**, *2*, 91.
(57) Reed, A. E.; Curtiss, L. A.; Weinhold, F. *Chem. Rev.* **1988**, *88*, 899−926.
(58) Glendening, E. D.; Landis, C. R.; Weinhold, F. *Wiley Interdiscip. Rev. Comput. Mol. Sci.* **2012**, *2*, 1−42.
(59) Schmidt, M. W.; et al. *J. Comput. Chem.* **1993**, *14*, 1347−1363.
(60) Matta, C. F.; Boyd, R. J.; Becke, A. *The Quantum Theory of Atoms in Molecules: From Solid State to DNA and Drug Design*; Wiley-VCH, 2007.

(61) Lu, T.; Chen, F. *J. Comput. Chem.* **2012**, *33*, 580−592.

(62) Muller, P. *Pure Appl. Chem.* **1994**, *66*, 1077−1184.

(63) George, P.; Glusker, J. P.; Bock, C. W. *J. Mol. Struct.: THEOCHEM* **1991**, *235*, 193−196.

(64) van Eis, M. J.; de Wolf, W. H.; Bickelhaupt, F.; Boese, R. *J. Chem. Soc., Perkin Trans.* **2000**, *2*, 793−801.

(65) Caramori, G. F.; Galembeck, S. E.; Laali, K. K. *J. Org. Chem.* **2005**, *70*, 3242−3250.

(66) Caramori, G. F.; Galembeck, S. E. *J. Phys. Chem. A* **2008**, *112*, 11784−11800.

(67) Vujovic, M.; Zlatar, M.; Milcic, M.; Gruden, M. *Phys. Chem. Chem. Phys.* **2017**, *19*, 9500−9508.

(68) Tsuzuki, S.; Fujii, A. *Phys. Chem. Chem. Phys.* **2008**, *10*, 2584−2594.

(69) Mooibroek, T. J.; Gamez, P. *Inorg. Chim. Acta* **2007**, *360*, 381−404.

(70) Frontera, A.; Gamez, P.; Mascal, M.; Mooibroek, T. J.; Reedijk, J. *Angew. Chem., Int. Ed.* **2011**, *50*, 9564−9583.

(71) Schottel, B. L.; Chifotides, H. T.; Dunbar, K. R. *Chem. Soc. Rev.* **2008**, *37*, 68−83.

(72) Hobza, P.; Havlas, Z. *Chem. Rev.* **2000**, *100*, 4253−4264.

(73) Allinger, N. L. *Molecular Structure: Understanding Steric and Electronic Effects from Molecular Mechanics*; John Wiley & Sons, Inc.: Hoboken, NJ, 2010; p 356.

(74) Bader, R. F. W.; Matta, C. F. *J. Phys. Chem. A* **2004**, *108*, 8385−8394.

(75) Reed, A. E.; Weinstock, R. B.; Weinhold, F. *J. Chem. Phys.* **1985**, *83*, 735−746.

(76) Ringer, A. L.; Figgs, M. S.; Sinnokrot, M. O.; Sherrill, C. D. *J. Phys. Chem. A* **2006**, *110*, 10822−10828.

DOI: 10.1021/acs.joc.8b00461
J. Org. Chem. 2018, 83, 5114−5122

APPENDIX B – Support Information to Cylindric Cage-Type Cyclophanes

B.1 Structural Parameters and Geometry Analyses

Match search at the Cambridge Structural Database (CSD) for cylindrophanes containing two π-systems, three backbone bridges with five atoms, one heteroatom at the third position of the bridges is depicted in Figure B1. The C_s isomer considered in this work was modeled from the crystallographic data of **KISDEW** (host at the bottom of Figure B1 **A**) and **KISDIA** (host-guest at the top of Figure B1 **A**).

Cylindrophanes **1**–**9** discussed in Chapter III are presented in Figure B3, and the cylindrophane-fluoride systems $\mathbf{1}{\cdot}\mathrm{F}^{-}$–$\mathbf{9}{\cdot}\mathrm{F}^{-}$ in Figure B4. Geometry parameters analysed with their labels are presented in the cylindrophane scheme in Figure B2. The data collected from the optimized structures of the empty hosts (**1**–**9**) is shown in Table B1, and for $\mathbf{1}{\cdot}\mathrm{F}^{-}$–$\mathbf{9}{\cdot}\mathrm{F}^{-}$ in Table B2.

The **top view** (left) in Figure B2, shows the asymmetric sides of the cyclophane. The side distances r_A, r_B, and r_C were measured from each **L** atom at the third position of the bridges. Corners **a**, **b**, and **c**, are used to differentiate the bridges. **Side view** (middle) in Figure B2 shows the **L**-H bond length, and $\nu_{\mathbf{L}\text{-H}}$ stretch, as well as the $\mathrm{H}\cdots\mathrm{F}^{-}$ contact, and the $\mathrm{R}_1\cdots\mathrm{R}_2$ height, which was measured from the centroid axis of the π-systems. The **perspective view** (right) in Figure B2, shows the $\mathbf{L}\cdots\mathrm{F}^{-}$ distance. It also shows the α bridge angles, the β hydrogen bond angles, and the γ dihedral. Values for

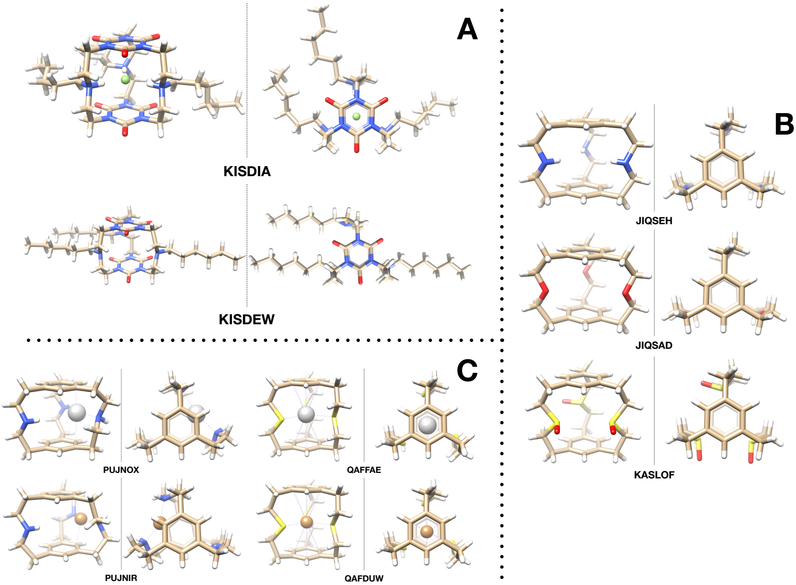
A
KISDIA
KISDEW
B
JIQSEH
JIQSAD
KASLOF
C
PUJNOX
QAFFAE
PUJNIR
QAFDUW

Figure B1 – Cylindrophanes crystal structures deposited at Cambridge Structural Database (CSD). Perspective (right), and from the top (left), images of the cylindrophanes are classified according to: **(A) KISDIA** and **KISDEW** are cationic hosts selective to F^-;[13,14] **(B)** JIQSEH, JIQSAD, and KASLOF are neutral empty **H**; **(C)** PUJNOX, PUJNIR, QAFFAE and QAFDUW are neutral **H**'s coordinating Ag^+ (silver) and Cu^+ (cupper).[15,16] Color-code: tan = carbon, blue = nitrogen, white = hydrogen, red = oxygen, and yellow = sulfur, green = F^-, silver = Ag^+, cupper = Cu^+.

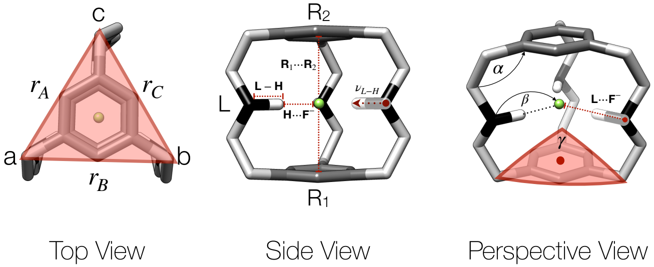

Top View Side View Perspective View

Figure B2 – Cylindrophane structural parameters scheme. **(Top View)** Cylindrophane side distances r_{A}, r_{B}, r_{C}, and corners a, b, c; **(Side View)** **L**-H bond length, $\mathrm{H} \cdots \mathrm{F}^-$ contact, $\mathrm{R}_1 \cdots \mathrm{R}_2$ height, and $\nu_{\mathbf{L}\text{-H}}$ stretch; **(Perspective View)** distance $\mathbf{L} \cdots \mathrm{F}^-$, and angles α, β, and γ. Color-code: gray = bridge atoms, black = binding group atom ($\mathbf{L}_{\mathrm{n}}$) , white = binding group hydrogen H_{n}, dim gray = π-systems, green = F^- or dummy atom (**X**).

$\mathbf{L} \cdots \mathrm{F}^-$, and $\mathrm{H} \cdots \mathrm{F}^-$ distances are shown at the same columns in Tables B1, and B2, in a $\mathbf{L} \cdots \mathrm{F}^-$ ($\mathrm{H} \cdots \mathrm{F}^-$) format. The **L**-H bond length, $\nu_{\mathbf{L}\text{-H}}$ stretch frequency, is presented in Table B7, together with the Infrared (IR) spectra for all host-guest system, in Section B.2.4 of this support information. Geometry parameters presented at the tables were collected from the crystallographic structure of the empty host (crystallographic structure of the empty host (**KISDEW**), and the host-guest system (**KISDIA**. The empty host (**KISDEW**) does not have the $\mathrm{H} \cdots \mathbf{X}$ distances because instead of having a $\mathrm{NH_2}^+$ binding group, it has long aliphatic chains that are bonded to the **L** nitrogen atoms (Figure B1). These aliphatic chains were added to the cylindrophane structure, according to the published paper, in order to be able to work with common organic solvents.[14]

Cylindrophane framework collected angles are shown in the scheme of Figure B2, in the **Perspective View** (right). The different angles analysed for the empty hosts, and the **HG** systems are presented in Table B3, and B4, respectively. Angle α is given concerning each aromatic rings, being that R_1 is the inferior (R_1), and R_2 is the superior

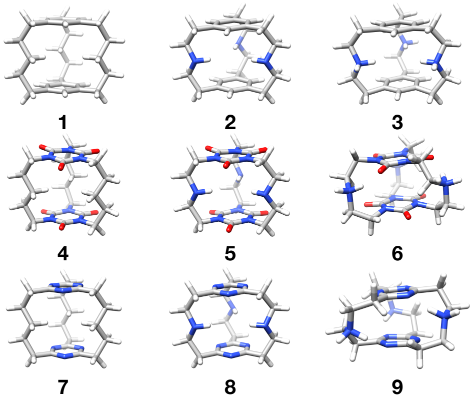

Figure B3 – Optimized structures of host **1**–**9**. The rows are separated by the π-systems (**R**): **BZN** (1st), **CA** (2nd), **TRZ** (3rd), and the columns by the binding groups (**L**): CH_2 (1st), NH (2nd) and NH_2^+ (3rd). Color-code: *grey* carbon, blue = nitrogen, white = hydrogen, red = oxygen.

Table B1 – Selected geometrical parameters of the cylindrophanes hosts (**H**) **1**–**9** scaffolds (Figure B3). Labels of the parameters presented in this table are in accord to Figure B2, in which in the absence of a F^- anion, a dummy atom (**X**) was placed in the midpoint between the centroid axis of the **R** systems.

H	r_A	r_B	r_c	$\mathbf{L}_a(H_a)\cdots\mathbf{X}$	$\mathbf{L}_b(H_b)\cdots\mathbf{X}$	$\mathbf{L}_c(H_c)\cdots\mathbf{X}$	$R_1\cdots R_2$
1	5.14	5.23	5.19	2.99 (1.89)	2.98 (1.81)	2.98 (1.89)	5.24
2	5.36	5.38	5.36	3.10 (2.09)	3.09 (2.07)	3.11 (2.10)	4.93
3	5.63	5.74	5.69	3.28 (2.27)	3.28 (2.26)	3.29 (2.28)	4.94
4	4.86	5.04	4.98	2.87 (1.76)	2.84 (1.74)	2.88 (1.78)	5.24
5	5.17	5.20	5.18	3.02 (2.00)	2.95 (1.92)	3.01 (1.99)	4.94
6	6.76	6.40	7.02	3.89 (3.40)	3.88 (3.40)	3.91 (3.45)	3.55
7	4.93	4.94	4.93	2.85 (1.75)	2.85 (1.75)	2.85 (1.75)	5.24
8	5.27	5.24	5.24	3.04 (2.06)	3.01 (2.03)	3.04 (2.06)	4.96
9	6.65	6.36	6.07	3.68 (3.14)	3.67 (3.14)	3.69 (3.13)	3.34
KISDEW	6.16	5.76	4.86	3.27 (—)	3.17 (—)	3.36 (—)	4.59

$r_{A,B,C}$ are the sides width of the cylindrophane cage.
$\mathbf{L_{a,b,c}}\cdots\mathbf{X}$ are the bridge $\mathbf{L}_n$ atom distances to the placed **X** atom.
$H_{\mathbf{a,b,c}}\cdots\mathbf{X}$ are the distances of the $\mathbf{L}_n$'s hydrogen to the centralized **X** atom.
$R_1\cdots R_2$ is the distance between the **R** systems.
X-Ray structure from Cambridge Structural Database (CSD) cod. **KISDEW**.

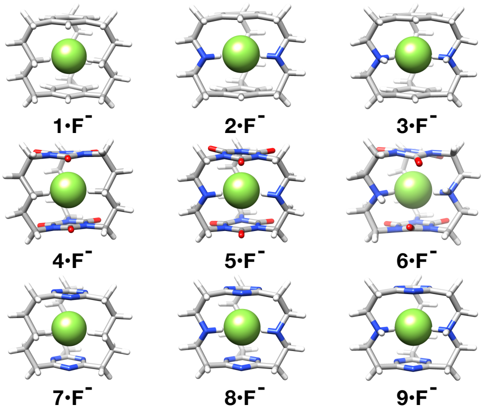

Figure B4 – Optimized structures of host-guests $\mathbf{1}\cdot F^-$–$\mathbf{9}\cdot F^-$. The rows are separated by the π-systems (**R**): **BZN** (1st), **CA** (2nd), **TRZ** (3rd), and the columns by the binding groups (**L**): CH_2 (1st), NH (2nd) and NH_2^+ (3rd). Color-code: *grey* carbon, blue = nitrogen, white = hydrogen, red = oxygen, and green = F^-.

Table B2 – Selected geometrical parameters (Figure B2) of the cylindrophane scaffolds $\mathbf{1}\cdot F^-$–$\mathbf{9}\cdot F^-$ interacting with F^- (Figure B4). All values presented in this table are in Å.

HG	r_A	r_B	r_C	$\mathbf{L}_a(H_a)\cdots F^-$	$\mathbf{L}_b(H_b)\cdots F^-$	$\mathbf{L}_c(H_c)\cdots F^-$	$R_1\cdots R_2$
$\mathbf{1}\cdot F^-$	4.97	5.11	5.04	2.91 (1.80)	2.89 (1.78)	2.93 (1.81)	5.47
$\mathbf{2}\cdot F^-$	4.88	4.82	4.83	2.79 (1.74)	2.74 (1.68)	2.84 (1.79)	5.45
$\mathbf{3}\cdot F^-$	4.75	4.62	4.68	2.68 (1.60)	2.60 (1.50)	2.82 (1.75)	5.48
$\mathbf{4}\cdot F^-$	4.97	5.28	5.16	2.96 (1.87)	2.95 (1.85)	2.99 (1.89)	5.18
$\mathbf{5}\cdot F^-$	4.88	4.90	4.89	2.82 (1.77)	2.79 (1.74)	2.86 (1.82)	5.25
$\mathbf{6}\cdot F^-$	4.65	4.80	4.78	2.74 (1.67)	2.65 (1.57)	2.44 (1.78)	5.17
$\mathbf{7}\cdot F^-$	4.97	5.12	5.05	2.92 (1.82)	2.90 (1.81)	2.93 (1.83)	5.31
$\mathbf{8}\cdot F^-$	4.87	4.77	4.81	2.78 (1.73)	2.76 (1.70)	2.80 (1.76)	5.29
$\mathbf{9}\cdot F^-$	4.73	4.58	4.65	2.68 (1.61)	2.64 (1.56)	2.73 (1.66)	5.35
KISDIA	4.69	4.99	4.85	2.77 (1.84)	2.86 (1.93)	2.77 (1.84)	5.38

$r_{A,B,C}$ are the sides width of the cylindrophane cage.
$\mathbf{L_{a,b,c}}\cdots\mathbf{X}$ are the bridge $\mathbf{L}_n$ atom distances to the placed **X** atom.
$H_{\mathbf{a,b,c}}\cdots F^-$ are the distances of the $\mathbf{L}_n$'s hydrogen to the centralized **X** atom.
$R_1\cdots R_2$ is the distance between the **R** systems.
X-Ray structure from Cambridge Structural Database (CSD) cod. **KISDIA**.

ring (R_2). They are indicated in parenthesis as ($R_1|R_2$). The β hydrogen bond angles for the empty hosts are hypothetical. They were measured placing a dummy atom (**X**) at the midpoint between the π-systems centroid axis. Dihedral angles γ are provided in modules in a ($R_1|R_2$) that differs each aromatic ring.

Angles α is the angle that forms between the bridge first and second atoms following the bridgehead atom of the π-systems. This measurement is related to the strain at the bridges since the tetrahedral bond angle expected for the carbon bond is ~ 109.5 ° Angles β is the angle that forms between the binding group atom (**L**) in each distinct bridge, and its internal hydrogen ($\mathbf{H}_{in}$), with the fluoride, i.e., is the H-bond angle formed between the H-bond donor (**L**) and the receptor (F^-). This angle is associated with the H-bond directionality, therefore to its strength. Excellent references to find more details into weak hydrogen bonds, as well as H-bonds in the solid state are the works of Desiraju and Steiner, respectively.[53, 215]. Angle $|\gamma|$ is the module value of the dihedral angle between R_1, and R_2, and its centroid. This angle was collected accounting for the first carbon in each bridge, and a dummy atom positioned at the centroid of the π-system, and is related to the strain accumulated at the π-systems, as aromatic rings are expected to be planar. Comparing γ in the empty **H** with the formed **HG** indicates how much strain the π-systems takes to accommodate the anion.

Table B3 – Selected angles of the **H**'s scaffold **1**–**9**, illustrated as indicated in Figure B2 perspective view, in the absence of the anionic guest a dummy atom **X** was positioned in the midpoint from the centroid of each π-systems. All angles values are in degrees (°).

H	α_{a} ($\mathrm{R_1}$|$\mathrm{R_2}$)	α_{b} ($\mathrm{R_1}$|$\mathrm{R_2}$)	α_{c} ($\mathrm{R_1}$|$\mathrm{R_2}$)	β_{a}	β_{b}	β_{c}	$\lvert\gamma\rvert$ ($\mathrm{R_1}$|$\mathrm{R_2}$)
1	112.7|112.8	112.8|112.7	112.8|112.9	174.4	174.5	173.7	2.2|2.2
2	112.6|112.6	112.6|112.6	112.8|112.8	170.4	171.3	170.6	0.2|0.2
3	113.8|113.8	113.6|113.7	113.8|113.9	165.9	165.9	165.2	5.0|4.9
4	112.8|112.8	112.8|112.6	113.3|113.3	179.9	180.0	178.6	1.8|1.8
5	112.6|112.6	112.4|112.4	112.9|112.9	173.0	178.4	177.4	0.3|0.3
6	118.9|114.7	114.4|119.1	114.9|119.7	109.8	109.3	108.2	10.0|10.2
7	111.4|111.4	111.4|111.3	111.4|111.4	175.6	175.3	175.6	2.4|2.5
8	111.5|111.5	114.5|111.4	111.6|111.6	158.3	160.7	158.5	1.0|1.0
9	118.1|114.1	118.2|112.6	112.3|118.4	112.2	112.1	114.6	1.0|2.1
KISDEW	112.6|112.1	112.0|112.0	116.8|113.8	—	—	—	3.0|2.31

Angle $\alpha_{\mathbf{a,b,c}}$ considers the angle between the π-systems ($\mathrm{R_1}|\mathrm{R_2}$) atom connected to the bridge, and the first and second carbon at the bridges from each **n** corner (Figure B2).

Angles $\beta_{\mathbf{a,b,c}}$ is the H-bond angle between $\mathbf{L}_{\mathrm{n}}$ and the **X** atom placed in the midpoint of the π-systems centroid.

Dihedral angle $|\gamma|$ ($\mathrm{R_1}|\mathrm{R_2}$) is measured between the first carbon in each bridge, and a **X** atom placed in the centroid of the π-systems.

[e] X-Ray structure from Cambridge Structural Database (CSD) cod. **KISDEW**.

Table B4 – Selected angles of the **HG** systems **1**·F^-–**9**·F^- , illustrated as indicated in Figure B2 perspective view. All angles values are in degrees (°).

HG	α_a ($R_1\vert R_2$)	α_b ($R_1\vert R_2$)	α_c ($R_1\vert R_2$)	β_a	β_b	β_c	$\vert\gamma\vert$ ($R_1\vert R_2$)
1·F^-	113.2|113.1	113.2|113.2	113.1|113.1	174.0	172.1	173.4	6.0|6.0
2·F^-	112.3|112.3	112.5|112.5	112.4|112.3	178.0	177.8	179.2	8.7|8.7
3·F^-	112.2|112.2	111.9|111.9	111.8|111.8	176.8	175.7	173.0	7.7|7.7
4·F^-	113.6|113.6	113.4|113.4	114.1|114.1	169.8	169.2	170.7	1.0|1.0
5·F^-	113.1|113.1	113.0|113.0	113.5|113.5	177.8	178.4	179.6	5.4|5.4
6·F^-	113.5|112.7	112.7|113.6	113.7|114.0	174.2	176.1	171.0	2.9|2.5
7·F^-	111.9|111.9	111.9|111.9	111.8|111.8	166.9	164.8	167.0	3.7|3.7
8·F^-	111.1|111.1	111.2|111.2	111.1|111.1	174.7	175.1	175.8	6.6|6.6
9·F^-	112.2|111.1	111.4|111.4	110.9|111.0	178.1	178.7	176.5	6.2|6.2
KISDIA	112.9|111.5	112.3|112.4	112.9|113.2	174.2	175.6	176.3	6.2|5.0

Angle $\alpha_{\mathbf{a,b,c}}$ considers the angle between the π-systems ($R_1|R_2$) atom connected to the bridge, and the first and second carbon at the bridges from each **n** corner (Figure B2).
Angles $\beta_{\mathbf{a,b,c}}$ is the H-bond angle between $\mathbf{L}_n$ and the F^- anion.
Dihedral angle $|\gamma|$ ($R_1|R_2$) is measured between the first carbon in each bridge, and a **X** atom placed in the centroid of the π-systems.
X-Ray structure from Cambridge Structural Database (CSD) cod. **KISDIA**.

B.2 Non-Covalent Interaction Analysis

B.2.1 Molecular Electrostatic Potential Maps (MEP)

The empty host's Electrostatic Potential Maps (MEP) were assessed as they provide qualitative information of electron density across the host framework. This is a prior step towards analysing the actual **HG** interactions since once the guest is interacting with the cylindrophane cages, the electron distribution is altered by the guest charge as well.

Perspectives view (bottom), aligned with the top view for the compounds **1**–**9** are found in Figures B5, B6, B7, and each illustrated set of hosts if accompanied of its color scale, according to the potential ranges applied to the structures. Figure B5 shows the MEP of compounds **1** (**BZN**), **4** (**CA**), and **7** (**TRZ**), which have **L** = CH_2 in common, with surface potential ranges of -0.001 a.u.(red) to 0.002 a.u.(blue), and an isovalue of 0.030 au. Figure B6 shows the MEP of compounds **2** (**BZN**), **5** (**CA**), and **8** (**TRZ**), which have **L** = NH in common, with surface potential ranges of -0.001 a.u.(red) to 0.002 a.u.(blue), and an isovalue of 0.030 au. Figure B7 shows the MEP of compounds **3** (**BZN**), **6** (**CA**), and **9** (**TRZ**), which have **L** = NH_2^+ in common, with surface potential ranges of 0.003 a.u.(red) to 0.550 a.u.(blue), and isovalue of 0.030 au.

Hosts **1**–**9** top view, shows their electron distribution on the outer part of their π-systems, the perspective shows the different electron density along the bridges. The top view of the π-systems is used to predict how the **R**'s will contribute to the anion-π interaction being that green to blue colors indicate electron deficiency, hence a better anion-π receptor. The colors also are related to the electron character of the π-systems: π-acidic (blue), neutral (green), π-basic (yellow). The same relationship of colors and electron density are applied to the bridges: electron-poor regions (blue), neutral (green), electron-rich (red).

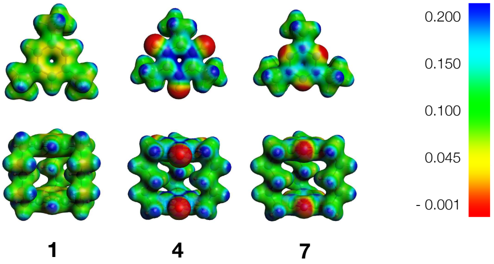

Figure B5 – MEP maps (left to right) **R** groups, **BZN**, **CA**, and **TRZ**, and **L** = CH_2. Maps for the neutral **H**'s **1**, **4**, and **7** (**L** = CH_2) with surface potential that ranges from -0.001 a.u.(red) to 0.002 a.u.(blue), and have an isovalue of 0.030 au.

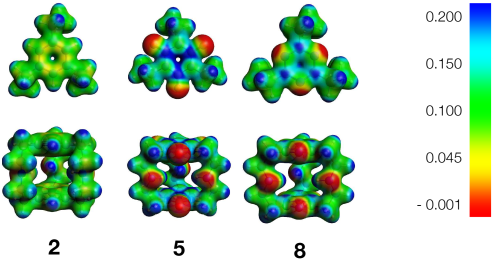

Figure B6 – MEP maps (left to right) **R** groups, **BZN**, **CA**, and **TRZ**, and **L** = NH. Maps for the neutral **H**'s **2**, **5**, and **8** (**L** = NH) with surface potential that ranges from -0.001 a.u.(red) to 0.002 a.u.(blue) and have an isovalue of 0.030 au.

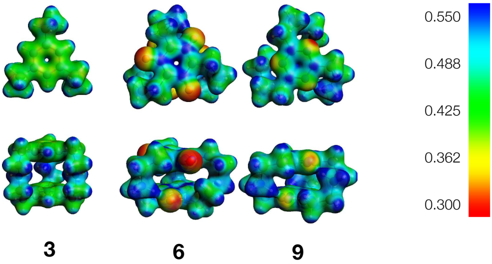

Figure B7 – MEP maps (left to right) **R** groups, **BZN**, **CA**, and **TRZ**, and **L** = NH_2^+. Charged **H**'s **3**, **6**, and **9** (**L** = NH_2^+) with surface potential that ranges from 0.003 a.u.(red) to 0.550 a.u.(blue), and isovalue of 0.030 au.

B.2.2 Energy Decomposition Analysis (EDA)

This section shows additional information concerning Energy Decomposition Analysis (EDA) for the **HG** systems in (kcal·mol^{-1}) units, except for the host ($q_{\mathbf{H}}$), and guest ($q_{\mathbf{G}}$) charges which are in (a.u.). A brief explanation of the theoretical background of the EDA analysis is found in Appendix C, C.3.2. In addition to the ΔE_{int}, ΔE_{prep} and the BDE, the $\Delta E_{\mathrm{Pauli}}$ repulsion, electrostatic potential attraction $\Delta V_{\mathrm{elstat}}$, stabilising orbital energies (ΔE_{oi}), and the induced dipole attractive forces (ΔE_{disp}), Hirshfeld charges for the host ($q_{\mathbf{H}}$), and guest ($q_{\mathbf{G}}$) are included in Table 1. The values in parenthesis correspond to the percentage of each stabilising contribution ($\Delta V_{\text{elstat}} + \Delta E_{\text{oi}} + \Delta E_{\text{disp}} = 100\%$), i.e., not accounting for the ΔE_{Pauli} repulsion .

The detailed information of the EDA done to the cylindrophane cage fragmentation proposed, separating the π-systems and first carbons of the bridges (Figure B8, Table B5), and the remaining three atoms of the bridges (Figure B9, Table B6), including the binding groups (**L**), is shown in this section. Like in at the **HG** EDA Table 1, the values presented at the tables are in (kcal·mol^{-1}) units, except for the host ($q_{\mathbf{H}}$), and guest ($q_{\mathbf{G}}$) Hirshfeld charges which are in (a.u.).

Figure B8 shows the fragmentation for the **R**'s, i.e., considering the first carbon that connects the backbone bridges. To complete the bridge carbon valence, a relaxed hydrogen was added to each carbon of the bridge, resulting in a methyl. Although we consider in our discussion the π-systems **BZN**, **CA**, and **TRZ**, the rings interacting with the fluoride in the fragmentation proposed are two 1,3,5-trimethylbenzene (**BZN**), 1,3,5-trimethylcyanuric acid (**CA**), and 2,4,6-trimethyl 1,3,5-triazine (**TRZ**). Likewise, Figure B9 presents the resulting fragmented bridges, in which relaxed hydrogen was added to each carbon of the bridge. For the sake of simplicity, the resulting fragmented bridges are discussed according to the **L**'s groups CH_2, NH, NH_2^+, and not the resulting molecules. All fragments have a closed-shell electron configuration.

B.2.3 Non-Covalent Interaction Index (NCI$_x$)

The NCI$_x$ images for all host-guest systems, $\mathbf{1}{\cdot}F^-$–$\mathbf{9}{\cdot}F^-$, are found in Figure B10. The differences in changes the π-systems, or the **L** binding groups are better seen in this image, but it follows the same logic behind what was presented at the Section 4.2.2.3, in Chapter III.

The top view image, Figure B11, better illustrates how the surfaces related to the non-covalent interactions within the **HG** sys-

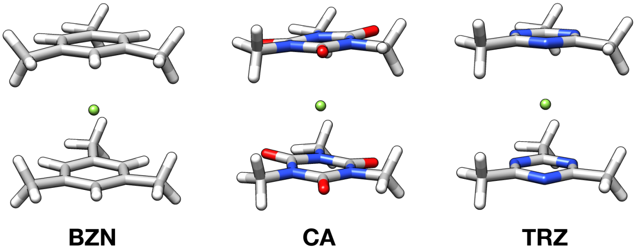

Figure B8 – Optimized structures of the π-systems (**R**) of **HG**'s **1**·F$^-$–**9**·F$^-$ (**BZN**, **BZN**, and **TRZ**) considering the original **HG**'s atoms coordinates, except for the hydrogens added to the first carbon of the bridges. Color-code: *grey* = carbon, blue = nitrogen, white = hydrogen, red = oxygen, green = F$^-$.

Table B5 – Energy Decomposition Analysis (kcal·mol^{-1}) and the Hirshfeld fragment charge analysis (a.u.) for the ring (**R**) fragments illustrated in Figure B8, of compounds **1**·F$^-$–**9**·F$^-$. Values in parenthesis correspond to the percentage of each stabilising contribution ($\Delta V_{\text{elstat}} + \Delta E_{\text{oi}} + \Delta E_{\text{disp}}$ = 100%).

R	ΔE_{int}	ΔE_{Pauli}	ΔV_{elstat}	ΔE_{oi}	ΔE_{disp}	$q_{\mathbf{G}}$	$q_{\mathbf{H}}$
1·F$^-$	-6.0	16.7	10.7	-30.0 *(90%)*	-3.5 *(10%)*	-0.860	-0.140
2·F$^-$	-7.5	17.3	9.2	-30.4 *(89%)*	-3.6 *(11%)*	-0.860	-0.140
3·F$^-$	-7.0	16.6	10.1	-30.1 *(90%)*	-3.5 *(10%)*	-0.859	-0.141
4·F$^-$	-47.0	21.4	-33.1 *(48%)*	-31.6 *(46%)*	-3.7 *(6%)*	-0.873	-0.127
5·F$^-$	-47.6	19.5	-32.8 *(49%)*	-30.5 *(45%)*	-3.8 *(6%)*	-0.877	-0.123
6·F$^-$	-46.0	22.8	-32.7 *(47%)*	-32.1 *(47%)*	-4.0 *(6%)*	-0.876	-0.124
7·F$^-$	-25.3	18.9	-22.4 *(28%)*	-28.5 *(64%)*	-3.3 *(8%)*	-0.878	-0.122
8·F$^-$	-26.3	19.3	-13.5 *(29%)*	-28.7 *(63%)*	-3.4 *(7%)*	-0.880	-0.120
9·F$^-$	-25.5	17.7	-11.9 *(28%)*	-27.9 *(65%)*	-3.4 *(7%)*	-0.882	-0.118

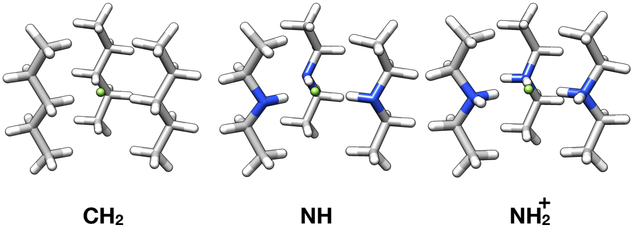

Figure B9 – Optimized structures of the bridge (**B**) in **HG**'s **1**·F^-–**9**·F^- , conserving three atoms in each original **B** branch, and the **L**'s groups. The distances were kept fixed as in the optimized **HG** structure, and relaxed hydrogens were added to complete the terminal atoms valance. Color-code: *grey* = carbon, blue = nitrogen, white = hydrogen, red = oxygen, green = F^-.

Table B6 – Energy Decomposition Analysis (kcal·mol^{-1}) and the Hirshfeld fragment charge analysis (a.u.) for the bridge fragments illustrated in Figure B9, of compounds **1**·F^-–**9**·F^- . Values in parenthesis correspond to the percentage of each stabilising contribution ($\Delta V_{\text{elstat}} + \Delta E_{\text{oi}} + \Delta E_{\text{disp}} = 100\%$).

B	ΔE_{int}	ΔE_{Pauli}	ΔV_{elstat}	ΔE_{oi}	ΔE_{disp}	$q_{\mathbf{G}}$	$q_{\mathbf{H}}$
1·F^-	-36.1	51.3	-33.4 *(38%)*	-51.6 *(59%)*	-2.9 *(3%)*	-0.789	-0.211
2·F^-	-63.8	50.2	-57.2 *(50%)*	-54.0 *(47%)*	-2.9 *(3%)*	-0.793	-0.207
3·F^-	-342.8	71.0	-344.8 *(83%)*	-66.1 *(16%)*	-3.1 *(1%)*	-0.767	2.767
4·F^-	-36.9	41.9	-21.8 *(35%)*	-48.1 *(61%)*	-3.0 *(4%)*	-0.799	-0.201
5·F^-	-62.3	44.7	-52.7 *(49%)*	-51.3 *(48%)*	-3.0 *(3%)*	-0.800	-0.200
6·F^-	-337.9	55.6	-332.1 *(84%)*	-58.1 *(15%)*	-3.2 *(1%)*	-0.788	2.788
7·F^-	-37.0	48.8	-31.9 *(37%)*	-50.7 *(59%)*	-3.1 *(4%)*	-0.793	-0.207
8·F^-	-63.4	52.2	-58.3 *(50%)*	-54.6 *(47%)*	-3.1 *(3%)*	-0.792	-0.208
9·F^-	-343.3	70.8	-345.7 *(83%)*	-65.2 *(16%)*	-3.3 *(1%)*	-0.772	2.772

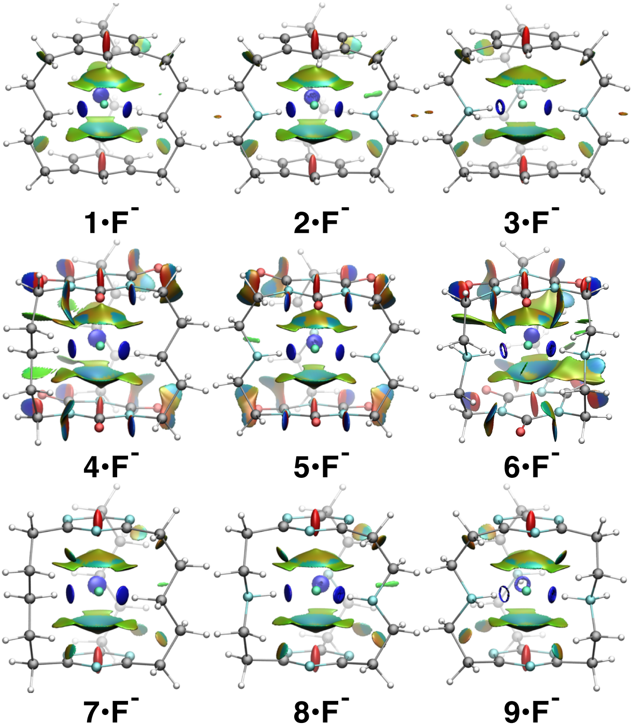
1·F$^-$ **2·F$^-$** **3·F$^-$**

4·F$^-$ **5·F$^-$** **6·F$^-$**

7·F$^-$ **8·F$^-$** **9·F$^-$**

Figure B10 – NCI$_x$ image for cylindrophanes-fluoride host-guest systems $\mathbf{1}\cdot\mathrm{F}^-$–$\mathbf{9}\cdot\mathrm{F}^-$. The rows are classified by the π-systems **BZN** (1st), **CA** (1nd), and **TRZ** (3rd), and the columns by the binding groups CH_2 (1st), NH_2^+ (2nd), and (3rd). Color-code: gray = carbon, cyan = nitrogen, white = hydrogen, and red = oxygen.

tem's framework are distributed. Hence, it reflects the symmetry of the compounds, as it is stands-out in **6**·F^-, showing various scattered surfaces. Note that we can see from this view that different pictures that are drawn in each **HG**, related to the π-systems. Not only the color can indicate the strength related to the *long-distance effects* of the **R** groups, but be also, the distribution, and size of the areas related to a color also contribute with rich information regarding the π-systems. Thus, one can easily see how the surface in **BZN** is more green (weaker **NCI**), and it increases in the size of the blue zone from **TRZ** to **CA**. The drawings of the blue zones clearly show as well the influence that the nitrogen atoms exert in the anion-π interaction, as the blue zones appear to be more abundant near the more polar atoms and red colors near the carbons.

Images of Figures B12, B13, and B14, show the contrast between the intramolecular non-covalent interactions found in hosts **3**, **6**, and **9**, to its host-guest systems. A detailed discussion was dedicated to the framework of compounds **6** and **9**, which present considerable distortion related to the intramolecular interactions. At the EDA analysis part of Chapter III, the existence of this intramolecular interaction was related to the higher ΔE_{prep} energy term in compounds **6**, and **9**, to form their **HG**'s 6·F^-, and 9·F^-.

B.2.4 Vibrational Frequency Analysis (IR)

Vibrational frequencies ($\nu_{\mathbf{L}\text{-H}}$) shown in Table B7, consider the stretching mode vibration for the hydrogens that are interacting directly with the F^- inside the cavity. Therefore, $\nu_{\mathbf{L}\text{-H}}$ refers to the hydrogens bonded to the **L** groups that point towards the fluoride, named internal hydrogens ($\mathbf{H}_{in}$). The external hydrogens to the cage, i.e., the **L** hydrogens outside the cavity ($\mathbf{H}_{out}$), are not presented in Table B7, but are indicated in the spectra of compounds **3**·F^-, **6**·F^-, and **9**·F^-, and will be explained according to the specific context.

Geometry parameters that are intimately related to the $\nu_{\mathbf{L}\text{-H}}$

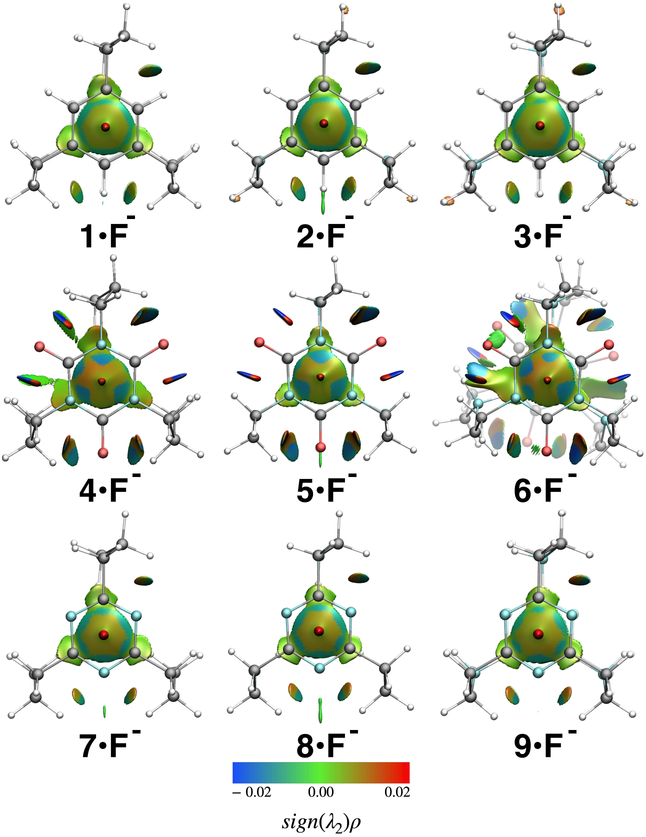
1•F-
2•F-
3•F-
4•F-
5•F-
6•F-
7•F-
8•F-
9•F-
– 0.02
0.00
0.02
sign(λ2)ρ

Figure B11 – Top view of the NCI$_x$ image for cylindrophanes-fluoride host-guest sytems **1**·F$^-$–**9**·F$^-$. Color-code: gray = carbon, cyan = nitrogen, white = hydrogen, and red = oxygen.

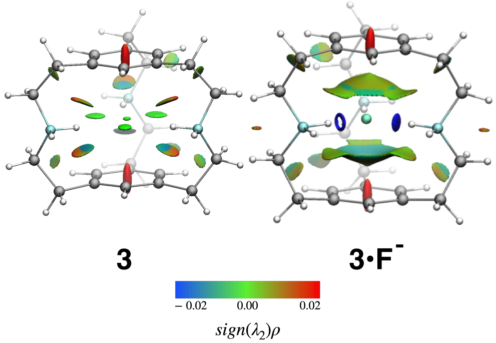

Figure B12 – NCI$_x$ image comparing host **3** (**BZN**, $NH_2{}^+$), with host-guest **3**·F^-, showing the differences in the intramolecular interactions in **3**, and the **NCI**'s interactions in **3**·F^-. Color-code: gray = carbon, cyan = nitrogen, and white = hydrogen.

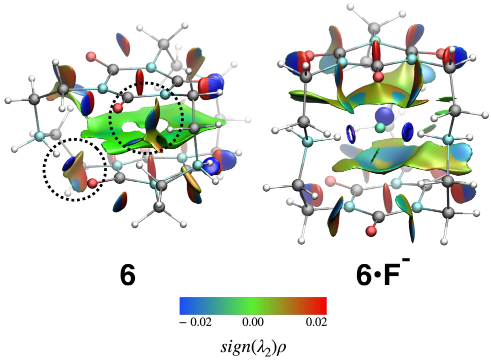

Figure B13 – NCI$_x$ image comparing host **6** (**CA**, $NH_2{}^+$), with host-guest **6**·F^-, showing the differences in the intramolecular interactions in **6**, and the **NCI**'s interactions in **6**·F^-. Intramoleular interactions discussed in the geometry analysis section are marked by a circle. Color-code: gray = carbon, cyan = nitrogen, white = hydrogen, and red = oxygen.

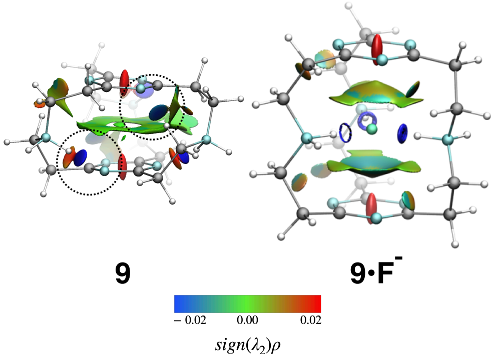

Figure B14 – NCI_x image comparing host **9** (**TRZ**, ${NH_2}^+$), with host-guest **9**·F^-, showing the differences in the intramolecular interactions in **9**, and the **NCI**'s interactions in **9**·F^-. Intramoleular interactions discussed in the geometry analysis section are marked by a circle. Color-code: gray = carbon, cyan = nitrogen, and white = hydrogen.

frequencies, i.e., $H \cdots F^-$, which is the distance from the **L** hydrogen to the F^-, and the **L**-H bond length. The letters associated with the variable in Table B7, refer to the corners that are shown in the scheme in Figure B2. The **HG**'s which presented stronger $\nu_{\mathbf{L}\text{-H}}$ frequencies specifically for the $\mathbf{H}_{in}$ of each specific corner **a**, **b**, or **c** were compounds **3**·F^-, **6**·F^-, and **9**·F^-, all of which have the ${NH_2}^+$ as the binding group. The other $\nu_{\mathbf{L}\text{-H}}$ values in Table B7 always present coupled vibrational modes between $\mathbf{H}_{in}$ of one or more corners but are more strong in the corners to which they were associated.

Figures B15, B16, and B17 show the calculated IR spectrum for pentane, diethylamine, and diethylammonium, at the BP86-D3/Def2-TZVP level of theory. They were calculated to serve as a reference to be associated with the $\nu_{\mathbf{L}\text{-H}}$ frequencies shown in Table B7, as well as to be compared in terms of intensity to the IR spectra that will be presented as follows. All the IR spectra were obtained from the geometry optimization procedure, as the numerical frequencies were always computed to make sure the optimized structures had no imagi-

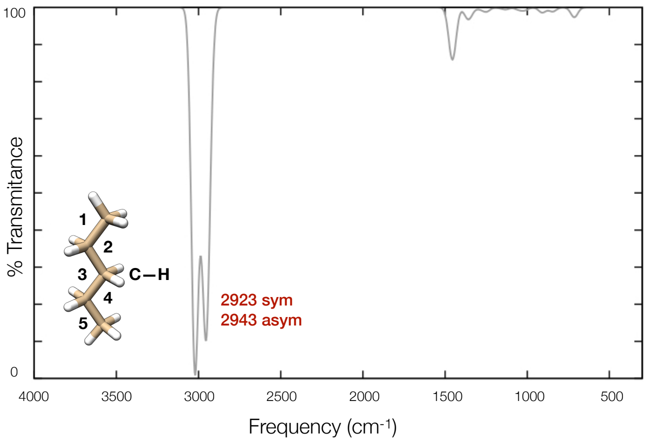

Figure B15 – Calculated Infrared Spectrum for pentane at BP86/Def2-TZVP level of theory. The noted peaks refer to the symmetric, and asymmetric C–H stretch in the third carbon.Color-code: tan = carbon, cyan = nitrogen, and white = hydrogen.

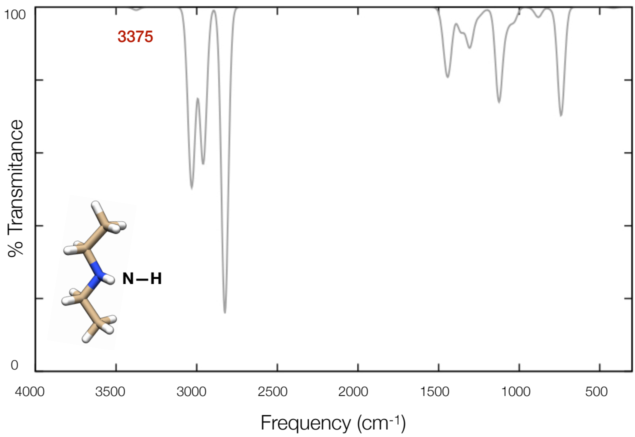

Figure B16 – Calculated Infrared Spectrum for diethylamine at BP86-D3/Def2-TZVP level of theory. The noted peak refers to the N–H stretch.Color-code: tan = carbon, cyan = nitrogen, and white = hydrogen.

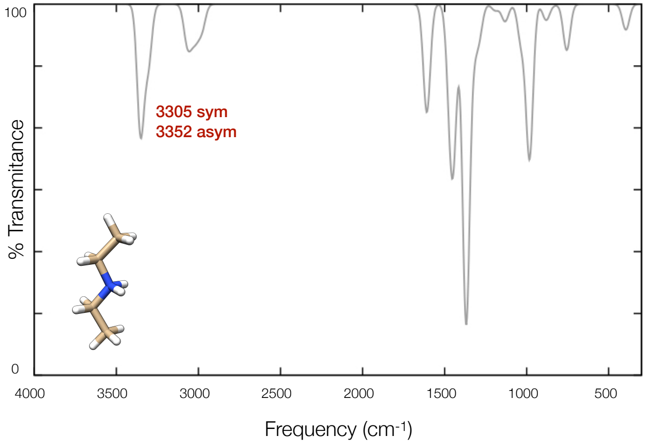

Figure B17 – Calculated Infrared Spectrum for diethylammonium at BP86-D3/Def2-TZVP level of theory. The noted peak refers to the N–H stretch.Color-code: tan = carbon, cyan = nitrogen, and white = hydrogen.

nary frequency. Therefore, the images in Figures B18–B26, shows how the calculated IR spectrum appears to be for **1**·F$^-$–**9**·F$^-$ hosts-guest systems. The assigned frequencies for for **3**·F$^-$, **6**·F$^-$, and **9**·F$^-$, refer to the internal hydrogen ($\mathbf{H}_{in}$) interacting with the F$^-$, according to corners **a**, **b**, or **c** in Figure B2, and to the hydrogen that is outside ($\mathbf{H}_{out}$) the cylindrophane cavity, also according to an specific corner.

B.3 Host-Guest Analysis

B.3.1 Relative Binding Energy (RBE)

The standard Gibbs free energies (ΔG) used to calculate the relative binding energies ($\Delta\Delta G_{\mathrm{bind}}$) were calculated with ORCA software (v.3.0.1)[121] in ideal thermodynamic conditions (T = 298.15 K, P = 1.00 atm, R = 8.315J/mol·K). The calculated ΔG values provided in this section, assume that **(1)** electronic state of the compounds have nondegenerate orbitals, **(2)** there are no thermal excited states in any

Table B7 – Selected **L** groups hydrogen stretch frequency ($\nu_{\mathbf{L}\text{-H}}$), and related geometry parameters $\mathrm{H}\cdots\mathrm{F}^-$, and **L**-H (Figure B2), for cylindrophane scaffolds $\mathbf{1}\cdot\mathrm{F}^-$–$\mathbf{9}\cdot\mathrm{F}^-$ interacting with F^- (Figure B4). All values related to bond length or distance in this table are in Å, and the IR frequencies in cm^{-1}.

HG	$r_{\mathbf{L}-\mathrm{H_a}}$	$\nu_{\mathbf{L}-\mathrm{H_a}}$	$\mathrm{H_a}\cdots\mathrm{F}^-$	$r_{\mathbf{L}-\mathrm{H_b}}$	$\nu_{\mathbf{L}-\mathrm{H_b}}$	$\mathrm{H_b}\cdots\mathrm{F}^-$	$r_{\mathbf{L}-\mathrm{H_c}}$	$\nu_{\mathbf{L}-\mathrm{H_c}}$	$\mathrm{H_c}\cdots\mathrm{F}^-$
$\mathbf{1}\cdot\mathrm{F}^-$	1.12	2686	1.80	1.12	2673	1.78	1.12	2746	1.81
$\mathbf{2}\cdot\mathrm{F}^-$	1.06	2838	1.74	1.06	2746	1.68	1.05	2962	1.79
$\mathbf{3}\cdot\mathrm{F}^-$	1.09	2458	1.60	1.11	2193	1.50	1.11	2734	1.75
$\mathbf{4}\cdot\mathrm{F}^-$	1.11	2838	1.87	1.11	2818	1.85	1.11	2861	1.89
$\mathbf{5}\cdot\mathrm{F}^-$	1.05	2982	1.77	1.05	2895	1.74	1.04	3028	1.82
$\mathbf{6}\cdot\mathrm{F}^-$	1.07	2732	1.67	1.08	2536	1.57	1.06	2897	1.78
$\mathbf{7}\cdot\mathrm{F}^-$	1.12	2759	1.82	1.12	2753	1.81	1.11	2805	1.83
$\mathbf{8}\cdot\mathrm{F}^-$	1.05	2866	1.73	1.05	2822	1.70	1.05	2884	1.76
$\mathbf{9}\cdot\mathrm{F}^-$	1.08	2562	1.61	1.09	2444	1.56	1.07	2740	1.66

$r_{\mathbf{L}-\mathrm{H}}$in the $\mathbf{L}_\mathrm{n}$ internal $\mathrm{H_n}$ bond length (Å) in corners (**n**) **a**, **b**, and **c** (Figure B2).
$\nu_{\mathbf{L}\text{-H}}$ is the $\mathbf{L}_\mathrm{n}$ hydrogens ($\mathrm{H_n}$) bond stretch (cm^{-1}) in corners (**n**) **a**, **b**, and **c** (Figure B2).
$\mathrm{H}\cdots\mathrm{F}^-$ is the $\mathbf{L}_\mathrm{n}$ hydrogens ($\mathrm{H_n}$) distance to the F^- in corners (**n**) **a**, **b**, and **c** (Figure B2).

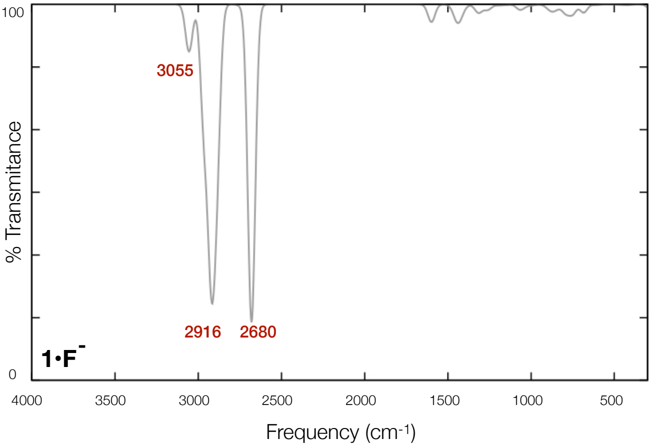

Figure B18 – Calculated Infrared Spectrum of compound $\mathbf{1}\cdot\mathrm{F}^-$. The stretch frequency ($\nu_{\mathbf{L}\text{-H}}$) associated with $\mathbf{H}_{in}$ can found in Table B7, along with $\mathrm{H}\cdots\mathrm{F}^-$, and **L**-H.

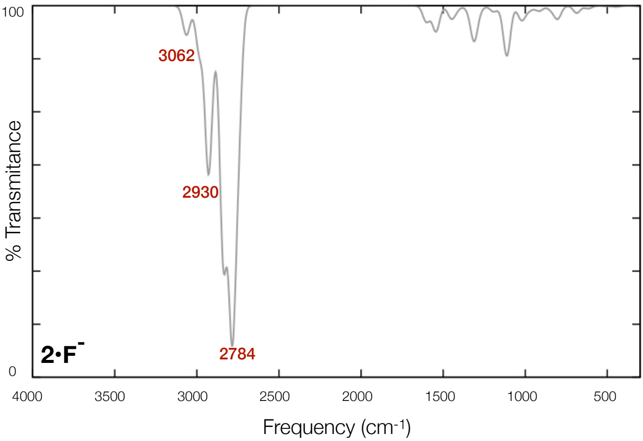

Figure B19 – Calculated Infrared Spectrum of compound **2**·F$^-$. The stretch frequency ($\nu_{\mathbf{L}\text{-H}}$) associated with **H**$_{in}$ can found in Table B7, along with H$\cdots$F$^-$, and **L**-H.

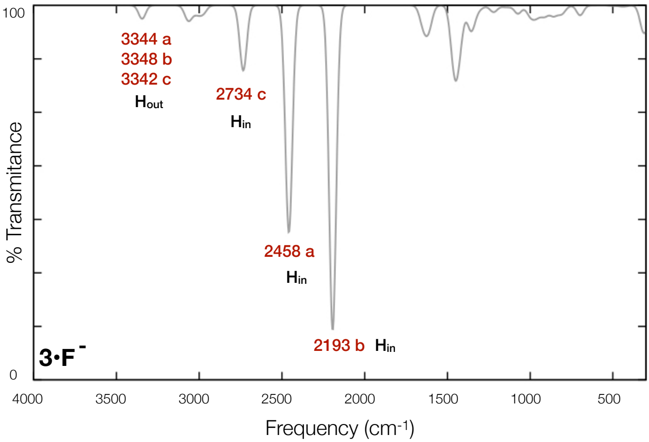

Figure B20 – Calculated Infrared Spectrum of compound **3**·F$^-$. The stretch frequency associated with **H**$_{in}$, H$\cdots$F$^-$, and **L**-H can found in Table B7. The **H**$_{out}$ frequencies, also assigned in the spectra, refer to the hydrogen bonded to **L** that remains outside the cavity.

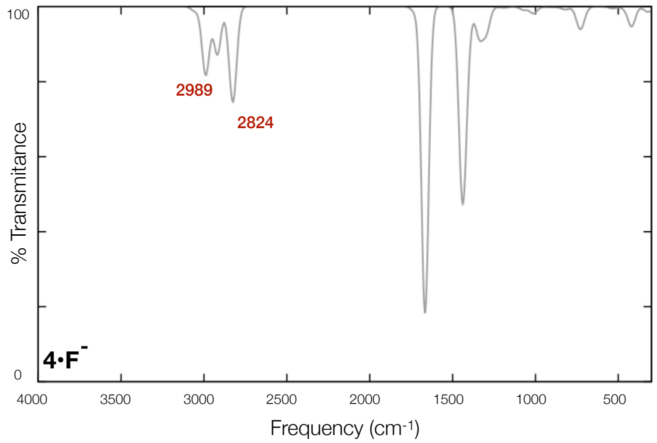

Figure B21 – Calculated Infrared Spectrum of compound **4**·F$^-$. The stretch frequency ($\nu_{\mathbf{L}\text{-H}}$) associated with $\mathbf{H}_{in}$ can found in Table B7, along with H$\cdots$F$^-$, and **L**-H.

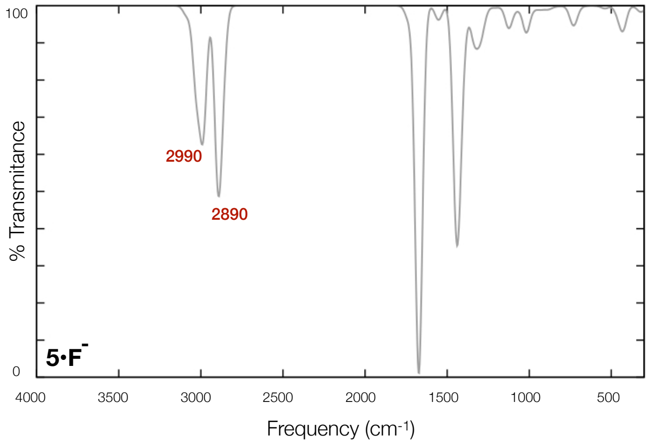

Figure B22 – Calculated Infrared Spectrum of compound **5**·F$^-$. The stretch frequency ($\nu_{\mathbf{L}\text{-H}}$) associated with $\mathbf{H}_{in}$ can found in Table B7, along with H$\cdots$F$^-$, and **L**-H.

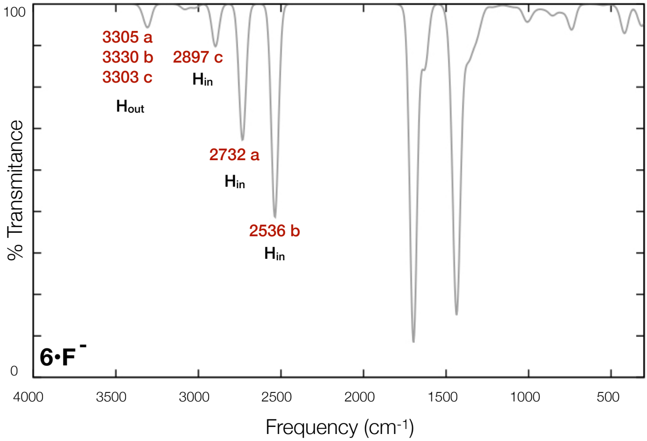

Figure B23 – Calculated Infrared Spectrum of compound **6**·F$^-$. The stretch frequency associated with $\mathbf{H}_{in}$, H$\cdots$F$^-$, and **L**-H can found in Table B7. The $\mathbf{H}_{out}$ frequencies, also assigned in the spectra, refer to the hydrogen bonded to **L** that remains outside the cavity.

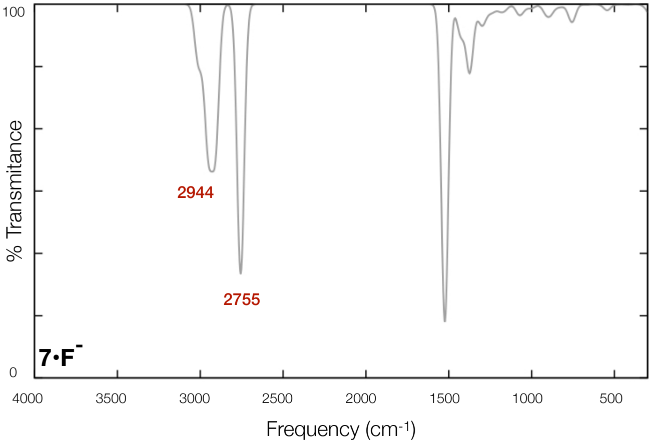

Figure B24 – Calculated Infrared Spectrum of compound **7**·F$^-$. The stretch frequency ($\nu_{\mathbf{L}\text{-H}}$) associated with $\mathbf{H}_{in}$ can found in Table B7, along with H$\cdots$F$^-$, and **L**-H.

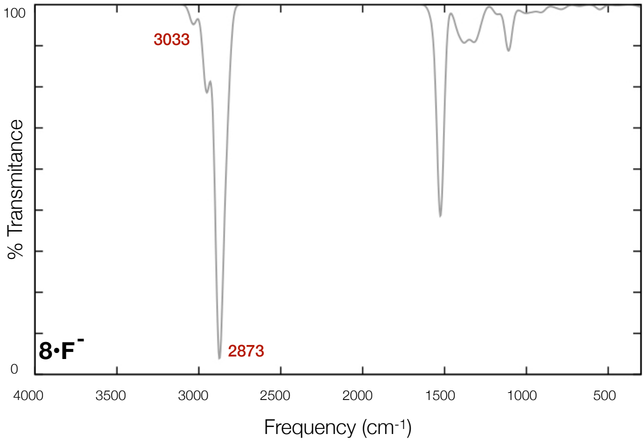

Figure B25 – Calculated Infrared Spectrum of compound **8**$\cdot$F$^-$. The stretch frequency ($\nu_{\mathbf{L}\text{-H}}$) associated with $\mathbf{H}_{in}$ can found in Table B7, along with H$\cdots$F$^-$, and **L**-H.

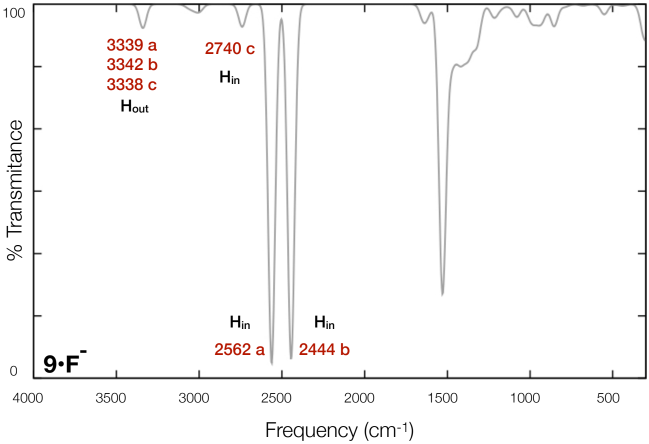

Figure B26 – Calculated Infrared Spectrum of compound **9**$\cdot$F$^-$. The stretch frequency associated with $\mathbf{H}_{in}$, H$\cdots$F$^-$, and **L**-H can found in Table B7. The $\mathbf{H}_{out}$ frequencies, also assigned in the spectra, refer to the hydrogen bonded to **L** that remains outside the cavity.

compound, **(3)** hindered rotations of low frequency modes are treated as vibrations, **(4)** equations are standard statistical mechanics for an ideal gas, and **(5)** all vibrations are strictly harmonic.

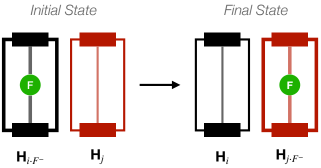

Figure B27 – Scheme representing initial and final states used to calculate the work, $\Delta\Delta G_{\mathrm{bind}}$, as relative binding energies. The $\Delta\Delta G_{\mathrm{bind}}$ is the energy required to take F^- from the **HG** system $\mathrm{H}_{i\cdots\mathrm{F}^-}$ (initial state), and place it inside the cavity of the empty **H** H_j (final state).

The standard thermodynamic variables related to energy are given for each molecule, and not for *ensembles*. Therefore we do not refer them here as thermodynamic values, as we do not account for a system of molecules. Despite this fact, the internal energy for one compound is calculated as stated by Equation B.1.

$$U = E_{el} + E_{ZPE} + E_{vib} + E_{rot} + E_{tras} \tag{B.1}$$

The considered E_{el} is the total electronic energy from the geometry optimization calculations which consider, in a simplistic representation, Equation B.2,

$$E_{el} = E_{kin-el} + E_{nuc-el} + E_{el-el} + E_{nuc-nuc} \tag{B.2}$$

the E_{ZPE} obtained from calculating vibrational frequencies, and it represents the zero temperature, E_{vib} considers the population of excited vibrational states, and it serves to correct E_{ZPE}, E_{rot} is the rotational thermal, and E_{tras} the translational thermal energy.

Enthalpies are obtained by the well-known Equation B.3,

$$H = U + k_B \cdot \mathrm{T} \tag{B.3}$$

in which k_B is Boltzmann's constant ($k_B = 1.380649 \times 10^{-23}\mathrm{J} \cdot \mathrm{K}^{-1}$), and to be able to provide the Gibbs free energies, the entropy is calculated as stated by Equation B.4,

$$\mathrm{T} \cdot S = \mathrm{T}(S_{el} + S_{ZPE} + S_{vib} + S_{rot} + S_{tras}) \tag{B.4}$$

considering that S_{el} is the electronic entropy, S_{vib} the vibrational entropy, S_{rot} the rotational entropy, and S_{trans} the translational entropy. To account for a correct rotational entropy, the rotational symmetry number (s_n) for nonlinear molecule must be considered as in Equation B.5, in which R is the ideal gas constant ($\mathrm{R} = 8.315\mathrm{J/mol} \cdot \mathrm{K}$).

$$S_{rot} = \mathrm{R} \cdot (\ln \frac{q_{rot}}{s_n} + 1.5) \tag{B.5}$$

All of the above equations leads us to obtain the free energies that were utilized in this work, as represented in Equation B.6.

$$G = H - \mathrm{T} \cdot S \tag{B.6}$$

The free energy for the fluoride did not need to be included in the calculations, as the anion does not participate in the initial, nor final state. Regardless, the F^- free energy was calculated by optimizing its electronic states as a closed shell anionic species, and the resulting free energy was calculated considering only the electronic, and translational components of the equations presented.

B.3.2 Conformational Analysis

The complete set of data regarding the EDA analysis for compounds $\mathbf{6}{\cdot}\mathrm{F}^-$ and its symmetric conformer $\mathbf{6}_{sym}{\cdot}\mathrm{F}^-$ is stated in Table

Table B8 – Energy Decomposition Analysis (kcal·mol^{-1}) and the Hirshfeld fragment charge analysis (a.u.) for compounds **6**·F^{-}, and the symmetric conformer $\mathbf{6}_{sym}$·F^{-} . Values in parenthesis correspond to the percentage of each stabilising contribution ($\Delta V_{\text{elstat}} + \Delta E_{\text{oi}} + \Delta E_{\text{disp}} = 100\%$).

HG	ΔE_{int}	ΔE_{prep}	BDE	ΔE_{Pauli}	ΔV_{elstat}	ΔE_{oi}	ΔE_{disp}	$q_{\mathbf{G}}$	$q_{\mathbf{H}}$
$\mathbf{6}_{sym}$ ·F^{-}	-341.89	38.22	-303.67	77.17	-345.79 *(83%)*	-67.55 *(16%)*	-5.72 *(1%)*	-0.798	2.798
6·F^{-}	-342.46	38.62	-303.84	78.63	-346.59 *(82%)*	-68.83 *(16%)*	-5.67 *(1%)*	-0.798	2.798

B8. For the sake of simplicity and purpose, the other **HG** systems are not included in this table. The top view for the NCI analysis for the stereoisomers is illustrated in Figure B28, which demonstrates the differences in the surface distribution, associated to the different regions within both isomers scaffold that are associated with non-covalent interactions. It is interesting to observe how the different conformations also affect the distribution of the colors in the plotted surfaces, indicating that the strength related to the **NCI** existent in each conformer is distributed differently.

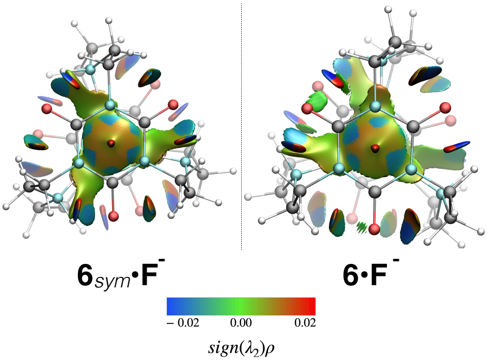

Figure B28 – Top view comparing the NCI for **HG**'s $\mathbf{6}_{sym}$ ·F^{-} (**CA**, $NH_2{}^{+}$) and **6**·F^{-} (**CA**, $NH_2{}^{+}$). Color-code: gray = carbon, cyan = nitrogen, and white = hydrogen.

The calculated infrared spectrum of $\mathbf{6}_{sym}$·F^{-} is presented by Figure B29, which shows marked in red, the stretching frequency ($\nu_{\mathbf{L}\text{-H}}$) peaks associated with the binding groups (**L**) hydrogens that do not interact with F^-, i.e., the hydrogens that are outside the cage ($\mathbf{H}_{out}$), and the internal hydrogens ($\mathbf{H}_{in}$), which interact directly with the coordinated fluoride.

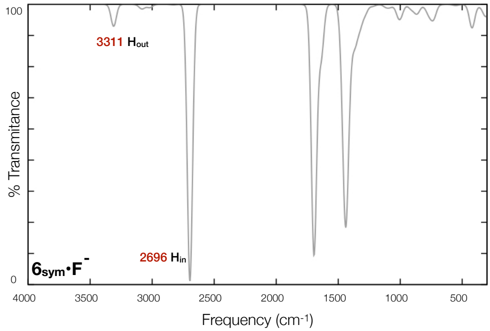

Figure B29 – Calculated Infrared spectrum displaying the $\nu_{\mathbf{L}\text{-H}}$ peaks for the external hydrogens ($\mathbf{H}_{out}$), and for the internal hydrogens ($\mathbf{H}_{in}$).

APPENDIX C – Computational Methods

The calculations presented in this work were mainly carried out in *Jupiter* Beowulf cluster, of the Molecular Structure Group $\langle \mathbf{GE}|\mathbf{EM} \rangle$ machine laboratory, which is localized in the Chemistry Department of the Federal University of Santa Catarina (UFSC). Calculations using the the Amsterdam Density Functional software, such as the EDA analysis and MEPs were performed at the *Tarsus* cluster of the University of Franca (UNIFRAN), which is located in Franca (SP), and belongs to the molecular electronics group of Prof. Dr. Renato Luis Tâme Parreira.

C.1 Density Functional Theory (DFT)

Hohenberg and Kohn (HK),[222, 223] in the mid 60s, have shown in the form of two theorems, that the electronic energy for a molecular system could be calculated if the exact form of the electrons spatial distribution, i.e., electron density ($\rho(r)$) was known. The HK theorem, enabled the use of a single variable, $\rho(r)$, to describe the energy of electrons with no reference of the wave function (ψ), and proved the existence of a functional $E[\rho(r)]$, which gives the exact ground state (GS) energy for the exact GS density. In their theorems, HK showed that the minimum energy could be reached for the exact density thus, giving rise to the variational principle to determine $\rho(r)$, and conceptually to obtain the exact GS energy. Their theorems stated that:

I. All quantum mechanical (QM) system observables (including energy) can be exactly calculated in the fundamental state as a functional of the GS electron density $\rho(r)$. In other words, the specification of the GS density $\rho(r)$ determines the external potential $\nu_{\text{ext}}(r)$ uniquely, which can be expressed as an equivalence between the potential $\nu_{\text{ext}}(r)$, the electron density $\rho(r)$, and the GS wave function Ψ_0:

$$\rho(r) \leftrightarrow \nu_{\text{ext}}(r) \leftrightarrow \Psi_0$$

II. The electronic density ($\rho(r)$) that minimizes the total energy corresponds to the exact electronic density of the system, that is, if the exact form of the functional $E[\rho(r)]$ is known, it is possible to obtain the minimum energy of the system variationally, which corresponds to the exact $\rho(r)$ of the system:

$$E[\rho_{\text{trial}}(r)] \geq E[\rho(r)]$$

A major problem from the HK theorem, however, remains to be solved: the unknown form of $\nu_{\text{ext}}(r)$ and $E[\rho(r)]$. The lack of knowledge about $E[\rho(r)]$ of HK theorems led to the development of the Density Functional Theory (DFT) by Kohn and Sham (KS),[223] which focused in providing the best form of the unknown density functional $E[\rho(r)]$, as presented in Equation C.1.

$$E[\rho(r)] = E_{\text{K}}[\rho(r)] + E_{\text{V}}[\rho(r)] + E_{\text{H}}[\rho(r)] + E_{\text{XC}}[\rho(r)] \tag{C.1}$$

Decomposing $E[\rho(r)]$ in Equation C.1, reveals that it depends on the sum of the kinetic energy of the electrons (E_{K}), the core-electron potential energy (E_{V}), the sum of the coulomb repulsion energy between electrons (E_{H}), and additionally, it depends on the exchange-correlation (XC) energy between the electrons (E_{XC}). The forms of E_{V} and E_{H} are well known from the HF method, but not so for E_{K} and E_{XC}. Therefore, this highlights the DFT ansatz, which is precisely to provide a density functional (DF), that describes the E_{K} and E_{XC} the best way possible to that the exact form of $E[\rho(r)]$ can be obtained.

C.1.1 Kohn-Sham Molecular Orbitals

Kohn-Sham Density Functional Theory (KS-DFT) showed to be an alternative route to solve the electronic problem. The advantage brought by DFT in contrast to other methods is that it takes into account XC effects, while also reducing computational cost. The reduced computational demand is made possible considering a system of non-interacting electrons moving under the effect of an attractive potential, i.e., the KS potential ($\nu_{KS}(r)$). The $\nu_{KS}(r)$ is defined with the exact one-electron density of the system of interest, which in principle produced the exact ground-state energy and density (Equation C.2).

$$[\hat{K} + \hat{\nu}_{\mathrm{KS}}]\varphi_i = [-\frac{1}{2}\nabla^2 + \nu_{\mathrm{KS}}(r)]\varphi_i = \varepsilon_{\mathrm{KS}}\varphi_i \tag{C.2}$$

The form of Equation C.2 is analogous to the HF electronic ansatz,[94] therefore it can also be solved self-consistently. The major difference from the HF method lies in the KS potential $\nu_{\mathrm{KS}}(r)$, which accounts for nuclear attractive potential ($\nu(r)$), electron-electron Coulombic repulsion ($\nu_{\mathrm{H}}(r)$), and an additional term that considers the exchange-correlation effects (ν_{XC}), as presented in Equation C.3.

$$\nu_{\mathrm{KS}}(r) = \nu(r) + \nu_{\mathrm{H}}(r) + \nu_{\mathrm{XC}}(r) \tag{C.3}$$

Since the form of $\nu_{\mathrm{XC}}(r)$ is unknown, DFT calculation reliability is heavily dependent on the choice of the density functional (DF). Most of modern DFT research is devoted to developing such XC density functional (XC-DF) approximations. However, this development was carried out with an unsystematic approach, which leads to the necessity of understanding the different functional strands developed, and in which cases they offer the best solution to the chemical problem.

C.1.2 Exchange-Correlation Density Functionals (XC-DF)

The remarkable success of DFT was due to the inclusion of a large part of the dynamic electron correlation via $\nu_{\mathrm{XC}}(r)$, which allowed to obtain higher accuracy in evaluating molecular properties, even comparable with sophisticated *ab initio* methods but with computational efforts similar to the ordinary HF method.[94, 96, 224] The vast number DF's created to approximate the form of $\nu_{\mathrm{XC}}(r)$, varying in quality, and depending on molecular systems and electronic properties studied, shows that DFT calculations can easily lead to inappropriate results that depend on the choice of XC-DF, since no universal DF is available so far to accurately describe a given electron density ($\rho(r)$). Over time, the many XC-DF's were constructed changing their form by adding more dependency on variables that influence $\nu_{\mathrm{XC}}(r)$ in order to reach higher accuracy, while increasing computational demand.

Density functionals vary from very simple to very complex, and can be classified into classes, such as the Local Density Approximation (LDA), Generalized Gradient Approximation (GGA), *meta*-GGA, *hybrid* GGA and *hybrid meta*-GGA, double-hybrid, etc. Mathematically, their forms can differ by the addition of theoretical and empirical parameters, or both. Perdew in 2001,[225, 226] created the "Jacob's ladder" to summarize the differences between XC-DF's (Figure C1). The idea in climbing "Jacob's ladder" is that each rung represents a different level of approximation towards higher accuracy results and dependency on $\rho(r)$. Therefore, each new rung adds to the former rung a new parameter that influences the XC-DF performance towards exact results. A major drawback with the higher rung's, however, is that computational cost os the sophisticated XC-DF increases considerably, and the difference in the quality of the obtained results is not always worth the cost.

The simplest model is the LDA, which was derived using a uniform gas electron gas density. In LDA, the electron density is assumed to be slowly varying, such that the XC energy can be calculated using formulas derived from a uniform $\rho(r)$. Significant improvements in the

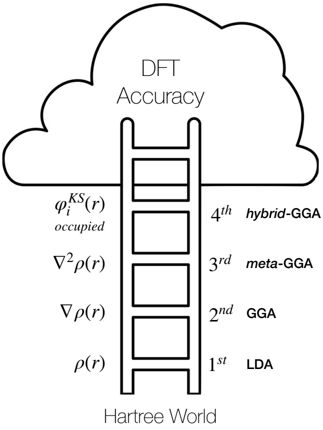

Figure C1 – The Jacob's ladder of DFT approximations to the exchange-correlation energy. The rungs represent different levels of approximation towards higher accuracy.

accuracy were obtained by making XC-DF also dependent on the first derivative of the density ($\nabla\rho(r)$), which led to the GGA functionals. The GGA method was proposed based on the idea of adding correlated movement by including $\nabla\rho(r)$ to the mathematical form of XC-DF. However, $\nabla\rho(r)$ in molecular systems is affected by the surrounding atoms, which makes the asymptotic character of $\nabla\rho(r)$ inappropriate for this description. Based on that, further refinements also added $\nabla^2\rho(r)$ as well as a percentage of exact HF exchange considerations ($\nu_{\mathrm{X}}(r, \varphi_i)$) into the functional by means of linear combination, thus leading to the form of a *hybrid* density functional.

The density functionals employed in this dissertation varied according to the chemical problem investigated. In Chapter II, which treated the molecular structure of the "iron maidens" employed the hybrid Perdew–Burke-Ernzerhof density functional **PBE0**,[122, 123] which has 25% of HF exchange along with the full PBE correlation energy, and is considered competitive with the widely used B3LYP, providing excellent accuracy. It is worth to mention that the popular *hybrid* functional

B3LYP, [183,188] which stands for Becke 3-parameter Lee-Yang-Parr, has excellent calculation performance in for structures, energies, and molecular properties,[224] and was the XC-DF used in the theoretical work of Mascal *et. al.*, which inspired the chapter of the cylindrophanes scaffold. Chapter III used **BP86**, which is a GGA XC-DF developed by Becke and Perdew,[188,189] and predicts excellent geometries and vibrational frequencies, performs well with transition metals and has been tested with different basis sets.[224]

C.1.3 Basis Functions and Sets

Non-covalent interactions between non-covalent groups is an excellent example in which different types of AOs can be combined to describe the molecular system better, as it leads to the polarization of the electron density of the interacting groups. To better describe the wave function of a specific molecular bonding situation, polarization functions can be used, which are denoted with an “*” or “**” symbol, or as (d) or (d,p), respectively. The polarization functions are contracted primitive Gaussian functions that result from the combination of s with p, and p with d orbitals that are added to specific atoms related to a particular polarization effect, and that cannot be specified only with s functions, such as the electron density of a hydrogen interacting with a negatively charged species.

Basis sets for the best description of anions, such as the fluoride anion which is studied in this work, diffuse functions, denoted by an “+” or “++” symbol, are required. Diffuse functions are "wider" than regular Gaussian functions, and they describe well electrons that are far from the nuclei, and accurate polarizabilities. Since the highest energy MOs in anions tend to be diffuse in terms of electron distribution, the best option for their description includes diffuse functions, such as the Pople[185] family of basis sets, e.g., the 6-31+G(d), which augments heavy atoms with additional consideration of on s, and one set of p functions.

In this regard, the robust Karlsruhe basis set **Def2-TZVP**[124,125,131], or valence triple ζ polarization, was employed for all the structures discussed in this research project. The **Def2-TZVP** basis set is well-known to yield in high accuracy results for computational calculations, meaning that its resulting values are not too far from the limit of accuracy that can be achieved for the DFT method. The choice for the **Def2-TZVP** basis set is also supported by the fact that they showed excellent accuracy when combined with the DFT BP86 exchange and correlation functional, also used in Part III. In the EDA analysis, calculated with the ADF2016[136–138] software, the TZ2P utilized is modeled with STOs, instead of GTOs, and for this reason, fewer STOs are needed to reach a certain level of accuracy, error associated with diffuse functions accounting for anions is diminished, and decreased computational cost is found.[227]

C.2 Dispersion Corrections

Intermolecular forces are the fundamental types of bonding interactions to study in supramolecular host-guest systems. The physical nature of these non-covalent interactions can be segmented into four major contributions:[57,228] ***(i)*** Pauli repulsive component that prevents molecules to collapse, ***(ii)*** an attractive or repulsive electrostatic interaction between permanent multipoles, ***(iii)*** polarization, which is the attractive interaction between a permanent multipole that induces an dipole on another molecule, and ***(iv)*** dispersion, which arises from instantaneous multipoles interactions. In weak interactions, such as the well-known Van der Waals (VdW) forces, dispersion effects are attributed to a stabilisation energy term.[192] By definition, dispersion interactions arise because the electron density of molecules is not static, i.e., in the presence of an external electromagnetic potential of a charged molecule, the electron density of the interacting molecules is reorganized, resulting in instantaneous attractive multipoles between the two species. This type of interaction between molecules is intimately related to the exchange-correlation energy in DFT, as it is caused by the correlation in the fluctuating polarizations of nearby particles.

The exchange-correlation energy E_{XC} is a relatively small part of a molecular system total energy, and it arises because electrons do not move randomly through the density, but instead, they have a correlated movement to avoid one another. Despite being a small contribution, it is needless to say that E_{XC} is undoubtedly very important to correctly address the physical nature of the **NCI**'s in molecular recognition and communication in supramolecular systems. KS-DFT functionals, including GGA and *hybrid*-GGA, are problematic in describing the electronic correlations in long distances weak **NCI** interactions. For a better description of dispersion interactions between two molecules, especially considering anions, dispersion corrections need to be added to the chosen DF.

Most DFT dispersion correction approaches include several empirical components.[94,96] The different methods currently available can be classified into four main classes: **(1)** vdW non-local density functionals, **(2)** semi-local density functionals, **(3)** DFT-D methods and **(4)** dispersion dispersion centered on atoms with monoelectronic potentials. Semi-classical corrections (DFT-D), treat complex dispersion interactions by semi-classical methods, then combine the resulting potential with a QM method, resulting in a hybrid classical-quantum hybrid scheme.[127,129,130,191,192] In the DFT-D scheme, the total energy (E_{tot}) of a system equals the sum of the KS energy (E_{KS}) and the dispersion correction (E_{disp}), as in Equation C.4.

$$E_{\text{tot}} = E_{\text{KS}} + E_{\text{disp}} \tag{C.4}$$

In Equation C.4, the total dispersion energy E_{disp} is the sum over all individual attractive atom pair (AB) contributions, which depends on ${C_n}^{\text{AB}}$ up to n^{th} dispersion coefficients order and the interatomic distance R_{AB}, exactly as in Equation C.5.

$$E_{\text{disp}}(R) = -\frac{C_6^{AB}}{R_{AB}^6} - \frac{C_8^{AB}}{R_{AB}^8} - \frac{C_{10}^{AB}}{R_{AB}^{10}} \cdots - \frac{C_{2n}}{R^{2n}} \tag{C.5}$$

More specifically in the DFT-D scheme, the general form of the E_{disp} treatment is written as in Equation C.6. In Equation C.6, the sum covers all atomic pairs of the system, and C_n^{AB} represents the adjustment of long-range distance interaction for molecular systems. This parameter is derived empirically, as well as calculated by methods that contribute to the required exchange and electronic correlation information. The factor s_n is typically used to adjust the correction to the repulsive behavior of the chosen functional.

$$E_{\text{disp}}^{\text{DFT-D}}(R) = \sum_{AB} \sum_{n} s_n \left[\frac{C_n^{AB}}{R_{AB}^n} \right] f_{damp}(R_{AB}) \quad n = 6, 8, 10, ... \tag{C.6}$$

The most up-to-date version of the DFT-D method is called DFT-D3, which has higher accuracy than previous versions, broad applicability, and fewer experimental parameters. Current implemented versions of dispersion corrections mostly are related to the specification of the dispersion coefficients in C_n^{AB} for the atomic pairs AB, and new forms to define atoms threshold radius, both calculated analytically.

C.3 Electron Density and Wave Function Analysis

Computational chemistry methods provide accurate approximations to the Schrødinger equation electronic ansatz. The molecular wave functions generated from the calculations enable the assessment of the electron distribution density, therefore to obtain the equilibrium energies and ground state geometries of a molecule.[94, 96]

The molecular wave function (Ψ) holds the information about all the chemical properties of the molecular system. Therefore, bonding analysis can only be done evaluating Ψ, and from this bond and orbital energies, as well as local topological analysis of the electron density surface is made possible. This, in turn, enables for the rationalization of the nature of chemical bonding, which the fundamental goal of theoretical chemistry.

C.3.1 Molecular Electrostatic Potential Maps (MEPs)

Molecular Electrostatic Potential maps (MEPs) are three-dimensional molecular surface mappings, obtained by multipole expansions and superposition of potentials, that are colored according to the energy values of total potential function $V_{\mathrm{MEP}}(\mathbf{r})$ on the surface level of the electron density (Equation C.7).[96]

$$V_{\mathrm{MEP}}(\mathbf{r}) = V_{\mathrm{nuc}}(\mathbf{r}) + V_{\mathrm{elec}}(\mathbf{r}) = \sum_{A} \frac{Z_A}{\|\mathbf{r} - \mathbf{r}_A\|} - \int \frac{\rho(\mathbf{r}^{'})}{\|\mathbf{r} - \mathbf{r}^{'}\|} d\mathbf{r}^{'} \quad \text{(C.7)}$$

Equation C.7 considers the atoms coordinates in the optimized structures, and assesses the interaction between the molecular system electron density and a point charge placed at position r. The total potential function ($V_{\mathrm{MEP}}(\mathbf{r})$), highlights the local electrostatic potential energies on the isosurface of a molecule. Isosurfaces are radial values of electron density that best approximate the size and shape of the molecule, therefore larger molecules with more electrons have larger isosurface values than small molecules with fewer electrons. The radial value of the isosurface is the radius value that will be used in the $V_{\mathrm{MEP}}(\mathbf{r})$. Regions of the 3D isosurface created are colored according to the potential energy values, which indicate the absence or concentration of negative charges. Therefore, high electrostatic potential is relative to the absence of electrons (blue), and lower electrostatic potential corresponds to the area of highest electron concentration (red), and intermediate values are colored according to the gradient of colors between red and blue. This visual aspect of MEPs providing a qualitative useful electronic characteristic of molecules that are to predict molecular reactive behavior, polarity, and electronegativity, to determine how molecules are likely to interact.[66,229]

C.3.2 Energy Decomposition Analysis (EDA)

Energy Decomposition Analysis (EDA) combines classical and quantum chemical concepts, to provide quantitative expressions of energy terms associated with chemical bonding process.[200,201,205,206] The theoretical background of variational EDA was independently carried out in the 70s by Morokuma [230], and by Ziegler and Rauk[202] in their Extended Transition State (ETS) scheme, which suggested that chemical bond formation can be interpreted by the sum of three meaningful energy terms that physically explain the bond energy stabilisation.

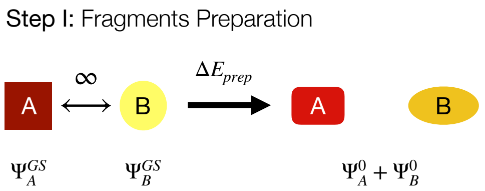

Figure C2 – EDA scheme presenting the first major step in the bond energy decomposition. In **Step I** the preparation energy (ΔE_{prep}) represents the geometry and electron density distortions of fragments **A** and **B**, into the final configuration they adopt in **AB**.

In the EDA scheme, the bond energy is assessed between two interacting fragments **A** and **B** that form a molecule **AB**. The bond formation process is separated in two major steps, the preparation energy (**Step I** in Figure C2), and the interaction energy (**Step II** in Figure C3). As presented in the scheme of Figure C3, **Step II** is further separated into three sub-steps. The bond dissociation energy (BDE), is composed of the energy changes from the preparation and interaction (Figure C4), thereby is obtained by adding ΔE_{prep} (ΔE_{prep}) with ΔE_{int} (ΔE_{int}) energy terms (Equation C.8).

$$-\mathbf{BDE} = (E_{\mathrm{A}} + E_{\mathrm{B}}) - E_{\mathrm{AB}} = \Delta E_{\mathrm{int}} + \Delta E_{\mathrm{prep}} \tag{C.8}$$

In **Step I** of Figure C2, the ground state (GS) configuration of the fragments **A** and **B** is distorted to the specific reference states **A** and **B** they have in the molecule **AB** ($\Psi_{\mathrm{A}}^{\mathrm{GS}} \quad \Psi_{\mathrm{B}}^{\mathrm{GS}} \rightarrow \Psi_{\mathrm{A}}^{0} + \Psi_{\mathrm{B}}^{0}$). The strain energy associated to this step is the ΔE_{prep} term, and accounts for geometry distortion and electronic changes (Equation C.9).

$$\Delta E_{\mathrm{prep}} = (\Psi_{\mathrm{A}}^{0} + \Psi_{\mathrm{B}}^{0}) - (\Psi_{\mathrm{A}}^{\mathrm{GS}} + \Psi_{\mathrm{B}}^{\mathrm{GS}}) \tag{C.9}$$

The promoted fragments **A** and **B** interact to form **AB** ($\Psi_{\mathrm{AB}}^{\mathrm{GS}}$). In **Step II**, compound **AB** interaction energy (ΔE_{int}) term is obtained by the energy difference between the ground state $\Psi_{\mathrm{AB}}^{\mathrm{GS}}$, and the prepared fragments Ψ_{A}^{0} and Ψ_{B}^{0}, as presented by Equation C.10. The ΔE_{int} energy is further partitioned into the well-defined energy terms $\Delta V_{\mathrm{elstat}}$, $\Delta E_{\mathrm{Pauli}}$, and ΔE_{oi}.

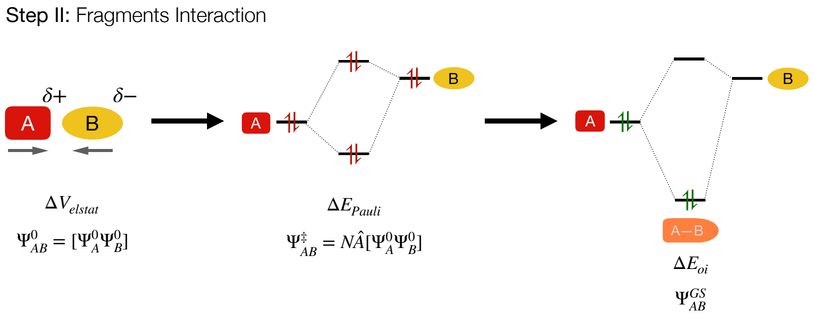
Step II: Fragments Interaction
$\delta+$
$\delta-$
A
B
ΔV_{elstat}
$\Psi_{AB}^{0} = [\Psi_{A}^{0}\Psi_{B}^{0}]$
A
B
ΔE_{Pauli}
$\Psi_{AB}^{\ddagger} = N\hat{A}[\Psi_{A}^{0}\Psi_{B}^{0}]$
A
B
A–B
ΔE_{oi}
Ψ_{AB}^{GS}

Figure C3 – EDA scheme presenting the second major step in the bond energy decomposition. **Step II** shows how the interaction (ΔE_{int}) energy is decomposed into the three sub-steps of the electrostatic stabilisation ($\Delta V_{\mathrm{elstat}}$), Pauli repulsion ($\Delta E_{\mathrm{Pauli}}$), and orbital stabilisation (ΔE_{oi}).

$$\Delta E_{\text{int}} = \Psi_{\text{AB}}^{\text{GS}} - (\Psi_{\text{A}}^{0} + \Psi_{\text{B}}^{0}) = \Delta V_{\text{elstat}} + \Delta E_{\text{Pauli}} + \Delta E_{\text{oi}} \tag{C.10}$$

The three sub-steps that represent ΔE_{int} term are shown in **Step II** of Figure C3. First, the distorted fragments **A** (Ψ_{A}^{0}) and **B** (Ψ_{B}^{0}) are brought from infinity into the position they adopt in the **B**, but no optimisation of the resulting wave function is done. The energy related from the fragments approximation is the quasiclassical electrostatic interaction (ΔV_{elstat}), and results from the overlap of the electrons densities ρ_{A}^{0} and ρ_{B}^{0} $\rho(r)$. The resulting ΔV_{elstat} energy term, commonly stabilising, is the wave function product $[\Psi_{\text{A}}\Psi_{\text{B}}]$ (Equation C.11), and does not obey the Pauli exclusion principle. Since $[\Psi_{\text{A}}\Psi_{\text{B}}]$ is not antisymmetric, the product wave function must be antisymmetrized ($\hat{\mathcal{A}}$) and normalized (N), leading to the intermediate wave function $\Psi_{\text{AB}}^{\ddagger}$, as shown in Equation C.11.

$$N\hat{\mathcal{A}}\Psi_{\text{AB}}^{0} = N\hat{\mathcal{A}}[\Psi_{\text{A}}\Psi_{\text{B}}] = \Psi_{\text{AB}}^{\ddagger} \tag{C.11}$$

The resulting orbitals from the orthonormalized $\Psi_{\text{AB}}^{\ddagger}$ are obtained from the combination of occupied and virtual, fragment orbitals. The amount of energy that is required to obtain $\Psi_{\text{AB}}^{\ddagger}$ is the destabilising ΔE_{Pauli} energy term that results due to an increase in the electrons kinetic energy, and electron-electron repulsion. In the final step, the $\Psi_{\text{AB}}^{\ddagger}$ molecular orbitals are allowed to relax and the optimal wave function $\Psi_{\text{AB}}^{\text{GS}}$, representing the ground state for **AB**. The stabilising orbital energy (ΔE_{oi}) term results from the difference of the $\Psi_{\text{AB}}^{\ddagger}$ density, $\rho_{\text{AB}}^{\ddagger}$, to the density of the ground state $\Psi_{\text{AB}}^{\text{GS}}$, i.e., $\rho_{\text{AB}}^{\text{GS}}$, which arises from donor-acceptor orbital charge transfer, polarization, and pairwise electron bonding stabilisations.

$$\Delta E_{\text{orb}} = E[\rho_{\text{AB}}^{\text{GS}}] - [\rho_{\text{AB}}^{\ddagger}] \tag{C.12}$$

This work considers ΔE_{int} as the $\mathbf{A}\cdots\mathbf{B}$ non-covalent interactions in a supramolecule **AB**. Nevertheless, any interacting molecular fragments, regardless of composing or not a supramolecule or complex, can be carried out with EDA, as it was also proposed in the fragmentation scheme of the cylindrophanes. The DFT-D3 level of theory utilized here accounts for dispersion corrections. Therefore a fourth term related to dispersion stabilisation (ΔE_{disp}) energy is included in ΔE_{int}, as shown in Equation C.13, and which is the Grimme's[191] empirical dispersion correction for the long-range dispersion effects between the interacting fragments.

$$\Delta E_{\text{int}} = \Delta V_{\text{elstat}} + \Delta E_{\text{Pauli}} + \Delta E_{\text{oi}} + \Delta E_{\text{disp}} \tag{C.13}$$

The bonding situation in **AB** can be connected to an actual physical observable by means of the bond dissociation energy (BDE) obtained. The BDE term involves geometry and electronic relaxation of the fragments **A** and **B** from **AB**, into free species **A** and **B** in their equilibrium geometry of the electronic GS, represented by $\Psi_{\text{A}}^{\text{GS}}$ and $\Psi_{\text{B}}^{\text{GS}}$, as in Equation C.9. The energy levels diagram in Figure C4, shows the energy levels related to the EDA method, as described also by Figure C2, and C3.

In Figure C4, the dashed line representing fragments **A** and **B** ground state, is meant to represent the different energies that **A** and **B** n their fundamental configuration. The stabilising energy terms appear below the energy lines and the destabilising above. The wave functions associated with each step are provided at the right side of the energy diagram.

C.3.3 Non-Covalent Index (NCI$_x$)

Non-Covalent Interactions index (NCI$_x$), calculated with the NCIPLOT code, is a non-covalent interaction descriptor tool recently developed by Johnson *et. al.*,[120] which enables to locally identify, and

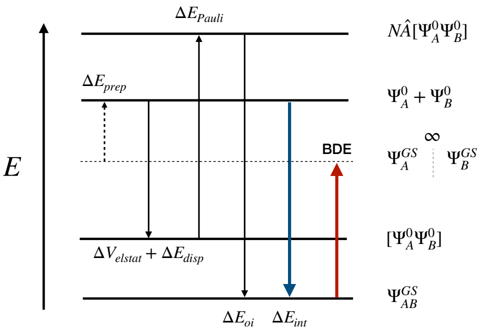

Figure C4 – Energy levels diagram, showing the relationship betwen all the enrgy terms derived from the EDA method. Figure adapted from the work of Contreras *et. al.*.[17]

classify non-covalent interactions in a given molecular system, by means of the electron density ($\rho(r)$) and its derivatives ($\nabla\rho(s)$). The visual assessment of non-covalent interactions (**NCI**'s) is made possible by the local topological analysis of the reduced density gradient ($s(r)$) (Equation C.14), which is a fundamental dimensionless quantity that describes non-homogeneous electron distribution, indicating characteristic zones of low $\rho(r)$ within the molecular framework, that are either involved in attractive (dispersive, electrostatic) or repulsive (steric), intra and intermolecular interactions (see color label (bottom) in Figure C6).

$$s(r) = \frac{1}{2(3\pi^2)^{1/3}} \frac{|\nabla\rho(r)|}{\rho(r)^{4/3}} \tag{C.14}$$

Particular **NCI** zones are identified by the regions in between bonded and non-covalent atoms that have reduced $\rho(r)$, found typically at $\nabla\rho(s)$ critical points (CPs), where $s(r)$ diverges ($\lim_{\rho(s)\to 0} s(r) = +\infty$). Thus, in a two-dimensional plot of $s(r)$ as a function of $\rho(r)$ throughout the structure of two interacting molecules, the appearance of steep peaks at low density characterizes the **NCI**'s (see dashed region in Figure C5). The three-dimensional query for the spatial coordinates that relate to these peaks retrieves the surfaces that represent the **NCI**'s in regions where $\rho(r)$ is low ($\rho(r) < 0.06$).

The different types of **NCI** are classified according to their nature and strength, i.e., they can be attractive, dispersive, and repulsive, and their magnitudes can vary from strong to weak. The NCI_x distinguishes the different types of **NCI**'s evaluating the sign of second eigenvalue of the density Hessian (λ_2) times the $\rho(r)$.

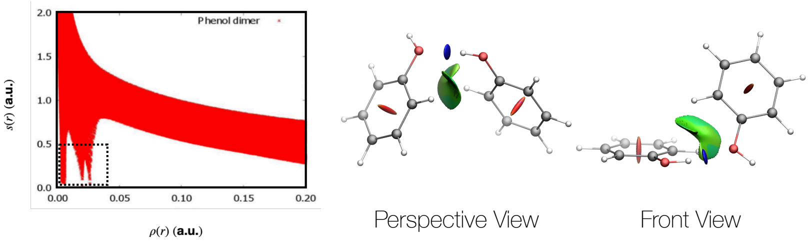

Figure C5 – NCIPLOT (left) of the reduced gradient ($s(r)$), as a function of the electron density ($\rho(r)$). Interacting phenol dimer (right), in a perspective, top, and front view, respectively. Figure adapted from the work of Contreras *et. al.*.[17]

To illustrate that, Figure C5 and Figure C6 show the **NCI**'s of phenol dimers interacting. In Figure, C5 the dashed area at the ploted graph of $s(r)$ by $\rho(r)$ (left) represents the steep peaks related to low density regions that enables to create the **NCI** surfaces in the dimers (right). Figure C6 presents the NCIPLOT at the top-left of the image, and the phenol dimers at the top-right. At the bottom there is a BGR gradient of colors that represents the the values for $s(s)$, $\rho(r)$, λ_2, and for $sign(\lambda_2) \cdot \rho(r)$, associated to their colors and to the types of interactions related to them. The interacting phenol dimer shows three different types of **NCI**'s: **(i)** intra-annular steric repulsion (small green-red ellipsoid surface), **(ii)** Van der Waals (VdW) $\mathrm{H} \cdots \mathrm{H}$ and π-π proximities (green surface), and **(iii)** strong H-bond between the hydroxy groups (rounded blue surface).

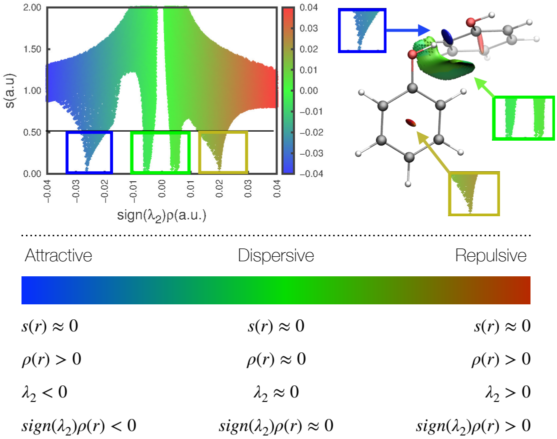

Figure C6 – NCIPLOT (top-left) of the reduced gradient ($s(r)$), as a function of sign of the second Hessian eigenvalue of the electron density ($sign(\lambda_2) \cdot \rho(r)$). Interacting phenol dimer (top-right), indicating the relationship of the **NCI** colored surfaces, with the steep peaks generated at the CPs ($\nabla\rho(s)$), and colored according to the sign of $\nabla^2\rho(r)$. BGR gradient of colors that classify the type, and **NCI**'s strength. Figure adapted from the work of Contreras *et. al.*.[17]

The sign of the Laplacian of density ($\nabla^2\rho(r)$) indicates the direction of the net gradient ($\nabla\rho(s)$) flux. Therefore, if $\nabla^2\rho(r) < 0$, then $\nabla\rho(s)$ density inflow an infinitesimal volume around a point r. Likewise, if $\nabla^2\rho(r) > 0$, $\nabla\rho(s)$ density outflow an infinitesimal volume around a reference point. This indicates if $\rho(r)$ is concentrated, or depleted in r, relative to the surroundings. The quantity related to the electron densities at the CPs ($\nabla\rho(s)$) differs the types of **NCI** according to their strength. Moreover, distinction between attractive and repulsive interactions are done by analyzing the accumulation or depletion of $\rho(r)$ in the plane perpendicular to the interaction, which is only possible by looking into the second eigenvalue of the electron-density Hessian (λ_2), which is the second derivative matrix of $\rho(r)$.

For instance, the Hessian eigenvalues being considered in the case of the interacting phenol dimers (Figures C5 and C6), differs the nature of the **NCI**'s by color (BGR) depending on the values of λ_2: steric benzene-ring interactions ($\lambda_2 > 0$), dispersive phenyl rings interaction ($\lambda_2 \approx 0$), strong H-bond ($\lambda_2 < 0$). Therefore, the different colors attributed to the types of **NCI**'s and their strength, is made possible due to the sign of the second eigenvalue ($sign(\lambda_2) \cdot \rho(r)$), together with the typical curvature (see areas indicated in the plot (top-left) of Figure C6).

C.3.4 Natural Bond Orbital (NBO)

The Natural Bond Orbital (NBO) analysis, developed Weinhold and co-workers in the mid-1980s,[75, 118, 119] is a comprehensive method to asses orbitals interactions based on a practical computational wave function (ψ) evaluation of the molecular system of interest. In contrast to Molecular Orbital (MO) theory, which does not assume the form of ψ, the NBO method derives ψ based on the approximation method used to optimize the molecular system, i.e., DFT, variational, and perturbative methods.

The fundamental concept of the natural orbital (NOs) was first introduced by Per-Olov Löwdin in 1955,[231], which consisted of a particular method to select one-particle orbitals. Conceptually, the natural orbital are obtained as linear combinations of atomic orbitals (AOs) that proceeds sequentially through hybridization (natural hybrid orbitals (NHO) formation), covalent bonding (natural bonding orbitals (NBOs) formation), and donor-acceptor delocalisation (natural local molecular orbitals (NLMOs) formation), as follows according to the canonical set of natural localized orbitals that are intermediate to atomic orbitals (AO) and molecular orbitals (MO):

$$\text{AOs} \rightarrow \text{NAOs} \rightarrow \text{NHOs} \rightarrow \textbf{NBOs} \rightarrow \text{NLMOs} \rightarrow \text{MOs}$$

Mathematically, natural orbitals Θ_i can be defined stated by

Equation C.15. In this equation, the eigenvalue p_k represents the occupancy of the eigenfunction Θ_k for the molecular electron density operator $\hat{\Gamma}$ of Ψ. The density operator $\hat{\Gamma}$ is the Hermitian 1-electron projection operator of the N-electron probability distribution ($|\Psi_2|$), which ensures that the "constructed" NOs form a complete orthonormal set of orbitals.

$$\hat{\Gamma}\Theta_k = p_k\Theta_k \quad (k = 1, 2, 3, ...) \tag{C.15}$$

Canonical orbitals obtained from self-consistently are hard to asses as they tend to be delocalised. In contrast, the fact that NOs are built by unitary transformations of occupied orbitals performed with no change of Ψ, leading to a new set of easier-to-asses purposely "constructed" orbitals, that is as legitimate as the canonical ones. The process by which NOs are built has the advantage of requiring fewer determinants when compared with other techniques, while still accounting for correlation effects.

The idea behind the "construction" of NBOs is that the localization of the canonical orbitals transforms them into center orbitals, bonding orbitals, core orbitals, and isolated pairs, providing the most accurate possible "natural Lewis-like" set of orbitals from ψ. The term localization refers to the fact that linear combination coefficients are chosen such that the new set of natural orbitals resembles the initial set as much as possible so that the resulting natural orbitals are not much different from the original AOs. The Lewis-like bonding pattern of electron pairs in NBOs means that they have "maximum occupancy" ($\approx 1 or 2$), which links them directly to valency and other bonding concepts such as hybridization, hyperconjugation, orbitals s, p, d, and f percentage character, etc. Further analysis of the NBOs in terms of population analysis derives the partial atomic charges (NPA), which are helpful to ensure the charge transfer description consistency between atoms.[118, 118]

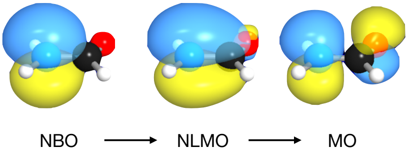

Figure C7 – Three linear combinations of NOs, showing visually the difference between NBOs, NLMOs and MOs. Illustration reproduced based on images from the NBO program website.[18]

The donor-acceptor interactions between occupied natural orbitals **i** (donor) and an empty anti-ligand **j** (acceptor) can be calculated through the determination of the stabilisation of the system by a second-order interaction ($\Delta E^{(2)}_{i \to j^*}$), to explain the final NBO wave function. The energy stabilisation of the donor-acceptor interactions is estimated by the second order perturbation theory analysis of the Fock matrix ($\hat{F}$), or the Kohn-Sham (KS) operator since this work is a DFT based computational study, according to Equation C.16.

$$\Delta E^{(2)}_{i \to j^*} = -q_i \frac{\left\langle \phi_i | \hat{F} | \phi_j^* \right\rangle^2}{\varepsilon_j^* - \varepsilon_i} \tag{C.16}$$

In Equation C.16, q_i is the occupation of the donor NBO, ϕ_i and ϕ_j^* are the donor and acceptor NBOs, and ε_i and ε_j^* are their energies, respectively.

Nevertheless, the NBO method usefulness to understand the aforementioned valency and bonding concepts of a chemical system, the NBO procedure is only an orbital-based conceptual model, whose utility is limited to cases where Lewis structures do not poorly represent the chemical compounds being analysed. It just provides a partial orbital view of bonding situations.

C.3.5 Quantum Atoms in Molecules (QTAIM)

QTAIM is a rigorous charge density topology analysis that defines chemical bonding and molecular structure based on electron density ($\rho(\vec{r})$) that was developed in the early 1960s by Richard Bader.[232] Since $\rho(\vec{r})$ is a three dimensional function it may be analysed in terms of its topology, i.e., maxima, minima and saddle points.[94] The local maxima points are associated to the nuclei of the atoms, which act as electron density local attractors, therefore driving the gradient of the electron density ($\nabla\rho(r)$) in each point of the space, towards the "strongest" attractor, or nuclei.

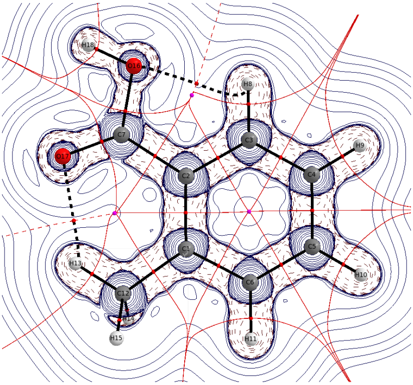

Figure C8 – Laplacian distribution of *o*-methylbenzoic acid: solid blue lines indicate charge depletion ($\nabla^2\rho < 0$), dashed blue lines indicate charge accumulation ($\nabla^2\rho > 0$), red spheres are bond critical points (BCPs), purple spheres are ring critical points (RCP), black lines are bond paths, red lines are zero flux surfaces.[19]

The atoms spatial disposition in the molecular architecture implicates in the $\nabla\rho(r)$ direction, and the resulting drawn regions within the atoms define the atomic basins. Stationary points that define zero flux regions are obtained by the gradient of the electron density ($\nabla\rho(\vec{r}) = 0$) and are denominated as critical points (CPs). In accord to the AIM theory, there must exist a BCP, in order for two atoms to be bonded, and a bonding path connecting two atoms, being that the bonding paths are regions where the electron density is the highest than in any other neighboring line between them. For instance, Figure C8 illustrates the topology of an *o*-methylbenzoic acid showing the atomic basins, according to Bader's QTAIM Theory.[19] The bond critical point (BCP) is near the proton, indicating that the electron density is mostly is related to the oxygen atom and that the lower charge concentration in this bond reflects the weak bond. Other critical chemical properties can be obtained employing the QTAIM method, such as by integrating the atomic basins, unambiguously assigning the atoms electrons, which yields their atomic charges, and the value of the electron density at the BCPs correlates with the bond order and strength.[19,117]

C.4 Isodesmic and Homodesmotic Reactions

The term "isodesmic" was introduced by the Quantum chemistry specialists Here, Ditchfield, Radom, and Pople in their publication of 1970 [233,234] Isodesmic reactions are hypothetical reactions rationally formulated to asses relative stability, strain, the heat of formation and repulsion between functional groups in a molecular structure.[144–147] The method was first introduced in the 1970s by Hehre *et. al.*,[233,234] to explain their molecular theory of bond separation, in the attempt to quantitatively estimate relative stabilities of organic compounds. The fundamental approach to create an isodesmic reaction is to propose different fragmentation schemes of the compound of interest, conserving both the number and types of bonds, in a balanced chemical equation.[94,96] Thus, the hypothetical reaction, such as in Equation C.17, can consider any molecules A, B, C and D, and the corresponding number of moles m, n, r, and s to balance the reaction. Equation C.18 shows an example of an isodesmic reaction.

$$mA + nB \rightarrow rC + sD \tag{C.17}$$

$$\mathrm{CH_3}^- + \mathrm{CH_3X} \rightarrow \mathrm{CH_4} + \mathrm{CH_2X}^- \quad \mathrm{X} = \mathrm{F, Cl, Br, I} \tag{C.18}$$

The reactants "broken" bonds must be essentially the same types of bonds that are formed in the products, and the heat of formation energy that is calculated depends on the difference in energy of the bonds being broken and formed, taking into account orbital hybridization. The versatility of the isodesmic reactions method enables one to propose various meaningful fragmentations of a molecular structure to build hypothetical reactions, and asses the energies associated to the reactions proposed based on the fragments, and the original molecule. Therefore, the key point is that the original molecular fragments energy differs from the energy of the fragments optimized "freely", i.e., without the constraints of the atomic disposition in the molecule being studied.

$$cyclo{-}(\mathrm{CH_3})_3{+}3\mathrm{CH_3}{-}{-}\mathrm{CH_3} \rightarrow 3\mathrm{CH_3CH_2CH_3} \quad \Delta\mathrm{H} = -110.9\ \mathrm{kJ}{\cdot}mol^{\text{-}1} \tag{C.19}$$

Homodesmotic reactions are a subclass of isodesmic reactions. In this subclass, the reactants and products contain equal numbers of carbon atoms in corresponding states of hybridization and proportions. With homodesmotic reactions it is easier to evaluate strain energy in rings. For instance, Equation C.19 shows an example of homodesmotic reaction of cyclopropane. Note that all C atoms are sp^2 hybridized, and there are six CH_3 and three CH_2 groups on each side of the equation. Since all bond types and groups are matched, ΔH represents the strain energy in the cyclopropane ring.